2021

Molecular Mechanisms Regulating Optic Fissure Fusion During Zebrafish Eye Development

Megan Weaver
University of Kentucky, mlweav2@g.uky.edu
Author ORCID Identifier:
https://orcid.org/0000-0002-6787-8040
Digital Object Identifier: https://doi.org/10.13023/etd.2021.021

STUDENT AGREEMENT:

I represent that my thesis or dissertation and abstract are my original work. Proper attribution has been given to all outside sources. I understand that I am solely responsible for obtaining any needed copyright permissions. I have obtained needed written permission statement(s) from the owner(s) of each third-party copyrighted matter to be included in my work, allowing electronic distribution (if such use is not permitted by the fair use doctrine) which will be submitted to UKnowledge as Additional File.

I hereby grant to The University of Kentucky and its agents the irrevocable, non-exclusive, and royalty-free license to archive and make accessible my work in whole or in part in all forms of media, now or hereafter known. I agree that the document mentioned above may be made available immediately for worldwide access unless an embargo applies.

I retain all other ownership rights to the copyright of my work. I also retain the right to use in future works (such as articles or books) all or part of my work. I understand that I am free to register the copyright to my work.

REVIEW, APPROVAL AND ACCEPTANCE

The document mentioned above has been reviewed and accepted by the student's advisor, on behalf of the advisory committee, and by the Director of Graduate Studies (DGS), on behalf of the program; we verify that this is the final, approved version of the student's thesis including all changes required by the advisory committee. The undersigned agree to abide by the statements above.

Megan Weaver, Student

Dr. Jakub Famulski, Major Professor

Dr. David Weisrock, Director of Graduate Studies

Molecular Mechanisms Regulating Optic Fissure Fusion During Zebrafish Eye Development

---

DISSERTATION

A dissertation submitted in partial fulfillment of the
requirements for the degree of Doctor of Philosophy in the
College of Arts and Sciences
at the University of Kentucky

By
Megan Weaver
Lexington, Kentucky
Director: Dr. Jakub Famulski, Professor of Cell and Developmental Biology
Lexington, Kentucky
2021

https://orcid.org/0000-0002-6787-8040

ABSTRACT OF DISSERTATION

Molecular Mechanisms Regulating Optic Fissure Fusion During Zebrafish Eye Development

Vertebrate retinal development requires timely and precise fusion of the optic fissure. Failure of this event leads to congenital vision impairment in the form of coloboma. Recent studies have suggested hyaloid vasculature to be involved in OF fusion. In order to examine this link, we analyzed optic fissure fusion and hyaloid vasculogenesis in the zebrafish pax2a noi mutant line. We first determined that pax2a$^{-/-}$ embryos fail to accumulate F-actin in the optic fissure prior to basement membrane (BM) degradation. Furthermore, using 3D and live imaging we observed reduced OF hyaloid vascularization in pax2a$^{-/-}$ embryos. When examining the connection between pax2a loss of function and hyaloid vasculature, we observed significant reduction of *talin1* expression, a regulator of hyaloid vasculature. In addition, cranial VEGF expression was found to be reduced in pax2a$^{-/-}$ embryos. Pharmacological inhibition of VEGF signaling phenocopied the pax2a$^{-/-}$ vasculature, F-actin and BM degradation phenotypes. Lastly, we determined that optic fissure associated hyaloid vasculature is a source of *mmp2, mmp14a and mmp14b* expression and showed that mmp2 is functionally necessary for degradation of optic fissure BM. We compared transcriptomic profiles between pax2a$^{-/-}$ and wildtype (WT) embryos. We sought to validate and investigate those targets which were thought to be of importance to the molecular machinery involved in fusion, particularly those involving the actin cytoskeleton and angiogenesis. This analysis uncovered a novel connection between regulation of angiogenesis and fusion. Loss of pax2a resulted in increased expression of an anti-angiogenic protease, ADAMTS1. 3D confocal and live imaging of retinal hyaloid vascularization in Tg[kdrl:mCherry] embryos indicated a significant deficit in ADAMTS1 mRNA injected embryos and phenocopied the pax2a mutant phenotype. We have also uncovered preliminary evidence that certain actin associated proteins are also differentially regulated, particularly rho-associated protein kinase (ROCK). Taken together we propose a pax2a driven mechanism that ensures proper and timely hyaloid vasculature invasion of the OF by negatively regulating ADAMTS1 expression. This enables the timely hyaloid vascularization of the

retina which in turn directly signals to initiate fissure fusion via cytoskeletal rearrangements and providing the BM remodeler mmp2.

KEYWORDS: Optic fissure fusion, coloboma, basement membrane, F-actin, hyaloid vasculature, pax2

Megan Weaver

(Name of Student)

01/15/2021

Date

Molecular Mechanisms Regulating Optic Fissure Fusion During Zebrafish Eye Development

By
Megan Weaver

Dr. Jakub Famulski
Director of Dissertation

Dr. David Weisrock
Director of Graduate Studies

01/15/2021
Date

DEDICATION

To Ollie, Theodore, and Lincoln. I did this all for you

TABLE OF CONTENTS

LIST OF TABLES

LIST OF FIGURES

CHAPTER 1. INTRODUCTION

The most challenging thing that will ever occur to you happened long before you had a conscious thought. You became you by completely building yourself from a single, solitary cell. Development of an organism is no easy feat, it begins with a single cell which divides into many. These cells then undergo specialization to become unique cell types. During this time, cells will interact with one another in their environment to coordinate this complex process. And finally, cells will move and arrange themselves into the proper spatial order to form all the structured organs and tissues in the body. Cell movements that shape tissues and organs, known as morphogenesis, is a beautifully complex process. Each tissue and organ in the body has a specialized way in which it creates its unique form. This process must be tightly regulated to ensure that the end result is a completely functional organ, failure could result in catastrophic consequences. Morphogenetic movements are able to create three-dimensional tissues from a two-dimensional sheet of cells through an intricate process of cellular coordination. Whereby cell-cell communication, signaling pathways, and morphogen gradients work in concert to perform a very precise task resulting in cell differentiation, proliferation, and death. A common by-product of morphogenetic movements resulting in three-dimensional tissues are gaps, fissures, or holes in those developing tissues. Filling these gaps is therefore an essential step of morphogenesis, failure to do so will affect tissue integrity, and often has disastrous consequences on the function of that tissue. The mechanism that development uses to fill these holes is epithelial fusion, a joining of epithelial cells. Epithelial fusion is a mystifying mechanism, it has been studied for over a century and yet there is still little insight into the direct cellular mechanics of this process. The overarching goal of my

dissertation has been to examine the molecular mechanisms behind epithelial fusion during early development.

1.1 Cellular Movement During Morphogenesis

1.1.1 Morphogenesis

Morphogenesis, an elusive process in which genetics lead to geometry, is involved in the six fundamental stages of vertebrate development. The six stages of vertebrate development begin with fertilization, where fusion of two gametes begins the intricate process resulting in an organism. The second stage is cleavage, where rapid cell division occurs resulting in a multi-cellular embryo. Once cleavage has created over 100 cells the embryo is then termed a blastula which contains two layers, the blastoderm and the fluid- or yolk-filled blastocoel. After formation, the blastula undergoes gastrulation where the 2 or 3 germ layers are created, ectoderm, endoderm, and mesoderm in organisms containing three germ layers. Next in development is somitogenesis, the formation of somites which differentiate into skeletal muscle, vertebrae, and dermis. The final stage of embryonic vertebrate development is organogenesis, where the organs of the embryo develop. Morphogenesis is the process by which tissues undergo organization and shape change to create the three-dimensional organs in the body. Each structure in the body has its own set of "code" which regulates the shape and therefore function of each individual organ. The genetic code that directs morphogenesis results in the coordinated movement of cells, these cells move in unison as a sheet which can undergo many types of morphogenetic movements. There are five main classes that can be used to describe the various morphogenetic movements during development; convergent extension, epiboly, involution, ingression, and invagination.

1.1.2 Convergent Extension

Convergent extension is the process by which cells will converge along one axis, narrowing the tissue, and extend outwards across a perpendicular axis (Figure 1.1 A). This process is a way to achieve elongation of tissue without further growth. This process is utilized amongst vertebrate and invertebrate species, and has been particularly well studied during the body axis elongation of the notochord [1]. Cell movement during convergent extension is unique from cellular migration. However, during convergent extension the cellular movements are a polarized movement between neighboring cells resulting in tissue remodeling [2]. During convergent extension there are two axes of polarization that guide the mediolateral intercalating movements, and the force generated from these movements are exerted onto the neighboring cells, not the extracellular matrix (ECM) [2]. There are two modes with which the intercalation of cells during convergent extension can occur. The first is the cell crawling mode, most notably associated with convergent extension of mesenchymal cells like the notochord [1]. Here membrane protrusions at both ends of the elongated cell, which closely resemble actin based lamellipodia, are used to crawl in between neighboring cells resulting in intercalation [1]. The second is the cell contraction mode, and it is associated with convergent extension of epithelial tissue [1]. In this mode actomyosin accumulates at the cell-cell junctions which then generates a contractile force between the cells resulting in shrinkage of the cell membranes which provides enough force to move neighboring cells [3]. One of the most vital molecular pathways governing both modes of convergent extension is that of the planar cell polarity (PCP) pathway, which is composed of cytoplasmic proteins

Dishevelled and Prickle, as well as transmembrane proteins Frizzled, Vangl, and Celsr [4]. Interestingly, studies have shown that Rho and its downstream effector Rho-associated protein kinase (ROCK) transduce the signals from the PCP components resulting in the cytoskeletal dynamics of actin polymerization and actomyosin contraction required for both modes of convergent extension [5, 6].

1.1.3 Epiboly

Epibolic movements involve the spreading and thinning of tissue through coordinated movement of an entire sheet of epithelial cells to enclose the deeper layers of the embryo (Figure 1.1 B). There are many different ways in which epiboly can be accomplished; cell division, cell shape change, cell intercalation, or a combination thereof [7]. Epiboly has been extensively studied during zebrafish gastrulation [8]. During epiboly, cells will dome outward at the area of the blastula and will undergo cell shape and location changes in order to extend vegetally towards the opposite pole, eventually encapsulating the entire embryo. There are two characteristics of epibolic movement, radial intercalation and the coordinated flattening of cells to allow for the spreading of the epithelial sheet. Radial intercalation is unique from that of mediolateral intercalation in that cells will exchange places throughout an entire multi-layered tissue instead of within the same plane. Radial intercalation does not require the polarization of cells and therefore does not use the PCP pathway as does mediolateral intercalation. The radial intercalations during epiboly require the use of cell adhesion molecules for proper formation, specifically E-cadherin [9]. Zebrafish *half-baked*/E-cadherin mutants show that cells will still intercalate but will not remain and these cells will travel back to their

starting position [9]. The proposed driving mechanism behind the cell shape changes which provide the tension needed for epiboly to complete has been shown to be through the recruitment of actin and myosin II to the margins of the enveloping layer [10]. It is proposed that myosin II is required after 50% epiboly has been reached in order to constrict the encapsulating layer and complete the envelopment of the embryo through a "purse-string mechanism" [11].

1.1.4 Involution

Involution involves the concerted inward movement of a sheet of cells from a growing external layer. These cells spread themselves along the internal surface of the remaining outer layer (Figure 1.1 C). Involution is involved in the formation of many processes including amphibian gastrulation, where migrating marginal cells involute at the dorsal lip of the blastopore. These involuting cells will create many structures including the archenteron, the prechordal plate, and the notochord. Involution also occurs during Drosophila head involution, where through dramatic cell shape changes the anterior tissues of the embryo are internalized [12]. The particular genes and pathways involved during involution are poorly understood and those that are known appear to be tissue/cell type specific [13]. An example of this is during the involution of cells through the dorsal lip in amphibians. A forkhead gene, MocuFH1, seems to control the involution of the presumptive notochord and mesenchymal cells [14]. When treated with antisense oligodeoxynucleotides, these two populations of cells fail to undergo involution at the dorsal lip [14]. However, the presumptive muscle cells are unaffected by the treatment, and involute in through the dorsal lip as usual [14].

1.1.5 Ingression

Ingression is conceivably one of the most studied morphological process. During ingression epithelial cells transform into migrating mesenchymal cells (Figure 1.1 D). To do so they change many properties about themselves, they change their cellular architecture, their motility, as well as their adhesive properties. One example is during primitive streak development during gastrulation. During primitive streak development epithelial cells lose their apico-basal polarity, as well as their adherent junctions [15]. Once again, cytoskeletal changes are crucial for ingression to occur, these cells must ingress out of the epithelium and become migratory within each individual cell which heavily depends on cytoskeleton function [16]. The beginning of cytoskeletal changes occurs by apical constriction as well as a disorganized basal cytoskeleton [16]. Finally, through the activity of matrix metalloproteases, the basement membrane of these cells are broken down [17]. Perhaps one of the most well-known examples of ingression is that of neural crest cells, which emigrate from the epithelium and migrate to other locations in the developing embryo. During neural tube development the neural plate epithelium rolls upward to form a cylindrical structure. Once the apposing sheets contact one another and begin to fuse, the cells located directly next to the fusing tissue near the dorsal midline undergo ingression, commonly referred to as epithelial to mesenchymal transition (EMT) [18]. These neural crest cells go on to contribute to the formation of a number of tissues in the developing embryo. Many signaling pathways have been associated with EMT such as TGF-β, FGF, EGF, HGF, Wnt/beta-catenin, Notch Ras-MAPK, and Hedgehog [19].

1.1.6 Invagination

Invagination, much like involution, involves the inward movement of cells. Unlike involution, invagination is the bending of a sheet of cells inward to create a pocket, as if being poked from the exterior surface (Figure 1.1 E). Invagination occurs during the development of many tissues and can be accomplished through two different types of mechanisms, axial and orthogonal [20]. Axial invagination occurs at a singular point and invaginates along the axis that the tissue will form, such as the initiating phase of gastrulation where the blastula cells invaginate to form the ectoderm and endoderm [20]. Orthogonal invagination occurs along a line instead of a singular point which creates a furrow, the axis of which is perpendicular to the area of invagination, as seen during the formation of the neural tube [20]. Broadly, there are two molecular mechanisms that can direct invagination, the cytoskeleton and the extracellular matrix. These two mechanisms have been shown to work both independently as well as in concert during development [21, 22]. The cytoskeleton is often used to drive apical constriction through the activation of Shroom, RhoA, ROCK, and actin-myosin contractility which result in a cytoskeleton driven invagination event [23]. The extracellular matrix, on the other hand, is used to stiffen the basal lamina which results in a resistance of the basal surface to deform [24]. To accomplish this, cells often swell their extracellular matrices by secreting a large chondroitin sulphate proteoglycan [24]. These proteoglycans can absorb water causing the matrix to swell. Due to this differential swelling the matrix buckles inward resulting in invagination of the sheet of cells [24]. One example of these two molecular mechanisms of invagination occurring simultaneously is during neural tube development. During neural tube folding there are

two distinct curvatures in the tissue, one being convex at the dorsolateral hinges, while the median hinge point is concave. The median hinge point shows apical constriction through use of the cytoskeleton, while the dorsolateral hinges are basal in origin through use of the ECM [25, 26].

1.2 Epithelial Fusion During Retinal Morphogenesis

1.2.1 Epithelial Fusion

All the various types of morphogenetic movements are crucial for proper development of an organism. However, these morphogenetic movements are just the initial steps in forming a functional three-dimensional organ. Often times, as a result of these cellular movements, gaps, fissures, or holes are created in the tissue. Filling these gaps is an essential process of morphogenesis. Failure to do so will affect tissue integrity, and often has disastrous consequences on the function of the organ. The mechanism which development uses to fill these gaps is called epithelial fusion. Epithelial fusion can be observed during the formation of many organs including, neural tube, heart, palatal shelf, urethra, uterine ligament, diaphragm, eyelid, optic fissure, and even dorsal closure in *Drosophila*. Epithelial fusion is susceptible to disturbance which results in congenital malformations. For example, failure of the neural tube to close results in several different disorders, including spina bifida, and anencephaly [27]. Failure of the epithelium to fuse in the heart results in many congenital heart defects [28]. Failure of the palatal shelf to fuse results in cleft palate [29]. And failure of the optic fissure to fuse results in coloboma [30]. Many of these congenital defects present themselves as part of syndromes, such as

CHARGE syndrome, where those affected experience colobomas, heart defects, and more [31]. This suggests that there are shared common mechanisms amongst fusion events, thus understanding mechanisms regulating one fusion event might be applicable to other fusion events as well.

1.2.2 Retinal Morphogenesis

1.2.2.1 Eye Field Specification

Vertebrate eye development is a highly conserved process which shares many of the same mechanisms amongst all vertebrate species [32]. Eye development begins with the specification of the eye field in the diencephalon. The specification of the eye field relies on the expression of a network of key transcription factors Six3, Rx, and Pax6 [33].

Six3 is one of the earliest transcription factors in eye specification, and is required for the repression of Wnt activity in the diencephalon [34]. Overexpression of *Six3* results in the formation of ectopic eyes in fish [35]. Loss of function of Six3 in mouse knock-out models result in the loss of markers anterior to the midbrain coupled with the expansion of markers posterior to the midbrain [36]. Congruently, overexpression of Wnt signaling represses *Six3* expression resulting in the same loss of eye field specification as Six3 mutants [37].

Pax6 has been considered the master eye regulating gene, though in more recent studies it is suggested that this title belongs to Six3 [38]. Pax6 mutant mice initially develop primitive eye structures but are unable to properly develop and disappear as development progresses [39]. Pax6 has the ability to activate transcription of Six3 and is

suggested to be the reason why ectopic expression of Pax6 has the ability to induce eye formation [40].

A class of retinal homeobox transcription factors known as Rx are also required during eye field specification. Rx genes are involved in the control of proliferation through regulation by Six3 and Optx2 [33]. Loss of function of Rx3 in zebrafish results in failure of optic vesicle evagination and thus complete absence of the retina [41].

Together Six3, Pax6, and Rx are required to restrict the expression of Otx2 [42]. Otx2 appears to be required to set up the eye field transcription network of Six3, Pax6, and Rx, but once this network has been established Otx2 expression is down-regulated in the eye field region [43]. It is suggested that Otx2 acts permissively during eye development to confer competence of the eye field region since it has been shown that Six3 can only induce ectopic eye formation within the Otx2 expression domain [35].

1.2.2.2 Eye Field Division

Once the eye field has been specified, it must then undergo division into two symmetrical primordium to eventually create the optic vesicles. To achieve this division members of the Shh-, Tgf-β-, and Fgf- families are secreted within this region [44]. Without proper regulation of these factors the eye field fails to undergo division and results in cyclopia, the formation of a single eye [44]. It is suggested that due to these secreted factors prospective hypothalamic cells migrate anteriorly through the eye field physically separating the eye field into the two symmetrical primordium [45].

Shh is a crucial morphogen for patterning of the eye primordium [46]. Through Fgf signaling the eye primordium is capable of responding to Shh signaling which must be tightly regulated [46]. As stated previously, absence of Shh results in cyclopia, alternatively, over expression of Shh result in the over development of proximal structures at the consequence of distal structures [47].

1.2.2.3 Evagination

Morphogenesis and proliferation usually go hand in hand, however, this appears to not be the case with optic vesicle evagination. Evagination of the optic vesicles is achieved through different mechanisms dependent upon species. In mouse, it is proposed that extensive cell shape changes are the driving force of evagination [48]. In zebrafish, migration of the retinal progenitor cells (RPCs) seem to be the driving force [49]. Cells immigrate to this region where they intercalate and epithelialize resulting in growth of the optic vesicle [50]. The optic vesicles then continue extending out from the diencephalon due to the continuous intercalation of newly arriving RPCs [51]. These migrating RPCs display a specific migratory pattern determined by signaling and cell adhesion molecules, and in zebrafish the migratory behavior seems to rely heavily on Rx3 [52]. At the onset of neurulation Rx3 positive RPCs show a delayed migration pattern in comparison to non-RPCs [49]. In the absence of Rx3, RPCs still form but they remain at the midline and fail to migrate outwards towards the lateral regions [51].

1.2.2.4 Optic Cup

The formation of the optic cup from the optic vesicle requires morphogenetic movements to create the bi-layered spherical structure. This is achieved through invagination of the optic vesicle once it reaches the overlying surface ectoderm. At this point the optic vesicle invaginates to create the optic cup which is attached to the optic stalk leading back to the forebrain. The overlying surface ectoderm invaginates to create the lens placode. It was previously thought that formation of the optic cup required the lens placode in order to form, but recent findings have shown that contact with the surface ectoderm is only required to initiate the invagination process through temporal regulation [52]. Once the optic vesicle reaches the surface ectoderm the optic cup will continue to form in the absence of the lens placode as observed through ablation experiments [53].

The invagination of the optic cup relies heavily on cell shape changes to direct the cellular movements [54]. This is achieved through basal constriction of the cells creating a triangular shape [54]. In the absence of Opo, a transmembrane protein responsible for controlling the location of focal adhesions, basal constriction fails to occur resulting in failure of the optic cup to form [54]. The basal constriction of these cells results in rim involution, whereby cells traverse the outer layer moving inward around the rim of the optic cup into the inner layer of the optic cup resulting in the bi-layered spherical optic cup [55]. Once the optic cup has formed it is comprised of an outer layer of retinal pigmented epithelium (RPE), an inner layer of neural retinal cells, retinal ganglion cells and their axons which traverse the length of the optic stalk to the forebrain, and a fissure

along the ventral length of the optic stalk. After fusion of this fissure the optic stalk becomes the optic nerve, and retinal morphogenesis has completed.

1.3 Fusion of The Optic Fissure

1.3.1 Optic Fissure Fusion

As a consequence of the formation of the three-dimensional retinal sphere from a flat sheet of cells is the formation of a fissure along the ventral length of the optic stalk. This fissure allows for migratory mesenchymal cells to enter the retina to establish vasculature networks onto the back of the lens. This vasculature is known as the hyaloid vasculature, and is a temporary circulatory system required for ocular development. In most species this circulatory system will degenerate once mature blood vessels begin to grow [56]. The optic fissure will undergo epithelial fusion to attach the adjacent lobes to sheath the retinal ganglion cell axons. The timing of fusion of the optic fissure varies by species, in humans this occurs between the 5^{th} and 7^{th} week of gestation, in zebrafish fusion occurs between 32 and 72 hours post fertilization (hpf) [57]. Like many other epithelial fusion events, when fusion fails to occur it results in congenital disorders. In the case of the optic fissure the result is coloboma.

1.3.2 Coloboma

Coloboma is a leading cause of pediatric blindness accounting for approximately 10% of all cases worldwide [58]. Approximately 1 child in every 10,000 births are diagnosed with coloboma, though incidence seems to be at a higher rate on the Indian

subcontinent. Coloboma is a spectrum disorder and can present itself to varying degrees. Depending on the location and degree to which the fissure was able to fuse will determine the amount of visual acuity the affected individual will have [58]. A large gap in the more proximal regions of the fissure will expose a significantly larger portion of the retinal ganglion cell axons to the external environment resulting in neuronal death and complete blindness in the affected eye [59]. While a small gap at the most distal regions of the fissure will mildly affect visual acuity [59]. There are many different coloboma classifications depending on the structure that has been affected. One of the most common classes of coloboma is iris coloboma, these are most commonly in the ventral region of the iris resulting in a keyhole like shape in the pupil. Lens coloboma are when a section of the lens is missing, and large lens colobomas can result in the displacement of the lens. Macular coloboma is when a portion of the macula, region of the retina responsible for central vision, is missing resulting in partial loss of vision. Optic nerve coloboma can appear with retinal or choroidal colobomata and can result in retinal detachments. While surgery can be performed to correct the appearance of colobomas and to repair retinal detachment, unfortunately, any visual loss experienced is permanent and is unable to be corrected. Fusion of the optic fissure doesn't occur simultaneously, it is a step wise process that begins in the medial regions of the fissure and "zippers" proximally and distally from this location. Due to this, failure of fusion could occur at any localized point resulting in a broad spectrum of effects on those who have this disorder [59]. Coloboma can also be unilateral affecting only one eye, or bilateral affecting both eyes. It is even suggested that cases of colobomata are underreported as small lesions in the proximal regions could go unnoticed with adequate vision function

[58]. Most of the work done on understanding coloboma investigates the spatial and temporal control of gene patterning preceding, during, and after optic fissure fusion. From this previous work several genetic pathways have been elucidated including BMP/TGF-β, retinoic acid (RA), SHH, FGF, Wnt/β-catenin, and a whole host of transcription factors.

1.3.3 Transcription Factors and Sonic Hedgehog

Most causes for coloboma are due to genetic abnormalities. However, for non-syndromic instances of coloboma in humans over 70% percent of individuals do not have an identified genetic cause [58]. Identification of the genetic cause in syndromic coloboma, however, is much higher [58]. Mutations in the transcription factors pax2 and pax6 (paired box) can result in coloboma, mutations in pax2 accounts for approximately 50% of individuals with renal coloboma syndrome [60]. It has been reported that 92 mutations have been found in the pax2 gene, and one particular mutation has been reported 57 times in individuals with coloboma [61]. Even though pax2 has been closely associated with coloboma little is known about how this transcription factor functions or what its targets are. Sox2, Sox4, and Sox11 (SRY-related HMG-box genes) have also been associated with coloboma [62]. It has been shown that Sox4 and Sox11 limit sonic hedgehog (shh) signaling in the ventral region of the optic cup and when mutated in zebrafish results in expression of shh in the ventral region leading to coloboma [62]. Transcription factors associated with the periocular mesenchyme (POM) have also been linked to coloboma, in particular pitx2 [63]. POM cells are a sub-population of cranial neural crest cells which migrate to the eye and develop many structures in the anterior

segment of the eye. POM cells are also partly responsible for the establishment of the hyaloid vasculature in the retina [64]. Many of these POM associated transcription factors have been observed to cause coloboma in the zebrafish model, however, these mutations are rare within human patients [64]. Many other transcription factors have also been linked to coloboma, for a comprehensive list of genes associated with coloboma see Table 1.1.

1.3.4 Bone Morphogenetic Protein/Transforming Growth Factor Signaling in Optic Fissure

Bone morphogenetic proteins (BMP)/Transforming Growth Factor-β (TFG-β) are a class of growth factors known for coordinating tissue architecture during morphogenesis. To date two particular BMP's have been shown to be required for optic fissure morphogenesis, BMP4 and BMP7. Sonic Hedgehog (SHH) restricts the expression of BMP4 to the dorsal regions of the retinal tissue [65]. BMP4 thus dorsally induces the expression of certain T-box transcription factors known for their repressive capabilities [65]. BMP4 also restricts a well-known eye patterning gene, Vax2, from the dorsal regions of the retina [66]. Tgfβ signaling can trigger changes to the extracellular matrix (ECM) and is also inhibited by BMP signaling [67]. In both mouse and zebrafish loss of Tgfβ2 results in coloboma [68]. It was specified that Tgfβ signaling in the optic fissure induces the expression of BMP4 antagonists to allow Tgfβ signaling to induce changes to the ECM permitting the fusion of the optic fissure [68]. BMP7 controls the formation of the optic fissure, and controls the early expression of Pax2 [69]. In mouse,

loss of BMP7 results in an absent hyaloid artery as well as microphthalmia/anophthalmia and failure of optic fissure formation [69].

1.3.5 Fibroblast Growth Factor Signaling in Optic Fissure

Fibroblast Growth Factor (FGF) signaling is required during eye development as it regulates the formation of the eye field as well as specifies the neural retina [70]. Research into FGF signaling usually focuses on its receptors as the genetic redundancy of FGFs is large, in mice alone there are 22 different FGF genes [70]. In mice, Fgfr1/Fgfr2 mutants display a coloboma phenotype and is considered to be caused by a loss of Pax2 expression [71]. Also in mice, it has been shown that mutations in the FGF genes which result in the activation of Ras-ERK signaling result in coloboma due to a loss of Pax2 in the optic fissure [72]. In humans, most instances of coloboma due to FGF mutations are a part of syndromes. Coloboma is observed in those with Noonan syndrome which is a result of a gain of function mutation in Ras/MAPK signaling [73]. Coloboma has also been observed in two families that have COMMAD syndrome which is the result of a mutation within the MITF gene [74].

1.3.6 Retinoic Acid Pathway in the Optic Fissure

Retinoic acid (RA) is responsible for establishing the dorsoventral axis in the retina. It upregulates Vax2 while simultaneously inhibiting Shh [75]. Retinoic acid also plays a role in the upregulation of both Foxc1 and Pitx2 in the POM [76]. Retinoic acid also acts in collaboration with the Hippo-YAP pathway in the regulation of migratory

neural crest cells, and both have been shown to be involved in optic fissure morphogenesis [77]. Mutations in several genes regulated by Hippo-YAP and Retinoic acid affect optic fissure closure, RBP4, PTCH1, ALDH1A3, and the RA synthesis gene STRA6 all result in colobomatous defects in human patients [78-80]. In both zebrafish and humans, mutations in Yap1 result in optic fissure closure defects [81]. Studies in yap mutant medaka fish show a loss of actinomyosin contractibility [77]. It is suggested that this loss of contractibility is the reason why zebrafish yap mutants have a loss of the ventral retinal pigmented epithelium (RPE) which affects the movement of cells around the optic fissure during closure [77]. The RA pathway has also been linked to coloboma through environmental causes by a maternal dietary deficiency in vitamin A (retinol) [82]. Amongst many different species such as pigs, rats, and even humans a maternal deficiency in vitamin A has resulted in offspring with congenital eye defects including coloboma [82]. Research has shown that eye defects can be rescued by adding an exogenous active metabolite of retinol, retinoic acid, in vitamin A deficient subjects, indicating that vitamin A operates through the RA pathway [83].

1.3.7 Wingless-related Integration Site/β-catenin in the Optic Fissure

Wingless-related Integration Site (Wnt)/β-catenin is a well known signal transduction pathway which has been shown to be tightly regulated in optic fissure closure. The Wnt/ β-catenin pathway requires tight regulation in the optic fissure as it has been shown that an up- and down-regulation of the pathway results in optic fissure defects [84, 85]. In mice the up-regulation of Wnt signaling by a mutation in Wnt

repressor Foxg1 results in a reduction of expression in Pax2 within the optic fissure resulting in coloboma [84]. Alternatively, in mice the down-regulation of Wnt signaling through a mutation in Wnt receptor Fzd5 resulted in an over expression of Pax2 in the optic fissure leading to coloboma [85]. Altering Wnt signaling has also been shown to affect other key genes and pathways in the optic fissure including Vax2, BMP, and RA, and all result in optic fissure defects [86]. However, mutations in the Wnt pathway are very rare amongst the human population. To date, the only mutation in humans found is in the Wnt receptor Fzd5 gene [87]. It was found in a large family with isolated coloboma where an autosomal dominant frameshift mutation in Fzd5 was thought to cause effects on the actin cytoskeleton within the optic fissure [87].

1.4 Molecular Mechanisms in Optic Fissure Fusion

With 70% of isolated coloboma cases being idiopathic [58], it suggests that the most advantageous method of understanding coloboma would lie in understanding the molecular mechanisms governing optic fissure fusion. Little is understood about the molecular mechanisms involved in optic fissure fusion. However, though little is known about each mechanism involved it has been shown that there are three crucial molecular machineries required for optic fissure fusion, the basement membrane, actin cytoskeleton, and endothelial cell migration [88] (Figure 1.2).

1.4.1 Basement Membrane

The basement membrane is a specialized type of extracellular matrix. The basement membrane is one of the few common features shared amongst all multicellular

animals, appearing very early on in their evolution [89]. This thin, tough, and flexible sheet of molecules is a crucial component of all epithelium. This sheet of molecules provides a multitude of functions to the epithelium. It is a barrier that distinguishes the boundaries of developing tissues [90]. The basement membrane provides the architecture of the epithelium, while also being a crucial component of cell-to-cell signaling [90]. Many other functions of the basement membrane involve determining cell polarity, promoting proliferation, cell survival, and differentiation, and also acts as a highway for migrating cells [90]. The basement membrane is made cell-autonomously and excreted from the cell to form its basement membrane [90]. The major components of the basement membrane are part of a class of ancient extracellular matrix macromolecules, laminin, collagen IV, perlecan, and nidogen [90].

1.4.1.1 Laminin

Laminin is the primary organizer of the basement membrane, in early development laminin is mostly the sole constituent of the basement membrane [91]. Laminins are a large family of proteins, there are at least 16 different isoforms expressed in mammals [91]. Each of these laminins contain three inter-coiled polypeptide chains, an $\alpha, \beta,$ and γ, which form a cross shaped structure (Figure 1.3). Each laminin isoform has its own polypeptide chain composition allowing them to associate in many different combinations, and as such the compositions of the laminins have a high level of cell type specificity [91]. Laminin will spontaneously organize itself into a network in vitro through interactions between its three short arms [91]. It is believed this is the mechanism through which it uses to organize itself in vivo while simultaneously using the long arm

to tether itself to receptors on the cell surface. It is thought that laminin is the scaffold which allows for the recruitment of all other basement membrane components [91]. The most studied laminin family member is laminin-111 (also known as laminin 1) named to correspond with its three polypeptide chains $\alpha 1, \beta 1, \text{and } \gamma 1$. The globular domain at the head of the α chain of laminin-111 binds to integrins on the cell surface. The globular domain at the head of β and γ chains promote self-assembly, while nidogen also has a binding site on the second globular domain on the γ chain. The long arm of the laminin molecule can bind to integrins, dystroglycan, and perlecan. The $\gamma 1$ chain is a component of most laminin heterotrimers, as such, mice lacking a functional $\gamma 1$ chain do not survive past embryogenesis due to a lack of a basement membrane [92].

1.4.1.2 Collagen IV

Like laminin, collagen IV has many different isoforms, $\alpha 1$(IV)- $\alpha 6$(IV). It consists of three independently synthesized protein chains, these long chains then twist together creating a superhelix (Figure 1.3). This superhelix has interruptions in more than 20 different regions to allow multiple bends in the protein. Collagen IV molecules interact through their terminal domains to assemble into the basement membrane. The NH_2 terminus binds to three other collagen IV molecules creating a quaternary assemblage of the molecules. This structure creates a flexible and felt-like network which gives the basement membrane its tensile strength. Unlike laminin, collagen IV does not seem to be required for the deposition and formation of the extracellular matrix as mice with null mutations in the Col4a1/2 which lack functioning α chains develop normally up

to E9.5 [93]. However, collagen IV has been shown to be required for the maintenance, integrity, and functionality of the basement membrane as the Col4a1/2 null mutation caused lethality in the mice at E10.5-11.5 due to severe structural deficiencies in the basement membrane [93].

1.4.1.3 Nidogen

Previously known as entactin, nidogen is a small sulfated monomeric glycoprotein consisting of three globular domains. Nidogens' second globular domain has the ability to bind both collagen IV and perlecan, while its third globular domain has the ability to bind to the γ chain of laminins (Figure 1.3). Due to these domains it has been proposed that nidogen acts as the cross-link between the laminin and collagen IV networks [94]. There are two known nidogen homologs in humans, nidogens 1 and 2. The two homologs appear to be redundant, loss of one functioning nidogen only presents subtle abnormalities [94]. However, loss of both copies of nidogen have been shown to result in severe abnormalities in mice [95]. Through deletion of the nidogen binding site on the laminin γ chain it was shown that nidogen is not detected in the basement membrane of most tissues showing that it fails to connect to the basement membrane without a laminin binding site, further validating that nidogen acts a cross link in the extracellular matrix [95].

1.4.1.4 Perlecan

Perlecan, a heparin sulfate proteoglycan, is a major component of basement membranes (Figure 1.3). Perlecan is also thought to be involved in the cross link between the laminin and collagen IV networks [96]. Perlecan also binds multiple growth factors that promote cell survival and differentiation [96]. It has also been observed that perlecan interacts with integrins, laminins, and dystroglycans to anchor the basement membrane to epithelial cells [97]. Like collagen IV, perlecan does not appear to be crucial to the formation of the basement membrane but is required for the maintenance of the basement membrane, especially in areas which undergo high levels of mechanical stress. Homozygous perlecan mutants form a normal basement membrane, however, in areas of high mechanical stress such as in the contracting myocardium, the basement membrane deteriorates in that region [98].

1.4.2 Basement Membrane During Optic Fissure Fusion

The basement membrane is crucial component of optic cup morphogenesis, without laminin the evagination of the eye field fails to occur [99]. Laminin a1, b1, and c1 mutants all display to some extent defects in the development of the optic cup [99]. Equally as important, however, is the precise timing and control of the degradation of the basement membrane in key regions during development. One such region that basement membrane degradation is crucial is in the optic fissure. One of the critical functions of the basement membrane is to act as a barrier to the external environment, however, this barrier is detrimental for fusion of epithelial tissues [90]. Many studies have shown that

failure to remove the basement membrane in the region of the optic fissure results in colobomas. In rats, a deficiency of RA signaling at later retinal development stages results in the retention of the basement membrane in the optic fissure and leads to coloboma [83]. Pax2 and Vax2 mutants also show a retention in their basement membranes in the optic fissure which also leads to coloboma [88, 100]. Previous work in our lab has shown the main constituents of the zebrafish optic fissure basement membrane. These include collagen 4a1 and 4a2, perlecan, nidogen 1a, 1b and 2a, and laminins a1, a4, b1, c1 and c3 [101]. It was determined that nidogen removal appears to be a key component to the degradation of the basement membrane [101]. It is hypothesized that removal of nidogen exposes the proteolytic sites on the other basement membrane components allowing for their degradation [101]. It is also possible that by affecting basement membrane integrity by the removal of nidogen this allows for protrusions involved in fusion to form [101]. While it has been known that removal of the basement membrane in the region of the optic fissure must occur to allow for fusion, it still remains poorly understood whether removal of the basement membrane is an active or passive process in the mechanisms underlying optic fissure fusion.

1.4.3 Basement Membrane Breakdown

There are a broad class of proteins known as metalloproteinases that have the ability to breakdown the basement membrane. These metalloproteinases are a major component of basement membrane breakdown and remodeling, not just during embryogenesis but throughout the life of an organism. There are three large families of metalloproteinases including matrix metalloproteinases (MMPs), a disintegrin and

metalloproteinases (ADAMs), and a disintegrin and metalloproteinases with thrombospondin motif (ADAMTS). MMPs are the largest family of metalloproteinases, so far over 20 human MMPs have been discovered. MMPs are crucial during organogenesis and branching morphogenesis and are the main enzymes involved in basement membrane degradation. Combined, MMPs have the ability to degrade all components of the basement membrane. Most MMPs are soluble proteins, though a few of the most recently discovered MMPs are membrane anchored and they have wide substrate specificities. All MMPs have a pro-domain and a catalytic domain, and some have a variable number of structural domains added. ADAMs, like MMPs, can be secreted or are single pass transmembrane proteins. ADAMs have a pro-domain, a metalloproteinase, disintegrin, cysteine-rich and a characteristic transmembrane domain. Not all ADAMs possess a functional protease domain, those that do are classified as sheddases because they cleave the extracellular portions off of transmembrane proteins. ADAMTS family of proteins is very closely related to ADAMs, they contain all the same domains as ADAMs except instead of a transmembrane domain they contain a characteristic thrombospondin motif. Unlike ADAMs and MMPs, ADAMTS are secreted enzymes. MMPs, ADAMs, and ADAMTS have a broad spectrum of substrate specificity, this contributes to the development and maintenance of many tissues and they participate in many physiological processes. These remodeling enzymes contribute to an extraordinary amount of processes including bone remodeling, angiogenesis, immunity, and wound healing to just name a few [102-104]. The enzymatic activity of these metalloproteinases is tightly controlled at the transcriptional level, by pro-peptide activation and by inhibition through tissue specific inhibitors of metalloproteinases.

Dysregulation of metalloproteinase activity leads to many pathological conditions such as inflammation, cancer, arthritis, dwarfism, and more [105-107].

1.4.4 Actin Cytoskeleton

Actin, which makes up the cellular cytoskeleton, is the most abundant protein in most eukaryotes and in some cell types, comprising approximately 15% of the cellular protein content [108]. The actin cytoskeleton is a dynamic network of proteins made up of actin and actin binding proteins. Actin is highly conserved amongst eukaryotes where the amino acid sequences of actin are upwards of 90% identical. The actin cytoskeleton has a diverse range of functions depending on the cell. Actin filaments organize underneath the plasma membrane and provide strength and shape to the cell. In vertebrates, there are three isoforms of actin an $\alpha, \beta,$ and γ, β- and γ- actin are most often found together in most non-muscle cells while α-actin is expressed only in muscle cells. The actin cytoskeleton is made up of asymmetrical globular or G-actin subunits which are tightly associated with an ATP or ADP molecule. The G-actin subunits then assemble in a head-to-tail manner which forms a right handed helix. This tight structure is about 8 nm wide and is called filamentous or F-actin. Due to the asymmetrical nature of G-actin the formation of F-actin has structurally different ends which are polarized and has an arrowhead like appearance. F-actin has a slow growing end termed minus end, and a fast growing end termed plus end. The subunits are positioned so that their nucleotide binding site points toward the minus end. The kinetic rate of association and dissociation is much higher, approximately 10 times higher, at the plus end. While individual actin filaments

are relatively flexible, in living cells these actin filaments interact with accessory proteins which cross-link the filaments together to form bundles. These actin filament bundles create extensive structures that are quite rigid. How these bundles are formed depends on the actions of actin binding proteins, which create specific cytoskeletal structures depending on the cell and the function needed by that cell. There are over 100 different actin binding proteins which can regulate assembly, disassembly, and/or spatial organization of actin filaments. The actin cytoskeleton creates many different structures which include microvilli, adhesion belts, the cell cortex, stress fibers, contractile rings, lamellipodia, and filopodia. These structures can then go on to perform its specialized function which can be classified into three broad categories, spatial organization of the cell, physical and biochemical connections to the external environment, and cell movement. During epithelial fusion the actin cytoskeleton has shown to be crucial in order for proper fusion to occur by creating specialized actin structures and through cell signaling.

1.4.5 Actin Cytoskeleton During Epithelial Fusion

1.4.5.1 Lamellipodia and Filopodia in Epithelial Fusion

The actin cytoskeleton has a diverse range of functions during epithelial fusion. Two specialized actin structures are thought to be of particular importance to achieve fusion, lamellipodium and filopodium. Lamellipodia were previously termed “ruffles” due to the ruffled like appearance of the protrusions formed [16]. Lamellipodia are made up of an actin dendritic network at the leading edge of the cell shown to be important in

mechano-sensing and thought to be the physical motor behind the pulling force in cell migration (Figure 1.4) [109]. Lamellipodia form from the nucleation of actin filaments, and most often the nucleating protein is the Arp2/3 complex [110]. Arp2/3 complex is made up of seven subunits, and the Actin-Related Proteins 2 and 3 closely resemble monomeric actin and aids the nucleation of new actin filaments [110]. The Arp2/3 complex binds to the sides of existing actin filaments and creates a new actin filament at a 70 degree angle from the original actin filament [110]. The activity of small GTPases from the Rho superfamily are required for the formation of both lamellipodia and filopodia. Lamellipodia formation requires the activation of Rac1, this then activates WAVE/Scar proteins which then in turn activate the Arp2/3 complex [111].

In stark contrast to lamellipodia, filopodia are finger-like structures made up of tightly bound parallel bundles of F-actin (Figure 1.4). However, as with lamellipodia, the growing end of the filopodium is pointed towards the plasma membrane. The formation of filopodia has been shown to depend upon the activation of the cdc42 pathway [112]. This results in the activation of proteins from the ENA/WASP family, which prevent the growing actin filaments from getting capped at their growing ends [112]. Formins can also become activated through these small GTPases. Formins create unbranched actin filaments by continuous barbed end nucleation and elongation [113].

One of the best studied examples of lamellipodia and filopodia involvement in epithelial fusion is during dorsal closure in *Drosophila* [114]. During *Drosophila* dorsal closure actin based protrusions emanate from the leading edge of the closing epithelial sheets and moves the sheet of cells towards the midline [114]. Once the epithelial sheets appose one another the sheets fuse together in zippering-type fashion [114]. Filopodia

extend across the gap between epithelial sheets and appears to sense the environment to find the location where it should make contact, as filopodia have been observed to ignore cells closest to it in favor of other more distant cells [114]. It has been observed that once cells directly appose one another lamellipodia and filopodia interweave at the cell-cell interface [114]. It also appears that filopodia penetrate through the plasma membrane of the apposing cell creating the initial cell-cell contacts and adhesions [114]. In line with these observations, inhibition of cdc42 and Rac1 results in blocking the formation of the actin filaments observed at the leading edges and results in a failure to close the dorsal epithelial sheets during *Drosophila* development [115]. There has also been evidence of lamellipodia and filopodia involvement in cranial and neural tube closure. In mice a conditionally ablated Rac1 results in failure of epithelial fusion in the cranial and neural tube regions. Rho associated kinase (ROCK) is a down-stream effector from the activation of Rho GTPases. ROCKI and ROCKII both play roles in actin filament assembly by inhibiting actin depolymerization. Mice deficient in ROCKI exhibit a disorganization of the actin cytoskeleton in the eyelid epithelium and the umbilical ring [116]. Due to this deficiency of ROCKI these mice fail to close the eyelid resulting in an open eye phenotype, as well as failure to close the ventral body wall resulting in omphalocele [116].

1.4.5.2 Integrins and Cell Signaling in Epithelial Fusion

Integrins are a superfamily of transmembrane cell adhesion receptors that form a heterodimer made up of an alpha and beta subunit. In zebrafish there are at least 17 different integrin or integrin-like genes encoding 9 different alpha subunits and 8

different beta subunits. Integrins are the main receptors which bind and respond to the extracellular matrix, making them crucial during development [117]. Integrins act in two very critical methods, they act as cell adhesion molecules as well as signal transducers [117]. Integrins usually have low affinity for their binding targets and have a high concentration on the cell surface [117]. This creates a large number of weak adhesions which allow for easily reversible attachments [117]. Integrins also transmit signals to the cell about the extracellular matrix with which it is bound and communication from the cell can transmit to the integrins inhibiting or enhancing their ability to bind to their target [117]. The interactions between the cell and the extracellular matrix is accomplished through the interactions between integrins and the actin cytoskeleton [117]. Integrins bind to scaffolding proteins which then bind to actin creating a crosslink between integrins and the actin cytoskeleton [117]. Several scaffolding proteins are known to interact between actin and integrin, some of which include talin, α-actinin, and filamin [117].

It has been observed that both integrins and their scaffolding binding partners are crucial during epithelial fusion. During mouse neural tube closure integrin $\beta 1$ is required during the "zippering" process of fusion [118]. Integrin $\beta 1$ is activated at the site of the zippering creating a focal anchorage at a shared point in the basement membrane creating novel cell-cell junctions [118]. When this integrin is lost these focal adhesions fail to develop and as such the neural tube fails to fuse resulting in spina bifida [118]. Interestingly it has been found that the scaffolding protein talin is directly linked to optic fissure fusion. It was shown that talin mutants fail to break down the surrounding basement membrane in the lobes of the optic fissure up to at least 72 hours post

fertilization [119]. As a result these zebrafish failed to close the fissure and consequently developed coloboma [119]. Talin has been purported to be the most crucial aspect of integrin adhesion complexes [120]. In *Drosophila* it was observed talin was required for all integrin adhesive functions, and similar results were found in mice lacking both talin genes [121]. This suggests that inside-out and outside-in communication between the actin cytoskeleton and the basement membrane surrounding the lobes of the optic fissure is crucial.

1.4.6 Hyaloid Vasculature

The eye is a highly metabolic organ, consuming more oxygen than even that of the brain. To provide the eye with the oxygen and nutrients it needs during early eye development, two vasculature networks are initially formed, the choroidal and hyaloid vasculature (Figure 1.5). Both vasculature networks originate from the same source, the ophthalmic artery which is derived from the carotid. These two vasculature networks thus form through angiogenesis, meaning they bud off from the primordial vessel. The choroidal vasculature network is formed posterior to the eye where it surrounds the optic cup. This network is closely associated with the retinal pigmented epithelium (RPE). The RPE constitutively expresses Vascular Endothelial Growth Factor (VEGF) which is crucial for maintaining the endothelial to epithelial association required for the maintenance of this vasculature network. Alternatively, the hyaloid vasculature forms in the anterior portion of the eye between the retina and the lens. The hyaloid vasculature takes advantage of the optic fissure to establish this network. After entering through the optic fissure the hyaloid artery will move through the vitreous and will eventually contact

the posterior end of the lens. After contact the hyaloid artery will begin to branch across the posterior side of the lens forming the tunica vasculosa lentis. The hyaloid vasculature is avenious and in order for drainage to occur the hyaloid network must form connections to the choroidal vasculature. The initial hyaloid artery is formed from a mesoderm derived endothelial cell lining and periocular mesenchyme (POM) derived pericytes [122]. However, after the initial formation of the hyaloid network it becomes solely mesoderm derived [122]. Several genetic markers of POM have shown expression in the migrating endothelial cells entering through the optic fissure to form the hyaloid vasculature, including Sox10, Pitx2, and FoxC1 to date [64, 123, 124]. In most animals the hyaloid vasculature regresses and is simultaneously replaced by retinal vasculature. However, zebrafish maintain the hyaloid vasculature which undergoes remodeling, moving away from the lens and towards the retina as the vitreous forms [125]. It is suggested that due to the closer proximity of the lens and retina in zebrafish it is more favorable to remodel rather than remake as is done in mammals [125]. It was widely believed for many years that these migrating endothelial cells were a passive process during optic fissure fusion, but more recent studies have found that these cells directly contribute to the fusion process [119].

1.4.6.1 Factors in Hyaloid Vasculature Establishment

One of the most well-known and studied factors that control the migration, establishment, and maintenance of the hyaloid vasculature is VEGF. VEGF is a highly potent angiogenic factor comprising five members of this gene family, VEGF-A through D and PGF, and has three receptors VEGFR1 through 3. Through many different studies

across many different species it has been shown that lack of VEGF expression, particularly that of VEGF-A, results in a loss of hyaloid vasculature [126-128]. Conversely, it has also been shown that overexpression of VEGF-A results in hypertrophy of the hyaloid vasculature and has consequences on the hyaloid vasculature regression required during mammalian development [129]. In mammals failure of the hyaloid vasculature to regress results in persistent hyperplastic primary vitreous [130]. This failure to regress is often from the inability to attenuate VEGF functioning [130]. VEGF can bind and essentially store itself to the extracellular matrix, interestingly VEGF can be cleaved by metalloproteinases which separates the matrix binding domain from the receptor binding domain [131]. Many therapies, including the treatment of cancer, have been deployed which use anti-angiogenic molecules to sequester VEGF ligands or inhibit VEGF function [132]. This therapy has also been deployed to treat persistent hyperplastic primary vitreous due to failure of hyaloid regression [133]. Many other genes also play a role in hyaloid vasculature development including ECM - cell membrane and lens gene expression, including MAGP1, Syn2, Mab21l2, and Laminin alpha 1 [134]. When these genes are knocked down all result in hyaloid vasculature defects [134].

1.4.6.2 Angiocrine Signaling by Endothelial Cells

Endothelial cells are not just a passive conduit for the circulation of blood, but can also provide instructive signals during organogenesis. During embryogenesis migrating endothelial progenitor cells invade into developing organs and create organ-specific vascular niches which will release tissue specific growth factors (angiocrine factors)

derived from the endothelium [135]. Angiocrine factors have been shown to be crucial during wound repair, a similar epithelial fusion event [136]. During wound repair it has been shown that capillary networks are in close physical proximity to hematopoietic, mesenchymal, neuronal, epithelial, stem and progenitor cells which allow for the instructive paracrine and juxtacrine factors provided by these tissue-specific endothelial cells [137]. Of particular interest is the angiocrine signaling that occurs in the development of the blood-retina barrier. The blood-retina barrier is established by the maturation of the retinal pigment epithelium (RPE), choroidal endothelial cells, and the basement membrane that lies between both cell types, Bruch's membrane [138]. Through co-culture experiments it was observed that choroidal endothelial cells secrete factors that remodel the basement membrane of the RPE, the integrin receptors sense this change in the basement membrane and start a signaling cascade through RhoGTPases which result in the modulation of RPE tight junctions as well as the fortification of the RPE barrier [138]. While angiocrine signaling has not been associated with optic fissure fusion to date, there is some evidence that hyaloid endothelial cells somehow contribute to basement membrane breakdown in the region of the optic fissure. Zebrafish cloche mutants, which reportedly lack all early vasculature, fail to break down the basement membrane in the beginning stages of optic fissure fusion, though it was ultimately stated to not result in coloboma as the basement membrane was eventually degraded [119]. Requirement of the hyaloid vasculature in optic fissure fusion is also corroborated by optic cup transplantation experiments, without the presence of the hyaloid vasculature ectopic eyes failed to undergo optic fissure fusion [139]. These experiments suggest an

angiocrine dependent mechanism during optic fissure fusion, where endothelial cells provide direct contribution to the fusion process.

1.5 Rationale, Hypothesis, and Specific Aims

Although optic fissure fusion has been studied for well over a century the direct molecular mechanisms governing this event are still poorly characterized. We know that the basic machinery involves the basement membrane, the actin cytoskeleton, and migrating endothelial cells, but how these components interact, what they do, and how they function are not understood. It has only been within the last decade that it was discovered that hyaloid vasculature is not just a passive process taking advantage of the optic fissure but is part of the molecular machinery driving this fusion event. The purpose of this dissertation was to form a comprehensive analysis on the behaviors of the molecular mechanisms of optic fissure fusion, in particular that of the hyaloid vasculature involvement in fusion. The overarching hypothesis of this dissertation was that the basement membrane, actin cytoskeleton, and the hyaloid vasculature are intimately linked to one another to drive optic fissure fusion, and the migrating endothelial cells are a key player during this process and is hypothesized to be due to the angiocrine signaling that these cells provide. This dissertation will show the first evidence, to date, of angiocrine signaling during optic fissure fusion provided by the migrating endothelial cells establishing the hyaloid vasculature. Additionally, we show how the other two molecular mechanisms, basement membrane breakdown and the actin cytoskeleton, behave and what they could possibly contribute to this process. This discovery was accomplished through the following aims:

1.5.1 Specific Aims

I. Characterize the basement membrane, actin cytoskeleton, and hyaloid vasculature in wild-type eye development.
    - Use whole mount immunohistochemistry and fluorescently tagged proteins to image the behaviors of these molecular mechanisms over the course of eye morphogenesis in the wild-type line of zebrafish.

II. Characterize the basement membrane, actin cytoskeleton, and hyaloid vasculature in Pax2 mutant eye development.
    - Use whole mount immunohistochemistry and fluorescently tagged proteins to image the behaviors of these molecular mechanisms over the course of eye morphogenesis in the coloboma model, Pax2 mutants, line of zebrafish.

III. Determine the consequences to optic fissure fusion in the absence of the hyaloid vasculature.
    - Use a vasculature specific drug inhibitor, DMH-4, to eliminate the hyaloid vasculature during eye development and assess the consequences to the basement membrane, the actin cytoskeleton, and ultimately optic fissure fusion.
    - Using DMH-4, assess the temporal requirement of the hyaloid vasculature cells during optic fissure fusion.

IV. Investigate endothelial cell contribution of metalloproteinases through angiocrine signaling resulting in the breakdown of the basement membrane.

- Use fluorescent whole mount *in situ* hybridization and qPCR in wild-type, pax2 mutant, and DMH-4 treated embryos to investigate any vasculature provided metalloproteinases during optic fissure fusion.

V. Determine the consequences to optic fissure fusion from the inhibition of mmp2.
   - Use a mmp2 drug inhibitor, ARP101, to diminish mmp2 during eye development and assess the consequences to the basement membrane thus optic fissure fusion.
   - Using ARP101, assess the temporal requirement of mmp2 during optic fissure fusion.

VI. Determine transcriptional differences between wild-type and pax2 mutant eyes.
   - Perform eye dissections, RNA extraction, and illumina sequencing on wild-type and pax2 mutant eyes at 48 hours post fertilization.

VII. Investigate the transcriptional differences between wild-type and Pax2 mutant embryos regarding actin cytoskeleton and hyaloid vasculature transcripts
   - Use whole mount *in situ* hybridization and qPCR to validate transcripts of interest from the RNA sequencing data.

VIII. Investigate ADAMTS1 anti-angiogenic properties during the establishment of the hyaloid vasculature
   - Perform mRNA injections into wild-type embryos to cause the over-expression of ADAMTS1 and assess the consequences to the hyaloid vasculature and the basement membrane.

Aims I, II, III, IV, and V are in Chapter 2

Aims VI, VII, and VIII are in Chapter 3

Table 1-1 Genes Associated with Coloboma. Adapted from [58, 140]

Gene	Animal Model	Human Mutation
ABCB6	Zebrafish	3
ACTB	N/A	Several
ACTG1	N/A	Several
Adamts16	Zebrafish	0
ALDH1A3	Mouse and zebrafish	Several
Aldh7a1	Zebrafish	0
ALG3	N/A	Several
ALX3	N/A	Several
Axin-2	Mouse	0
Axin2	Mouse	0
BCOR	Zebrafish	Several
BMP7	Mouse	Several
C12ORF57	N/A	Several
CC2D2A	N/A	Several
cdh2(ncad)	Mouse and Zebrafish	0
Cdon	Mouse	0
CEP290	N/A	Several
CHD7	Mouse	Several
CREBBP	N/A	Several
CRIM1	N/A	Several
CRYAA	Mouse	Several
Ctnna1	Mouse	0
Dkk	Mouse	0
DPYD	N/A	Several
Efna5	Mouse	0
EphB2	Mouse	0
FADD	N/A	5
Fbn2	Mouse	0
FLNA	N/A	Several
FOXE3	N/A	Several
Foxg1	Mouse	0
FZD5	Mouse and zebrafish	Several
GDF3	Zebrafish	Several
GDF6	Mouse and zebrafish	Several
GZF1	N/A	Several
hdac1	Zebrafish	0
HMGB3	Xenopus	2
HMX1	Mouse and zebrafish	2
IGBP1	N/A	3
INPP5E	N/A	Several
Ipo13	Zebrafish	0
Jag1	Mouse	0
KCTD1	N/A	Several
KIAA1279	N/A	5

Gene	Animal Model	Human Mutation
NAA10	N/A	Several
Nlz1/2	Zebrafish	0
Nr2f1,Nr2f2	Mouse	0
NRAS/HRAS/KRAS	N/A	Several
opo(ofcc1)	Medaka fish	0
OTX2	N/A	Several
PAX2	Mouse and zebrafish	Several
PAX6	Mouse	Several
PDE6D	Zebrafish	Several
PIGL	N/A	Several
Pitx2	Mouse	Several
POMT1	N/A	Several
PORCN	N/A	Several
PQBP1	N/A	Several
PTCH1/2	Zebrafish	Several
PTPN11	N/A	Several
PUF60	N/A	Several
RAB3GAP1	N/A	Several
RBP4	N/A	Several
RPGRIP1L	N/A	Several
RX	Mouse	Several
SALL1	Mouse	Several
SALL2	Mouse	1
SALL4	N/A	Several
SEMA3E	Zebrafish	Several
sfrp1a/sfrp5	Zebrafish	0
SHH	Mouse and zebrafish	Several
SIX3	N/A	Several
SIX6	N/A	7
Smad7	Mouse	0
SMCHD1	N/A	Several
SMOC1	Mouse	1
SMOH	N/A	4
Sox11	Zebrafish	0
SOX2	Mouse	Several
Sox4	Zebrafish	0
SRD5A3	N/A	Several
STRA6	Zebrafish	Several
TBX1	N/A	Several
Tbx2	Mouse	0
TBX22	N/A	Several
TENM3	N/A	4
TFAP2A	Mouse and zebrafish	Several
TMEM216	N/A	Several

Table 1.1 Continued

KMT2D	N/A	Several
Lamc1 & Lar	Zebrafish	0
LCP1	N/A	1
lmo2	Zebrafish	0
LRP2	N/A	Several
Lrp6	Mouse	0
MAB21L2	Mouse and zebrafish	Several
MAF	Mouse	Several
MIR204	N/A	1
MITF	Mouse	4
MKS1	N/A	Several
MSX2	Mouse	1

TMEM237	N/A	Several
TMEM67	N/A	Several
TWF1	N/A	1
Vax1	Mouse	0
Vax2	Mouse and zebrafish	0
VSX2/CHX10	Mouse and zebrafish	Several
WDR11	N/A	10
WSHC5	N/A	6
YAP1	Zebrafish	3
ZEB2	N/A	Several
ZIC2	Zebrafish	Several

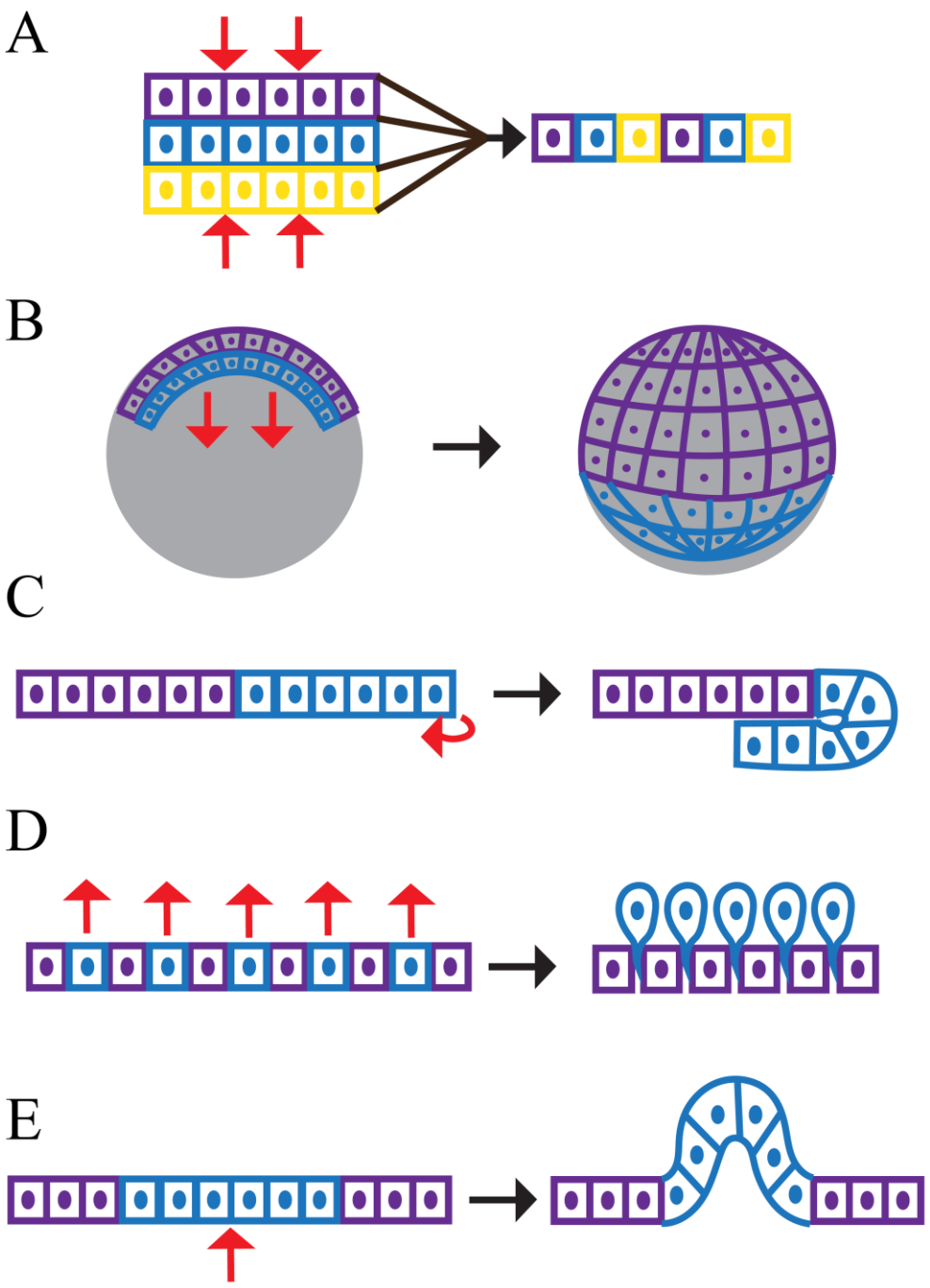

Figure 1-1Morphogenetic Movements.
Models depicting the five main methods of morphogenetic movements. Red arrows indicate the direction of force generated on the tissue. **A.** Convergent extension, three layers of cells (blue, purple, and yellow) intercalate into one sheet. **B.** Epiboly, a sheet of cells (purple and blue) spreads to envelop the embryo. **C.** Involution, cells (blue) turn inward creating an underlying layer. **D.** Ingression, cells (blue) lose contact with neighboring cells undergoing epithelial to mesenchymal transition and exiting the tissue. **E.** Invagination, cells (blue) bend inward to form an in-pocketing.

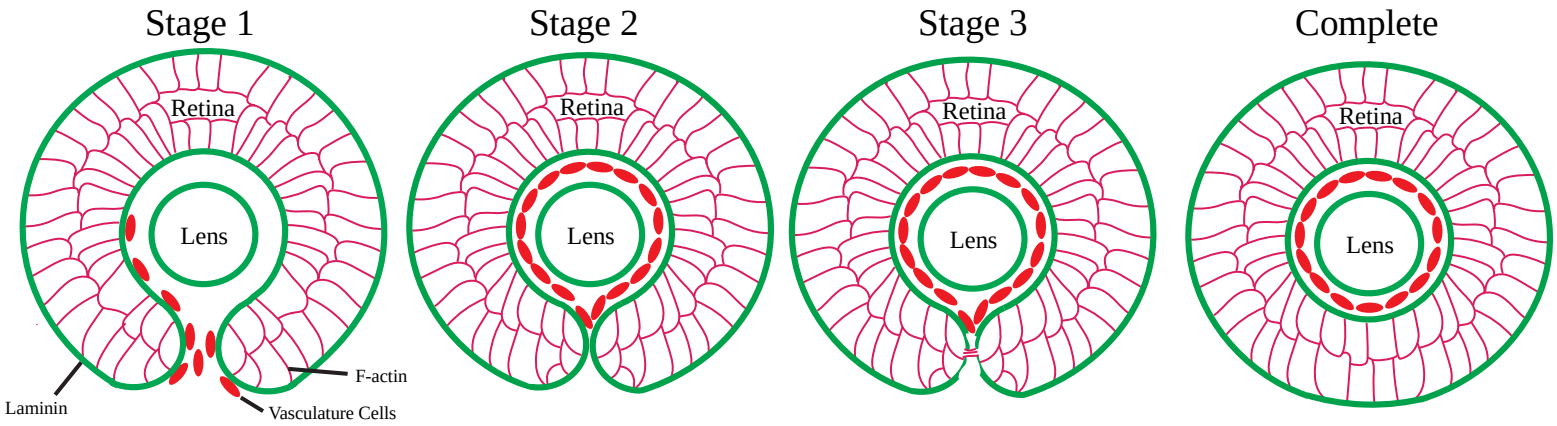

Figure 1-2Basic Model of Optic Fissure Fusion.

Diagram depicting the three major molecular mechanisms involved in optic fissure fusion in order of which they occur.

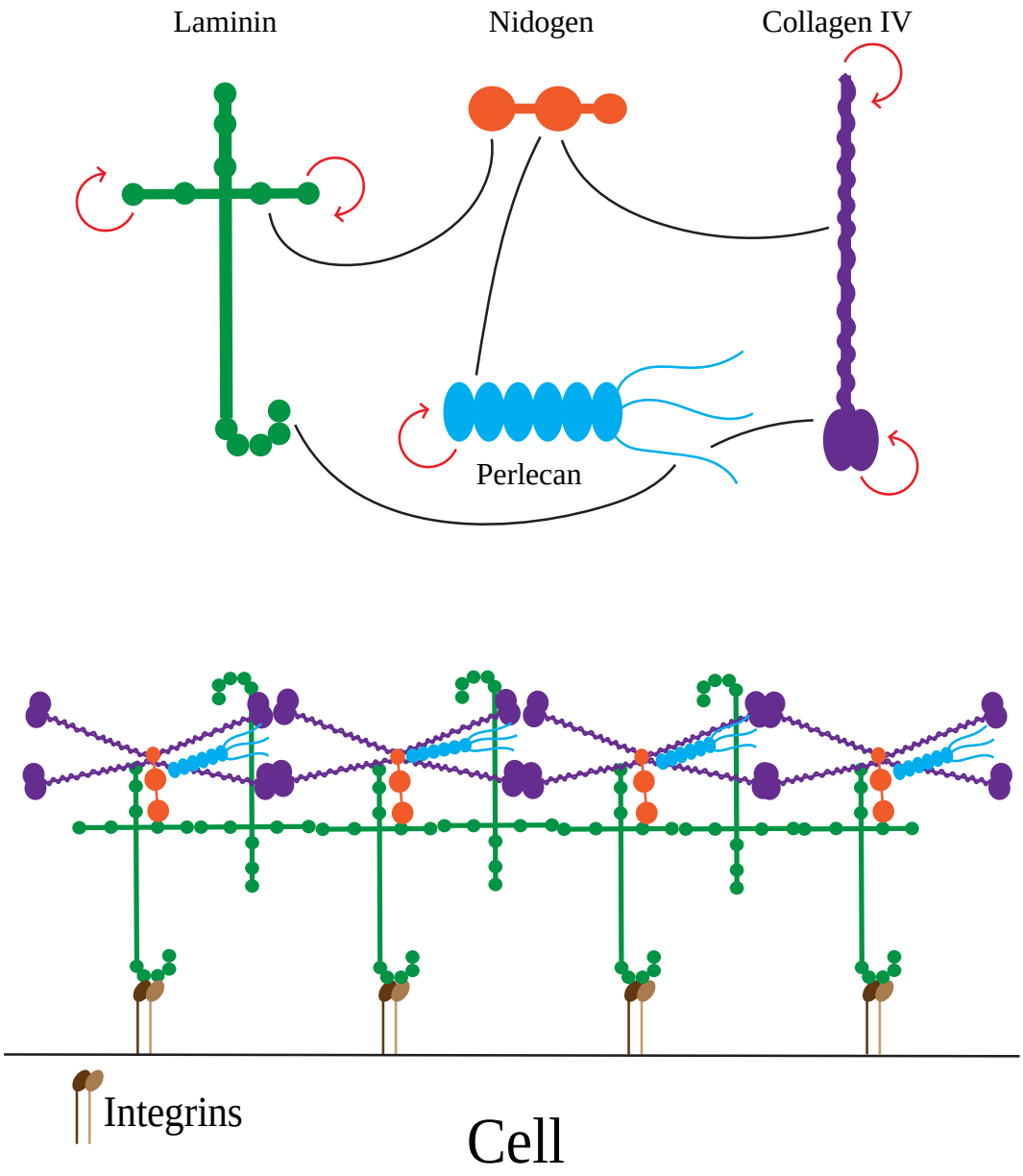

Figure 1-3 Basement Membrane

Diagram showing the four major components of the basement membrane. Laminin, perlecan, and collagen IV are capable of self-assembly (red arrows). Nidogen can bind to all other three components of the basement membrane, and perlecan can bind to both laminin and collagen IV. Laminins anchor the basement membrane to the cell via integrin binding.

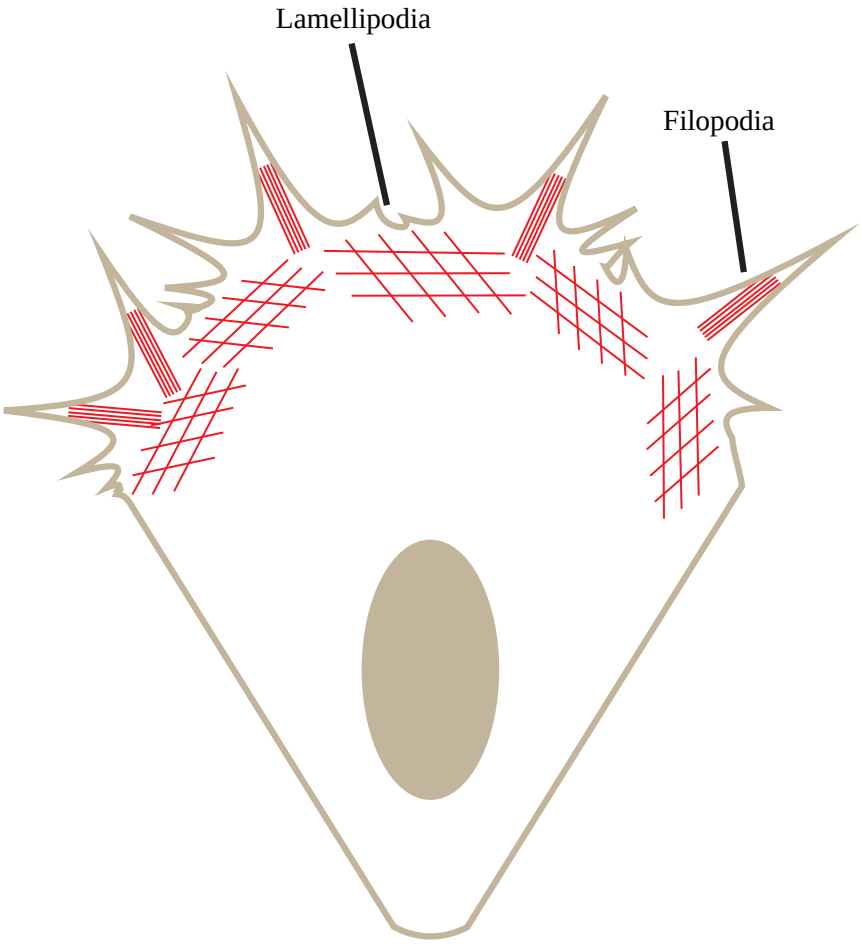

Figure 1-4 Lamellipodia and Filopodia
Diagram depicting lamellipodia formed through dendritic actin polymerization, and filopodia formed through tight parallel bundles of actin polymerization.

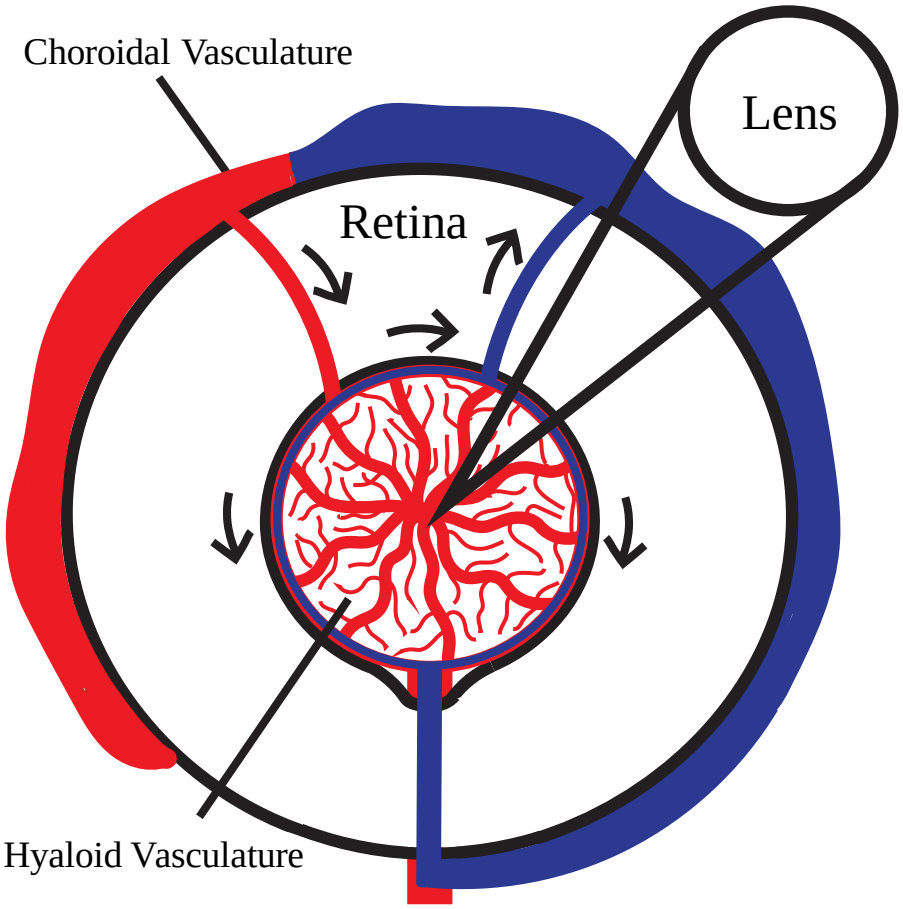

Figure 1-5 Completed Superficial Embryonic Vasculature
Schematic depicting the completed embryonic superficial vasculature network. Red indicates artery, blue indicates vein. Arrows show direction of blood flow.

CHAPTER 2. MATERIALS AND METHODS

Zebrafish and embryo maintenance

Zebrafish were maintained using husbandry procedures approved by University of Kentucky IACUC committee. Embryos were kept at 28.5^{o}C in E3 embryo media. AB and TL strains were used as wild-type, Tg[*kdrl*:mCherry] transgenic line was used to visualize retinal vascularization [141], Tg[*rx3*:GFP] was used to visualize retinal cells [142].

Pax2^{noi} embryos were a gift from Dr. Gregory-Evans. Genotyping analysis was conducted by amplifying the region of gDNA with the noi mutation using the forward primer: 5'- CTCGCTCTGCCTCCATGATTG3-'and the reverse: 5'- GGCACTGAAAGAGCACAGG -3'. The resultant 460bp amplicon was digested with TaqI (NEB) which would recognize and digest the WT allele sequence but not the mutant allele.

Cloche (clo^{m39}) mutant line was a gift from Dr. Mason Posner. Embryos were phenotyped for heart edema and genotyped as described by Reischauer *et al*., 2016 [143].

Immunohistochemistry (IHC)

Dechorionated embryos were fixed with 4% PFA in PBS at room temperature for 3h and washed with PBST 4 times for 5 minutes. Embryos were then permeabilized with Proteinase K, 30μg/mL 10 minutes for 24-28 hpf, 50μg/mL 15-20 minutes for 32-48 hpf and 75μg/mL 20 minutes for 56-72 hpf, washed 2 times in PBST for 5 minutes and blocked overnight at 4^{o}C with 10% sheep serum, 0.8% Triton X-100 and 1% BSA in PBS. Primary mouse anti-laminin antibody (ThermoFisher – 1:100) in blocking buffer (1% sheep serum, 1% BSA and 0.8% Triton X-100 in PBS) were incubated overnight at 4^{o}C and washed 5 times in PBST for 15 minutes. Secondary antibody, goat anti-rabbit (Alexa Fluor® 488 – Abcam – 1:1000), DAPI 1:1000, and phalloidin (Alexa Fluor® 555 - 1:50) were incubated overnight at 4^{o}C in the dark. Tg[*kdrl*:mCherry] embryos were

treated with proteinase K as described above and stained with DAPI 1:1000 overnight. The embryos were washed 2 times in PBST for 15 minutes and visualized using a Nikon C2+ confocal microscope equipped with a 40X (1.15NA) water immersion objective. Embryos were embedded in 1.2% low melting point agarose on glass bottom 35mm dishes (Fluorodish, World Precision Instruments). Images were captured in steps of 3.5 microns for a total of 31.5 microns using Nikon Elements software. Image adjustment, such as cropping and brightness/contrast was performed using Adobe Photoshop.

Analysis of Fluorescence signal

Fiji software (https://fiji.sc) was used to measure the fluorescence intensity of laminin and phalloidin signal from raw image data. In order to account for variability in staining, normalization values were measured for laminin and actin pixel intensity where an area directly outside of the choroid fissure was measured and a ratio was generated between the two values (Appendix 2.1B). In cases where the fissure edges were farther apart then the size of the box used for analysis, the box was divided into two and used to measure fluorescence intensity on each side of the fissure. Measured values from both boxes was added and then normalized. For Tg[krdl:mCherry], 3D reconstructions of the optic fissure were generated and individual cells were counted (from the opening of the OF through the back of the lens).

Statistics

Student's t-test was used to compare individual time points. One-way ANOVA was used to analyze across treatments. Graphs are displayed as mean +/- standard deviation. Analysis was performed using Prism8 graphing software (GraphPad).

Total RNA Sequencing

WT and Pax2$^{-/-}$ embryos were dissected and collected at 48 hpf and RNA was extracted from dissected eyes using trizol. Pax2a$^{-/-}$ embryos were phenotyped by distinct

heart defects only observed in pax2a$^{-/-}$ embryos, as verified by previous genotyping experiments. Dissected eyes were suspended in 1 mL of trizol and sheared with a 22-gauge needle. Samples were incubated at room temperature for 5 minutes, then 200 μL of chloroform was added and vortexed for 1 minute. Samples were then centrifuged at 12,000 g for 15 minutes at 4℃. Aqueous phase was removed and put into fresh RNAse free tube. 3 μL of Glycoblue was added to samples and vortexed for 5 seconds. 500 μL of 100% Isopropanol was then added and vortexed for an additional 10 seconds. Samples then were incubated at room temperature for 10 minutes. Samples were then centrifuged at 12,000 g for 10 minutes at 4℃. Supernatant was removed and 1 mL of 75% EtOH was added and vortexed for 10 seconds. Samples were then centrifuged at 7,500 g for 5 minutes at 4℃. Supernatant was removed and samples then underwent a pulse centrifugation and any remaining supernatant was removed. Samples were then air-dried for 7 minutes at room temperature under a fume hood. 20 μL of RNAse free ddH_2O was added to the samples and mixed until pellet dissolved. Samples were finally incubated at 60℃ for 12 minutes and then stored at -80℃.

The RNA then underwent a DNase treatment using the DNA-free Kit. 2 μL of 10X DNaseI Buffer, and 1 μL of rDNaseI was added to the entire 20 μL sample. Samples were incubated at 37℃ for 20 minutes, and then 2 μL of DNase Inactivation Reagent was added. Samples were then incubated at room temperature for 2 minutes, mixing samples 3 times. Samples were centrifuged at 10,000 g for 1.5 minutes. Supernatant was then removed and placed into fresh RNase free tube and stored at -80℃.

Purified total RNA was sent to Applied Biological Materials Inc. for Illumina sequencing (PE150bp, 30-40 million reads/sample). Bioinformatic analyses were completed using RSEM. Those transcripts which had a greater than 0.95 posterior probability of being differentially expressed were considered significant. Panther (http://pantherdb.org) was used for gene ontology and pie chart generation.

Whole-mount in situ hybridization (WISH)

Whole-mount in situ hybridization was performed as previously described [144]. RNA probes were generated using PCR with T7 promoter sequence linkers and subsequently transcribed [DIG or FITC labeled] using T7 polymerase (Roche). Primer sequences are all found in Table 2.1. Images were captured using a Nikon Digital sight DS-Fi2 camera mounted on a Nikon SZM800 stereo scope using Elements software. Dissected eyes from 24, to 72hpf embryos were mounted in 70% glycerol and imaged under DIC using a Nikon TiE compound microscope equipped with a 20X (0.7NA) objective and Elements software. Image adjustment, such as cropping and brightness/contrast was performed using Adobe Photoshop.

qPCR analysis

32hpf embryos were anesthetized with tricane, tail tips were collected for genotyping and the heads, dissected just posterior of the eyes, were fixed in RNAlater. After genotyping, embryos corresponding to WT and pax2a-/- were pooled, 5-10 embryos, and total RNA isolated using a RNAaqueous kit (Ambion). DMSO and DMH4 treated embryos were harvested in the same fashion absent any genotyping. qPCR was performed as previously described [145]. Primer sequences are all found in Table 2.1.

2 color fluorescent in situ hybridization

FWISH was performed as previously described [146]. Images were collected using a Nikon C2+ confocal microscope with a 20X (0.95NA) objective and images were adjusted for brightness and contrast using Adobe Photoshop.

Live imaging analysis

Live imaging of Tg[kdrl:mCherry] embryos was conducted using a Nikon C2+ confocal microscope equipped with at 20X (0.95NA) water immersion objective. 22 hpf

embryos were imbedded in 1.1% low gelling agarose in 1-inch glass bottomed Flourodish cell culture dishes (World Precision Instruments) and covered in embryo media, 3-amino benzoic acidethylester (tricaine) to anaesthetize the embryos and 1-phenyl 2-thiourea (PTU) to inhibit pigmentation. Z-stacks 75μm thick with a step size of 2.5μm were captured over the course of 6 hours at 10 minute intervals. The time lapse data were reconstructed in 3D using Elements software. Image adjustment, such as cropping and brightness/contrast was performed using Adobe Photoshop. After imaging, embryos were removed and genotyped.

Inhibitor treatments

Embryos were incubated in embryo media with 5, 25, 50, or 100 μM of DMH-4 (Sigma Life Science) in DMSO starting at 12hpf. Fresh DHM4 containing media was added every 12hpf for timepoints past 24hpf. For ARP101 (Tocris) treatments embryos were dechorionated and treated with 10, 15, 20, 25 or 30μM ARP101 in fish water from 24 to 48hpf, unless stated otherwise.

Cloning and mRNA synthesis.

Full coding domain sequences for *adamts1* (NCBI reference sequence XM_021475923.1), were amplified from 24hpf zebrafish cDNA using primers 5'-CTCGAGTCAACAGGGAGTCAGATTGC-3' for *adamts1*, cloned into pGEMT (Promega), digested with AsiSI/XhoI, BamHI/XhoI respectively and subsequently cloned into pCS2+. All constructs were verified by sanger sequencing (Eurofinsgenomics). mRNA was synthesized from linearized pCS2 constructs using SP6 mMessage mMachine kit (Ambion) and purified using YM-50 Microcon columns (Amicon, Millipore).

Alt-R-crRNA CRISPR injections

Alt-R mmp2 crRNA, tracrRNA was pre-designed and synthesized by IDT. Duplex formation and dilution with Alt-R Cas9 v.3 enzyme was carried out as described by Hoshijima *et al*. 2019 [147].

Ethics Statement

The use of zebrafish in this study was approved by the University of Kentucky IACUC committee, Institutional PHS Assurance #D16-00217 (A3336-01) with a protocol number: 2015-1370.

Table 2-1 Primer Sequences
WISH

Gene	Primer Sequences
Pax2a probe FORWARD	ATGGATATTCACTGCAAAGCAG
Pax2a T7 probe REVERSE	TAATACGACTCACTATAGGGCTAGTGGCGGTCATAGGCAGTG
tln1 probe FORWARD	GCTATCGCTGTCACCGTTCAG
tln1 T7 probe REVERSE	TAATACGACTCACTATAGGGGATGCCTTTGGTCATGCGGATG
mmp2 probe FORWARD	ATGATGTCCGTTAAGTTTTTC
mmp2 T7 probe REVERSE	TAATACGACTCACTATAGGGCTCAGGACAGAATCCGTAAGT
mmp14a probe FORWARD	ATGTTACCGAAACTGCAGACG
mmp14a T7 probe REVERSE	TAATACGACTCACTATAGGGCACTCGCCAGAACCACTTTTC
mmp14b probe FORWARD	ATGATCTGGAGCGGGTTTACG
mmp14b T7 probe REVERSE	TAATACGACTCACTATAGGGGAACCACTTACCCTTAAACAC
vegfAA probe FORWARD	GAAGTTAATTTTAGCGGATTCG
vegfAA T7 probe REVERSE	TAATACGACTCACTATAGGGGTGATAGCAGCGACACACATTG
vegfAB probe FORWARD	GCATGGGATTACTTCTGTGATG
vegfAB T7 probe REVERSE	TAATACGACTCACTATAGGGCTTCATGTCCGTTCTCAAGTC
vegfC probe FORWARD	ATGCACTTATTTGGATTTTCTG
vegfC T7 probe REVERSE	TAATACGACTCACTATAGGGCACACATTTGGTGCGGTTGAG

Table 2.1 Continued

rorb probe FORWARD	CTCAGCACCCTCAACCACGAG
rorb T7 probe REVERSE	TAATACGACTCACTATAGGGTCATTTGGGCATGACGGCGGC
kdrl probe FORWARD	CAAGTGGCTAAAGGCATGGAG
kdrl T7 probe REVERSE	TAATACGACTCACTATAGGGGACGGGTGGTGTGGAGTAACG
ROCK1 probe FORWARD	GAGATTATGAACCGTAAGGAC
ROCK1 T7 probe REVERSE	TAATACGACTCACTATAGGGTTAGCTGGGCTTTCCTGGGAC
ROCK2b probe FORWARD	CACTCCATCATCAAATACCAG
ROCK2b T7 probe REVERSE	TAATACGACTCACTATAGGGTCACCTGTTCTTGCTGGAGGG

qPCR

Gene	Primer Sequences	Primer Sequences2
tln1	TTGGGGCAATTCCAGCAAAC	TGCTTCGCACAGGTTGTTAG
cldn5b	TACATCGTCGCAGGCTTGTT	GATGCTGCCCATCCGATGTA
tjp1a	CACAGAAGCAAGAGCCTGGA	AAAACCCGGTGCCCTGTG
flt4	CAGTCCAAAACAGCCAGCAC	CAACTCCACAGGCGAGTCTT
vegfaa	CAACGCGTATCGCAGCATAAT	AAGGCTCACAGTGGTTTTCTT
vegfab	TGTTGTATGTGACGGTGGGG	GCAAAACCGTGGTTCCAGAC
vegfc	TGGAGAAAGACGCTGTGCAT	TGCACTGAAGCTCCTCACTG
mmp2	TCAGGGTCGAGATGATGGGT	GAAAAGGAGCTCATGGGGACA
mmp14a	ACGCAGCTTATGAACGCAAT	TCCTGTGCCAAGCTCCTTAA
mmp14b	TCTTCAAAGGGGACAGGCAT	CACCAGTTCCCAGTTCTCCT
ROCK1	CAGGAAAGCCCAGCTAACCA	CGTGTGAGGTTATTGCAGAGG
ROCK2a	GGGAAGTCCAGCTGGTTAGG	TCCTCCCAGAAGAAGGCAGA
ROCK2b	CTGACGAGGCATATCCAGCC	CTGCTCACGACCACATACTTC

CHAPTER 3. HYALOID VASCULATURE AND MMP2 ACTIVITY PLAY A ROLE DURING OPTIC FISSURE FUSION IN ZEBRAFISH.

Megan L. Weaver, Warlen P. Piedade, Nishita N. Meshram, and Jakub K. Famulski

Contributions: Warlen P. Piedade contributed to figures 3.2, 3.3, and 3.5.
Nishita Meshram contributed to figures 3.2, 3.3, 3.4, and 3.5.

3.1 ABSTRACT

Vertebrate retinal development requires timely and precise fusion of the optic fissure (OF). Failure of this event leads to congenital vision impairment in the form of coloboma. Recent studies have suggested hyaloid vasculature to be involved in OF fusion. In order to examine this link, we analyzed OF fusion and hyaloid vasculogenesis in the zebrafish pax2a noi mutant line. We first determined that pax2a$^{-/-}$ embryos fail to accumulate F-actin in the OF prior to basement membrane (BM) degradation. Furthermore, using 3D and live imaging we observed reduced OF hyaloid vascularization in pax2a$^{-/-}$ embryos. When examining the connection between pax2a loss of function and hyaloid vasculature, we observed significant reduction of *talin1* expression, a regulator of hyaloid vasculature. In addition, cranial VEGF expression was found to be reduced in pax2a$^{-/-}$ embryos. Pharmacological inhibition of VEGF signaling phenocopied the pax2a$^{-/-}$ vasculature, F-actin and BM degradation phenotypes. Lastly, we determined that OF associated hyaloid vasculature is a source of *mmp2, mmp14a and mmp14b* expression and showed that mmp2 is functionally necessary for degradation of OF BM. Taken together we propose a pax2a driven mechanism that ensures proper and timely hyaloid

vasculature invasion of the OF in order to facilitate availability of the BM remodeler mmp2.

3.2 INTRODUCTION

Ocular development is a highly conserved process amongst vertebrate species. Assembly of the hemispherical, retinal structure from an initially flat sheet of cells requires many complex morphogenetic movements. One such morphogenetic movement involves the invagination of the optic vesicle which results in a fissure forming at the ventral region of the developing retina. This fissure, known as the choroid or optic fissure (OF), enables hyaloid vasculature cell migration into the developing retina and subsequent establishment of the hyaloid vasculature. Hyaloid vasculature is a temporary circulatory system required for ocular development, and in most cases will degenerate once mature blood vessels begin to grow [125, 148-150]. As soon as the hyaloid vasculature has been established, the two opposing retinal epithelial sheets of the OF will undergo fusion. Thereby, they encase the ganglion cell axons localized in the optic stalk and complete retinal morphogenesis. Failure of OF fusion leads to a congenital blinding disorder known as coloboma [151-153]. Coloboma is a prevalent cause of pediatric blindness, accounting for approximately 10% of cases worldwide [152, 154]. This makes it one of the leading causes of pediatric blindness. Coloboma is a spectrum disorder presenting unilaterally or bilaterally and ranging in severity from minor visual impairment, to complete blindness in the affected eye [155]. This spectrum of severity is associated with the location and degree to which the OF was able to fuse and the severity of subsequent loss of ganglion cell axons [153].

Coloboma has been studied for many decades in many different species. Work over this time has led to a general outline of the signaling and morphogenetic pathways required for proper OF formation and fusion (recently reviewed in [156]). In particular, opposing action of bone morphogenetic protein (BMP) and sonic hedgehog (Shh) signaling establishing the dorsal-ventral pattern of the optic vesicle and ensuring proper expression of optic stalk and OF regulators pax2, vax1 and vax2 [157, 158]. However, the actual molecular mechanisms driving OF fusion remains largely unknown. The process of epithelial tissue fusion is not unique to the eye and occurs throughout development, encompassing neural tube closure, palatal shelf formation and eyelid development [159]. Epithelial fusion has been studied for over a century, and is known to involve transcriptional regulation, cell signaling pathways and morphogen gradients [160, 161]. The actin cytoskeleton is thought to be a crucial component of the machinery driving epithelial fusion in many tissues [162]. The importance of the actin cytoskeleton during epithelial fusion involves lamellipodial and filopodial projections between the two opposing epithelia. These help to "zipper" the cells together to form a single continuous sheet. When lamellipodial and filopodial projections are precluded, epithelial fusion often fails [163]. Lamellipodia and filopodia have been observed during OF fusion almost 3 decades ago [164-166]. However, the functional and regulatory mechanisms behind these projections remain unknown. Another cellular mechanism known to be directly involved in epithelial fusion is the degradation of the basement membrane (BM). During epithelial fusion, the BM acts as a physical barrier restricting the establishment of cell-cell contacts, which must be removed in order to complete fusion. Recent work from several labs, working on different species, has characterized progressive removal of the BM during OF

fusion [88, 119, 167, 168]. However, the molecular mechanisms facilitating this process, in particular BM degradation, also remain largely unknown. It was recently suggested that hyaloid vasculature cells migrating through the OF could potentially signal or facilitate BM degradation [119]. Hyaloid vasculature nourishes the developing retina and lens while connecting to the choroid vasculature for proper blood flow [125]. Hyaloid vasculogenesis takes advantage of an open OF so that vasculature cells can migrate into the developing optic cup. Once OF fusion is completed, hyaloid vasculature is fully established. James *et al.* 2016, showed that mutations in zebrafish *talin1* (*tln1*), an actin cytoskeleton scaffolding protein known to be required for endothelial cell migration [169], result in OF fusion defects. Theirs, and previous studies also indicated that *cloche* mutants, which lack all early hyaloid vasculature, have delayed BM breakdown in the region of the OF [119, 170]. Since the hyaloid vasculature requires an open fissure to complete establishment of its network, it has been proposed that migrating hyaloid vasculature cells may regulate the timing of fissure fusion. This mechanism could potentially involve vasculature-mediated activation of the fusion machinery within the retinal rim cells, or direct supply of molecular factors, such as matrix proteases [171]. In support of this hypothesis, recent optic cup transplantation experiments in zebrafish embryos confirm that in the absence of hyaloid vasculature, ectopic retinal OFs fail to initiate fusion [139]. Hence, there is a clear link between OF fusion and hyaloid vasculature.

In our current study, we have undertaken a detailed analysis of zebrafish OF fusion in the pax2a$^{-/-}$ coloboma model [172]. This included characterizing the timing of BM degradation, cytoskeletal responses, morphological apposition and hyaloid

vascularization. When comparing pax2a$^{+/+}$ and pax2a$^{-/-}$ eyes we discovered decreased OF hyaloid vascularization and OF fusion failure. In particular we found that pax2a$^{-/-}$ embryos exhibit a decrease in *tln1*, hyaloid vasculature makers as well as *VEGFaa, VEGFab* and VEGF*c* expression. Modulation of vascularization via pharmacological inhibition of VEGF signaling phenocopied the pax2a$^{-/-}$ hyaloid vasculature and coloboma phenotypes. Mechanistically, we also show that hyaloid vasculature is a source of *mmp2, mmp14a* and *mmp14b* and that mmp2 activity is necessary for OF BM degradation. Taken together, we propose a novel pathway for the regulation of OF fusion where pax2a mediates proper timing and abundance of hyaloid vasculature cell recruitment to the OF and subsequent vasculature supplied mmp2-dependent BM degradation.

3.3 RESULTS

3.3.1 Optic fissure basement membrane degradation is preceded by F-actin accumulation.

Several recent studies have undertaken a detailed time course to map out the exact timing of OF fusion in numerous species, including zebrafish [88, 119, 167, 168]. Overall, in zebrafish, the data point to ~32-36hpf as the time of OF fusion initiation, as observed by BM degradation. To decipher the molecular mechanisms regulating OF fusion we also performed a detailed time course analysis of OF BM degradation using laminin immunohistochemistry (IHC) while additionally analyzing F-actin. Our goal was to determine whether changes in F-actin levels in the OF were correlative with fusion. James *et al*, 2016 had recently suggested that infiltrating vasculature endothelial cells migrating through the fissure could be a source of signal for fissure fusion. In fact, they

had shown that interactions between vasculature and the fissure resulted in an increase of F-actin [119]. As such, we first performed whole mount IHC for laminin deposition in embryos starting at 24hpf. We sampled every 4 hours up to 48hpf and then at 56 and 72hpf (Figure 3.1A). To analyze the progression of the fusion process, we quantified the laminin signal within the OF from 3D confocal scans. We quantified distal, medial and proximal regions of the fissure (Appendix 2.1A). Regions of the BM outside the OF and juxtaposed to the developing lens were used to normalize the laminin signal (Appendix 2.1B). When comparing results from the three regions we did not observe significant differences in the distribution of laminin or F-actin (Appendix 2.1C). Going forward we focused on quantifying laminin signal in the central proximal region (medial) of the fissure (Figure 3.1C). This region has been previously shown to represent the site of fusion initiation, is known to interact with hyaloid vasculature and is easily identified in 24-72hpf embryos [119]. In agreement with recent studies in zebrafish, we found that OF fusion initiates at ~32-36hpf and does so in a central region of the fissure, subsequently proceeding proximally and distally. From observing distance between the fusing lobes of the retina in our time course for OF laminin status, Figure 3.1A, we observed apposition to complete between 36-44hpf (Figure 3.1A). By 48hpf, we observed most of the laminin signal was removed from the OF, and by 72hpf, little to no laminin persists in the region (Figure 3.1A, C).

To track F-actin levels during fusion we stained the laminin labeled embryos with phalloidin and quantified the signal within the fissure. To normalize phalloidin staining intensity we used an interior region of the retina (Appendix 2.1B). Our analysis revealed an increase in OF associated F-actin signal between 24-32hpf, preceding the time that

BM degradation is initiated (Figure 3.1D). The observed increase of F-actin signal correlates with the timing of hyaloid vasculature migration (24-32hpf) into the fissure. The nature of our assay did not precisely identify the cellular source of F-actin but it likely predominantly consisted of retinal rim and hyaloid vasculature cells. Taken together, we conclude that BM degradation is preceded by an increase of F-actin within the OF.

3.3.2 Optic fissure fusion mechanics are disrupted upon loss of pax2a function.

In order to test our hypothesis that an increase in F-actin is involved in the initiation of OF fusion we compared our findings to an established model of coloboma, the pax2a noi line [172]. Pax2 is required for OF fusion in several model systems and has been documented in human coloboma cases [173-175]. The noi mutation is predicted to result in a loss of pax2a function due to a premature stop codon at position 198 [176]. Originally characterized for their no-isthmus phenotype, pax2a$^{noi/noi}$ embryos (referred to as pax2a$^{-/-}$ from this point on) elicit a fully penetrant unfused OF [177, 178]. Unfortunately, homozygous mutants are not viable and do not enable the study of coloboma at juvenile or adult stages. We hypothesized that examining the molecular events leading to OF fusion in the pax2a noi system would inform us whether these events are functionally important. Similar to our WT study, we examined apposition, laminin and F-actin levels throughout the time of OF fusion (Figure 3.1B, D, Appendix 2.2). In stark contrast to WT, pax2a$^{-/-}$ embryos did not exhibit a significant decrease in laminin signal between 32-48hpf. In fact, as expected, laminin appeared to be largely retained in the OF of pax2a$^{-/-}$ embryos up to 72hpf (Figure 3.1B,C). Previous studies in

pax2a null mice had also indicated failure of BM degradation and retention of laminin [175]. While there is a moderate decrease in laminin signal in pax2a$^{-/-}$ embryos from 32-36hpf (p=>0.0001), there was no significant loss of laminin signal between 36-48hpf. This result is significantly different in WT embryos (p=>0.0001) which display a major decrease in laminin signal during this time. IHC images clearly show that laminin persists in the pax2a$^{-/-}$ fissure up to and including 72hpf (Figure 3.1B). When examining OF F-actin levels in pax2a$^{-/-}$ embryos we did not detect the expected increase between 24 and 32hpf (Figure 3.1D). In fact, up to 48hpf F-actin levels measure significantly lower than in WT embryos. Similar results were also observed when quantifying distal and proximal regions of the fissure (Appendix 2.1D). Our data therefore suggest that the absence of OF F-actin accumulation between 24 and 32hpf, correlates with failure to initiate fusion. Lastly, when examining retinal lobe distance in pax2a$^{-/-}$ embryos we did not observe any significant defects in the degree of apposition up to 48hpf (Appendix 2.2). Taken together, we conclude that in the absence of pax2a, F-actin fails to accumulate in the OF and this correlates with the failure to degrade the BM. Based on our findings, we therefore conclude that retinal lobes still become apposed by 48hpf in pax2a mutants. In summary, we propose that accumulation of F-actin is necessary for the initiation of OF BM degradation. We therefore next sought to investigate the source of OF F-actin accumulation.

3.3.3 Loss of pax2a function leads to reduced hyaloid vasculature within the optic fissure.

Work by James *et al.* 2016, suggested that F-actin accumulation in the OF may result from interaction between retinal rim cells and invading hyaloid vasculature. To test this possibility, we examined hyaloid vasculature in pax2a$^{-/-}$ Tg[kdrl:mCherry] embryos. Using 3D *in vivo* time-lapse confocal microscopy we recorded migration of mCherry expressing cells through the OF from 24 to 30hpf (Figure 3.2A). At 24hpf, both WT and pax2a$^{-/-}$ embryos contain mCherry expressing cells within the fissure. However, over the next six hours of imaging it is apparent that pax2a$^{-/-}$ embryos have significantly fewer mCherry expressing cells pass through the OF (Figure 3.2A). To visualize this effect, we fixed WT and pax2a$^{-/-}$ Tg[kdrl:mCherry] embryos at 24, 32, 36 and 48hpf to collect and render 3D confocal stacks (Figure 3.2B). Starting as early as 32hpf, we noticed a clear reduction in the number of vasculature cells within the OF and retina. Furthermore, we counted the number of mCherry positive cells found within the OF at 32 and 36hpf (Figure 3.2C). The data indicated that in pax2a$^{-/-}$ embryos there is a significant reduction in the number of mCherry expressing cells at both 32 and 36hpf (Figure 3.2C). Additionally, using 3D rendering, we noted that in 48hpf pax2a$^{-/-}$ embryos the hyaloid vasculature established in the back of the lens is reduced in size and lacks proper connections to the newly forming choroidal and superficial vasculature systems. In the previously aforementioned study, James *et al.* 2016 also showed that tln1 is necessary for hyaloid vasculature recruitment to the OF and subsequent fusion. Since pax2a$^{-/-}$ embryos lack BM degradation, fail to initiate F-actin accumulation and have reduced hyaloid vascularization (Figure 3.1,2), we sought to examine *tln1* expression in this model. To examine *tln1* expression status we performed whole mount *in situ* hybridization (WISH)

for *tln1* comparing WT siblings to pax2a$^{-/-}$ mutant embryos. WT expression of *tln1* was observed in the OF between 28 and 48hpf coinciding with pax2a expression (Figure 3.2D, Appendix 2.3). In pax2a$^{-/-}$ embryos, OF *tln1* expression appears significantly reduced compared to WT while retaining similar expression in periocular regions (Figure 3.2D). *Tln1* expression is also reduced in the mid brain-hind brain boundary, another region of strong *pax2a* expression (Figure 3.2D, Appendix 2.3A). Our WISH data was further supported by qPCR results showing a significant decrease in *tln1* expression at 32hpf (Figure 3.2E). Finally, to verify our observations were indicative of reduced hyaloid vasculature we also analyzed expression of additional vasculature markers *flt4, tjp1a* and *cldn5b [64, 179]*. qPCR comparison of 32hpf WT and pax2a$^{-/-}$ embryo heads indicated a significant decrease of *flt4, tjp1a* and *cldn5b* expression, validating our observation of overall reduced vasculature in mutant embryos (Figure 3.2E). Overall, our data indicate that pax2a$^{-/-}$ embryos exhibit decreased expression of *tln1* and impaired hyaloid vascularization of the OF.

3.3.4 Inhibition of VEGF signaling impairs optic fissure fusion mechanics.

Based on our discovery of impaired OF hyaloid vasculature in pax2a$^{-/-}$ embryos, we next examined whether this phenomenon is associated with failure of OF fusion. Hence, we turned our attention to vascular endothelial growth factor (VEGF) signaling. VEGF, the ligand for vascular endothelial growth factor receptor (VEGFR), is a prime candidate for regulating the migration and proliferation of hyaloid vasculature cells. In support of this notion, when examining expression patterns for VEGF ligands, vegfaa, ab, and c we found *vegfaa, ab,* and *c* to be expressed in the head and periocular regions

(Figure 3.3A). In order to test for a link between the loss of pax2a function and VEGF signaling we analyzed *vegfaa*, *ab* and *c* expression in pax2a$^{-/-}$ embryos. Fluorescent wholemount in situ hybridization (FWISH) at 32hpf indicated a decrease of *vegfaa*, *ab* and *c* expression in the cranial regions of mutant embryos (Fig 3A). These results were also supported by qPCR (Figure 3.3B). Our data therefore suggest that a decrease in VEGF signaling may be a factor responsible for reduced hyaloid vascularization of the OF in pax2$^{-/-}$ embryos. This finding may also explain the severe vascular phenotypes pax2a$^{-/-}$ embryos develop, in particular heart edema and other cardiac misfunction.

In order to test whether VEGF signaling plays a direct role in hyaloid vascularization of the OF and subsequently fissure fusion we sought to inhibit VEGF activity. We therefore took advantage of a dorsomorphin derivative, DMH4, which has been shown in zebrafish to selectively inhibit VEGF signaling independent from BMP [180]. Based on published working concentrations, we conducted a dose response to examine DMH4 effects on hyaloid vasculature using Tg[*kdrl*:mCherry] as a readout [180]. Treatment of embryos from 12-24hpf, ranging from 1-100μM, resulted in a dose dependent reduction of mCherry signal in the developing retina (Appendix 2.4A). We decided to use the 100μM concentration for subsequent experiments as this concentration was able to completely inhibit vascularization of the retina up to 56hpf without any significant impact on overall embryo health (Appendix 2.4B,C). Embryos were treated starting at 12hpf and examined for fissure fusion status via whole mount laminin IHC at 24, 32, 36, 48, 56 and 72hpf (Figure 3.3C). 3D confocal imaging revealed a persistence of laminin signal within the fissure up and including 72hpf in all embryos examined (Figure 3.3C). This was in contrast to DMSO treated embryos which exhibited no defects

in OF fusion (Appendix 2.4D). Long term treatment with 100μM DMH4, 56hpf+, did result in a degree of retinal toxicity (Appendix 2.4B). To circumvent this effect, we also treated embryos from 12-72hpf with 25 and 50μM DMH4 (Appendix 2.4B). Toxicity appeared reduced at the lowest concentration, 25μM, while still eliciting a failure of OF fusion phenotype in 87.5% of treated embryos (Figure 3.3D, Appendix 2.4E). Observed retention of OF laminin signal at 48hpf in DMH4 vs DMSO treated embryos generated an overall pattern of results very similar to what we observed in pax2a$^{-/-}$ (Figure 3.3E). While DMH4 treatment did result in a significant reduction of OF laminin signal from 36-48hpf ($p=<0.0002$), OF laminin levels of DMH4 treated embryos were significantly higher than DMSO controls at 48hpf (Figure 3.3E). When measuring the degree of retinal lobe apposition at 48hpf, we saw no negative effects of DMH4 treatment. This suggests that the observed failure of OF BM degradation is unlikely to result from optic cup morphogenesis delay (Appendix 2.2). However, it remains possible that apposition is initially delayed by DMH4 treatment yet completes by 48hpf. In addition to laminin, we also imaged and quantified OF F-actin levels during DMH4 treatment (Figure 3.3F). Similar to pax2a$^{-/-}$ embryos, DMH4 treatment prevented the accumulation of OF F-actin between 24-32hpf (Figure 3.3F). This was in contrast to DMSO treated embryos which exhibited the expected accumulation of F-actin in the fissure between 24-32hpf.

To show timing specificity of our DMH4 treatments we also performed a time course analysis. When treating embryos with DMH4 starting at 12hpf we observed total inhibition of fissure fusion, indicated by retention of OF laminin signal at 48hpf. However, when DMH4 was added at later time points, 24, 28 or 32hpf we observed a corresponding decrease in fissure fusion failure (Figure 3.4A,B). Interestingly, starting

DMH4 treatment at 32hpf had little effect on OF fusion. To correlate our DMH4 time course treatment to hyaloid vasculature, we imaged vasculature using the Tg[*kdrl*:mCherry] line (Figure 3.4C). Starting DMH4 treatment at 24 or 28hpf significantly reduced the number of hyaloid vasculature cells in the OF at both 32 and 36hpf and by 48hpf, little to no vasculature was observed (Figure 3.4C). Quantification of hyaloid cells within the fissure at 32 and 36hpf supported these observations (Figure 3.4D). Importantly, the degree of OF hyaloid vascularization correlated with the rates of OF fusion failure observed (Figure 3.4B). Significant reduction directly correlated to an increase in fusion failure (Figure 3.4B). On the other hand, delay of DMH4 treatment until 32hpf did not eliminate all hyaloid vasculature in the OF at 48hpf and correlated with increased rates of OF fusion (Figure 3.4B). Sufficient hyaloid vasculature recruitment to the OF is therefore critical at early stages of OF fusion, 24-28hpf.

Lastly, in order to confirm the source of tln1 in the OF as hyaloid vasculature, we assessed *tln1* expression after DMH4 treatment. Fluorescent whole mount in situ hybridization (FWISH) indicated a significant decrease of *tln1* but not *pax2a* expression in DMH4 treated embryos (Figure 3.4E). qPCR analysis supported our observation (Figure 3.4F). This suggests that *tln1* is most likely expressed by the vasculature cells within the OF. Based on these findings, we conclude that inhibition of VEGF signaling results in failure of F-actin accumulation and basement membrane breakdown due to the absence of hyaloid vasculature cells in the OF.

3.3.5 Hyaloid vasculature is a source of mmp2 necessary for OF BM degradation.

The above data confirm and support a model where hyaloid vasculature drives or initiates the OF fusion process. However, a missing key to this model is the mechanism by which vasculature cells induce fissure fusion. James *et al* 2016, along with others, have suggested vasculature cells may be a source of BM degradation enzymes, such as matrix metalloproteases (mmp). To investigate this further, we used WISH to examine mmp expression within the OF between 24-48hpf. Our examination of mmp expression indicated that *mmp2, 14a* and *14b* were expressed within the fissure between 28-36hpf (Appendix 2.5A and Famulski lab unpublished data). Mmp2 had recently been associated with OF fusion in the mouse while evidence from an mmp2 metalloproteinase activity probe in zebrafish indicated mmp2 activity is present in the developing eye and likely OF [181, 182]. mmp14 is an activator of mmp2 and its co-expression with mmp2 within the fissure suggests mmp2 is in fact active [183, 184]. To test whether mmp2 fits within our model we assayed *mmp2, mmp14a and mmp14b* expression in pax2a$^{-/-}$ and DMH4 treated embryos. In both cases, OF expression of *mmp2, mmp14a and mmp14b* was reduced as observed by FWISH and confirmed by qPCR (Figure 3.5A, B, Appendix 2.5B). This suggested that all three may be expressed by the hyaloid vasculature cells. To assess this, we performed two color FWISH for *mmp2* and *kdrl*. Confocal imaging verified that *mmp2* expression is co-localized with that of *kdrl* within the OF (Figure 3.5C). Conversely, when performing two color FWISH for *mmp2* and *rorB*, a retina specific probe, we did not detect co-localization of the signals. We therefore conclude that the source of mmp2 in the OF is most likely hyaloid vasculature cells.

Finally, to determine whether mmp2 activity is necessary for OF fusion we treated embryos with ARP101, a specific mmp2 inhibitor previously shown to be effective in zebrafish [185]. Treating embryos with ARP101 from 24-48hpf inhibited OF BM breakdown in a dose dependent manner (Figure 3.6A, Appendix 2.6A,B). When compared to DMSO, embryos treated with 15 or 20μM ARP101 either completely or partially retain their OF BM up to 48hpf (Figure 3.6B). To ensure that inhibition of mmp2 activity is not affecting hyaloid vasculature migration into the OF we imaged Tg[*kdrl*:mCherry] DMSO or ARP101 treated embryos from 24-48hpf. OF associated vasculature appeared unchanged at 32, 36 and 48hpf (Figure 3.6C). Furthermore, quantification of hyaloid cells within the fissure at 32 and 36hpf indicated that inhibition of mmp2 activity does not have any effects on OF vascularization (Figure 3.6D). Lastly, we also examined *pax2a* expression in ARP101 treated embryos and did not observe any negative effects (Appendix 2.6C). We therefore concluded that mmp2 activity is necessary for BM breakdown in the OF. To determine when mmp2 activity is required we performed a time course of the ARP101 treatment starting between 24-32hpf and assayed BM status at 48hpf (Figure 3.6E). Treatments started later than 30hpf had little to no effect on OF BM degradation, indicating that mmp2 activity is optimally required between 24-30hpf (Figure 3.6E). This finding also correlates with the observed timing of *mmp2* expression in the OF (Appendix 2.5A). However, because we cannot determine exactly how quickly ARP101 inhibits enzymatic activity in our assay, active mmp2 may persist in the OF longer than 30hpf. Lastly, in addition to pharmacological inhibition of mmp2 function, we also sought to examine the consequences of *mmp2* gene inactivation. To do so, we employed the recently introduced Alt-R-crRNA/Cas9 system which has

been shown to provide highly effective CRISPR mediated F0 gene knockouts in zebrafish [186]. Injection of a pre-designed *mmp2* crRNA duplex with Cas9 enzyme resulted in ~53% of embryos displaying a coloboma like phenotype at 72 hpf (Appendix 2.7). Confocal imaging of laminin staining indicated a partial failure in OF BM degradation and persistence of a minor fissure. The observed phenotype was similar to but not as pronounced as observed in pax2-$^{-/-}$ embryos at 72hpf. This may result from incomplete F0 phenotypes. As such, future examination of germline transmitted loss of function alleles of *mmp2* will be necessary to fully examine the functional consequence on OF fusion. Taken together, we propose that mmp2 activity is part of the mechanism involved in OF BM degradation and subsequent fusion of the fissure.

3.4 DISCUSSION

Studies of OF fusion dating back several decades have been suggesting a direct connection between the fusion process and hyaloid vasculature found within the fissure. In fact, this hypothesis has been recently strengthened by data showing that a reduction of hyaloid vasculature in the fissure, or removal of optic vesicles from sources of vasculature inhibits or significantly delays fusion [119, 139]. In our study, we have characterized a pax2a driven mechanism that ensures proper vascularization of the OF and expression of BM remodelers *mmp2, 14a* and *14b*. In conclusion, our findings further validate the notion that hyaloid vasculature is an active and necessary component of the machinery driving OF fusion in zebrafish.

Several recent reports, including this one, have comprehensively characterized OF fusion timing [88, 119, 167, 168]. Work from zebrafish, mice and chick all point to an

orderly progression involving: **1)** retinal growth and cellular rearrangement leading to nasal and temporal retinal lobe apposition, **2)** invasion of the fissure by endothelial and neural crest cells forming the hyaloid vasculature system, **3)** cellular signaling, either between retinal rim cells or between rim cells and the migrating vasculature cells, **4)** degradation or removal of the basement membrane to enable physical connection of the rim cells and subsequent formation of a continuous retinal epithelial sheet via re-polarization and cell-cell adhesion. Step 1 has been nicely characterized in a few recent publications outlining the flow of retinal cells and morphological formation of the fissure [68, 187, 188]. For step 2, several reports have carefully characterized the formation of the hyaloid vasculature system, including migration of hyaloid vasculature precursor cells into the fissure as soon as it forms [125, 148, 149]. Importantly, perturbation of this process, or removal of the developing eye from its source, has been shown to lead to fissure fusion failure [119, 139]. To date, steps 3 and 4 are the least understood. Recent work from our lab has characterized the composition of core BM components within the fissure [167]. Additionally, work from other labs has identified several molecular components associated with cell-cell adhesion and epithelial sheet fusion to function within the fissure, including β-catenin, n-cadherin, and netrin [84, 119, 168, 189-191]. However, the timing and the molecular mechanism organizing and regulating these components remains uncharacterized. Finally, the elephant in the room has always been the identity of the BM degradation mechanism. To date, only adamts16 has been functionally examined in context of fissure fusion while mmp2 activity was detected during mouse OF fusion and mmp23bb was implicated in the fusion process from transcriptomic data [182, 191, 192].

While attempting to address the mechanistic aspects of steps 3 and 4 using the pax2a noi model we first uncovered a relationship between F-actin and BM degradation. Work by *James et al. 2016* suggested that F-actin accumulation may be indicative of hyaloid cell interaction with retinal rim cells. During our detailed time course analysis, we discovered that BM degradation is in fact preceded by an increase in F-actin signal within the OF (Figure 3.1). When assayed in pax2a$^{-/-}$ embryos the F-actin accumulation is absent while the hyaloid vasculature in the OF is also diminished. The timing of F-actin accumulation coincides with the active migration of hyaloid vasculature cells through the fissure (Figure 3.2). Furthermore, we showed pharmacologically, via VEGF inhibition, that hyaloid vasculature is necessary for the accumulation of F-actin and OF BM degradation. Transcriptionally, we showed that the decrease in hyaloid vasculature in pax2a$^{-/-}$ embryos coincides with a significant decrease in *tln1* expression. Tln1 is a key regulator of endothelial cell migration, recently shown to be directly involved in OF fusion [119]. In fact, loss of *tln1* function has been previously shown to decrease OF associated vasculature and inhibit BM degradation [119]. In our study, we detected a significant decrease in *tln1* expression upon VEGF inhibition (DMH4 treatment), suggesting that *tln1* expression within the OF is associated with hyaloid vasculature. Tln1 is known to be a direct link between the actin cytoskeleton and the BM via integrin [193, 194], and has been associated with the formation of adhesion junctions [195, 196]. One could therefore hypothesize several different models for its role in OF fusion. We predict that tln1 is regulating the ability of hyaloid vasculature cells to migrate properly through the OF, however we cannot rule out the possibility that tln1 directly participates in the OF fusion process. The absence of *tln1* expression is most likely a correlation to

the decrease of hyaloid vasculature cells within the fissure of pax2a$^{-/-}$ embryos. In support of this we observed a significant decrease in *tln1* expression upon DMH4 inhibition and therefore absence of hyaloid vasculature in the OF. As such, the decrease in *tln1* expression is likely indicative of decreased numbers of hyaloid vasculature cells which require *tln1* expression for proper migration into the fissure and or proliferation.

Our study strongly supports the notion that vasculature plays an integral part in OF fusion. Proper execution of angiogenesis is therefore a potential mechanism to ensure timely vascularization of the OF. The deficiency of hyaloid vasculature in pax2a mutant embryos may therefore result from a decrease in VEGF signaling. Using WISH and qPCR we detected a significant decrease in cranial *vegfaa, ab* and *c* expression. VEGF signaling is critical for angiogenesis and proper vasculogenesis throughout the embryo, a decrease in its activity is therefore likely to result in a series of deficiencies, including hyaloid vascularization of the OF. These findings supported the observation that pax2a mutants suffer from severe heart malfunction and subsequent edema and hemorrhage. The mechanisms of how pax2a regulates VEGF signaling remains unknown at this time and will need to be investigated in future studies. The observed decrease in VEGF expression does not directly correlate to regions of *pax2a* expression, which therefore suggests indirect regulation or negative VEGF feedback signaling during early development in the absence of pax2a function. In addition, phenotypes resulting from reduced VEGF signaling and therefore vasculogenesis may stem from subsequent circulation and cardiac function defects as well.

The last aspect of our proposed model pertains to the OF BM degradation mechanism. It had been suggested that vasculature may be the source of BM degradation

activity during OF fusion [119]. To that end, we have discovered that *mmp2* is expressed within the hyaloid vasculature during OF fusion (Figure 3.5). In fact, timing of *mmp2* expression correlates with the expected timing for initiation of BM degradation (Appendix 2.5). When we examine pax2a mutants or inhibit hyaloid vasculature completely (DMH4 treatment) we no longer detect expression of *mmp2* or *mmp14a* and *14b*. Delayed treatment with DMH4 also resulted in absence of *mmp2* expression (90% of embryos after 24-32hpf treatment (n=10) and 63% in 28-32hpf treated embryos (n=11). Furthermore, using ARP101, a specific mmp2 inhibitor, we showed that mmp2 activity is necessary for OF BM degradation, specifically between 26-32hpf (Figure 3.6). Mmp2 has been implicated in OF fusion previously. Mouse studies have shown *mmp2* expression within macrophages residing in the OF. Furthermore, recent examination of mmp2 activity, using a reporter construct, indicates that mmp2 is active in the eye and likely the OF [181]. Mmp14 is a known to activate mmp2 activity by cleaving the inhibitory pro-peptide of mmp2 [183, 184]. As such, co-expression of *mmp2* and *14* is further indicative of mmp2 playing a functional role in OF BM degradation. In the current study we did not directly assay the functional role of mmp14, but based on previous work linking mmp2 activation to mmp14, it is likely that mmp14 is also going to be necessary for zebrafish OF fusion.

To date, the only BM degradation enzyme to be associated with OF fusion is adamts16. Loss of adamts16 function in zebrafish, via morpholino, led to a coloboma like phenotype which the authors credited to the inability to degrade laminin in the fissure [192]. We have not been able to reproduce *adamts16* expression within the fissure. Recent studies in mice, zebrafish and chick have compared expression in OF cells pre,

during and post fusion [168, 191, 197, 198]. Surprisingly, none of these studies identified any obvious candidates for carrying out BM degradation, including *mmp2* and *mmp14*. However, it remains possible that the OF tissue examined lacked the hyaloid vasculature and therefore prevented the identification of *mmp2* and *mmp14* as candidates. In addition, expression of *mmp2, 14a* and *14b* is transient in the fissure which may have contributed to their OF expression being missed by other groups. Our data indicate mmp2 activity is necessary for BM degradation of the OF, but it does not rule out a role for additional proteases. There may be several proteases involved in OF BM degradation, such as adamts16, mmp2 and others, yet inhibition of just one could trigger failure of the degradation process and lead to fissure fusion failure. Continuing studies into matrix protease activity will be needed to fully characterize the degradation mechanism(s) during OF fusion.

Recent studies of hyaloid vasculature during OF fissure fusion have also included examination of the cloche mutant line, which is considered to be avascular. Importantly, *cloche* mutants (clo^{m39}) display a delay but not a complete lack of OF fusion [119]. This fact confounds our and other's results that suggest hyaloid vasculature plays a role in OF fusion [139]. With our new finding that mmp2 plays a significant role in OF fusion we therefore examined *mmp2* expression in clo^{m39} mutants (Appendix 2.8). Interestingly, clo^{m39} embryos did display *mmp2* expression within the OF, albeit at visibly reduced levels. This finding suggests that clo^{m39} embryos either still retain a population of cells (possibly POM or NCC) that are found within the fissure and express *mmp2*, or that not all vasculature is eliminated in these mutants. On that note, previous examination of vasculature markers in clo^{m39} mutants indicated that *fli1* was still expressed in the retinal

region suggesting some degree of vasculature may remain [199]. The persistence of even low levels of mmp2 may explain why OF fusion is delayed, but not eliminated in clo^{m39} mutant embryos. Furthermore, we also note that in our DMH4 treatments, which generate an avascular phenotype, we appear to block OF fusion completely, which is also in contrast to clo^{m39} mutants. This discrepancy may result from the absence of VEGF signaling which may be playing a secondary role to that of angiogenesis. An angiogenesis independent role of VEGF may involve signaling in other cell types such as the POM or NCC which are known to migrate through the OF. Future studies into mmp2 activity and VEGF signaling as well as interaction of POM and NCC with the OF will be of high priority.

In conclusion, we present a new model for the mechanism of OF BM degradation where pax2a functions to enable hyaloid vasculature invasion of the OF. Once in the fissure, vasculature cells express *mmp2, 14a* and *14b* to initiate BM degradation. As soon as fusion begins, vasculature becomes restricted from the fissure and ultimately the two retinal lobes fuse. Our model aligns with the molecular events observed in the fissure, including accumulation of F-actin at the time of vasculature migration through the fissure (24-28hpf), expression of mmps (26-36hpf) and subsequent BM degradation (32-48hpf). In the current study we relied on pharmacological inhibition of VEGF signaling and mmp2 activity. Pharmacological inhibition can have potential off target effects, in particular developmental delays or toxicity. While we have partially controlled for these potential off target effects our future plans are to extend the analysis of these pathways with the use of genetic tools as to minimize potential for off target effects.

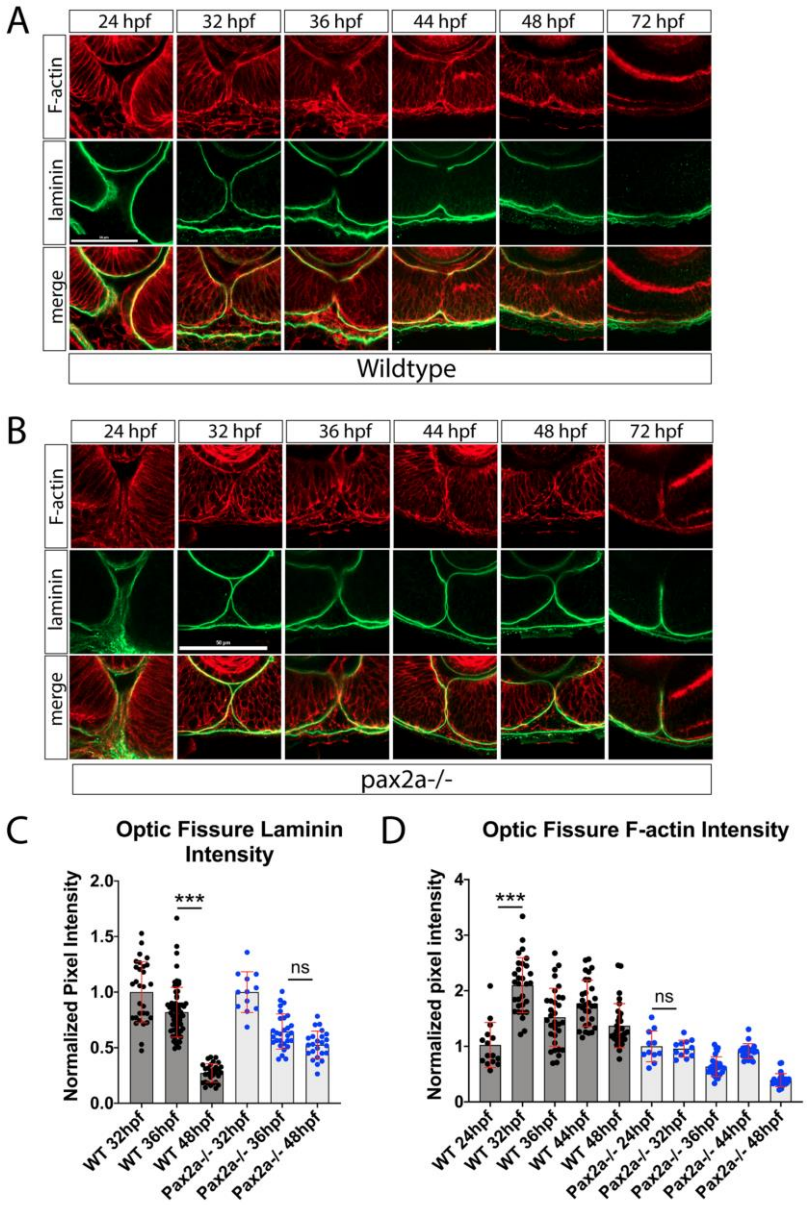

Figure 3-1 An increase in F-actin dynamics preceding laminin degradation during optic fissure fusion is disrupted in pax2a$^{-/-}$ embryos.

A) Whole mount immunohistochemistry was used to simultaneously visualize F-actin (red) and laminin (green) during OF fusion, 24-72hpf. Central-proximal sections obtained using confocal imaging were collected and quantified. Scale bar = 50μm. B) Whole mount Immunohistochemistry was used to simultaneously visualize F-actin (red) and laminin (green) during OF fusion, 24-72hpf, in pax2$^{-/-}$ embryos. Central-proximal regions of the OF are displayed. Scale bar = 50μm. C) Quantification of laminin signal intensity within the OF, normalized to regions of laminin staining juxtaposed to the lens. Relative pixel intensities are displayed. ANOVA $p<0.0001$. D) Quantification of F-actin intensity (phalloidin staining) within the OF, normalized to regions of F-actin signal within the lobe of the retina. Relative pixel intensities are displayed. ANOVA $p<0.0001$.

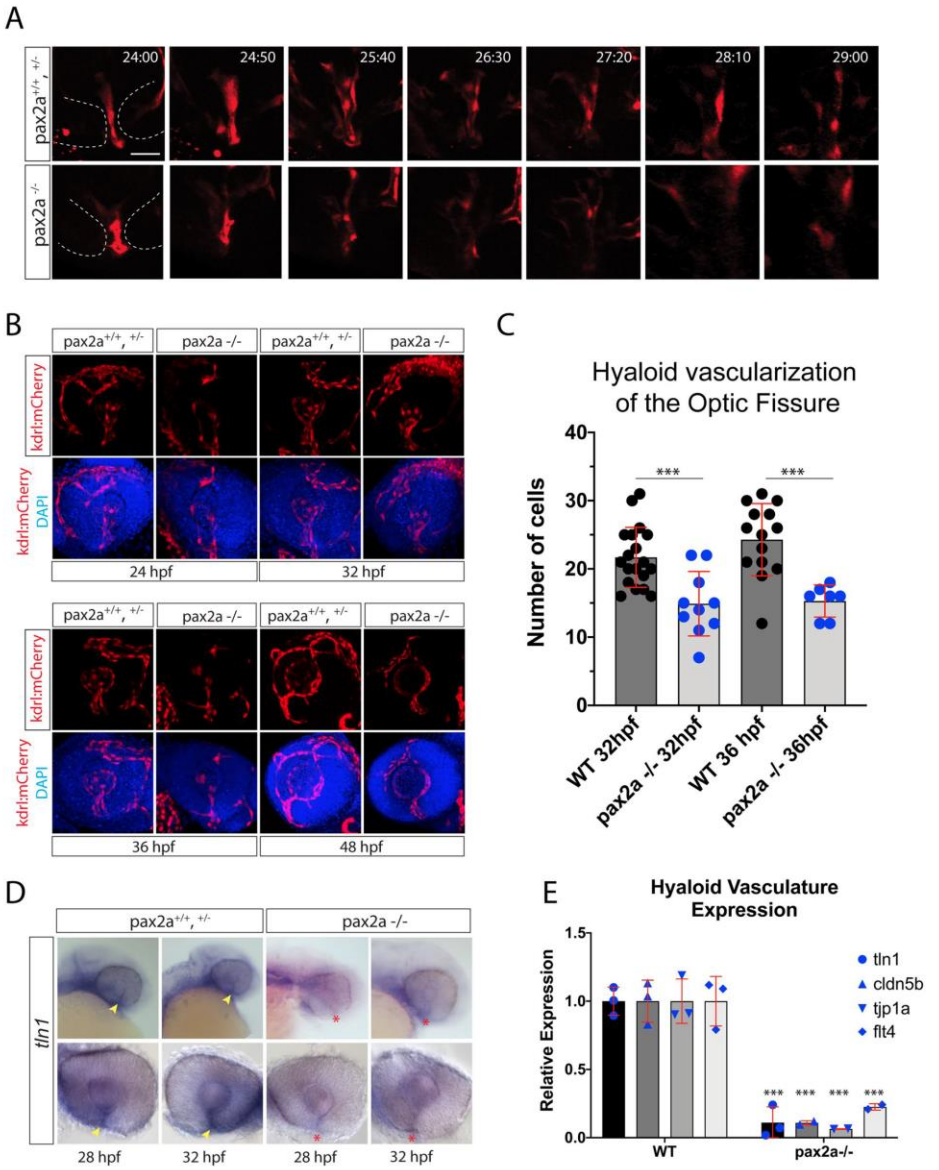

Figure 3-2 Pax2a is necessary for recruitment of hyaloid vasculature into the optic fissure.

A) *In vivo* 4D confocal imaging of Tg[*kdrl*:mCherry] pax2a$^{+/+,+/-}$ or pax2a$^{-/-}$ embryos. Time lapse series depicting the region of the OF (dotted white lines) and mCherry positive vasculature endothelial cells migrating through the fissure from 24-29hpf. Scale bar = 10m. B) Comparison of pax2a$^{+/+,+/-}$ and pax2a$^{-/-}$ vascularization during OF fusion, 24-48hpf. 3D reconstructions of whole mount Tg[*kdrl*:mCherry] (red) pax2a$^{+/+,+/-}$ or pax2a$^{-/-}$ embryos with DAPI (blue) stained DNA. Scale bar = 50μm. C) Quantification of the number of mCherry positive cells from 3D confocal stacks within the region of the OF. Individual embryo results are depicted. ANOVA p<0.0001. D) Whole mount in situ hybridization comparing *tln1* expression between pax2a$^{+/+,+/-}$ and pax2a$^{-/-}$ embryos at 28 and 32hpf. *tln1* signal within the OF (yellow arrowhead) appears reduced in Pax2a$^{-/-}$ embryos (red *). E) qPCR analysis of *tln1* expression from heads of pax2a$^{+/+}$ and pax2a$^{-/-}$ embryos at 32hpf confirms a reduction in *tln1* expression.

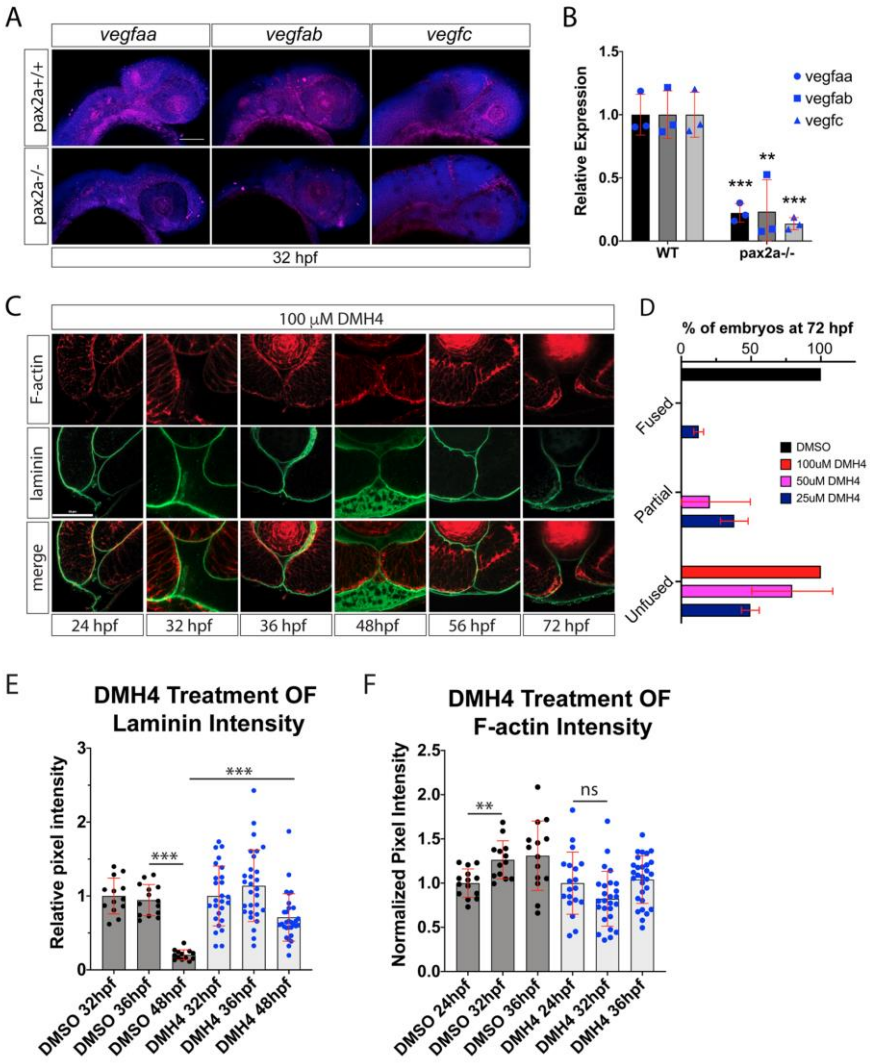

Figure 3-3 Inhibiting angiogenesis disrupts optic fissure fusion mechanics.
A) Fluorescent whole mount in situ hybridization of *vegfaa*, *vegfab* and *vegfc* at 32hpf in WT and pax2a$^{-/-}$ embryos. Loss of pax2a results in decreased *vegfaa, ab* and *c* expression. DAPI is depicted in blue. Scale bar = 100μm. B) qPCR results for *vegfaa*, *vegfab* and *vegfc* expression from heads of pax2a$^{+/+}$ and pax2a$^{-/-}$ embryos at 32hpf. C) 3D confocal images of Tg[*kdrl*:mCherry] (red) embryos treated with 100μM DMH4 between 24-72hpf. DNA was stained with DAPI (blue). Scale bar = 50μm. D) Quantification of 48hpf DMH4 treated embryos for fissure fusion (absence of laminin signal), partial fusion (partial retention of laminin) or failure to fuse (retention of laminin throughout the fissure). n= 22 (DMSO), 52 (100μM), 22 (50μM), 24 (25μM) ANOVA p<0.0001. E) Quantification of laminin signal intensity within the central-proximal region of the OF, normalized to regions of laminin staining juxtaposed to the lens. Relative pixel intensities are displayed. ANOVA p<0.0001. F) Quantification of F-actin signal intensity (phalloidin staining) within the central-proximal region of the OF, normalized to regions of F-actin signal within the lobe of the retina. Relative pixel intensities are displayed. ANOVA p<0.0001.

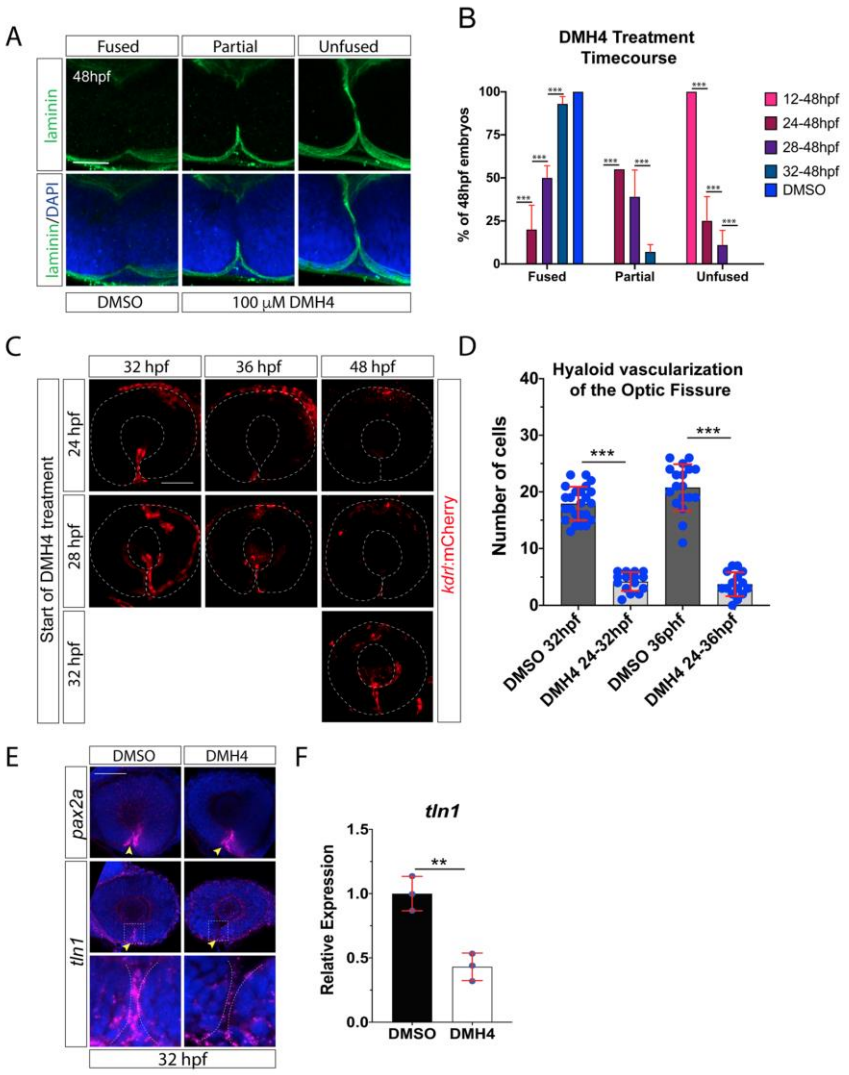

Figure 3-4 VEGF signaling is plays a role in optic fissure fusion.

A) Whole mount Immunohistochemistry was used to visualize laminin (green) at 48hpf after DMSO or DMH4 treatment. Central-proximal regions of the OF are displayed depicting fused, partially fused or unfused optic fissures. Scale bar = 50μm. B) Quantification of 48hpf DMH4 treated embryos for fissure fusion (absence of laminin signal), partial fusion (partial retention of laminin) or failure to fuse (retention of laminin throughout the fissure). n= 41 (12-48hpf), 38 (24-48hpf), 38 (28-48hpf), 44 (32-48hpf), 40 (DMSO). ANOVA $p<0.0001$. C) 3D reconstructions of whole mount Tg[*kdrl*:mCherry] embryos treated with 100 μM DMH4 at various time points. Broken white line outlines the retina. Scale bar = 50μm. D) Quantification of the number of mCherry positive cells from 3D confocal stacks within the region of the OF after DMSO or DMH4 treatment. Individual embryo results are depicted. ANOVA $p<0.0001$. E) Fluorescent whole mount in situ hybridization of *pax2a* or *tln1* probe at 32hpf in DMSO or DMH4 treated embryos. OF expression is indicated with a yellow arrowhead. DMH4 treatment does not appear to alter *pax2a* expression but eliminates *tln1* expression from the OF. Broken white lines outline the retinal lobes. Scale bar = 50μm F) qPCR results for *tln1* expression in DMH4 treated embryos.

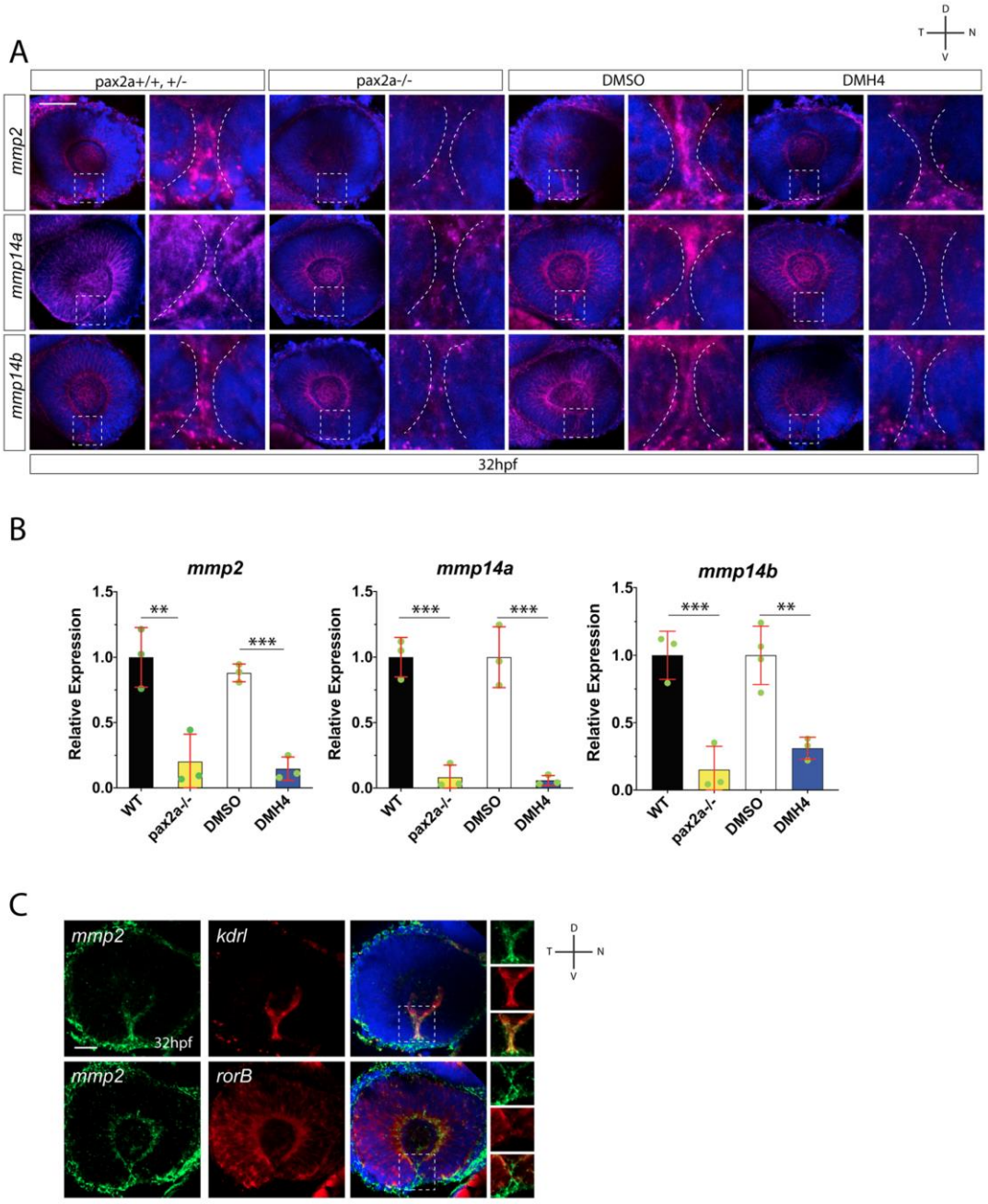

Figure 3-5 Hyaloid vasculature is a source of mmp2 during optic fissure fusion.
A) Fluorescent whole mount in situ hybridization comparing *mmp2, mmp14a* and *mmp14b* expression in WT vs pax2a$^{-/-}$ and DMSO vs DMH4 treated embryos at 32hpf. Broken white lines outline the OF retinal lobes. *mmp2, 14a* and *14b* expression within the OF is reduced in pax2a$^{-/-}$ and DMH4 treated embryos. Scale bar = 50μm. B) qPCR analysis confirms a decrease in expression of *mmp2, 14a* and *14b* in both pax2a$^{-/-}$ and DMH4 treated embryos. C) Two color whole mount in situ hybridization simultaneously examining *mmp2* and *kdrl*, or *mmp2* and *rorB* expression at 32hpf. DNA was stained with DAPI. Scale bar = 50μm. Clear overlap of signal is observed for *mmp2* and *kdrl*, but not *mmp2* and *rorB*.

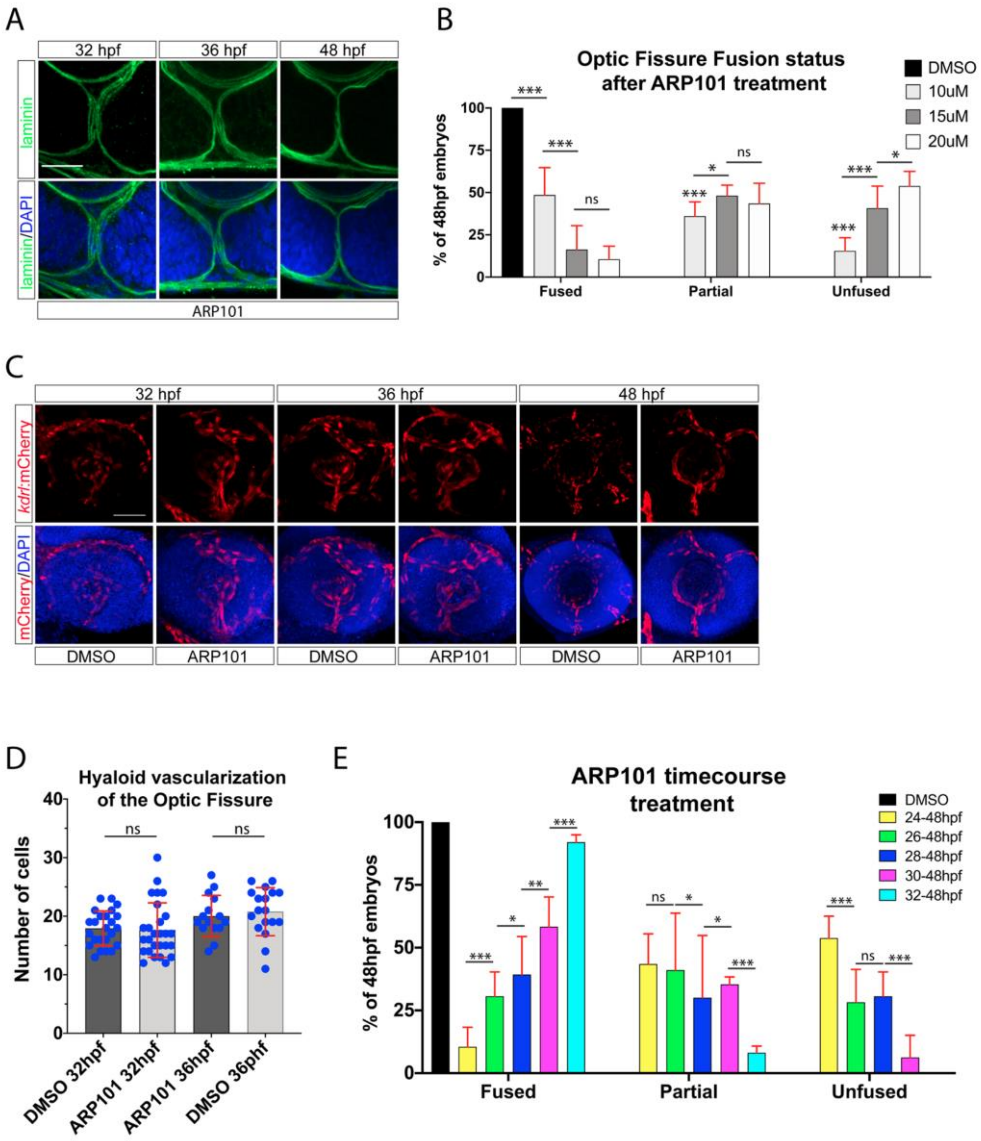

Figure 3-6 Proper timing of mmp2 activity is required for optic fissure fusion.
A) Whole mount Immunohistochemistry was used to visualize laminin (green) and DAPI (blue) in ARP101 treated Tg[*rx3*:GFP] embryos at 32, 36 and 48hpf. Stacks of central-proximal regions of the OF are displayed. Scale bar = 50μm. B) Quantification of 48hpf ARP101 treated embryos for fissure fusion (absence of laminin signal), partial fusion (partial retention of laminin) or failure to fuse (retention of laminin throughout the fissure). n= 41 (10μM), 38 (15μM), 42 (20μM) ANOVA p<0.0001. C) 3D reconstructions of whole mount Tg[*kdrl*:mCherry] (red) embryos treated with 20 μM ARP101 from 24-32, 36 or 38hpf. DNA was stained with DAPI (blue). Scale bar = 50μm. D) Quantification of the number of mCherry positive cells from 3D confocal stacks within the region of the OF after DMSO or 20 μM ARP101 treatment. Individual embryo results are depicted. E) Quantification of 48hpf ARP101 treated embryos for fissure fusion, partial fusion or failure to fuse after various treatment initiation times from 24-32hpf. n= 42 (24-48hpf), 29 (26-48hpf), 29 (28-48hpf), 23 (30-48hpf), 37 (32-48hpf). ANOVA p<0.0001.

CHAPTER 4. TRANSCRIPTOMIC PROFILING OF ZEBRAFISH OPTIC FISSURE CLOSURE IN PAX2 MUTANTS REVEALS NOVEL ANTI-ANGIOGENIC AND ACTIN ASSOCIATED PROTEIN TRANSCRIPTS.

4.1 Abstract

Prevalent throughout embryogenesis, the fusion of epithelial tissue to seal naturally occurring gaps is critical for proper organogenesis. One such event occurs during vertebrate eye development and involves fusion of the optic fissure. The optic fissure forms as a consequence of optic cup morphogenesis and serves as a conduit for the migration of endothelial vasculature during hyaloid angiogenesis. Failure of optic fissure fusion results in a congenital blinding disorder known as coloboma. Recent studies have linked hyaloid vasculature precursor cells to be potential triggers for initiating optic fissure fusion. In order to examine this link, we analyzed the transcriptional and molecular events associated with optic fissure fusion and hyaloid angiogenesis in the zebrafish pax2a^{noi} mutant coloboma model. To examine how the fusion process is disrupted in the absence of pax2a function, we compared transcriptomic profiles between pax2a$^{-/-}$ and wildtype (WT) whole retinas. We sought to validate and investigate those targets which were thought to be of importance to the molecular machinery involved in fusion, particularly those involving the actin cytoskeleton and angiogenesis. This analysis uncovered a novel connection between regulation of angiogenesis and fusion. Loss of pax2a resulted in increased expression of an anti-angiogenic protease, ADAMTS1. Injection of ADAMTS1 mRNA into one cell

Tg[*kdrl*:mCherry] embryos, attempting to mimic the pax2a increase in expression, resulted in decreased hyaloid vasculature which phenocopies the pax2a-/- phenotype. Based on the ability of migrating endothelial cells to activate integrin signaling we also began looking for the possibility of reduced actin associated transcripts in our RNA sequencing data. We uncovered preliminary evidence that certain actin associated proteins are also differentially regulated, particularly rho-associated protein kinase (ROCK). Taken together, we propose that Pax2a negatively regulates ADAMTS1 expression. This enables timely hyaloid vascularization of the retina which in turn directly signals to initiate fissure fusion via cytoskeletal rearrangements and subsequent basement membrane remodeling.

4.2 Introduction

Epithelial fusion is the process by which two distinct populations of epithelial cells become apposed and eventually fuse to create a single continuous sheet. This process can be observed at several stages during development, including the closure of the neural tube, the palatal shelf, presumptive genitalia, eyelids, and the optic fissure of the developing retina [27, 200-202] Formation of a fully functioning human eye requires precise and coordinated cellular mechanisms during very early development. One such mechanism is responsible for the formation of the eye, which forms a 3D structure from a flat sheet of cells. This leads to the creation of a gap (fissure), at the ventral region of the eye. This fissure, the optic fissure, remains open during morphogenesis of the eye to allow the establishment of the hyaloid vasculature. The hyaloid vasculature is a temporary circulatory system developed during eye morphogenesis [122]. As soon as the hyaloid vasculature has been established, the two opposing retinal epithelial sheets of the

optic fissure will undergo fusion to seal the optic stalk which houses the retinal ganglion cell axons. Failure of optic fissure fusion leads to a congenital blinding disorder known as coloboma [30, 130]. Coloboma is a leading cause of pediatric blindness, accounting for approximately 10% of cases worldwide [152, 154]. Coloboma is a spectrum disorder presenting unilaterally or bilaterally and ranging in severity from minor visual impairment, to complete blindness in the affected eye [155]. This spectrum of severity is associated with the location and degree to which the optic fissure was able to fuse and the severity of subsequent loss of ganglion cell axons [153]. Epithelial fusion has been studied for over a century, and is known to involve transcriptional regulation, cell signaling pathways, and morphogen gradients [160, 161]. However, in regard to the optic fissure we are still lacking a basic understanding of how these molecular mechanisms coordinate and directly facilitate fusion. Recent work has begun to implicate some of the cellular processes involved in optic fissure fusion. For example, the actin cytoskeleton is known to be a crucial component of the machinery driving fusion of the optic fissure as well as other tissues [162]. The actin cytoskeleton is thought to be involved in fusion by the formation of lamellipodia and filopodia projections between the apposing epithelia. It is thought that these projections help to “zipper” the cells together [164-166]. It has been observed that fusion often fails when lamellipodial and filopodial projections are precluded [163]. However, while it has been observed that actin protrusions likely play a functional role during optic fissure fusion, it still remains to be determined what actin cytoskeletal components are required during optic fissure fusion. Another cellular mechanism known to be directly involved in epithelial fusion is the breakdown of the basement membrane (BM). During epithelial fusion, the BM acts as a physical barrier

which must be removed in order for fusion to complete. Recent work, including our own, across several species has characterized progressive removal of the BM during choroid fissure fusion [88, 119, 167, 168]. However, the molecular mechanisms facilitating this process, in particular BM breakdown, remain largely unknown. James *et al.* 2016, showed that zebrafish *cloche* mutants, which lack all early hyaloid vasculature, have delayed basement membrane breakdown in the region of the choroid fissure [119]. James *et al.* 2016 also reported that talin1 mutants, an actin scaffolding protein required for migration, fail to breakdown the basement membrane resulting in coloboma [119]. This finding was the basis of our investigation into vasculature in our pax2a coloboma model. Our previous work has shown a direct requirement for migrating endothelial cells. In the absence of all vasculature through the use of drug inhibition results in a retention of the basement membrane [203]. There is therefore a clear link between optic fissure fusion initiation and hyaloid vasculature migration through the fissure. There are two proposed mechanisms that hyaloid vasculature regulates optic fissure fusion, the secretion of proteins involved in the fusion process, as observed in our previous work showing vasculature supplied mmp2 [203]. Another role that the vasculature could be playing is through angiocrine signaling. Angiocrine signaling is known to provide growth factors and other proteins capable of stimulating epithelial cells to modify themselves, including the stimulation of actin cytoskeletal rearrangements [136, 138]. Finally, the sheer presence of the endothelial cells themselves could initiate fusion by exerting force on the rim cells of the optic fissure while passing through [135]. This could lead to mechanosensation by the basement membrane of the rim cells which would induce intracellular signaling via integrin receptors linked to the actin cytoskeleton. Coloboma

has been studied for many decades in many different species. This has led to a general outline of the signaling and morphogenetic pathways required for proper optic fissure formation and fusion (recently reviewed in [156]). This study aims to further analyze zebrafish optic fissure fusion comparing WT and the pax2a$^{-/-}$ coloboma model to expand upon our previous findings [203]. Using transcriptomic analysis to compare WT and pax2a$^{-/-}$ eyes we discovered misregulation in angiogenic signaling, resulting in decreased vascularization of the early retina and optic fissure fusion failure. In particular we found that pax2a$^{-/-}$ embryos exhibit an increase in *A disintegrin and metalloproteinase with thrombospondin motifs 1 (*ADAMTS1) expression, an anti- angiogenic protease [204, 205]. Overexpression of ADAMTS1 both phenocopied the pax2a$^{-/-}$ hyaloid vasculature and coloboma phenotypes. Once we knew how crucial migrating endothelial cells were to the fusion process and how this process could possibly be disrupted in a coloboma model, via ADAMTS1, we next sought to understand potential mechanisms that these endothelial cells act through. We decided to specifically look at actin cytoskeleton and its accessory proteins since the actin cytoskeleton is essential for cell signaling and several studies have shown how endothelial cells contribute angiocrine signaling to the actin cytoskeleton [135, 136, 138]. Looking at the transcriptomic data again several actin associated transcripts which were differentially expressed between WT and pax2a$^{-/-}$ embryos, in particular (ROCK). This led us to propose a novel pathway for the regulation of optic fissure fusion where pax2a mediates proper regulation of anti-angiogenic factors in order to facilitate hyaloid vasculature migration through the optic fissure.

4.3 Results

4.3.1 Pax2a retinal transcriptomic profile during optic fissure fusion.

Although pax2 has been studied in many systems, there are currently no obvious transcriptional targets of pax2 that would directly point to the mechanistic regulation of optic fissure fusion. In an effort to understand the absence of vasculature and F-actin (as discussed in previous published work [203]) observed in pax2a$^{-/-}$ embryos we compared retinal transcriptomic profiles between WT and pax2a$^{-/-}$ embryos. Eyes from 48hpf WT and pax2a$^{-/-}$ embryos were isolated and total RNA was subsequently purified and sequenced using Illumina sequencing. 48hpf was chosen for our experimental time point as pax2a$^{-/-}$ embryos are easily phenotyped at this age thanks to observable heart malformations. When comparing three replicates for WT and pax2a$^{-/-}$ embryos using RSEM software, we detected 1215 transcripts significantly upregulated (>95% confidence interval) and 1202 transcripts significantly downregulated (Figure 4.1A, D). Gene ontology analysis indicated a wide spread of biological function being affected, including cytoskeletal signaling, adhesion and developmental processes (Figure 4.1B, E). In support of our previous publication we found that tln1, an actin scaffolding protein known to be required for cell migration, was significantly down regulated in pax2 mutants. The distribution of biological function between up- and down-regulated genes was highly similar (Figure 4.1B, D). When comparing gene ontology between up- and down-regulated genes in pax2, they shared a similar pattern and trend. Among the most commonly represented biological function from both lists were cellular processes, which included signal transduction, actin-based processes, cell communication, and cellular organization. There were only two biological pathways that showed a disproportionate

favor, the angiogenesis pathway which was more heavily represented in the genes down-regulated in pax2 mutants. This further confirms results in our previous work that pax2 mutants have reduced vasculature. The other biological pathway heavily favored genes up-regulated in pax2 mutants, the Wnt signaling pathway. One gene of interest that came out of this data was a gene labelled as a metalloprotease called ADAMTS1 which was up-regulated in pax2 mutants, however, it was also associated with the angiogenesis pathway through its antiangiogenic capacity [204, 205]. Actin cytoskeletal proteins were evenly represented amongst the two groups, perhaps representing the loss of vasculature associated actin related proteins. However, two different genes which perform similar functions as down-stream effectors of the Rho signaling pathway were down-regulated in pax2 mutants, ROCK1 and ROCK2b [206]. A list of top 20 up and down regulated genes is outlined in Figure 4.1C and F. Results of all the statistically significant up and downregulated genes identified in our assay are presented as supplementary data (Appendix Tables 1.1 and 1.2).

4.3.2 Anti-angiogenic protease *adamts1* is upregulated in optic fissure of pax2a mutant embryos.

Having previously established a connection between pax2a function and recruitment of hyaloid vasculature cells into the optic fissure [203], we next sought to examine the mechanism. To do so, we examined our transcriptomic comparison of WT and pax2a$^{-/-}$ eyes, with a focus on angiogenic regulation. This examination revealed misexpression of *a disintegrin and metalloproteinase with thrombospondin motifs 1* (adamts1), a secreted protease known to be involved in regulating VEGF signaling [207].

Being a member of the ADAMTS family, adamts1 contains three thrombospondin motifs enabling it to directly bind and sequester VEGF [205]. Furthermore, the protease activity of adamts1 has bene shown to target thrombospondin 1 and 2 for cleavage, ultimately liberating their active forms which bind to and block VEGF from binding the VEGF receptor [204]. Our RNA sequencing data indicated that *adamts1* expression was upregulated almost two-fold in pax2a$^{-/-}$ eyes. This would suggest that the expression of *adamts1*, and therefore its anti-angiogenic activity, is normally somehow kept in check by pax2a. Pax2a has not been reported to harbor transcriptionally repressive function, so this may involve an indirect mechanism. To confirm our RNA sequencing results we performed WISH, examining *adamts1* expression at 28 and 36hpf. In agreement with our transcriptomic analysis, we observed an upregulation in *adamts1* in the ventral region of pax2a$^{-/-}$ eyes, specifically surrounding the optic fissure (Figure 4.2A). This was further confirmed using qPCR (Figure 4.2B). To test whether upregulation of *adamts1* expression would have direct effects on hyaloid vascularization and optic fissure fusion we injected Tg[*kdrl*:mCherry] embryos with *adamts1* mRNA. We subsequently examined hyaloid vasculature using 3D confocal imaging between 24-48hpf. Injection of *adamts1* mRNA resulted in a significant decrease in the number of *kdrl*:mCherry cells found within the optic fissure (Figure 4.2B, C). The observed decrease mirrored the results from pax2a$^{-/-}$ embryos (Figure 4.2C). Our findings therefore suggest that *adamts1* expression needs to be tightly regulated in order to ensure proper vascularization of the retina, including the optic fissure. Furthermore, the observed up-regulation of *adamts1* expression in pax2a$^{-/-}$ embryos may explain the resulting optic fissure hyaloid vasculature deficiency.

4.3.3 Overexpression of *adamts1* inhibits optic fissure fusion mechanics.

Having mimicked the vasculature phenotype of pax2a mutants by over expressing *adamts1*, we next examined whether it had any effects on optic fissure fusion. To do so, we performed whole mount laminin and F-actin staining in *adamts1* mRNA injected embryos at 24, 32, 36, and 48hpf (Figure 4.3A). Confocal imaging of the fissure indicated that *adamts1* mRNA injection also phenocopied pax2a$^{-/-}$ associated persistence of laminin and therefore failure of optic fissure fusion. Quantified levels of laminin persisting at 48hpf was similar to pax2a$^{-/-}$ embryos (Figure 4.3B). Similar to pax2a$^{-/-}$ embryos, we again noted a lack F-actin accumulation between 24-32hpf in *adamts1* overexpressing embryos (Figure 4.3C). As was observed with pax2a$^{-/-}$, timing for apposition of the lobes was not affected in adamts1 overexpressing embryos (Appendix 2.2). Taken together, our data suggest that maintaining proper levels of *adamts1* expression is necessary to enable VEGF signaling and subsequent recruitment of hyaloid vasculature required for initiation of optic fissure BM remodeling.

4.3.4 Rho-associated protein kinase (ROCK) is down-regulated in pax2 mutants

Having established a definitive link between the hyaloid vasculature cells and optic fissure fusion, we next sought to understand how migrating endothelial cells operate during optic fissure fusion. I felt there was a high probability that these migrating endothelial cells were eliciting cytoskeletal responses in and around the fissure, as these endothelial cells have been shown to act in a number of processes which require the actin

cytoskeleton, including mechanosensation and angiocrine signaling [135, 136, 138]. Angiocrine signaling has also been shown to contribute to integrin signaling, which activates the Rho family of GTPases and subsequently mediates cytoskeletal responses [138]. To investigate whether the actin cytoskeleton and/or its accessory proteins were impacted in pax2 mutants, we turned once again to the RNA sequencing data. When comparing WT and pax2a-/- whole retina RNA sequencing data two particular transcripts were of interest, Rock1 and Rock2b. Rho-associated Protein Kinase (ROCK) is a down-stream target of RhoA, B, and C. ROCK's have a diverse range of function, of interest for this work was their involvement in actin cytoskeleton organization, cell adhesion, and extracellular matrix remodeling [116]. ROCK1 had over a 25 fold change, showing a dramatic reduction of ROCK1 expression in pax2 mutants. ROCK2b was also down-regulated in pax2 mutants with an approximately 6 fold reduction. To validate these results, we performed qPCR on cDNA of dissected eyes from WT and pax2 mutants for all known ROCK's in zebrafish, ROCK1, ROCK2a, and ROCK2b. qPCR results validated down-regulation of ROCK's in pax2a mutant eyes (Figure 4.4A). We next performed whole-mount *in situ* hybridizations for Rock1 and Rock2b using embryos from an in-cross of pax2a$^{+/noi}$ heterozygous fish. The results show that in approximately 25% of embryos, expected mendelian ratio, the expression appeared reduced compared to the other 75% of embryos, indicating that these 25% were likely homozygous pax2 mutants (Figure 4.4B). To examine the functional consequence of Rock down regulation, I attempted ROCK inhibition using a drug called Y-27632 which is a selective ROCK inhibitor, previously having been successfully used in zebrafish [208]. Y-27632 inhibits both ROCK1 and ROCK2 by competing with its ATP binding sites. I performed the drug

treatment using Y-27632 at various concentrations starting at 24 to 48 hpf, and from 32 to 48 hpf. This experiment, however, has so far been unsuccessful, with almost zero phenotypic abnormalities across the entire embryo even at concentrations of up to 100 μM. ROCK is expressed ubiquitously throughout the entire zebrafish embryo and the odds ROCK inhibition having no effect on the embryo seems unlikely. I have therefore concluded it is possibly an ineffective batch of the drug and warrants further study using fresh inhibitor or trying other ROCK inhibitors. In the future, if drug inhibition is still unsuccessful the most effective way to understand ROCK's function during optic fissure fusion would be to create a transgenic line of zebrafish which would express a dominant negative form of ROCK, lacking a kinase domain, under the control of a heat shock promoter [209]. It is likely a ROCK CRISPR mutant would not survive the earlier stages of development and would thus be unsuitable for studying optic fissure fusion.

4.4 Discussion

While optic fissure fusion has been studied extensively, spanning decades and across many different species, we still lack the functional knowledge of the mechanics driving this process. We have previously characterized some aspects of optic fissure fusion in zebrafish and found a definitive link between the hyaloid vasculature and fusion of the optic fissure, where without vasculature fusion fails to occur. It is becoming widely accepted now that vasculature (or the POM cells which contribute to the hyaloid vasculature) is involved in this process, however, it still remained unknown as to why vasculature would be affected in coloboma, specifically in pax2 mutants. It became the focus of this study to investigate how a transcription factor could control angiogenesis during optic fissure fusion. We characterized a pax2a driven mechanism that ensures

proper vascularization of the optic fissure by restricting anti-angiogenic activity of adamts1 to enable hyaloid vasculature invasion of the optic fissure. Proper vascularization of the eye is crucial to optic fissure fusion. We have shown here and previous work that a reduction in vasculature leads to fusion failure, however, it has also been reported that hypertrophic hyaloid vasculature also results in fusion failure likely due to the increased distance between the lobes of the fissure [210].

In our transcriptomic comparison of WT and pax2a mutants we discovered a connection between fissure fusion and angiogenesis. In the absence of pax2a function we observed an upregulation of *adamts1*, an anti-angiogenic regulator. Examining *adamts1* expression in the eye further confirmed an upregulation of expression in the ventral regions of pax2a$^{-/-}$ retinas. Encoding 3 thrombospondin (thsb) motifs able to directly bind and sequester VEGF, in addition to targeting thsb1 and 2 for cleavage into their active VEGF inhibiting form, adamts1 is well known for its anti-angiogenic function in cancer, aortic and renal biology [211]. In our study, we show that upregulating adamts1 expression reduces the number of hyaloid vasculature cells in the OF. Up regulation of adamts1 also prevents the accumulation of F-actin and subsequent BM remodeling. Taken together we propose that the reduction in hyaloid vasculature observed in pax2a$^{-/-}$ embryos likely stems from an upregulation of adamts1 leading to suppressed VEGF signaling and therefore limited vascularization of the optic fissure.

In our transcriptomic comparison we also uncovered a potential connection between optic fissure fusion and the actin cytoskeleton. In the absence of pax2 there was a marked decrease in the expression of two up-stream activators of actin based focal adhesions, ROCK1 and ROCK2b. This was further validated by both qPCR and WISH.

So far this is one of the few correlations to have been made between an actin cytoskeleton regulator and a coloboma model. I speculate that ROCK is required in the epithelium of the fissure, previously a study revealed its requirement during fusion of the eyelid and ventral body wall in mice [116]. When ROCK is knocked out in mice, the contractile ring surrounding the eyelid epithelium fails to contract resulting in an inability to close the gap [116]. ROCK1 is a negative regulator of VEGF endothelial cell activation, it has been previously reported that ROCK inhibition stimulates the migratory behavior of various cell types including endothelial cells [212]. Since ROCK inhibition has a stimulatory effect on endothelial cell migration it seems unlikely that hyaloid vasculature cells are the contributors of ROCK expression in the optic fissure. During palatal fusion in mice it has also been observed that when inhibiting ROCK the epithelia still appose, however, cell intercalation and neighbor exchange fail to occur resulting in cleft palate [213]. It is therefore plausible that ROCK activity is required to begin the actual combining of the two epithelial sheets in the optic fissure and that the activation of ROCK could be triggered by the migrating endothelial cells. This preliminary data will hopefully provide the groundwork for future studies involving ROCK activity during optic fissure fusion.

Taken together, these findings further validate the knowledge that hyaloid vasculature is an active component of the machinery driving optic fissure fusion in zebrafish. We present a new piece of data to add to our model for the mechanism of optic fissure fusion, where pax2a restricts expression of *adamts1* in the ventral retina to enable hyaloid vasculature invasion of the optic fissure. Once in the fissure, vasculature cells express *mmp2, 14a* and *14b* to initiate BM remodeling. Once fusion begins, vasculature

becomes restricted from the fissure and ultimately the two retinal lobes fuse. For future studies it will be important to understand how pax2a regulates *adamts1* expression and to examine whether mutations in *adamts1* resulting in mis-expression of this transcript are potential markers for coloboma. It will be equally important to further investigate the mechanisms behind actin cytoskeletal rearrangements with an emphasis on ROCK. I believe ROCK is vital to the actual combining of the two sheets of epithelium, to test whether ROCK acts in this manner it would be most effective to create a transgenic line of zebrafish to express a dominant negative version of ROCK under the control of a heat shock promoter. This would then allow us to assess the effects of ROCK inhibition on the removal of the basement membrane and whether or not the hyaloid vasculature is affected. If the vasculature is not affected by the knock down of ROCK but still results fusion failure it would support this hypothesis. If this connection were to be made, it would be the first direct link between an actin cytoskeleton protein and coloboma.

A

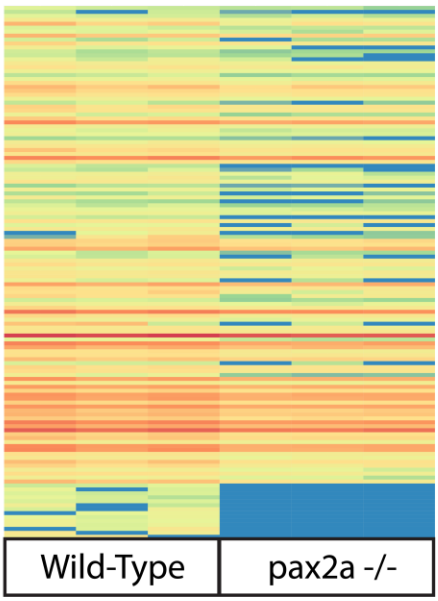

B

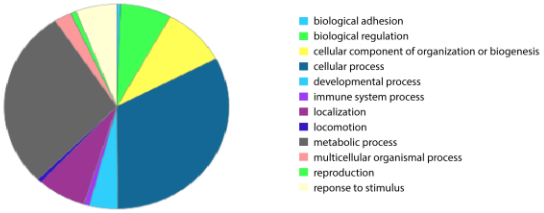

C

Gene ID	Gene Name	GO Term
aifm1	Apoptosis-inducing factor, mitochondrion-associated 1	oxidoreductase activity
sumo3a	small ubiquitin-like modifier 3a	protein sumoylation
lim2.1	Lens intrinsic membrane protein 2.1	Membrane
tfb2m	transcription factor B2, mitochondrial	transferase activity
tln1	Talin 1	actin binding
mgst2	microsomal glutathione S-transferase 2	enzyme activator activity
si:ch211-57b15.1	si:ch211-57b15.1	NA
ptprna	protein tyrosine phosphatase, receptor type, Na	protein dephosphorylation
dnajb11	DnaJ (Hsp40) homolog, subfamily B, member 11	protein folding
krt96	Keratin 96	structural molecule activity
sept9a	septin 9a	GTP binding
si:rp71-36a1.5	si:rp71-36a1.5	membrane
si:dkey-9c18.3	si:dkey-9c18.3	NA
arf5	ADP Ribosylation Factor 5	GTP binding
dock1	Dedicator Of Cytokinesis 1	small GTPase mediated signal transduction
hbbe1.1	Embryonic 1 beta-globin	Hemoglobin Complex
zgc:152951	Zgc:152951	electron transfer activity
pcbp3	Poly(rC)-binding protein 3	RNA binding
gpsm1b	G protein-signaling modulator 1b	GTPase regulator activity
abracl	Costars family protein ABRACL	regulation of actin filament-based process

D

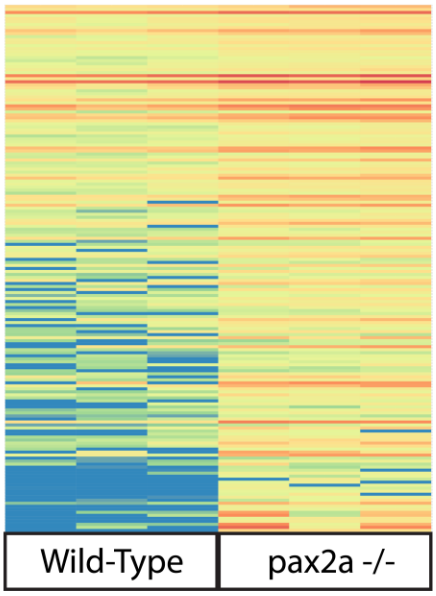

E

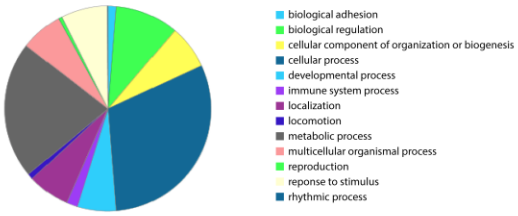

F

Gene ID	Gene Name	GO Term
gmnn	geminin, DNA replication inhibitor	regulation of DNA replication
col11a1a	collagen, type XI, alpha 1a	extracellular matrix structural constituent
fubp3	far upstream element (FUSE) binding protein 3	RNA binding
si:dkey-26g8.4	Cathepsin Lb	proteolysis
ublcp1	ubiquitin-like domain containing CTD phosphatase 1	protein dephosphorylation
smarcal1	SWI/SNF related, matrix, actin dependent regulator of chromatin, a-like 1	DNA repair
he1b	hatching enzyme 1b	metalloendopeptidase activity
anxa3a	annexin A3a	regulation of NMDA receptor activity
si:dkey-269i1.4	cathepsin L1-like	proteolysis
zgc:174855	zgc:174855	
gsta.1	glutathione S-transferase, alpha tandem duplicate 1	glutathione metabolic process
tbc1d7	TBC1 domain family, member 7	activation of GTPase activity
srek1	splicing regulatory glutamine/lysine-rich protein 1	regulation of alternative mRNA splicing
scg5	secretogranin V	neuropeptide signaling pathway
ggact.3	gamma-glutamylamine cyclotransferase, tandem duplicate 3	lyase activity
si:dkey-26g8.4	Cathepsin L1-like	proteolysis
si:dkey-239j18.3	si:dkey-239j18.3	proteolysis
ahsa1a	AHA1, activator of heat shock protein ATPase homolog 1a	ATPase activator activity
he1a	hatching enzyme 1a	metalloendopeptidase activity
dpf3	D4, zinc and double PHD fingers, family 3	zinc ion binding

Figure 4-1 Retinal transcriptomic comparison between WT and pax2a$^{noi/noi}$.
A) Heat map representing transcripts found to be significantly down regulated in pax2a$^{-/-}$ embryos. B) Gene ontology for pax2a$^{-/-}$ downregulated transcripts. C) Top 20 downregulated transcripts are outlined in order of fold change. D) Heat map representing transcripts found to be significantly upregulated in pax2a$^{-/-}$ embryos. E) Gene ontology for pax2a$^{-/-}$ upregulated transcripts. F) Top 20 upregulated transcripts are outlined in order of fold change.

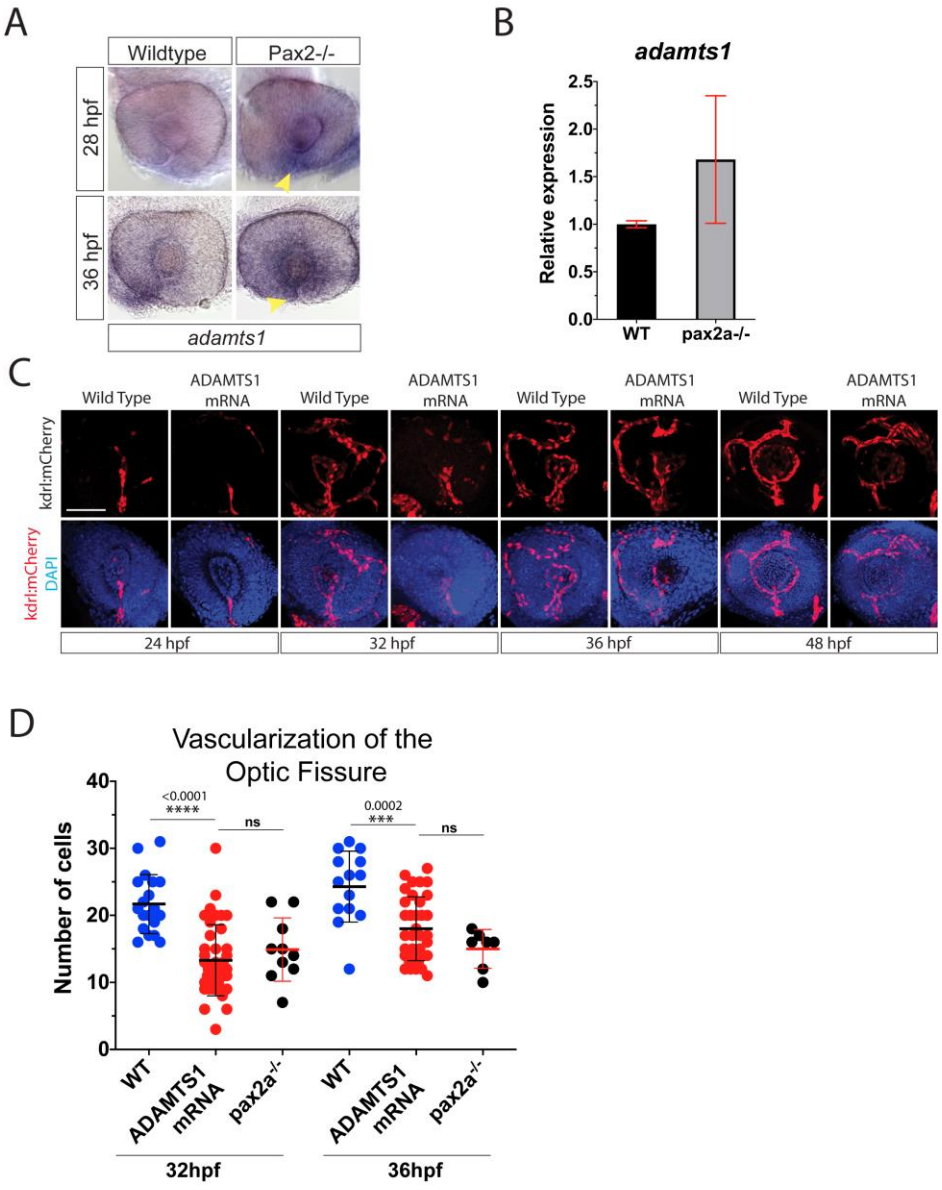

Figure 4-2 ADAMTS1 inhibits retinal vascularization.

A) Wholemount in situ hybridization comparing ADAMTS1 expression between WT and pax2a$^{-/-}$ embryos at 28 and 32hpf. ADAMTS1 signal within the optic fissure (yellow arrowhead) is clearly increased in Pax2a$^{-/-}$ embryos. B) qPCR results for ADAMTS1 expression from heads of pax2a$^{+/+}$ and pax2a$^{-/-}$ embryos at 32hpf. C) Comparison of WT and ADAMTS1 mRNA injected embryo vascularization during optic fissure fusion, 24-48hpf. 3D reconstructions of whole mount Tg[kdrl:mCherry] (red) WT or ADAMTS1 mRNA injected embryos with DNA stained by DAPI (blue). Scale bar = 50um. D) Quantification of mCherry positive cells from 3D confocal stacks within the region of the optic fissure. Individual embryo results are depicted. * p<0.001, ANOVA p<0.0001.

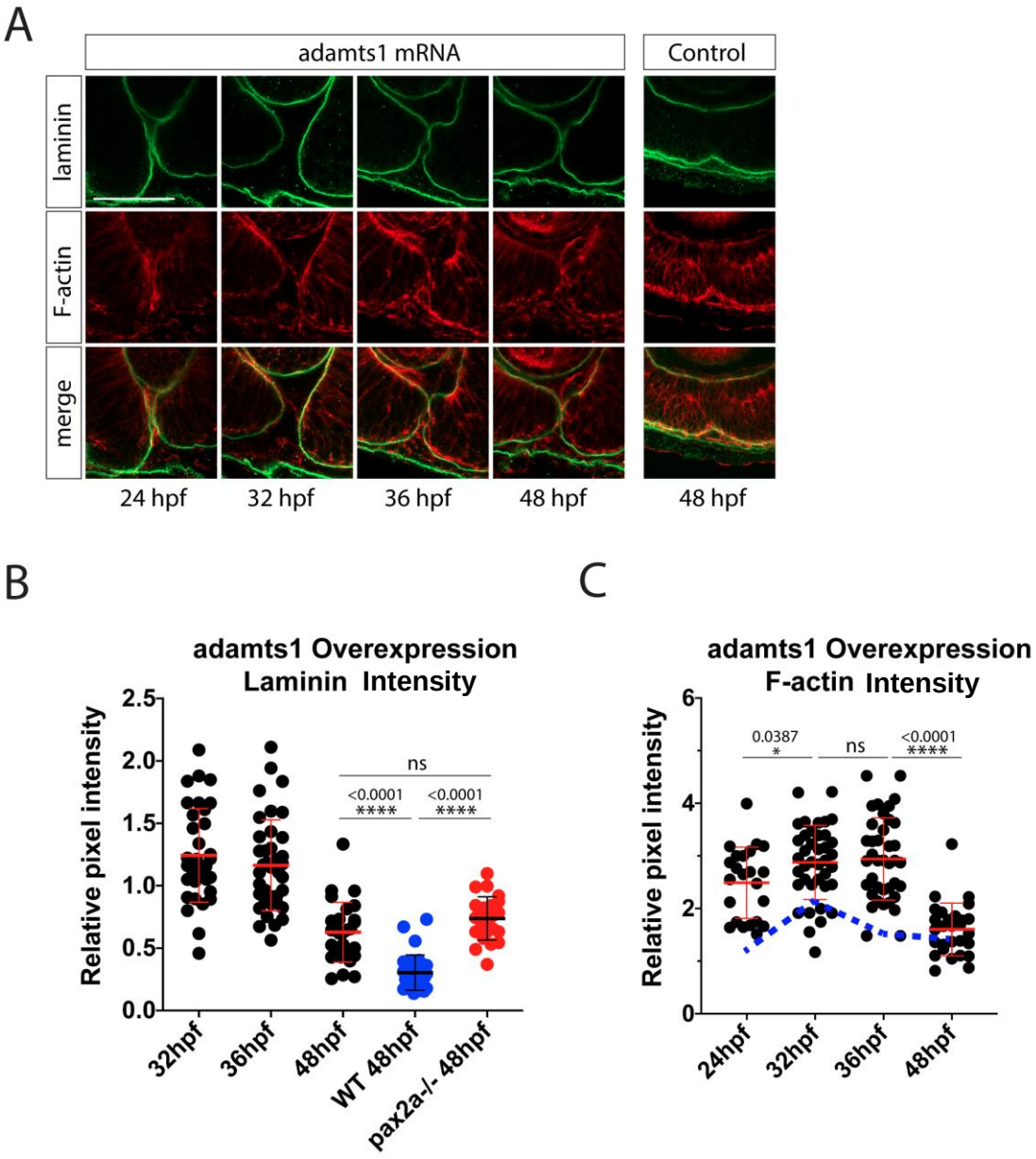

Figure 4-3 ADAMTS1 misregulation leads to failure of optic fissure fusion.

A) Whole mount Immunohistochemistry was used to simultaneously visualize F-actin (red) and laminin (green) during optic fissure fusion, 24-72hpf in ADAMTS1 mRNA injected embryos. Central-proximal sections obtained using confocal imaging were collected and quantified. Scale bar = 50um. B) Quantification of laminin signal intensity within the optic fissure, normalized to regions of laminin staining juxtaposed to the lens. Relative pixel intensities are displayed. A green dotted line depicts the trend in laminin intensity over time, blue line depicts WT trends. ANOVA $p<0.0001$. C) Quantification of F-actin signal intensity (phalloidin staining) within the optic fissure, normalized to regions of F-actin signal within the lobe of the retina. Relative pixel intensities are displayed. A red dotted line represents the trend in F-actin intensity over time, blue line represents WT trends. ANOVA $p<0.0001$.

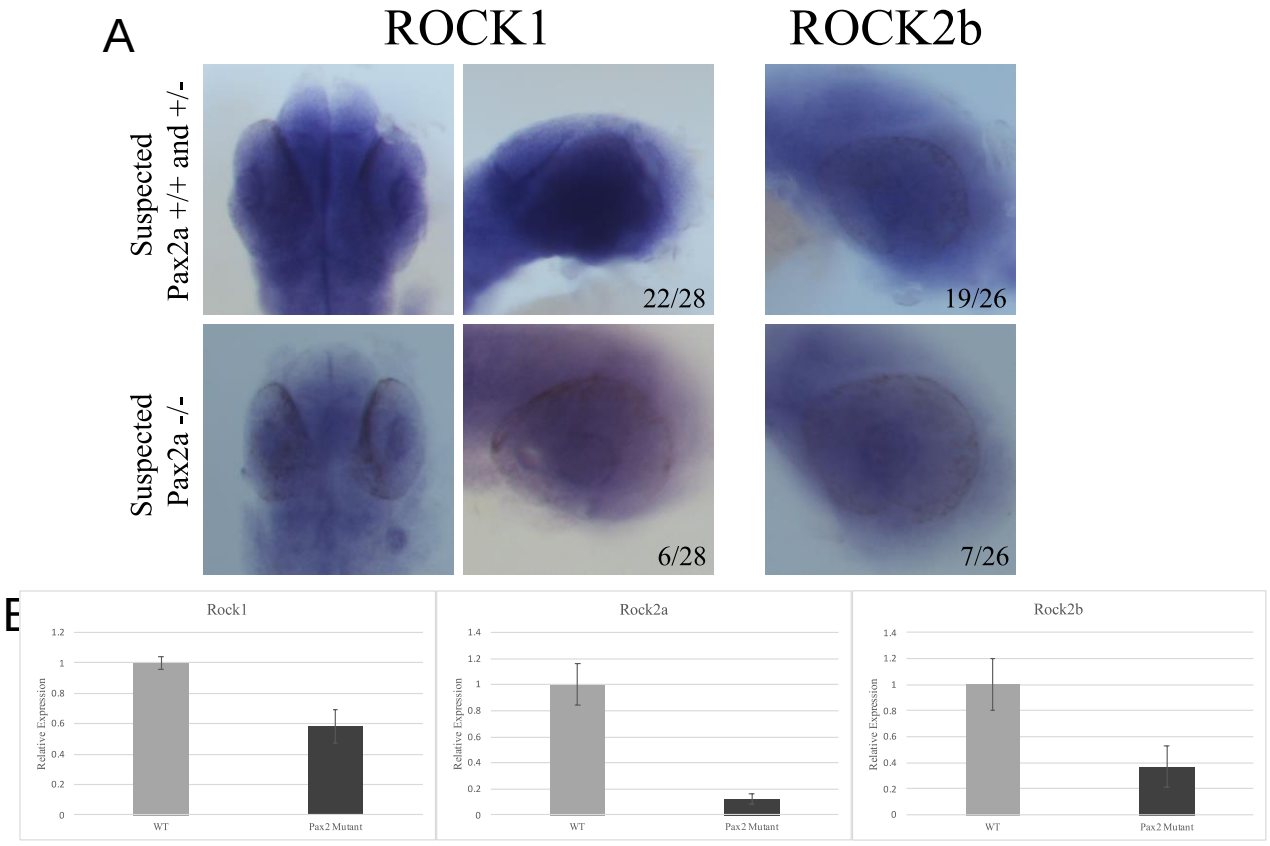

Figure 4-4 Down-Regulation of ROCK1, ROCK2a, and ROCK2b in pax2 mutants.
A) Wholemount in situ hybridization comparing ROCK1 and ROCK2b expression between WT and pax2a$^{-/-}$ embryos at 32hpf. ROCK1 and ROCK2b signal within the eye is clearly decreased in the suspected Pax2a$^{-/-}$ embryos. **B)** qPCR results for ROCK1, ROCK2a, and ROCK2b expression from heads of pax2a$^{+/+}$ and pax2a$^{-/-}$ embryos at 32hpf.

CHAPTER 5. DISCUSSION

On the surface, epithelial fusion seems like a simple process: push sheets of cells close together and glue them. The actual process is anything but simple, requiring precise coordinated cell movements, specific spatially and temporally controlled expression of many genetic factors, detailed cell-cell communication and so much more. Many tissues throughout morphogenesis require epithelial fusion, including the heart, neural tube, eye, and more [27, 200-202]. For almost every epithelial fusion event there is an associated congenital birth defect: malformed hearts, spina bifida and coloboma to name a few [27, 200-202]. Often times these congenital defects present themselves as part of syndromes, as is the case in CHARGE syndrome where many epithelial fusion events have failed to occur [31]. Based on the presence of these syndromes where multiple fusion events fail to occur properly it is highly reasonable to assume that these events share some core common mechanisms. Therefore studying one fusion event could potentially be advantageous for understanding the mechanisms governing other fusion events as well.

Optic fissure fusion presents a unique system to be able to understand the mechanisms governing epithelial fusion. In zebrafish fusion of the optic fissure occurs rapidly, retinal morphogenesis is completed by 72 hours post fertilization. Eye development is easily accessible to study as it develops peripheral to the organism, allowing for detailed analysis of the mechanisms that occur during fusion. Like with most fusion events, failure of optic fissure fusion results in a congenital disorder, in this case coloboma [57]. Coloboma is a prevalent cause of pediatric blindness, accounting for approximately 10% of all pediatric blindness cases worldwide [58]. This blindness is due to the open fissure which exposes the retinal ganglion cell axons to the external

environment resulting in neuronal death preventing the transduction of signals from the eye to the brain. While some colobomas can be traced back to environmental causes, such as in the case of vitamin A deficiency resulting in a failure to activate the RA pathway [78]. Most causes of coloboma, however, are the result of genetic aberrations. Unfortunately, only approximately 30% of non-syndromic coloboma cases have a definitive genetic link, and of those 30% many do not reveal a functional explanation as to their requirement in fusion [140]. Pax2 is one of the 30% of known genetic abnormalities which lacks a functional explanation to its requirement in optic fissure fusion [174]. Nevertheless, pax2 is a cause of coloboma across many species, including humans [173]. Approximately 50% of renal coloboma cases in humans can be traced back to a mutation in pax2, of which 92 mutations have been found and one particular mutation has been reported 57 times [61]. This makes pax2 mutants an effective model to study coloboma and the mechanisms which go awry during the process of optic fissure fusion.

Much of the decades of previous work on optic fissure fusion has focused on the genes and genetic pathways required for this process to occur. Most of these mutations result in a morphological coloboma, where failure of the proper patterning and morphogenetic movements of the eye fail to occur resulting in a large morphological gap between the lobes of the fissure and not due to any defects in the actual epithelial fusion process. This morphological based coloboma also presents difficulty when trying to understand the direct mechanisms involved in the actual joining of the two tissues. It has been reported in some species, such as mouse and chick, that mechanisms such as apoptosis and cell proliferation play a role in fissure fusion [168, 214]. However, due to

their involvement in optic fissure formation and growth it is nearly impossible to say whether these mechanisms are directly involved in the fusion process or are the result of morphogenesis [88]. The direct cellular machinery is still the most poorly understood aspect of optic fissure fusion. What is known about the cellular machinery driving this process can be summed up in three broad mechanisms. Two mechanisms have long been accepted to be involved in epithelial fusion in general, basement membrane removal and actin cytoskeletal rearrangements. The basement membrane that surrounds epithelial tissue performs important tasks, one of which is to provide a barrier that distinguishes the boundaries of tissues [90]. This important role for the basement membrane becomes problematic when epithelial fusion needs to occur as it keeps the tissues separate and within separate boundaries. It also hinders the actin cytoskeleton from being able to form necessary structures to contact and communicate between the fusing sheets [90]. The requirement of basement membrane removal has been the consensus and commonality amongst all vertebrate species studied to date [140].

The actin cytoskeleton has been observed during epithelial fusion across many different fusion events such as *Drosophila* dorsal closure and mouse neural tube development, to name a few [162]. It is generally accepted that the actin cytoskeleton forms critical structures to aid in fusion by forming lamellipodia and filopodia [163]. These structures help to connect and communicate to the apposing tissue and acts as a zippering-type mechanism, seaming the tissues together along the length. In a recent study, RNA sequencing was performed comparing human and murine laser captured microdissections of the optic fissure and found that there was high conservation in their gene set enrichment patterns [215]. Patel, et al. discovered that genes involved in the

epithelial to mesenchymal transition were enriched in the human optic fissure during the fusion process [215]. Patel, et al. further showed that cells at the fissure margins delaminate and create cellular protrusions which then go on to rearrange to create a continuous sheet [215]. It was also noted that apoptosis was not observed in the human optic fissure during fusion [215].

The third mechanism, specifically in optic fissure fusion, has only recently been elucidated and is still in its infancy, the hyaloid vasculature. For many decades it was believed that the hyaloid vasculature was only a passive process, merely taking advantage of the open fissure to establish the vasculature network at the back of the lens. However, it is now understood that migrating POM-derived endothelial cells forming the hyaloid vasculature are critical to the fusion process [139]. With these cells' ability to produce secreted factors which could affect fissure fusion they are quickly becoming a key area of study. James et al. showed that in zebrafish talin1 mutants, an actin scaffolding protein known to be required for cell migration, the hyaloid vasculature was greatly reduced and optic fissure fusion failed to occur [119]. In this same work James et al. also showed that in cloche mutants, which lack all early vasculature, basement membrane degradation was delayed compared to normal optic fissure fusion [119]. Basement membrane degradation, actin cytoskeletal rearrangements, and the establishment of the hyaloid vasculature painted the backdrop to our understanding of the cellular machinery involved in optic fissure fusion. This, however, was merely a beginning, so much was still left unanswered. Which cellular mechanism is the initiating factor? How is the basement membrane removed? What kind of changes happen to the actin cytoskeleton? Why are migrating

vasculature cells required during optic fissure fusion? These questions were the basis of this dissertation.

Our broad hypothesis was that basement membrane removal, actin cytoskeletal rearrangements, and migrating vasculature cells were intimately connected to one another, without one, the others fail to occur. The beginning of this research was performing a detailed analysis of the three known mechanisms involved in optic fissure fusion. We needed to pinpoint the precise timing and behaviors of each of these mechanisms before we could even begin to understand and test how they interact with one another. Through whole mount immunohistochemistry using wild-type embryos and staining for laminin, a marker for the basement membrane, we discovered that degradation of the basement membrane begins at approximately 32 hours post fertilization (hpf). This degradation begins medially and the epithelial sheets fuse along the ventral axis proximally and distally from this median. The degradation continues until around 48 hpf around the time which laminin can longer be detected within the vast majority of the optic fissure. We also characterized the actin cytoskeleton through phalloidin staining. We discovered that an increase in f-actin staining immediately preceded (between 24 to 32 hpf) basement membrane degradation in the lobes of the optic fissure. This suggests that actin remodeling plays some part in initiating basement membrane degradation. The final mechanism we extensively characterized was the establishment of the hyaloid vasculature and its relationship to the other mechanisms. Using a transgenic line of zebrafish which fluorescently tags the VEGF receptor kdrl, we determined that endothelial cells begin migrating into the optic cup before 24 hpf, as development continues the number of vasculature cells continues to increase until by 48

hpf individual cells are no longer distinguishable. One of the major challenges in this characterization was examining the actin cytoskeleton. This was due to the presence of these migratory cells, it became nearly impossible to distinguish the behavior of the actin cytoskeleton associated to the epithelial cells surrounding the optic fissure and the actin cytoskeleton associated to the migrating endothelial cells. Regardless of our inability to distinguish the individual behaviors of the actin cytoskeleton we knew that migrating endothelial cells were the first to appear in the optic fissure, ever before increases in f-actin and basement membrane degradation occur. We now felt we had a clear understanding of the behavior of these three cellular mechanisms during optic fissure fusion, but it told us little in the way of their function. We next wanted to see if in fact these three cellular mechanisms were involved in optic fissure fusion by doing the same analysis in a coloboma model, pax2a. We hypothesized that since we feel the three cellular mechanisms are intimately linked, that in coloboma all three mechanisms would be aberrant. By performing the same analyses on pax2a mutants that were performed on wild-type embryos we confirmed our hypothesis that in coloboma these cellular mechanisms show great irregularities. In pax2a mutants we observed a retention of the basement membrane up to and including 72 hpf, well beyond the time when the basement membrane has been completely degraded in wild-type. The actin cytoskeleton, also, fails to undergo the required rearrangements, as an increase in f-actin staining could not be detected in the optic fissure when it was detected in wild-type. Finally, in pax2a mutants the hyaloid vasculature is malformed compared to wild-type and through cell counting we were able to confirm that there is a significant reduction in the number of endothelial cells migrating through the optic fissure. And further confirmation was provided through

qPCR analysis which showed that several transcripts specifically associated to the hyaloid vasculature were down-regulated in pax2a mutants, including the actin scaffolding protein talin1. Due to the findings from pax2a mutants, and the fact that endothelial cells are the first to arrive on scene, we hypothesized that these endothelial cells were crucial and were possibly the catalyst that initiates the subsequent mechanisms involved in optic fissure fusion. One of the most well-known mechanisms for the growth of vasculature is VEGF signaling (vascular endothelial growth factor), interestingly it was discovered that several VEGF ligands are down-regulated in pax2 mutants when compared to their wild-type counterpart. This allowed us to test our hypothesis of vasculature being required for optic fissure fusion by inhibiting VEGF signaling. To do so we used DMH-4 which blocks VEGF signaling and we then were able to assess the consequences to optic fissure fusion. We found that when vasculature is precluded from the optic cup the basement membrane fails to degrade and an increase in f-actin is unable to occur and ultimately resulting in coloboma. By performing a drug inhibition time course for the spatial requirement of these vasculature cells we also found that these cells are required early in optic cup morphogenesis to complete optic fissure fusion, when treated from 12 hpf to 48 hpf this resulted in a 100% inhibition of optic fissure closure. However, when treatment began at 24 hpf almost 25% of fissures were able to fuse, beginning at 28 hpf approximately 50% were able to fuse, and beginning at 32 hpf approximately 90% were still able to fuse. By this point we had been able to provide a considerable amount of evidence to show that these migrating endothelial cells are undoubtedly required for proper optic fissure fusion. Although we knew that vasculature cells were involved in the fusion process and suspected they might be the initiating

mechanism, we still didn't know why these vasculature cells were involved. Previous literature searches had revealed that endothelial cells participate in angiocrine signaling, a process in which endothelial cells can deposit proteins which aid in development and repair, including extracellular matrix components (ref). We wanted to test the possibility of endothelial cells providing extracellular matrix remodelers like metalloproteases, which would contribute to basement membrane degradation in the optic fissure. To test this we first had to determine which metalloproteases had expression in the fissure. To do so we performed whole mount in situ hybridizations (WISH) and further performed whole mount fluorescent in situ hybridizations (FWISH) on the potential targets. From these experiments we were able to uncover three promising metalloproteases which show expression at the appropriate time during optic fissure fusion, mmp2, mmp14a and mmp14b. Interestingly, mmp14 is an activator of mmp2 so it seemed promising that these metalloproteases showed strong expression in the optic fissure together. We wanted to ascertain which cells were providing this metalloprotease, the epithelial or endothelial cells. We performed two-color FWISH probing for mmp2 and an eye specific promoter (rorB), and mmp2 and kdrl. From this we saw an overlapping expression between mmp2 and kdrl, providing evidence to our presumption that endothelial cells could participate in angiocrine signaling while passing through the optic fissure by depositing mmp2 to degrade the basement membrane. However, this didn't reveal if mmp2 is actually involved in fusion, it could simply be a metalloprotease which the migratory cells use to help them detach from their temporary connections to basement membranes along their migration path. To test whether mmp2 activity is required for optic fissure fusion, we obtained an mmp2 specific inhibitor ARP101. When treated at concentrations of 20 μM

from 24 to 48hpf approximately 90% of embryos had either partial or complete retention of the basement membrane, suggesting that 90% of embryos treated with the mmp2 inhibitor developed coloboma. This showed the first direct evidence of possible endothelial cell contribution to optic fissure fusion, showing for the first time a functional component of these cells.

After these findings, where we showed direct functional evidence to the requirement of endothelial cells in optic fissure fusion, we wanted to understand how it was possible for vasculature to be impacted by pax2 function or lack thereof. To do so we undertook the painstaking task of collecting zebrafish eye tissue at 48 hpf and extracting RNA for sequencing. Once the bioinformatic analyses were complete we began separating our results into separate groups based on their gene ontology looking at the pathways and biological processes these genes could be separated into. Based on this we made a novel discovery of a possible mechanism through which pax2 can modulate hyaloid vasculature establishment. What we initially thought was a metalloprotease actually had ability to function as an anti-angiogenic protein called ADAMTS1. ADAMTS1 was up-regulated in pax2a mutants by about 2-fold, suggesting that pax2a directly or indirectly inhibits the expression of this anti-angiogenic protein. ADAMTS1 has been implicated in cancer metastasis when there is a loss of its function, showing that there is indeed a role for ADAMTS1 in the regulation of angiogenesis. One we had validated this finding through qPCR, we wanted to see if we could mimic the effect by performing overexpression experiments. Upon analysis of ADAMTS1 injected embryos we were amazed to see almost a direct imitation of the pax2a mutant phenotype. ADAMTS1 mRNA injected embryos showed a reduced number of endothelial cells

entering through the optic fissure, and when comparing cell counts there was not a significant difference to that in pax2a mutant. We also performed immunohistochemistry on these injected embryos and discovered that just as in pax2 mutants there is a failure to degrade the basement membrane as well as the failure to dramatically increase f-actin accumulation in the optic fissure. So now we felt we knew, at least in part, how the endothelial cells were being modulated during optic fissure fusion. At this point we also felt we had a firm grasp on the impact the endothelial cells have on the basement membrane of the optic fissure. One area that we felt we still lacked any concrete evidence for was the potential effects the migrating endothelial cells have on the actin cytoskeleton. After searching the RNA sequencing data again and separating out actin associated proteins, we became interested in two genes that were down-regulated in pax2a mutants, ROCK1 and ROCK2b. These two genes caught our attention for their involvement in many epithelial fusion events, when mutated across different species and under different circumstances it has resulted in open eyelids, open ventral body wall, and has a diverse range of functions from cell adhesion to extracellular matrix remodeling. Through qPCR and WISH staining of a clutch of pax2a mutant in-cross embryos I was able to validate our RNA sequencing data. This showed promising results leading toward a link between coloboma and the actin cytoskeleton, but further work needs to be done to further this work.

This dissertation made a novel discovery in the field of coloboma, one of the first direct links to the cellular mechanisms used during fusion (Figure 5.1). We found that slightly before 24 hpf in zebrafish embryos the endothelial cells begin migrating through the open optic fissure. These endothelial cells are required for fusion to occur, when

precluded fusion fails to occur. In the pax2a coloboma model we also discovered a novel technique in which pax2a modulates the migration of these cells. These endothelial cells contribute both directly and indirectly to the fusion process by providing a source of the metalloprotease mmp2 which is one of the components required for basement membrane degradation in the optic fissure beginning at 32 hpf. These endothelial cells might also possibly contribute to the actin cytoskeletal dynamics in the epithelial cells via integrin signaling, activating Rho signaling to ROCK, though further work needs to be done. At 48 hpf we see a complete lack of the basement membrane in the fissure region, a continuous sheet of epithelial cells, and a formed vasculature network at the back of the lens, and thus completing eye morphogenesis. This work begins to uncover the cellular machinery involved in fusion. This provides advantages in the fight against coloboma as it specifies cellular markers that could potentially contribute to genetic screening for this disease and others. In the past, we've relied on single gene studies which contribute only a single gene to screening efforts. By finding the cellular mechanisms used during this process a large scale screening can be done for genes associated with all the cellular machinery involved.

Future work in the field of optic fissure fusion should focus on endothelial cells and their mechanisms for regulating this process. It is my belief these cells are the crux of optic fissure fusion and more work needs to be done to investigate how they do what they do. Firstly, I believe it would be beneficial to perform single cell RNA sequencing on FACS sorted eye cells, separating endothelial cells (kdrl transgenic line) from epithelial cells (rx3 transgenic line). The biggest challenge here are the technical aspects, to once again compare wild-type and coloboma transcriptional differences the most beneficial

time to examine them would be at 32 hpf when fusion is just beginning, this puts timing to the early evening when accessing the required materials is difficult. This is also challenging at 32 hpf as pax2a mutants do not have a visible phenotype until 48 hpf so a wide scale genotyping on live embryos would have to be undertaken. Further work also needs to focus on differentiating hyaloid endothelial cells' actin cytoskeleton from the fissure epithelial cells' actin cytoskeleton. Talin1 is thought to be associated to the endothelial cells and is required for their migration, and I hypothesized that ROCK is associated to epithelial cells and is required for cytoskeletal dynamics involved in fusion of the tissue. However, these cannot be fully resolved without the ability to distinguish the actin cytoskeleton of endothelial cells from the actin cytoskeleton of epithelial cells. It is highly probable that integrin signaling is involved in fusion through angiocrine signaling from endothelial cells. By examining integrin mutants we could begin to uncover the potential mechanisms through which endothelial cells contribute to cytoskeletal dynamics in optic fissure fusion. Additional validation also needs to be performed on this dissertation's findings by examining mmp2 and ADAMTS1 mutants. I have generated CRISPR mutants for both of these genes that are currently maturing. The mmp2 line needs to be examined to ensure that knock-out of mmp2 results in coloboma as was observed in the inhibitor study. It will be interesting to see if ADAMTS1 mutants also develop coloboma. It has been observed that pax2 levels need to be precisely controlled, we've shown that lack of pax2a function results in coloboma, however, overexpression of pax2 also results in coloboma [216]. It has also been reported that over production of vasculature in the retina also results in coloboma [210]. By observing ADAMTS1 mutants we can discern if reduction of ADAMTS1 results in hypertrophic

vascularization of the retina resulting in coloboma, requiring a precise concentration of expression much like pax2. Along these same lines it would also be beneficial to investigate if overexpression of pax2a will result in a down-regulation of ADAMTS1.

Not only is this dissertation an advancement for our understanding of optic fissure fusion, but also could be the advancement for other epithelial fusion events as well. Our finding of endothelial cell requirement in optic fissure fusion is not unique to optic fissure epithelial fusion. In mouse neural tube closure endothelial cells were shown to be required, when endothelial cells were not properly modulated and directed this resulted in severe phenotypes one being neural tube defects [217]. Angiogenesis has also been shown to be required during wound healing, and is thought to be due to angiocrine signaling leading to proliferation and differentiation of progenitor cells [136]. This dissertation further confirms and expounds upon the idea of endothelial cell requirements during epithelial fusion. It would be very beneficial to our understanding of epithelial fusion if we began to investigate a potential role for endothelial cells in other epithelial fusion events

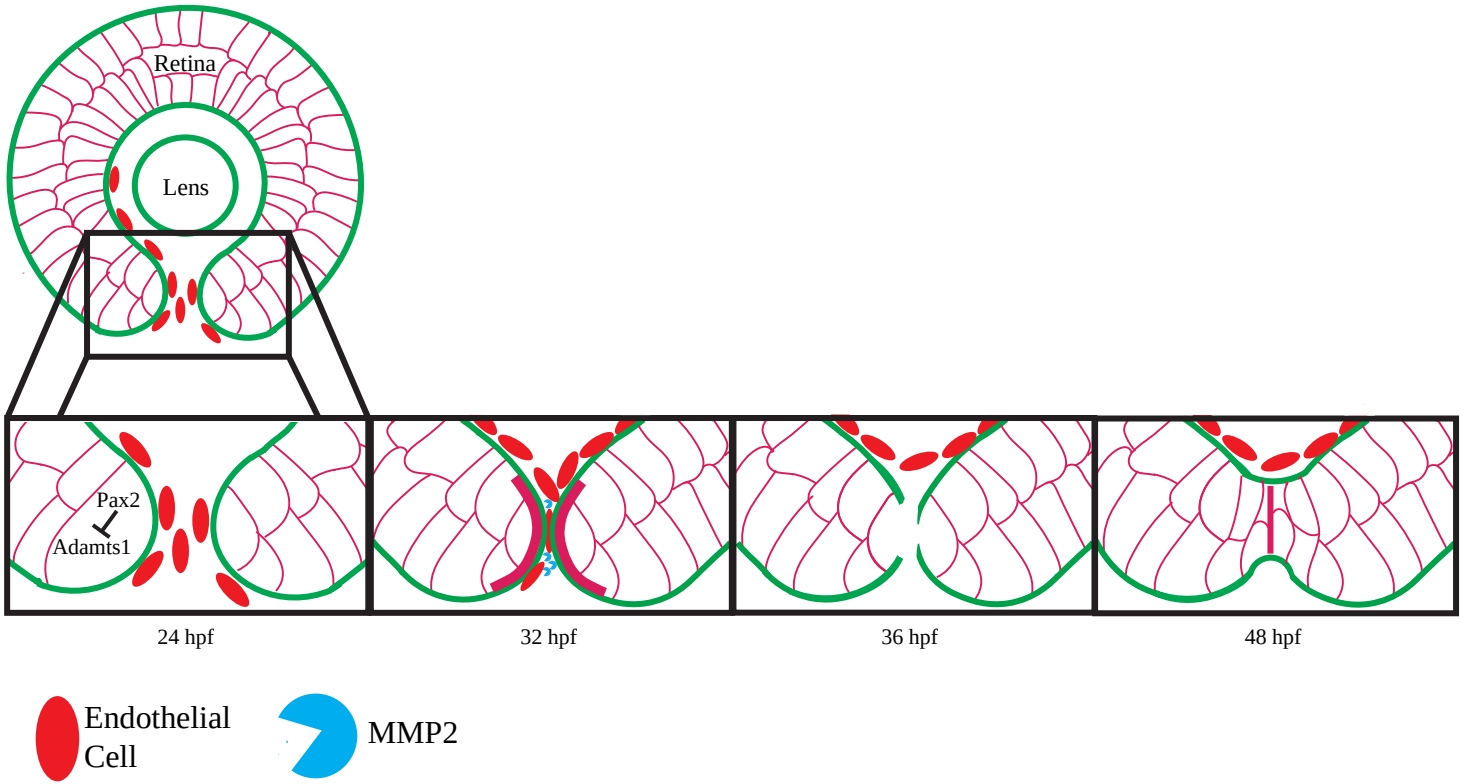

Figure 5-1Detailed Model of Optic Fissure Fusion.
Proposed model for optic fissure fusion. Magenta marks filamentous actin, green marks the basement membrane.

APPENDICES

APPENDIX 1: DIFFERENTIAL TRANSCRIPT EXPRESSION PROFILE BETWEEN PAX2 MUTANTS AND WT.

Table A1.1: Down-regulated genes in pax2 mutants.

Gene ID	PPDE	PostFC
aifm1	1	1223.99707
si:ch211-57b15.1	1	175.669227
si:rp71-36a1.5	1	140.545568
krt96	1	159.577655
si:dkey-9c18.3	1	135.672416
arf5	1	116.803923
dock1	1	111.340616
sumo3a	1	699.778621
lim2.1	1	694.142353
zgc:152951	1	97.6461015
pcbp3	1	93.498624
ddx43	1	47.0232655
abracl	1	78.7184492
tfb2m	1	283.563781
znf1034	1	38.8839082
nsun5	1	17.3779661
tln1	1	249.437187
ptprna	1	173.271619
crygs1	1	65.1862175
mgst2	1	194.272308
si:ch73-7i4.2	1	27.2410028
si:dkey-126g1.7	1	11.3613672

Table A1.1: Continued

Gene ID	PPDE	PostFC
hn1l	1	12.4968928
zdhhc16a	1	18.0239348
sept9a	1	142.868951
pyroxd2	1	76.7017298
gpsm1b	1	81.5093272
cryl1	1	73.8133177
atp8b1	1	69.0944517
slc16a8	1	11.9456451
zgc:195170	1	8.53785003
si:ch211-180n24.3	1	7.97368407
emc4	1	4.84517879
zgc:158803	1	5.1361905
ccdc15	1	5.36868841
cyp1b1	1	4.84809106
ftr36	1	3.92235
nedd1	1	3.71353033
si:dkeyp-53d3.5	1	3.43253567
gsta.1	1	3.42834504
gsta.1	1	3.42834504
crybb1l3	1	3.31490641
nags	1	2.99342656
trpm2	1	2.61882
yif1b	1	2.56620613
zgc:171242	1	2.50632681
ndufb2	1	2.26997051

Table A1.1: Continued

Gene ID	PPDE	PostFC
wdr11	1	2.26390257
capn3a	1	2.2636352
nif3l1	1	2.26196314
si:ch73-111m19.2	1	2.19476442
cyp17a1	1	2.13605558
si:ch73-111m19.2	1	2.14361341
si:ch211-210c8.7	1	2.12701659
gja8b	1	2.06529674
crygmxl1	1	2.06431522
lim2.5	1	1.90946226
abhd17aa	1	1.88126807
dnajb6b	1	1.85337252
pabpc4	1	1.82916711
pld3	1	1.82056501
spg20a	1	1.79453331
crygmx	1	1.77666289
si:ch211-152c2.3	1	1.78464777
usp45	1	1.77463243
ccdc85cb	1	1.77711578
cx23	1	1.74621358
slc25a22	1	1.72877889
cryba4	1	1.6950759
tdh2	1	1.70536566
arsj	1	1.65984403
lamp1	1	1.65161519

Table A1.1: Continued

Gene ID	PPDE	PostFC
lctlb	1	1.63883046
otc	1	1.63219085
gja8a	1	1.59332984
mipa	1	1.59090101
oxa1l	1	1.58340918
sptbn5	1	1.58041002
rps25	1	1.56500706
exoc3	1	1.56852543
scp2a	1	1.55977927
dpp3	1	1.53549039
lim2.1	1	1.52576615
eif4ba	1	1.48108286
daam1b	1	1.48283158
ank3b	1	1.47309668
mipb	1	1.47151262
pitrm1	1	1.44887687
wdr48b	1	1.44611811
si:ch211-214j24.14	1	1.94211311
CU570881.1	1	6.78543573
zgc:92275	1	4.23766612
crybb1	1	1.71609167
slc25a15b	1	3.23368643
rac1b	1	1.60544192
cps1	1	1.60689024
dusp11	1	3.28844067

Table A1.1: Continued

Gene ID	PPDE	PostFC
si:dkey-221j11.3	1	2.11172447
dennd2db	1	2.43279657
zgc:153929	1	1.98064232
rgs12b	1	62.8409305
srsf2b	1	1.47707825
si:dkey-183c16.7	1	13.0146393
dusp22b	1	2.27505567
asna1	1	56.2488278
cap2	1	1.51908495
fuca1.2	1	1.56651662
map7d1b	1	2.50556695
vamp8	1	1.4582063
p3h3	1	1.71118286
#N/A	1	2.08389311
myo3b	1	2.14868484
rabif	1	2.13834441
si:dkey-105i14.1	1	3.62992484
pebp1	1	1.73882751
rock1	1	25.3621951
agt	1	58.8429679
alg12	1	1.80945907
lman1	1	1.5279362
si:dkey-147f3.4	1	2.09715543
cryba1b	1	1.53629026
lcmt2	1	7.38642605

Table A1.1: Continued

Gene ID	PPDE	PostFC
CR847505.1	1	2.00613265
gpr22a	1	58.9490895
si:ch211-161h7.8	1	1.83852528
nom1	1	1.47612084
ascc2	1	1.48866247
aifm5	1	1.77670654
tubb6	1	1.81145175
lim2.3	1	1.58248375
cast	1	1.52337612
acad8	1	1.65017367
atp5j	1	58.1667188
si:ch211-271b14.1	1	4.61968968
phkg2	1	1.75324828
ascc1	1	1.79211659
lctla	1	1.66701741
mfsd2b	1	1.86878124
rock2b	1	6.79767627
crybb1l2	1	1.53754283
si:rp71-36a1.5	1	16.6577328
sncga	1	1.74153709
tp53inp2	1	1.45399487
hmbsb	1	55.9932726
fbxl4	1	1.5696002
zgc:193541	1	1.57657677
capn3a	1	1.57116732

Table A1.1: Continued

Gene ID	PPDE	PostFC
si:dkeyp-80d11.4	1	20.6510718
dap3	1	1.45876876
ncam3	1	2.69695494
rnf146	1	5.81313939
rmdn1	1	3.32221771
cx23	1	1.76681385
sub1a	1	1.85500891
dmrt1	1	51.2481844
itprip	1	2.10199487
UBA6	1	1.62157642
tpi1b	1	1.64792889
cmtm7	1	1.66102804
adgre9	1	18.9178814
bmpr1ba	1	1.48208161
itga2.3	1	9.48822663
coq2	1	1.58976076
snrnp35	1	5.78146624
ppp1r7	1	53.7696831
crygn2	1	1.58095118
engase	0.99999999	1.61017979
crybb1l1	0.99999999	1.48527984
hsf4	0.99999999	1.56782213
cryba2a	0.99999999	1.52431995
ggctb	0.99999999	1.67449333
#N/A	0.99999999	19.1301108

Table A1.1: Continued

Gene ID	PPDE	PostFC
tbc1d7	0.99999999	2.80969394
coro7	0.99999999	6.18818573
cfl2	0.99999999	1.49370552
CU570881.3	0.99999998	2.11755421
lim2.5	0.99999998	1.91023961
pax2a	0.99999998	6.78650436
kpna4	0.99999998	15.6249193
cbx2	0.99999997	3.99260728
hbbe1.1	0.99999997	105.902985
chfr	0.99999996	2.64468057
srrm1	0.99999996	1.73461837
map2k2a	0.99999996	1.54454791
rab1ab	0.99999995	1.57140359
dnajb11	0.99999994	160.269319
cryba1l1	0.99999994	1.57377739
cars2	0.99999994	2.1521133
alpl	0.99999994	1.87004743
oat	0.99999993	2.05824632
si:dkeyp-73d8.9	0.99999993	15.0767668
alkbh6	0.99999993	1.49683117
gle1	0.99999992	3.14754418
paqr3b	0.99999992	2.48499927
dennd3b	0.99999992	26.293977
npc2	0.99999991	9.37448709
ell2	0.99999989	1.49504146

Table A1.1: Continued

Gene ID	PPDE	PostFC
grifin	0.99999988	2.02773908
zgc:123295	0.99999987	4.1125871
cyp2k8	0.99999986	1.8099226
psmb7	0.99999986	1.75487666
nrl	0.99999985	1.8069002
TDRD7 (1 of many)	0.99999984	1.73659262
zgc:198419	0.99999983	4.5448607
alkbh1	0.99999983	1.6768179
crybb2	0.99999983	5.18024141
ddx43	0.99999983	17.1825958
mustn1a	0.99999983	8.93863489
polh	0.99999982	4.76200218
krt222	0.99999981	2.05228912
krt5	0.99999979	1.71033081
DNAH10	0.99999978	3.73671831
stk24b	0.99999975	50.6381636
apaf1	0.99999972	45.7857349
nadk2	0.99999969	1.94148452
npm1a	0.99999964	1.8523304
rnf44	0.9999996	2.10459288
cox6b1	0.99999954	1.82301315
ms4a17a.8	0.99999948	3.38703217
plcxd1	0.99999941	1.83893967
gsto2	0.99999939	1.45118731
nucb1	0.99999934	3.78901511

Table A1.1: Continued

Gene ID	PPDE	PostFC
si:ch211-198g14.4	0.99999929	4.64968836
plcb3	0.99999922	1.89038588
kpnb3	0.99999921	70.5079153
ncs1a	0.99999913	4.77662414
ppp1r13l	0.99999909	1.63056225
gbgt1l3	0.99999895	5.16494507
upb1	0.99999894	1.83222994
fah	0.99999888	2.10977636
crygm2d10	0.99999873	1.6257291
aatf	0.99999871	1.81229155
lim2.4	0.99999866	1.55456654
b3gat3	0.99999856	1.56667896
rnf213a	0.99999855	1.75125497
CU929052.1	0.99999851	1.59986814
krt222	0.99999806	2.08429438
si:dkey-66a8.7	0.99999801	3.37314446
cryba2b	0.9999977	1.62916318
tssc4	0.99999762	2.28817405
dhx40	0.99999758	2.69060175
dnase1l4.2	0.99999747	1.65174174
fli1b	0.99999746	2.13903918
vetz	0.99999737	6.9774706
slc25a15b	0.99999733	1.63327092
gtf2f2a	0.99999733	1.48762735
CABZ01009708.1	0.99999729	7.32508867

Table A1.1: Continued

Gene ID	PPDE	PostFC
yif1b	0.99999719	1.87811913
elovl8b	0.9999971	3.08625651
arl16	0.99999632	4.30365674
rpl30	0.99999572	3.73752824
si:ch211-110e21.4	0.99999494	1.9678438
tsen54	0.99999443	1.56210688
grtp1a	0.99999429	3.93572394
fbxl3b	0.99999413	6.77888696
CABZ01084225.1	0.99999385	47.2480885
si:dkeyp-73d8.6	0.99999299	45.9496467
si:dkey-13n23.3	0.99999296	2.5385895
zgc:100832	0.99999245	1.47224445
si:ch211-255g12.6	0.99999203	3.81044639
ugt5b2	0.99999102	2.0851078
nnt2	0.99998971	2.6948858
ern1	0.99998941	2.64396353
gmds	0.99998914	4.40703883
mrc1a	0.99998882	1.52029426
pdcd5	0.99998776	1.45326914
si:ch73-204p21.2	0.99998744	2.09409472
si:ch211-157b11.12	0.99998632	3.00711252
tango6	0.99998497	73.7546973
si:ch73-281f12.4	0.99998414	1.81719242
tomm40	0.99998315	10.579481
pdgfaa	0.99998148	1.95182545

Table A1.1: Continued

Gene ID	PPDE	PostFC
cct8	0.9999793	2.31810813
vdac1	0.99997762	9.86898347
fam161b	0.99997658	4.0967888
ablim3	0.99997505	1.47215069
aifm4	0.99997496	2.66574247
vps26b	0.99997492	2.26824301
cryba2b	0.99997371	1.44821852
vwa1	0.99997347	1.4909354
si:dkey-262k9.4	0.9999716	2.53036937
fam117aa	0.99996981	1.49639138
psip1b	0.99996929	2.99620151
pnp5a	0.99996577	1.67919183
ndufa1	0.99996108	1.92982224
ascc3	0.99996065	1.50769842
foxi2	0.99995996	1.51486128
NAPSA	0.99995937	1.55556349
mylka	0.99995809	1.84965425
chrne	0.99995726	2.12600375
CABZ01094849.1	0.99995647	1.46047706
tmem107	0.99995594	49.6969667
rwdd	0.99995341	1.65893455
plpp1a	0.9999515	1.72251411
sprn2	0.99995112	1.77495768
mettl26	0.99995054	1.69643824
zgc:136439	0.99994981	1.64683941

Table A1.1: Continued

Gene ID	PPDE	PostFC
ruvbl1	0.9999492	2.93279286
sash1a	0.99994471	1.60057577
cldn12	0.99994412	60.0968843
zgc:101716	0.99994364	1.94767793
CU459012.1	0.9999394	1.48985218
pigr	0.99993628	2.26705729
si:ch211-219a15.3	0.99993415	4.55017415
rbm39a	0.99993037	1.66007852
ints10	0.99992692	11.0237361
pde4cb	0.99992688	5.12396905
si:dkey-79f11.7	0.99992283	5.05453674
si:ch73-111m19.2	0.99992196	1.45434574
prpsap1	0.99991189	1.53003315
mibp	0.99991124	1.69516215
tma16	0.99990892	1.4521418
wdr55	0.99990199	3.56272814
si:ch211-66k16.27	0.99990112	2.84187921
si:dkey-12j5.1	0.99989726	1.66907093
tmem17	0.99988971	1.60818914
ppa1b	0.99988901	4.81460436
slc16a8	0.99988704	43.9083338
pax2a	0.99988662	4.06164295
casp7	0.99987887	1.81812348
atp6v0a1a	0.99986267	1.50149016
rnpep	0.99986265	1.50248073

Table A1.1: Continued

Gene ID	PPDE	PostFC
si:dkeyp-2e4.3	0.9998582	2.44070041
scaf4a	0.99985144	6.3933154
si:dkey-26m3.3	0.99984702	1.74852389
crygm2d8	0.99984678	1.53097877
prpf8	0.99983712	4.9201693
brf2	0.99983243	2.25170028
cx23	0.99982901	1.60869914
rbpms2b	0.99980491	1.73186733
rab4a	0.99979591	1.6847137
zgc:158846	0.99979367	31.5286328
commd1	0.99979017	1.55930685
itga2.3	0.99978443	4.2771078
cica	0.99976018	41.1959819
malt1	0.999759	3.34750251
bod1l1	0.99975731	9.09496507
si:dkey-261j11.3	0.9997531	1.77944191
42993	0.99973487	1.51714524
rbm39a	0.99973356	1.47439292
rnf34a	0.99973336	1.75915986
dtwd2	0.99972077	1.72006039
mpped2a	0.99972016	32.5580078
CR933791.2	0.99971927	3.27982281
trpv4	0.99971765	2.17703217
ggt1a	0.99970297	1.58616604
tppp	0.99970228	8.25552791

Table A1.1: Continued

Gene ID	PPDE	PostFC
apooa	0.99965681	2.88784954
si:ch211-264e16.1	0.99963493	2.39559255
tubgcp5	0.99961663	5.32353255
apaf1	0.99958797	2.86180472
CABZ01085177.1	0.99958356	2.58997286
gfap	0.9995812	1.50124367
brf1a	0.99957332	3.57032962
snu13a	0.99956005	1.70802978
col28a1a	0.99952056	1.45732635
ccdc127b	0.99949035	3.11935788
sptlc3	0.99948548	1.73405455
si:ch211-245n8.4	0.9994782	1.57060769
ndufa4	0.99940293	1.83210307
cep97	0.99939637	43.8091499
thyn1	0.99934831	1.70517312
zgc:194125	0.99931666	5.76729451
wnt5b	0.99931648	1.68119178
ehmt1a	0.9993046	1.87654878
cars	0.99929838	1.84299387
dnase1l4.2	0.99929022	5.90812952
gss	0.99926297	1.68269843
tagapb	0.99925649	4.19828835
znf1156	0.99925388	2.7711738
rad51b	0.99924574	1.91152316
neu4	0.99924123	3.0380974

Table A1.1: Continued

Gene ID	PPDE	PostFC
zgc:171435	0.99923297	2.96143816
borcs7	0.99920318	1.57831473
APBA3	0.99919107	1.58086061
trim2a	0.99913752	1.74917993
gja8a	0.99910053	1.91053323
ppm1bb	0.99909997	6.54259548
mllt3	0.99909297	1.59082337
gemin8	0.99908491	1.72856285
si:dkeyp-41f9.3	0.99902658	2.27342844
pttg1	0.99901023	1.4547877
CABZ01017733.2	0.99898879	2.52185913
si:dkey-250l23.4	0.99897471	1.49278173
bag5	0.99889185	1.45172344
tg	0.99888699	4.16034917
adprh	0.9988756	2.6621234
si:dkey-93n13.1	0.99878054	2.54997607
zgc:101783	0.99873615	2.09015323
crygm2d2	0.99872877	1.7872225
crygm2d18	0.99872235	1.56372307
necab1	0.99871626	6.89174956
crygm2d13	0.9986437	32.172129
flad1	0.9985978	2.81680295
arglu1b	0.99856812	1.54702655
nrp2b	0.99855951	9.23551662
prpf18	0.99852081	2.81507736

Table A1.1: Continued

Gene ID	PPDE	PostFC
CABZ01056516.1	0.99848177	1.88996358
abcb6b	0.99847751	1.63195204
ghrb	0.99841373	2.1246351
gba	0.99840894	1.5459978
CR388055.1	0.99835951	8.38118796
CABZ01104045.1	0.99822521	3.09104858
cyp1b1	0.99821377	4.23301803
dgcr14	0.99819288	1.4540346
naa15b	0.99816171	2.14548158
zgc:153901	0.99813824	2.37028815
stk25a	0.99811129	1.6808346
hps1	0.99808501	5.20504829
crygm2d10	0.99803451	1.54346497
acox3	0.99798949	1.64901789
sfxn1	0.9979626	3.67337931
dph6	0.99794754	1.66754809
orc3	0.99786918	4.11144521
ftr34	0.99778972	7.12927033
hspa5	0.99776347	1.45900932
CR388166.2	0.99774393	4.80751572
CR847505.1	0.99767147	1.56087377
creb3l3l	0.99763926	28.9280217
klhdc3	0.99754477	1.49959371
plxnb2b	0.99739686	2.8708384
zgc:113333	0.99739433	2.46406697

Table A1.1: Continued

Gene ID	PPDE	PostFC
lace1a	0.99738843	2.55480026
CABZ01076758.1	0.99738747	2.03221845
b4galt4	0.99734815	1.61207282
hmga1a	0.99733818	27.2336772
GRB14	0.99722118	4.25034902
opa1	0.99720239	7.04487531
hsf1	0.99711966	2.4653613
hagh	0.99711242	42.0700683
aldh1a3	0.99697862	1.73063958
havcr2	0.99691498	2.24716526
adam8b	0.99683177	2.3934117
hao2	0.99667813	1.45767521
anxa11b	0.99665607	1.85238107
pvrl1b	0.9966317	1.50586087
si:ch211-105c13.3	0.99659112	1.58270309
krt1-19d	0.99656907	1.49066487
nudt22	0.99653157	1.54375413
CAPN2 (1 of many)	0.9964168	3.76333227
aifm5	0.99637373	1.5049305
kera	0.99634127	1.46945741
hao2	0.99620531	1.53216224
grhl2a	0.99615744	1.47061948
dctn4	0.99605291	1.93311304
dusp8b	0.9959429	1.70674605
gja8b	0.99592218	5.75569377

Table A1.1: Continued

Gene ID	PPDE	PostFC
slc8a2b	0.99590537	3.00473688
zgc:110249	0.99585384	1.56521469
srsf1a	0.9957298	2.31580174
zgc:162613	0.99568074	2.42296574
plcd4a	0.99543533	1.88003062
CR759830.1	0.99535448	1.72946897
erbb2ip	0.99515345	7.54838897
hmg20b	0.99512041	1.59115006
gmnn	0.99500198	1.87787088
znf1149	0.99485221	2.27037118
glmp	0.99455088	1.45732006
rhobtb2a	0.99451278	1.7608224
trpc6b	0.99445783	4.48237794
eno1a	0.99440949	46.4447679
MFAP4 (1 of many)	0.99437498	5.34202918
dhrs13a.1	0.99434608	1.52869638
cryba1a	0.99426025	1.81056152
CASKIN2	0.99414096	2.2137431
irf6	0.99390149	1.44744897
selm	0.99383238	1.70120157
crybb1l3	0.99371216	2.97624852
NPNT (1 of many)	0.99362616	1.95726061
zer1	0.99360223	2.80517208
si:dkey-31f5.11	0.99353156	11.1294797
trap1	0.99346372	1.77854316

Table A1.1: Continued

Gene ID	PPDE	PostFC
ddx3b	0.99333702	1.75648871
hnrpkl	0.99332646	2.45360045
fam198a	0.99303582	2.13154654
si:ch211-284e13.4	0.99283436	8.43875312
crygm2d4	0.99275242	1.46073229
uxt	0.99233654	1.60243282
zgc:101858	0.99209436	1.45613599
taf9	0.99204649	1.97353727
si:ch211-173d10.1	0.99199547	1.68915066
slc5a8	0.99166367	2.12299005
ngfb	0.99166004	1.44577767
arhgef37	0.99164547	1.562217
rpl22	0.99163915	3.13135745
ppp1r13bb	0.99156071	1.56393958
ago4	0.99116545	2.19502113
erf	0.99114441	1.65065804
mecp2	0.99111311	38.6749009
zdhhc15b	0.99090374	4.27276771
map1sb	0.99082125	5.04991096
abi2b	0.99072228	1.69961379
xirp1	0.99059602	1.75159236
akap1b	0.9900875	1.44567166
cryba1a	0.98994725	1.54555777
crygm2d20	0.98980548	1.50404838
si:ch73-134f24.1	0.98963798	3.79514899

Table A1.1: Continued

Gene ID	PPDE	PostFC
BX548028.1	0.98945111	3.49002902
kaznb	0.98896385	2.9465309
rpp25l	0.98893984	1.48102682
MFAP4 (1 of many)	0.99437498	5.34202918
dhrs13a.1	0.99434608	1.52869638
cryba1a	0.99426025	1.81056152
CASKIN2	0.99414096	2.2137431
irf6	0.99390149	1.44744897
selm	0.99383238	1.70120157
crybb1l3	0.99371216	2.97624852
NPNT (1 of many)	0.99362616	1.95726061
zer1	0.99360223	2.80517208
si:dkey-31f5.11	0.99353156	11.1294797
trap1	0.99346372	1.77854316
ddx3b	0.99333702	1.75648871
hnrpkl	0.99332646	2.45360045
fam198a	0.99303582	2.13154654
si:ch211-284e13.4	0.99283436	8.43875312
crygm2d4	0.99275242	1.46073229
uxt	0.99233654	1.60243282
zgc:101858	0.99209436	1.45613599
taf9	0.99204649	1.97353727
si:ch211-173d10.1	0.99199547	1.68915066
slc5a8	0.99166367	2.12299005
ngfb	0.99166004	1.44577767

Table A1.1: Continued

Gene ID	PPDE	PostFC
arhgef37	0.99164547	1.562217
rpl22	0.99163915	3.13135745
ppp1r13bb	0.99156071	1.56393958
ago4	0.99116545	2.19502113
erf	0.99114441	1.65065804
mecp2	0.99111311	38.6749009
zdhhc15b	0.99090374	4.27276771
map1sb	0.99082125	5.04991096
abi2b	0.99072228	1.69961379
xirp1	0.99059602	1.75159236
akap1b	0.9900875	1.44567166
cryba1a	0.98994725	1.54555777
crygm2d20	0.98980548	1.50404838
si:ch73-134f24.1	0.98963798	3.79514899
BX548028.1	0.98945111	3.49002902
kaznb	0.98896385	2.9465309
rpp25l	0.98893984	1.48102682
grem2b	0.98840721	1.6401085
stat5b	0.98818129	2.2384188
trmt2b	0.98799964	1.62792379
asb8	0.98763456	6.32303274
hsc70	0.98739015	1.49960826
cyp26a1	0.98733145	1.64335689
rpl37	0.98725961	2.92008536
si:ch211-28p3.4	0.98701276	3.0210299

Table A1.1: Continued

Gene ID	PPDE	PostFC
zgc:136439	0.98694594	9.58528702
dnaaf2	0.98686954	4.10438419
iqcb1	0.98647642	14.8057006
crygm2d10	0.98626777	1.92092397
btr22	0.98577043	8.44109199
rcn3	0.98499508	1.56897787
ca14	0.9848079	1.7047417
si:ch73-281n10.2	0.98456979	2.76853798
si:dkeyp-89c11.3	0.98431684	1.92360526
agla	0.98413602	1.98005925
zgc:153116	0.98400883	1.70434076
ctbp2a	0.98383447	1.53984914
micu2	0.98366744	1.7372849
clec19a	0.98189703	1.45307978
emc9	0.98158258	1.74015908
nrp1b	0.98123275	1.55739945
gulp1b	0.98112447	1.62498013
ccni	0.98083135	1.5056777
bmp7b	0.98074939	2.11860707
cyb5a	0.98040352	13.7938711
eef2a.1	0.98013775	1.4510759
zgc:172121	0.98000405	1.82363909
tfg	0.9798687	1.58011965
fblim1	0.97979129	1.77328086
abl1	0.9794695	1.50009617

Table A1.1: Continued

Gene ID	PPDE	PostFC
cep19	0.97874227	2.4618082
doc2d	0.97848231	3.49920863
znf1073	0.97838562	2.16310443
CABZ01085201.1	0.97830492	2.96636405
tfeb	0.97829145	1.46413418
acp6	0.97792259	1.5256828
znf1118	0.97774921	3.39687326
ilf3a	0.97707425	1.84330217
ptrh2	0.97704389	1.5029118
tgm1	0.97657977	1.5338101
pdlim2	0.9759612	1.59719201
secisbp2	0.97592857	25.5378271
RCCD1 (1 of many)	0.97539801	1.68445582
vac14	0.97488809	5.93408401
zgc:66474	0.97372109	3.39204342
olfml2bb	0.97371175	2.82580675
CABZ01075923.1	0.97274973	2.26923045
tfdp1b	0.97245876	1.55551519
abca4a	0.97225083	4.7715995
CR589875.3	0.97170361	2.75512657
atrn	0.97145862	4.66187743
CABZ01055168.2	0.9714083	1.63583948
cmc2	0.97050977	1.70432897
arv1	0.96991978	1.48332418
CABZ01065076.1	0.96937527	2.19358276

Table A1.1: Continued

Gene ID	PPDE	PostFC
hipk1a	0.96877742	1.8625903
si:ch211-223a10.1	0.96857825	5.35573704
znf1152	0.9676443	3.63460721
ggps1	0.96751221	3.70570249
fam173a	0.96744173	3.86747503
crygm2d3	0.96695004	1.60396175
dnmt3bb.3	0.96686231	2.6999396
CU693379.1	0.96668328	1.52661285
tagapb	0.9654193	1.83986801
glb1l	0.96497259	1.85660888
twistnb	0.96435182	1.77734076
ndnl2	0.96381045	2.85173594
si:dkey-82i20.1	0.96380499	2.62985496
kaznb	0.96334556	2.02298041
anapc4	0.9631407	1.56027347
cln8	0.96289215	13.4774094
zgc:112052	0.96139714	1.44930654
zgc:171727	0.96086624	1.70111235
fam49ba	0.95946633	1.855808
tpcn1	0.95910115	1.48385356
wdr48a	0.9589923	1.62285736
cluap1	0.95827713	2.61477459
zdhhc7	0.95786733	1.50000559
flnca	0.95758306	3.23763588
thumpd3	0.95686314	1.50815049

Table A1.1: Continued

Gene ID	PPDE	PostFC
slc2a3a	0.95601753	3.34083472
znf1166	0.95598227	4.55499374
frs2a	0.95597591	2.09852415
derl3	0.95435887	1.62321733
ctnna2	0.95395215	2.04026997
csnk2b	0.95359456	2.18662568
cdk4	0.95316458	2.45041839
stat6	0.9526223	2.48125567
map7d1a	0.95201836	2.85615694
dclk2a	0.95168893	3.23282027
txn2	0.95167271	1.95248048
spag9a	0.95122725	1.46292078
zgc:113314	0.95026817	4.54549698
gcnt4a	0.94979986	1.48342598
hccsa.1	0.9496067	1.4601552
si:dkey-245p14.7	0.9489146	1.45676336
sowahab	0.94813264	2.1742691
tshr	0.94716513	2.05431466
gpr31	0.94647795	13.2846251
zfand5b	0.94560466	2.34123755

Table A1.2: Up-regulated genes in pax2 mutants

Gene ID	PPDE	PostFC
gsta.1	1	0.00605684
gmnn	1	0.00236076
col11a1a	1	0.00254868
fubp3	1	0.0031324
ublcp1	1	0.00443801
smarcal1	1	0.00462374
pde6g	1	0.02375396
tbc1d7	1	0.0062857
aldh2.2	1	0.03090445
scg5	1	0.00674314
ggact.3	1	0.00719755
srek1	1	0.00643062
nppa	1	0.01164394
kat5b	1	0.04170289
ahsa1a	1	0.00758063
eed	1	0.0080722
zer1	1	0.02303175
dpf3	1	0.00797029
tdrd3	1	0.00932432
pcbp3	1	0.01034905
mhc1ula	1	0.01467228
nefmb	1	0.01010116
si:ch211-24o10.6	1	0.01057941
acox3	1	0.01163691
ppdpfa	1	0.12514072

Table A1.2: Continued

Gene ID	PPDE	PostFC
polh	1	0.03515468
lin37	1	0.01228555
si:dkey-71b5.3	1	0.01294887
brf2	1	0.05558196
dclk2a	1	0.01219264
rnf17	1	0.01389209
sema3gb	1	0.015136
si:ch211-125e6.8	1	0.03272142
zgc:172253	1	0.01342178
rfx1a	1	0.01294848
anxa11b	1	0.04866037
si:dkey-147f3.4	1	0.02478841
actr2b	1	0.03317023
anxa3a	1	0.00550592
si:dkey-271j15.3	1	0.04660447
si:dkey-26g8.4	1	0.00829112
slc16a3	1	0.00965152
CR550302.3	1	0.01057006
trrap	1	0.21584799
irf6	1	0.01398657
si:dkey-207l24.2	1	0.05698701
nedd1	1	0.07552394
si:dkey-121n8.8	1	0.10626453
zfr	1	0.01319333
si:ch211-149k12.3	1	0.07293431

Table A1.2: Continued

Gene ID	PPDE	PostFC
mhc1uma	1	0.06937348
igfbp6b	1	0.07147004
prkcq	1	0.07391903
tnnt2a	1	0.08817417
emc4	1	0.0895896
adh8b	1	0.11792317
si:ch211-181d7.3	1	0.12295161
prl	1	0.12017863
zgc:195023	1	0.12569586
DNAH10	1	0.16942855
znf1105	1	0.13822185
aldh2.2	1	0.15241552
fancl	1	0.1444089
znf1048	1	0.16402274
plin2	1	0.16403027
znf1034	1	0.18687438
gsta.2	1	0.18085137
si:dkey-5i16.5	1	0.18748923
zgc:173714	1	0.20999774
si:ch211-160d14.15	1	0.22822963
eef1db	1	0.22287253
ntrk3a	1	0.27797563
zgc:174703	1	0.29096933
tert	1	0.28974784
arl13a	1	0.31013017

Table A1.2: Continued

Gene ID	PPDE	PostFC
si:ch1073-190k2.1	1	0.30376193
il1rapl1a	1	0.3123487
si:ch1073-340i21.3	1	0.31130225
si:ch211-108d22.2	1	0.31005669
CR792418.2	1	0.33536041
srsf2b	1	0.32807851
tbc1d7	1	0.32250552
zgc:158803	1	0.33672707
scg2a	1	0.35062128
KRTCAP2 (1 of many)	1	0.35836328
tenm1	1	0.37730235
rcvrn2	1	0.39002411
nucb1	1	0.39293702
atp1b1b	1	0.43567966
RNPS1 (1 of many)	1	0.44174727
myl9b	1	0.45103869
adamts1	1	0.44705479
slc43a2a	1	0.46419371
agtr2	1	0.46218335
zgc:194627	1	0.48479429
BX936382.1	1	0.48711738
BX324003.1	1	0.4915192
abat	1	0.49261779
adh8b	1	0.50732741
ACTC1 (1 of many)	1	0.07224994

Table A1.2: Continued

Gene ID	PPDE	PostFC
znf979	1	0.18126761
nkx2.4a	1	0.2021106
GUCY2C (1 of many)	1	0.3443919
nub1	1	0.14429663
uts1	1	0.06183254
nup43	1	0.11502627
eno1b	1	0.07687637
si:dkeyp-4c4.1	1	0.36378464
phka2	1	0.50035147
slc16a9b	1	0.17178494
htr2aa	1	0.01643461
si:dkey-45h7.1	1	0.47751149
slc43a2a	1	0.30613397
capn12	1	0.3479607
hsbp1b	1	0.05548599
mt2	1	0.26694464
f8	1	0.16074891
BX324179.3	1	0.33614006
BX901907.6	1	0.26215142
slc1a4	1	0.15797326
znf995	1	0.32190552
fgfr1bl	1	0.3510277
ccdc177	1	0.44522542
slc2a3a	1	0.4137739
si:dkey-147f3.4	1	0.0837128

Table A1.2: Continued

Gene ID	PPDE	PostFC
lgals1l1	1	0.37934349
znf1147	1	0.08193842
si:dkey-242h9.3	1	0.2540002
si:ch211-223a21.4	1	0.36493309
CR749167.2	1	0.10761652
disc1	1	0.01686798
CABZ01074309.1	1	0.31134412
CABZ01059415.2	1	0.09291659
si:dkeyp-94g1.1	1	0.01445691
grid2ipb	1	0.38371713
add2	1	0.50906471
rps25	1	0.17436522
serpinb1l2	1	0.17340022
CR792418.1	1	0.34514169
flnca	1	0.01318045
BX663613.2	1	0.31368995
znf1121	1	0.10248789
znf395b	1	0.51509725
si:ch211-223a21.6	1	0.01746367
CDHR1 (1 of many)	1	0.22887757
theg	1	0.01879636
zgc:174224	1	0.42871578
srsf2a	1	0.06525884
si:dkey-6f10.5	1	0.29589366
dhdhl	1	0.48421107

Table A1.2: Continued

Gene ID	PPDE	PostFC
aptx	1	0.19691078
ch25hl1.1	1	0.33840597
clcn2c	1	0.26789997
gcdhb	1	0.24512506
znf1062	1	0.20305682
si:ch1073-296i8.2	1	0.52581858
tpi1b	1	0.01904369
epb41l3a	1	0.46450579
atp1a1a.2	1	0.36962255
kctd7	1	0.40297206
gpr19	1	0.26318709
nrxn3a	1	0.13405496
acot11b	1	0.18663379
CABZ01088933.1	1	0.45514622
cldn7b	1	0.16934132
si:ch211-111e20.1	1	0.19462454
nup205	1	0.39737498
opn1lw2	1	0.23384836
cgnb	1	0.21116152
mybpc3	1	0.12868531
CR792418.3	1	0.31223861
si:ch211-198c19.3	1	0.22238102
si:ch211-207i1.2	1	0.25235196
BX000534.1	1	0.00372337
CU207221.1	1	0.2039744

Table A1.2: Continued

Gene ID	PPDE	PostFC
si:dkey-122c11.8	1	0.31334123
BX649341.2	1	0.35945158
nppb	0.99999999	0.01627465
BX323994.1	0.99999999	0.1114317
otpb	0.99999999	0.45651345
si:ch211-256e16.11	0.99999999	0.1622364
anxa1b	0.99999999	0.5166512
tpm4a	0.99999999	0.1624046
map1lc3b	0.99999999	0.53569482
tnni1b	0.99999999	0.09825563
si:dkey-112g5.13	0.99999999	0.18950452
si:dkey-16p6.1	0.99999999	0.18928537
lingo2a	0.99999998	0.36833509
zgc:174855	0.99999998	0.00604256
FKBP15 (1 of many)	0.99999998	0.12550064
rock2b	0.99999998	0.13597191
si:dkey-84j12.1	0.99999998	0.41554627
hspb11	0.99999997	0.05682637
hydin	0.99999997	0.01887102
slc8a1a	0.99999997	0.29133813
si:dkey-269i1.4	0.99999997	0.00595867
gnb2l1	0.99999997	0.47063333
aspg	0.99999997	0.44627924
astn1	0.99999997	0.27853299
dap1b	0.99999997	0.19655153

Table A1.2: Continued

Gene ID	PPDE	PostFC
kiaa0907	0.99999996	0.07222343
irbp	0.99999996	0.39165389
znf1106	0.99999996	0.44388768
BX957278.1	0.99999996	0.49481015
impg2b	0.99999995	0.19513826
npdc1a	0.99999995	0.49223924
nsmfb	0.99999995	0.49570044
cx43	0.99999995	0.02002255
he1b	0.99999994	0.00536729
si:dkey-26g8.4	0.99999993	0.00742039
vmhcl	0.99999992	0.16366526
si:ch211-197e7.3	0.99999991	0.52009958
f2r	0.99999991	0.48535001
rps6kl1	0.99999989	0.20512967
nrxn2b	0.99999987	0.33225849
si:dkeyp-82a1.1	0.99999987	0.01904509
cmlc1	0.99999987	0.11093626
si:dkey-92j16.2	0.99999987	0.27043652
znf1157	0.99999986	0.24069362
tor4aa	0.99999986	0.18322423
CT027772.3	0.99999985	0.29867134
pcloa	0.99999984	0.43372962
fam184a	0.99999983	0.26126644
42796	0.99999982	0.53660844
atp1a3b	0.99999981	0.47172488

Table A1.2: Continued

Gene ID	PPDE	PostFC
BX571711.1	0.99999976	0.32284419
pcdh1g18	0.99999976	0.42250717
zgc:174154	0.99999976	0.00804295
thbs4b	0.99999975	0.23118379
znf977	0.99999974	0.34438838
fhl2a	0.99999973	0.45685578
scn4ba	0.99999972	0.07022859
he1a	0.99999969	0.00819939
dnph1	0.99999968	0.35437231
si:dkey-26g8.5	0.99999961	0.01032659
si:dkey-7j14.5	0.99999954	0.18644607
si:dkey-239j18.3	0.9999995	0.0075251
junbb	0.99999943	0.43790282
ctslb	0.99999942	0.00889435
znfl1	0.99999941	0.20701605
cfap36	0.99999935	0.01958596
gngt2a	0.9999993	0.4050215
znf1119	0.99999925	0.46128681
prpf3	0.99999923	0.50640869
micu3b	0.99999908	0.46813479
syt1a	0.99999904	0.52186761
si:dkey-26g8.4	0.99999904	0.00925787
gpr22a	0.99999888	0.24416183
si:dkey-81e3.2	0.99999882	0.52677003
si:ch211-181d7.1	0.99999879	0.04530496

Table A1.2: Continued

Gene ID	PPDE	PostFC
cstf2	0.99999877	0.45558629
pdcb	0.9999986	0.26736076
tspan2b	0.99999858	0.51315374
nek7	0.99999857	0.32629349
he1a	0.9999983	0.00762769
npc1	0.99999825	0.01955754
ahdc1	0.99999821	0.5379481
si:ch211-214b16.3	0.99999815	0.29170238
si:ch73-14h1.2	0.99999801	0.18166907
cnksr2b	0.99999781	0.46450493
acin1a	0.99999777	0.02079049
zgc:174855	0.9999976	0.01367869
CR388363.1	0.99999758	0.51692887
c1qtnf4	0.99999741	0.38287378
syngr3a	0.99999728	0.45035044
eif3c	0.99999686	0.48468976
lrfn2b	0.99999684	0.44072086
gsta.1	0.99999647	0.16304539
zgc:172075	0.99999637	0.24973437
CT956057.1	0.99999628	0.17513741
fxyd6l	0.99999607	0.14701245
ndfip1l	0.99999595	0.36873527
si:ch211-223a21.6	0.99999568	0.37847979
CABZ01032454.1	0.99999513	0.21525651
aanat2	0.99999494	0.53106594

Table A1.2: Continued

Gene ID	PPDE	PostFC
ptprna	0.99999404	0.23099451
sez6l	0.99999386	0.14239586
CR847893.3	0.99999384	0.1665221
fam20a	0.99999377	0.12860207
adar	0.99999348	0.44769287
gle1	0.99999335	0.00801162
sall1a	0.99999331	0.51108119
nadl1.2	0.99999309	0.41834251
rfng	0.99999263	0.14409881
slco5a2	0.99999146	0.53376039
ggact.2	0.99999062	0.19809603
opn1sw1	0.99999056	0.13566756
myl7	0.99999004	0.09274435
bmp7b	0.9999898	0.30189624
nr4a2a	0.99998928	0.17682409
c1galt1a	0.99998925	0.33147259
si:ch211-194h1.2	0.99998909	0.29492706
zgc:174153	0.99998908	0.01571141
mybpc3	0.99998905	0.11037837
BX548044.7	0.99998835	0.05211966
p2ry11	0.99998699	0.15300167
BX511155.1	0.99998606	0.53358307
si:ch211-113d22.2	0.999986	0.37050545
gnb3b	0.99998556	0.02068565
si:ch211-145h19.3	0.9999848	0.39354973

Table A1.2: Continued

Gene ID	PPDE	PostFC
si:ch1073-155h21.2	0.99998443	0.3588151
sh2b1	0.99998437	0.3860128
fn1b	0.99998428	0.14378086
apobb.1	0.99998229	0.09242128
si:dkey-16b10.2	0.99998093	0.25532652
TTC9	0.9999809	0.52745814
slc43a3a	0.99998036	0.4935222
setd8b	0.99997993	0.28637834
abcb4	0.99997919	0.47901977
lca5	0.99997904	0.02063078
si:dkey-269i1.4	0.99997904	0.01903747
RAC1 (1 of many)	0.99997904	0.32246713
BX324179.1	0.99997888	0.40549971
gria3a	0.99997813	0.34424777
cdkl5	0.99997803	0.420323
plgrkt	0.9999778	0.38095655
col17a1b	0.99997729	0.01314006
si:dkey-286j17.4	0.9999772	0.32145018
atp6v0a1b	0.99997637	0.44181414
oxr1b	0.99997633	0.19362888
zp2l2	0.9999743	0.02199306
si:ch211-256e16.11	0.99997352	0.13986696
he1b	0.99997258	0.02282588
luzp2	0.99997139	0.35329778
hhla2a.2	0.99997104	0.30281634

Table A1.2: Continued

Gene ID	PPDE	PostFC
si:ch1073-127d16.1	0.99997043	0.32632915
pnp5b	0.99997025	0.29533656
nrxn2a	0.99996873	0.4250459
si:ch1073-366l7.1	0.99996727	0.37106907
prickle2b	0.99996598	0.21852975
aatkb	0.99996537	0.23448957
CR847850.1	0.99996514	0.17674901
bc2	0.99996495	0.05986953
si:ch211-93f2.1	0.99996077	0.50500491
myom1b	0.99995932	0.39651079
fn1b	0.99995762	0.11232947
u2af2b	0.99995593	0.31532612
BX914205.3	0.99995509	0.10837343
adgrb3	0.99995467	0.18501697
BX640584.2	0.99995417	0.53284409
BX322541.1	0.99995356	0.31353973
si:ch211-165i18.2	0.99995176	0.18903043
CR931788.1	0.99995172	0.24675288
atp5o	0.99995136	0.20038995
mpp3a	0.99995021	0.52516293
CABZ01002768.1	0.99994937	0.22169614
arrdc3a	0.99994648	0.51975915
mtmr1a	0.99994502	0.28070692
pou3f3a	0.99994433	0.44230918
zgc:110821	0.99994034	0.49414883

Table A1.2: Continued

Gene ID	PPDE	PostFC
BX000703.1	0.99993805	0.34392657
srsf7a	0.99993709	0.01527172
vipas39	0.99993582	0.36641068
gsta.2	0.99993502	0.23226863
atp1a1a.3	0.99993282	0.40810091
git2b	0.99993176	0.16288131
mapta	0.99992941	0.51561394
si:dkeyp-9d4.3	0.99992788	0.41909251
AL928808.1	0.99992644	0.14391856
arr3b	0.99992288	0.25712168
si:ch211-282j17.13	0.99991595	0.04561393
si:ch211-235m3.10	0.9999129	0.51852354
dnase1l4.2	0.99991105	0.05647451
mfap4	0.99991046	0.35300431
eef1db	0.99991019	0.46422003
fli1b	0.99990926	0.01652762
trpm1a	0.99990064	0.4800735
CR388165.2	0.99990014	0.24042398
gnaq	0.99989913	0.33903861
si:dkey-14k9.2	0.99989605	0.42620912
RASSF5	0.9998929	0.02427608
commd1	0.99988542	0.1763567
LHX3	0.99988166	0.51142684
snrnp35	0.99987969	0.43557735
si:dkey-19a16.7	0.99987202	0.07018983

Table A1.2: Continued

Gene ID	PPDE	PostFC
nrgna	0.99986854	0.36166558
CR361561.1	0.99986302	0.53207609
apof	0.99986096	0.14434438
#N/A	0.99985941	0.32650324
ppp3r1a	0.99985049	0.07054015
si:dkey-103d23.5	0.99984223	0.06579386
cbx5	0.99983682	0.23748332
ppfia3	0.99982417	0.48046714
chd	0.9998145	0.50444185
ilf3a	0.99979959	0.35162936
camta1b	0.9997943	0.50547858
trip10a	0.99979284	0.08712916
fgfr1bl	0.999784	0.07293974
MREG	0.99978366	0.32333976
tmem151a	0.99978327	0.45913585
ctslb	0.9997776	0.01053025
si:dkey-16p19.1	0.9997757	0.11990754
galnt13	0.99977564	0.49255122
gnb5b	0.99976854	0.40939435
ogfrl2	0.99976392	0.30383139
BX005448.1	0.99976207	0.51731988
kcnn3	0.99975601	0.43523744
pde9a	0.99975099	0.40524452
slc16a9a	0.99975002	0.45470445
si:dkey-265e15.2	0.99974628	0.45671906

Table A1.2: Continued

Gene ID	PPDE	PostFC
si:dkey-63j12.4	0.99974299	0.27294906
BX548067.2	0.99972938	0.41980011
BX571760.1	0.99972549	0.35638927
si:dkey-265c15.6	0.99972421	0.2317945
kbtbd7	0.99972157	0.02098151
zfpm2a	0.99971423	0.12914748
adcy8	0.99971032	0.44743017
cyp2p7	0.9996982	0.14511267
tbkbp1	0.9996973	0.32085361
znf995	0.99969253	0.33400782
si:dkey-207m2.4	0.99969194	0.10649332
pde6c	0.99967916	0.43102165
pik3ip1	0.99965659	0.40449202
CABZ01055017.1	0.99965531	0.16724577
CR450780.5	0.99964515	0.15697399
STX3 (1 of many)	0.99964283	0.54176976
CABZ01076666.1	0.99962856	0.03607037
zgc:56585	0.99962397	0.42477835
capgb	0.99962323	0.17859531
pik3ap1	0.99962049	0.2788905
pcnxl2	0.99961905	0.40958864
si:ch211-111e20.1	0.99960794	0.21902183
smtla	0.99959106	0.13179384
meis3	0.99958584	0.40726959
esr2b	0.99958487	0.19111696

Table A1.2: Continued

Gene ID	PPDE	PostFC
si:rp71-36a1.3	0.99957462	0.12413078
foxp2	0.99957183	0.17788992
si:ch211-233h19.2	0.9995265	0.29795032
gata5	0.9995221	0.22390887
nrg2b	0.99952022	0.49071232
mamdc2b	0.99951438	0.20066243
palmda	0.99949614	0.53539551
zgc:174650	0.99949605	0.46882009
aatka	0.99948406	0.33106956
robo3	0.99947399	0.52580485
arpp21	0.99946131	0.17905093
ubald1a	0.99943311	0.14558743
plch2b	0.99941744	0.29725076
zgc:174862	0.99941116	0.03098591
ska3	0.99940779	0.33853889
TULP2	0.99940681	0.46356169
sypb	0.99940662	0.45209877
si:ch211-160f23.7	0.99940474	0.32220536
BX569782.1	0.99938975	0.11218363
si:dkey-242h9.3	0.9993791	0.24226441
pimr140	0.99937648	0.34795996
actn2b	0.99936892	0.52684436
si:dkey-17o15.2	0.99935655	0.34166514
tlx1	0.99935163	0.32815912
kank1a	0.99934268	0.15567464

Table A1.2: Continued

Gene ID	PPDE	PostFC
glrbb	0.99933051	0.39962525
snap25b	0.99932995	0.52458432
si:dkey-17m8.2	0.99931364	0.16763477
and1	0.99929729	0.44088156
si:ch211-137i24.12	0.99922915	0.30406675
CR361561.2	0.99916814	0.51668512
si:ch211-237i5.4	0.99916601	0.46815971
si:dkey-15j16.6	0.99913094	0.05887786
clstn2	0.99910238	0.40919186
fmr1	0.99908162	0.05598639
rock2b	0.99906025	0.25128439
lcat	0.99905384	0.41946461
pgap2	0.99902124	0.18219928
rtn1b	0.99901482	0.14984629
BX548067.4	0.99900623	0.37333621
zgc:172051	0.99896586	0.29981927
upf3a	0.99891803	0.27721657
cyp3c4	0.99891437	0.28911372
gngt1	0.99886624	0.39153483
slc25a23a	0.99885307	0.19903103
zbtb12.1	0.99880117	0.05108555
#N/A	0.99879076	0.29417649
tph1a	0.99876626	0.28592932
gria2a	0.99875441	0.36911053
atp10d	0.99875357	0.53192828

Table A1.2: Continued

Gene ID	PPDE	PostFC
STK19 (1 of many)	0.99874336	0.42211276
gria2a	0.99868907	0.41654551
lin7b	0.99868348	0.42339228
smc1a	0.99865029	0.21612456
si:dkey-33c12.11	0.99860824	0.24289676
CR361547.1	0.99858121	0.54184368
cpeb1b	0.99856564	0.35662865
vmhc	0.99854042	0.3707909
hadhaa	0.99853789	0.02408856
fam118b	0.99849721	0.2936514
si:ch211-198c19.3	0.9984391	0.17071168
sorbs2a	0.99839987	0.07941511
unc5da	0.99834257	0.46699416
nrsn1	0.99833169	0.4815366
tssc4	0.99829327	0.32854313
cep170ab	0.99824139	0.20235369
BX548173.2	0.99822428	0.48671549
BX088603.1	0.99822417	0.37982781
atp2a2a	0.99821767	0.19310722
pofut1	0.99821104	0.39122323
tmem30c	0.99821082	0.49440203
svopl	0.99803434	0.14001985
si:dkey-199m13.5	0.99796626	0.5338679
usp28	0.99796	0.39340668
sorbs2b	0.99792967	0.49360822

Table A1.2: Continued

Gene ID	PPDE	PostFC
prss59.1	0.99789646	0.06478723
cnp	0.99788786	0.29033878
clstn1	0.9977331	0.45891161
olfm1b	0.99770209	0.26797938
si:dkey-16p19.1	0.99769172	0.44490378
grtp1a	0.99765923	0.28861649
anos1a	0.9975957	0.48956643
ankrd6b	0.99757064	0.47614088
necab1	0.99756925	0.1677846
fam210aa	0.99756863	0.33668483
EML5	0.9975263	0.28571868
h6pd	0.99747697	0.08355315
si:dkey-72l14.3	0.9974624	0.32762292
si:dkey-247i3.5	0.99745893	0.23279795
si:dkey-106c17.2	0.9973468	0.06308066
tnni1b	0.99722671	0.14537484
foxi1	0.99721862	0.46869515
smc1a	0.99865029	0.21612456
si:dkey-33c12.11	0.99860824	0.24289676
CR361547.1	0.99858121	0.54184368
cpeb1b	0.99856564	0.35662865
vmhc	0.99854042	0.3707909
hadhaa	0.99853789	0.02408856
fam118b	0.99849721	0.2936514
si:ch211-198c19.3	0.9984391	0.17071168

Table A1.2: Continued

Gene ID	PPDE	PostFC
sorbs2a	0.99839987	0.07941511
unc5da	0.99834257	0.46699416
nrsn1	0.99833169	0.4815366
tssc4	0.99829327	0.32854313
cep170ab	0.99824139	0.20235369
BX548173.2	0.99822428	0.48671549
BX088603.1	0.99822417	0.37982781
atp2a2a	0.99821767	0.19310722
pofut1	0.99821104	0.39122323
tmem30c	0.99821082	0.49440203
svopl	0.99803434	0.14001985
si:dkey-199m13.5	0.99796626	0.5338679
usp28	0.99796	0.39340668
sorbs2b	0.99792967	0.49360822
prss59.1	0.99789646	0.06478723
cnp	0.99788786	0.29033878
clstn1	0.9977331	0.45891161
olfm1b	0.99770209	0.26797938
si:dkey-16p19.1	0.99769172	0.44490378
grtp1a	0.99765923	0.28861649
anos1a	0.9975957	0.48956643
ankrd6b	0.99757064	0.47614088
necab1	0.99756925	0.1677846
fam210aa	0.99756863	0.33668483
EML5	0.9975263	0.28571868

Table A1.2: Continued

Gene ID	PPDE	PostFC
h6pd	0.99747697	0.08355315
si:dkey-72l14.3	0.9974624	0.32762292
si:dkey-247i3.5	0.99745893	0.23279795
si:dkey-106c17.2	0.9973468	0.06308066
tnni1b	0.99722671	0.14537484
foxi1	0.99721862	0.46869515
ppp1r10	0.9971817	0.31566413
eif3ja	0.99716268	0.10759212
arsh	0.99714327	0.51084012
socs2	0.99707086	0.33862715
zgc:113333	0.99701473	0.48806542
syn2b	0.99697139	0.16181821
CR788231.1	0.99694096	0.46205745
penka	0.99686597	0.24151652
arr3a	0.99674751	0.33671613
rcan3	0.99653441	0.42763208
mdkb	0.99652328	0.4792949
tulp4b	0.99640019	0.3400266
plch2a	0.9963892	0.43414676
si:ch73-366i20.1	0.99626497	0.18688615
pou2f1b	0.9962637	0.02252641
CU570691.1	0.99623741	0.31135079
dnajb4	0.99620725	0.50764527
ildr2	0.99618784	0.429353
tapbp.2	0.99617898	0.28674961

Table A1.2: Continued

Gene ID	PPDE	PostFC
sept9a	0.9961613	0.27769595
hspb7	0.99615524	0.41688574
cdh18a	0.99609341	0.43477686
BX663505.2	0.99605135	0.29371093
rdh5	0.99604646	0.43069853
CR392001.1	0.99598014	0.45047628
nlgn3a	0.99596324	0.50170763
ckba	0.99595455	0.29232671
celsr3	0.99584857	0.53324135
rcvrn3	0.99578257	0.4186381
slc30a8	0.9957401	0.50888327
si:dkey-238i5.3	0.99562058	0.45159519
eef1da	0.99548107	0.42087634
pkd1b	0.99547678	0.17922092
si:ch73-233f7.1	0.99541097	0.27060703
arpc4l	0.99540159	0.33397983
si:ch211-219a15.3	0.99538616	0.02617741
ypel2a	0.99536953	0.47145165
rtkn2a	0.99533576	0.36806433
akap6	0.99516938	0.47976634
cd3eap	0.99499816	0.1297364
ACTC1 (1 of many)	0.99497978	0.12838549
irs2a	0.99496498	0.32848364
snx19a	0.99494703	0.22426436
atp6v0a1a	0.99486819	0.54378237

Table A1.2: Continued

Gene ID	PPDE	PostFC
si:ch211-117l17.4	0.99485799	0.53449259
si:ch1073-416d2.4	0.99481988	0.27280906
CABZ01054391.1	0.99476265	0.54061221
CR450780.3	0.99471676	0.45661858
si:dkey-61n16.5	0.99470348	0.4480572
tanc1a	0.99467751	0.22942662
polh	0.99456912	0.32963852
atp2b3b	0.99453908	0.39885767
si:dkey-15j16.3	0.99451645	0.12377964
mcf2la	0.99446661	0.35998886
impg1b	0.99408334	0.5276069
guk1b	0.99399637	0.3992008
casq2	0.99391508	0.25234985
CR293532.2	0.99382183	0.30193611
MPP4 (1 of many)	0.99368021	0.17820716
zgc:113162	0.99365896	0.54493411
si:ch211-260e23.9	0.99363777	0.38735105
spegb	0.99363588	0.49379843
si:ch211-93f2.1	0.99359625	0.540328
gna15.1	0.99356414	0.41281225
ftr19	0.9934938	0.39801259
dpp6b	0.99332427	0.33522735
znf1051	0.99325023	0.3657999
st8sia5	0.99317221	0.11021142
slc18a3a	0.99304098	0.12690647

Table A1.2: Continued

Gene ID	PPDE	PostFC
serp2	0.99303	0.34916793
fli1b	0.99301507	0.07298589
cep55l	0.99292065	0.25585232
acta1b	0.99281556	0.20926185
rgs8	0.99274697	0.4378912
si:dkey-253d23.3	0.99267489	0.42125889
opn1lw2	0.99261065	0.15683271
fam161b	0.99257004	0.42795112
grm8a	0.99253304	0.44719067
fgfbp2b	0.99242545	0.2897598
rab11bb	0.99220361	0.53381992
twf2b	0.99201412	0.23613863
si:dkey-21e13.3	0.99184247	0.53498727
pou4f3	0.99182861	0.49661927
ccdc25	0.99163652	0.29962577
zgc:162509	0.99146588	0.3126065
tpm4a	0.99145388	0.09958568
42796	0.9912496	0.04546687
si:dkey-222b8.4	0.99113274	0.39885113
hand2	0.9910868	0.47909457
rs1a	0.99088979	0.13095277
chchd6a	0.99060067	0.36740341
tfg	0.9905928	0.26433446
slc38a5a	0.99055222	0.36036061
smpx	0.99048703	0.26622748

Table A1.2: Continued

Gene ID	PPDE	PostFC
zgc:123105	0.98986653	0.24153466
znrf3	0.98983536	0.04391429
zgc:113531	0.98979116	0.51391876
calb1	0.98975339	0.16767843
c3b.2	0.98957542	0.17765725
si:dkey-66l17.4	0.9893992	0.51583976
sult4a1	0.98928161	0.43535851
hdc	0.98896129	0.06750581
si:ch211-79g12.2	0.98892337	0.26166782
cnih3	0.98881535	0.3110016
noto	0.98863457	0.2052465
drgx	0.98843264	0.30796203
alg12	0.98820982	0.29418768
ppp2r2cb	0.98819323	0.51668074
impg2b	0.98818767	0.34561901
oxct1a	0.98811745	0.54101178
vmhcl	0.98809193	0.20945583
si:dkey-33i11.4	0.98763609	0.35345677
s100u	0.98761248	0.37089481
slc25a15a	0.98755591	0.1897895
fn1b	0.98697321	0.1878315
si:dkeyp-72g9.4	0.98672307	0.21862989
nupr1	0.98652818	0.51315228
si:dkey-147f3.8	0.9864812	0.25121241
pcdh2g1	0.98647784	0.48782806

Table A1.2: Continued

Gene ID	PPDE	PostFC
nlgn2b	0.98631225	0.49507378
hn1a	0.98610062	0.44222616
ndufb2	0.98587561	0.49353525
trim46a	0.98561541	0.44012316
lztfl1	0.98558362	0.31935219
znf1031	0.98552297	0.27992984
kcnj13	0.98523455	0.54101153
znf1057	0.98521796	0.25606035
fads2	0.98498678	0.49090429
zgc:113142	0.98476021	0.40221139
wdr48a	0.98473442	0.1353603
nlgn3b	0.98464672	0.28900974
plxna4	0.98455123	0.47478424
arl16	0.98427536	0.54250124
ncapg2	0.9842736	0.38835764
FAM184A (1 of many)	0.98426004	0.53075272
abcg2a	0.9837326	0.02346977
ppifb	0.98334978	0.13571935
si:ch211-157b11.12	0.98296842	0.42474795
pde6h	0.98256823	0.16049071
si:dkey-105e17.1	0.98225519	0.24679011
taf8	0.98192987	0.19510277
CABZ01064771.1	0.98176596	0.37632913
c6	0.98164716	0.42118817
ltk	0.9814763	0.4889662

Table A1.2: Continued

Gene ID	PPDE	PostFC
CR936465.1	0.98135577	0.08774286
zgc:153395	0.98086674	0.23058634
cadm4	0.98058407	0.06138467
camk2n1a	0.98034432	0.41572865
cyp2x7	0.97998169	0.51793515
znf1131	0.97979638	0.4735899
myh7ba	0.97969455	0.22438734
si:dkey-16b10.1	0.97929879	0.44544289
si:ch73-389b16.1	0.97875434	0.23958235
gria4a	0.97861614	0.26259505
itm2ca	0.97753555	0.43704432
cry1ba	0.97666774	0.33856193
znf994	0.97663852	0.46073918
BEGAIN	0.97592993	0.10225209
timp2b	0.97590496	0.52736743
tnk1	0.97588672	0.05899409
si:ch211-129p6.2	0.97586531	0.31341198
ptprea	0.97559587	0.42453101
si:ch211-214b16.4	0.97484417	0.29770599
bub1ba	0.97484319	0.39636886
dhx40	0.97294287	0.30948921
cntn5	0.97287777	0.38254809
iqgap2	0.97247808	0.1843422
rp1l1a	0.97100286	0.40675409
cacng2a	0.97087352	0.4570898

Table A1.2: Continued

Gene ID	PPDE	PostFC
KDELR3 (1 of many)	0.97085599	0.49625291
terf1	0.97057376	0.37724518
zgc:73340	0.96932261	0.31925491
si:dkey-263j23.1	0.96878114	0.32598928
CABZ01075274.1	0.9685992	0.37816227
si:dkey-7i4.1	0.96805313	0.43934928
scg2b	0.96610063	0.41028188
neflb	0.96601728	0.3631633
arrdc3b	0.96542687	0.41347113
gnat2	0.96537125	0.41841261
si:ch73-190f9.4	0.96520906	0.48903437
dusp3a	0.96520644	0.50400501
si:dkey-121n8.7	0.9649275	0.26397169
znf1037	0.9644884	0.49286282
wu:fb15h11	0.96443468	0.51443917
dcxr	0.96400181	0.23025058
best2	0.96360649	0.17632091
HAPLN1 (1 of many)	0.96300039	0.53719484
dpf1	0.96269164	0.48531478
txnipb	0.96253993	0.40760013
si:dkey-71l4.4	0.96251744	0.16573605
si:dkey-19b23.7	0.96242286	0.08607903
CU019657.1	0.96148095	0.0815658
tfa	0.96097901	0.05897177
slc6a1a	0.96074925	0.4744116

Table A1.2: Continued

Gene ID	PPDE	PostFC
s100s	0.96023075	0.52694675
stat5b	0.9598209	0.23982466
marveld2a	0.95959336	0.34466221
lactbl1a	0.95938868	0.34126686
zgc:112285	0.95909538	0.48311105
gria3a	0.95878225	0.48271079
znf1045	0.9587422	0.28303742
CABZ01007222.1	0.95873271	0.37222436
wdcp	0.95868921	0.30433753
aldoaa	0.95812396	0.13957413
fam19a5a	0.95732088	0.23665981
flnb	0.95683468	0.48648732
atoh1a	0.95633242	0.46995944
nudt4a	0.95556182	0.05090048
slc25a36a	0.95552038	0.31423411
si:dkey-84j12.1	0.95546887	0.3112841
syncripl	0.95540168	0.53187346
ext1c	0.95491243	0.32431173
stmn4l	0.95463368	0.43816975
si:dkey-92i17.2	0.95445004	0.4047597
slc4a4a	0.9540154	0.49042554
rwdd	0.9535332	0.45741438
lbr	0.95348921	0.07580637
nsfa	0.95291503	0.31128612
trpc1	0.95290547	0.43829102

Table A1.2: Continued

Gene ID	PPDE	PostFC
bmf2	0.95256271	0.34001067
tbk1	0.95190409	0.45565895
si:dkey-179k24.5	0.95178885	0.25049258
sfxn2	0.95168976	0.20745988
tlx2	0.95150031	0.46849491
rptor	0.95087934	0.52624772
spire1a	0.95035563	0.47267528
si:dkey-14o6.8	0.94906939	0.36394209
acp5a	0.94900787	0.398649
ezra	0.94876884	0.29818762
NR4A2 (1 of many)	0.94826882	0.44024088
nlgn4a	0.94822785	0.14391656
nub1	0.94786208	0.53860431
si:ch73-359m17.2	0.94777675	0.20374278
prdm2a	0.94759204	0.41787615
si:dkeyp-35e5.9	0.94744637	0.53169761
serpini1	0.94722541	0.38752968
rac3b	0.94641459	0.10355966
CR450842.5	0.94549936	0.41332942
si:dkey-20i20.10	0.94533106	0.51265615
bves	0.94513289	0.1359183
camkk1b	0.94483436	0.35851054
ppp1r14ba	0.94473267	0.47664948

APPENDIX 2: SUPPLEMENTARY FIGURES

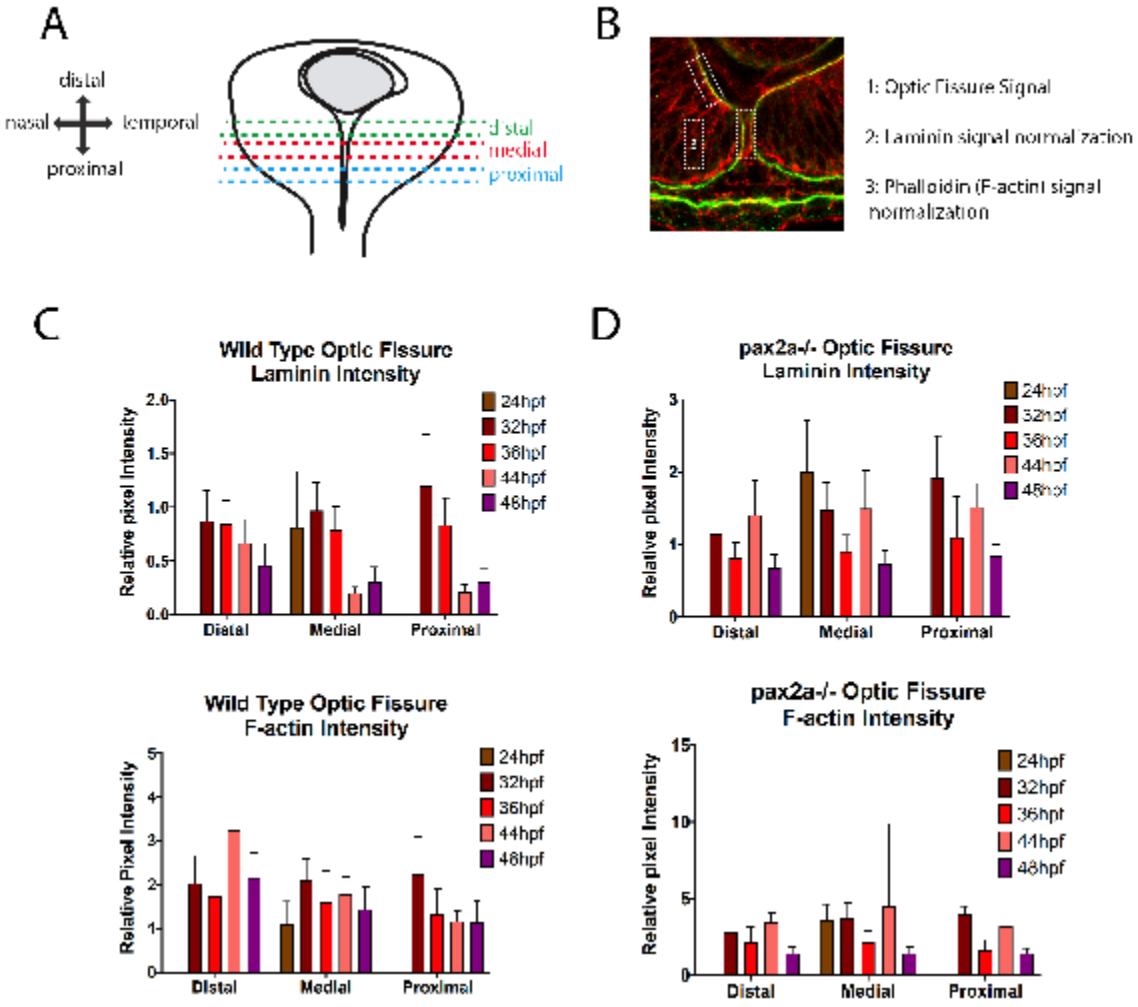

Appendix 2.1: Optic Fissure quantification

A) Graphical representation of the region of OF analyzed using confocal microscopy. **B**) Sample image depicting regions of the OF (1), laminin normalization (2) and F-actin normalization (3) used for signal intensity quantification**. C)** Quantification of laminin and F-actin signal intensity in wild type embryos within the distal, medial and proximal regions of the OF, normalized to regions of laminin staining juxtaposed to the lens and F-actin signal within the lobe of the retina. Relative pixel intensities are displayed. ANOVA $p<0.0001$. **D)** Quantification of laminin and F- actin signal intensity in pax2a$^{-/-}$ embryos within the distal, medial and proximal regions of the OF, normalized to regions of laminin staining juxtaposed to the lens and F-actin signal within the lobe of the retina. Relative pixel intensities are displayed. ANOVA $p<0.0001$.

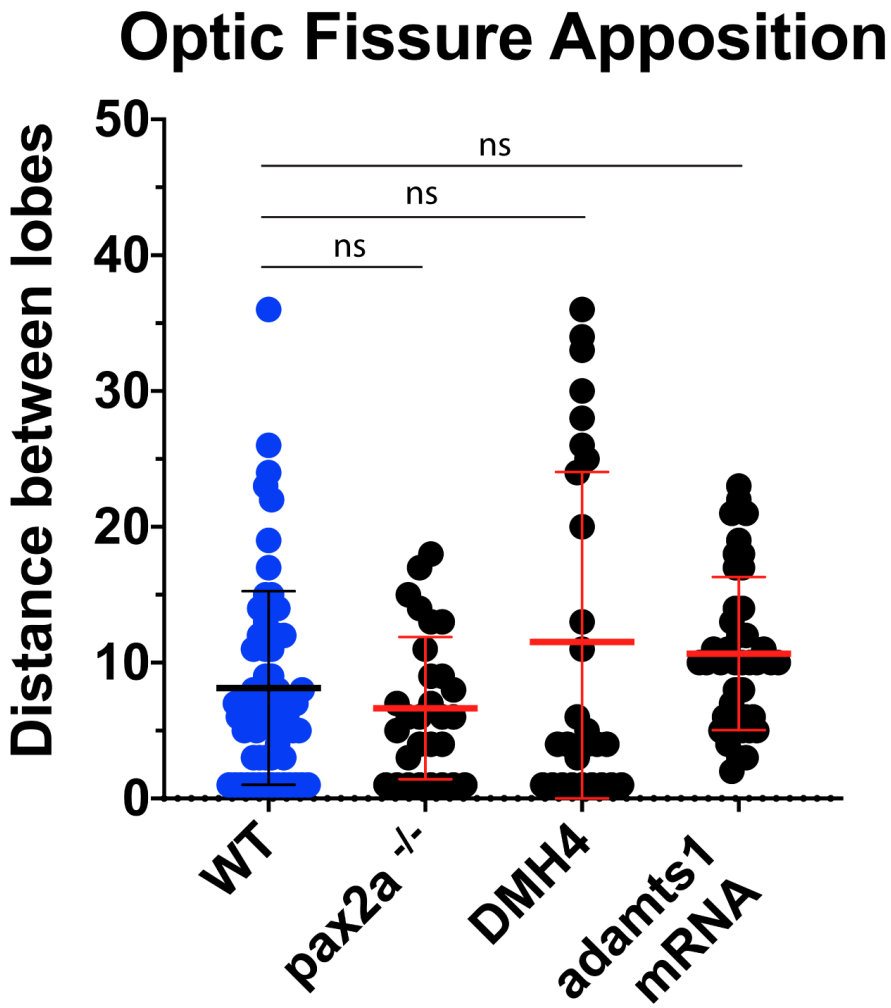

Appendix 2.2: Optic Fissure apposition measurements.
Measurements of the distance between retinal lobes (apposition) in WT, pax2a$^{-/-}$ or DMH4 treated or embryos at 48hpf. Measurements were made using laminin staining as reference for edges of retinal lobes. Distance was measured as pixels.

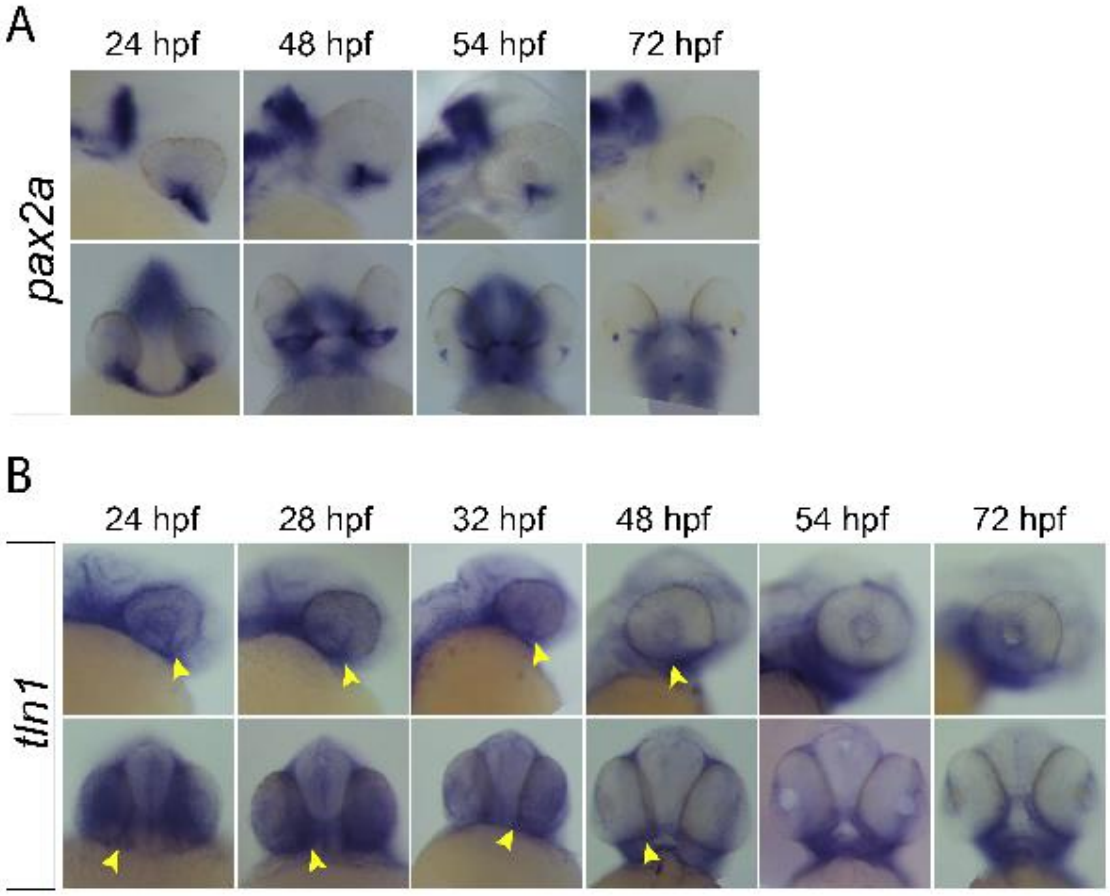

Appendix 2.3: *pax2a* and *tln1* expression during development
A) Whole mount in situ hybridization of *pax2a* probe at 24, 48, 54 and 72hpf. Lateral (top) and ventral (bottom) images depicting OF expression are shown. Pax2a expression persists in the fissure up to 54hpf. **B**) Whole mount in situ hybridization of *tln1* probe at 24, 48, 54 and 72hpf. Lateral (top) and ventral (bottom) images depicting OF expression are shown. *tln1* expression is detected in the OF from 24-48hpf (yellow arrowheads).

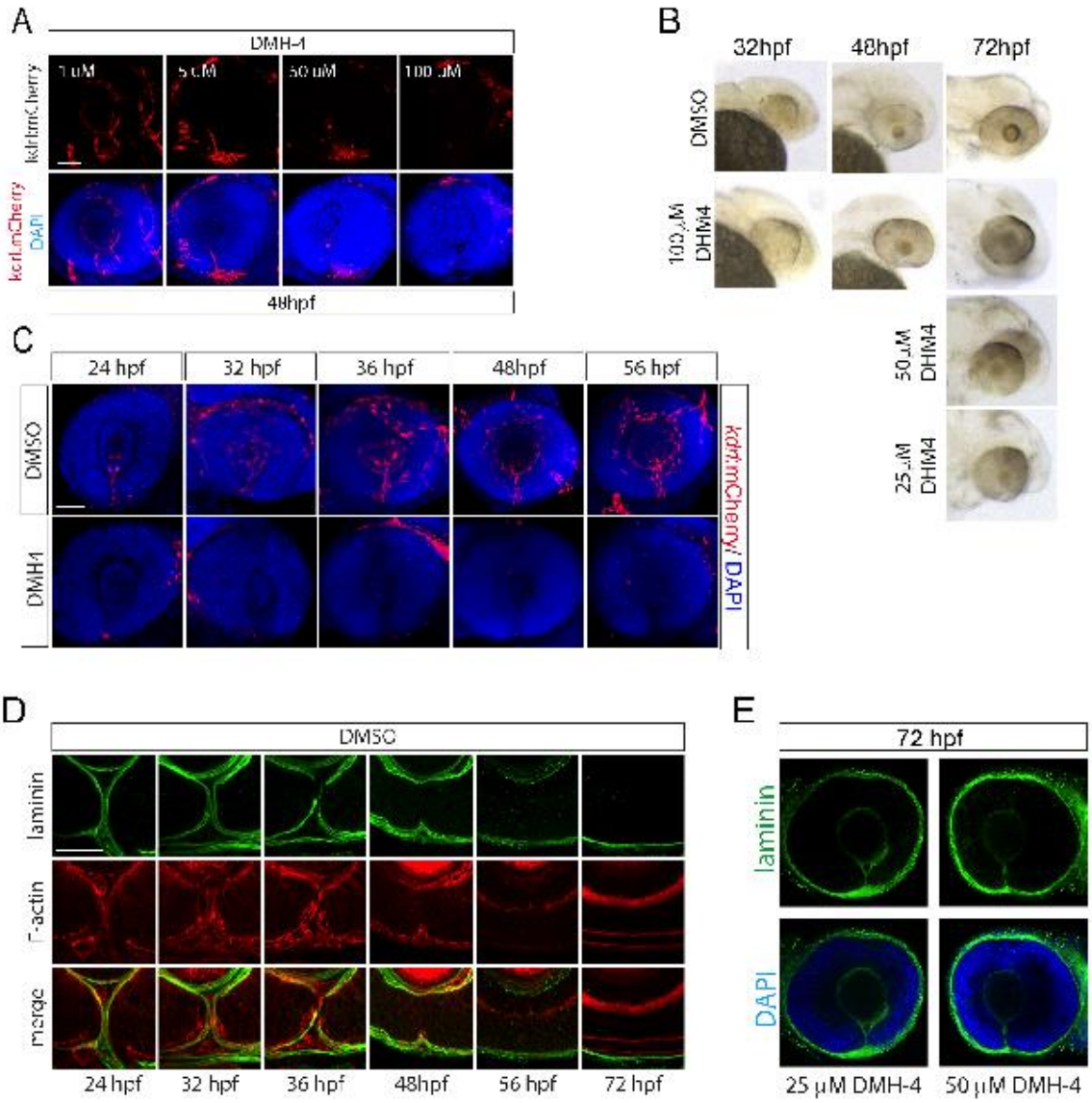

Appendix 2.4: DMH4 dose response

A) 3D reconstructions of 48hpf whole mount Tg[*kdrl*:mCherry] (red) embryos treated with 1, 5, 50 or 100uM DMH4. DNA stained with DAPI (blue). Increasing concentration of DMH4 eliminates mCherry expressing cells from the OF and retina. Scale bar = 50µm. **B)** Brightfield images of DMSO or DMH4 treated embryos at 24, 48 and 72hpf. **C)** 3D reconstructions of whole mount Tg[*kdrl*:mCherry] (red) embryos treated with DMSO or 100µM DMH4 from 12-24, 32, 36, 48 or 56hpf. DNA was stained with DAPI (blue). Scale bar = 50µm. **D)** Whole mount Immunohistochemistry was used to simultaneously visualize F-actin (red) and laminin (green) in DMSO treated embryos from 24-72hpf. Central-proximal regions of the OF are displayed. Scale bar = 50µm. **E)** Whole mount Immunohistochemistry was used to visualize laminin (green) and DNA (blue) 25 or 50µM DMH4 12-72hpf treatment. Central-proximal regions of the OF are displayed. Scale bar = 50µm.

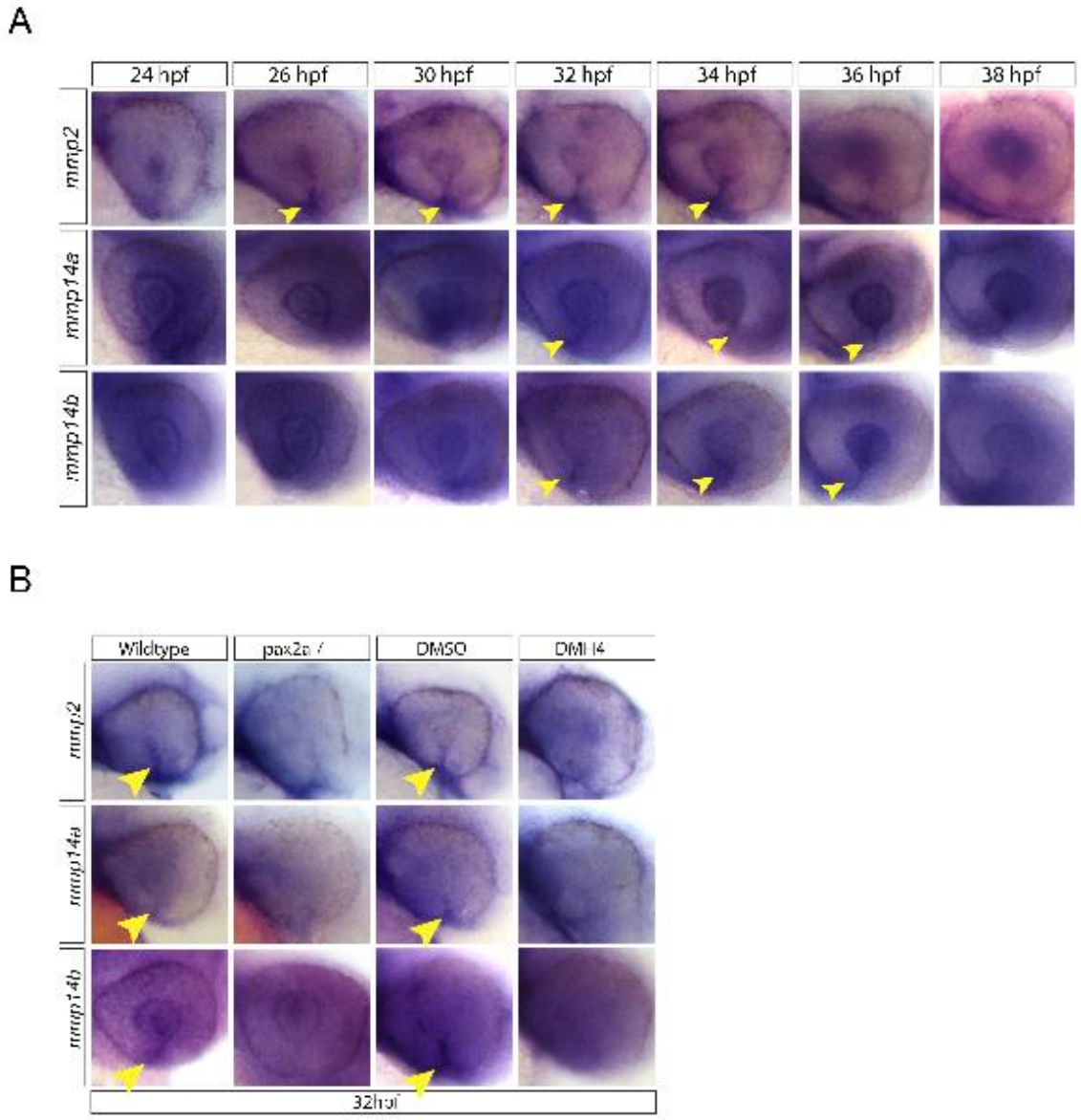

Appendix 2.5: Time course of *mmp2, mmp14a* and *mmp14b* ocular expression
A) Whole mount in situ hybridization of *mmp2, mmp14a, mmp14b* probes at 24, 26, 30 32, 34, 36 and 38hpf. *Mmp2* expression is present in the OF from 26-34hpf (yellow arrowheads). *Mmp14a* expression is present in the OF from 32-36hpf (yellow arrowheads). *Mmp14b* expression is present in the OF from 32-36hpf (yellow arrowheads). **B)** Whole mount in situ hybridization comparing *mmp2, mmp14a* and *mmp14b* expression in WT vs pax2a$^{-/-}$ and DMSO vs DMH4 treated embryos at 32hpf. *Mmp2, 14a and 14b* signal within the OF (yellow arrowhead) appears decreased in pax2a$^{-/-}$ and DMH4 treated embryos.

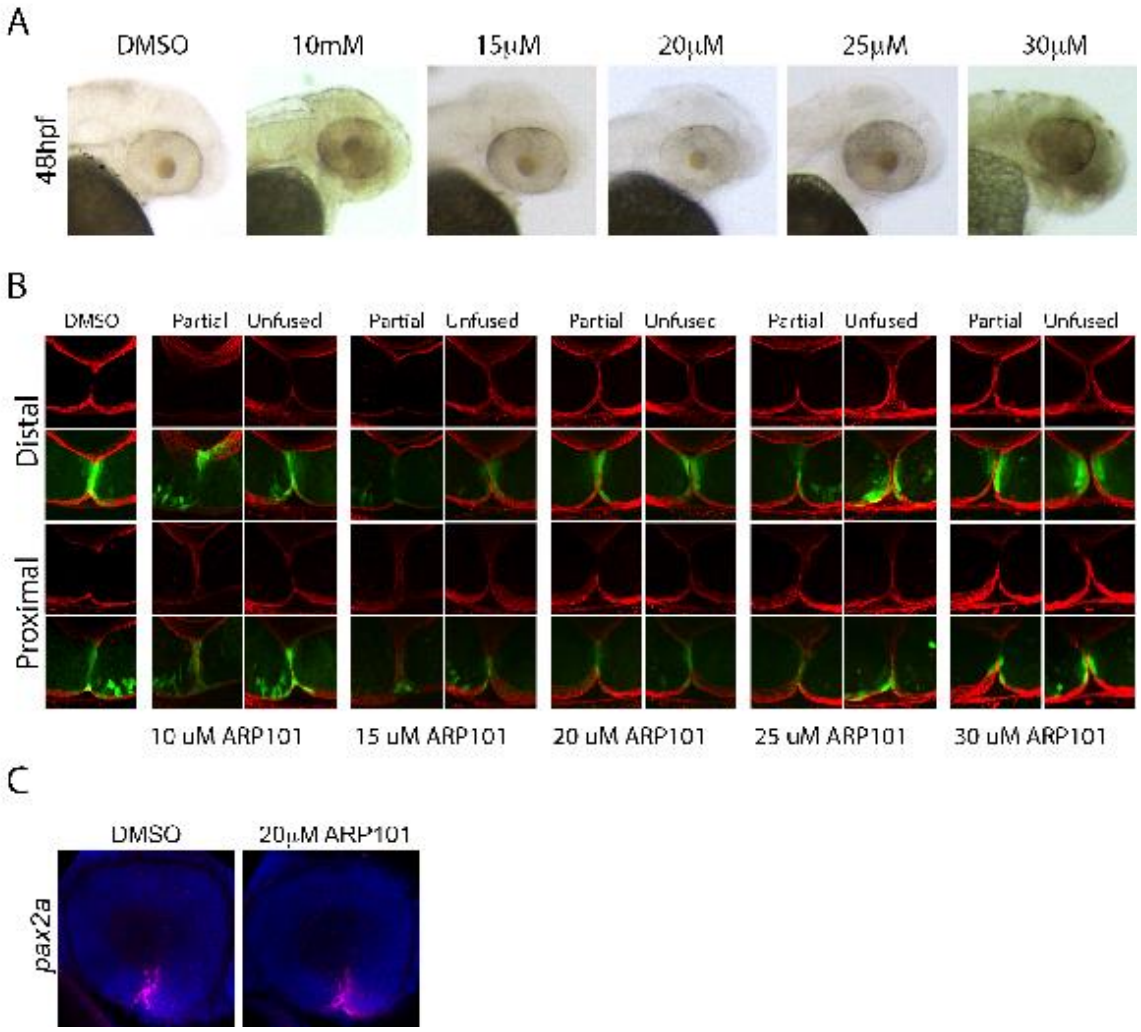

Appendix 2.6: ARP101 treatment dose response
A) Brightfield images of DMSO and ARP treated embryos at 48hpf. Concentrations of ARP101 exceeding 20uM result in toxic effects. **B)** Whole mount Immunohistochemistry was used to visualize laminin (red) in ARP101 treated Tg[*rx3*:GFP] embryos at 48hpf. Central-proximal and distal regions of the OF are displayed. Scale bar = 50µm. **C)** Fluorescent whole mount in situ hybridization of *pax2a* probe at 32hpf in DMSO or 20µM ARP101 treated embryos. OF expression is indicated with a yellow arrowhead. ARP101 treatment does not appear to alter *pax2a* expression in the OF. Broken white lines outline the retinal lobes. Scale bar = 50µm.

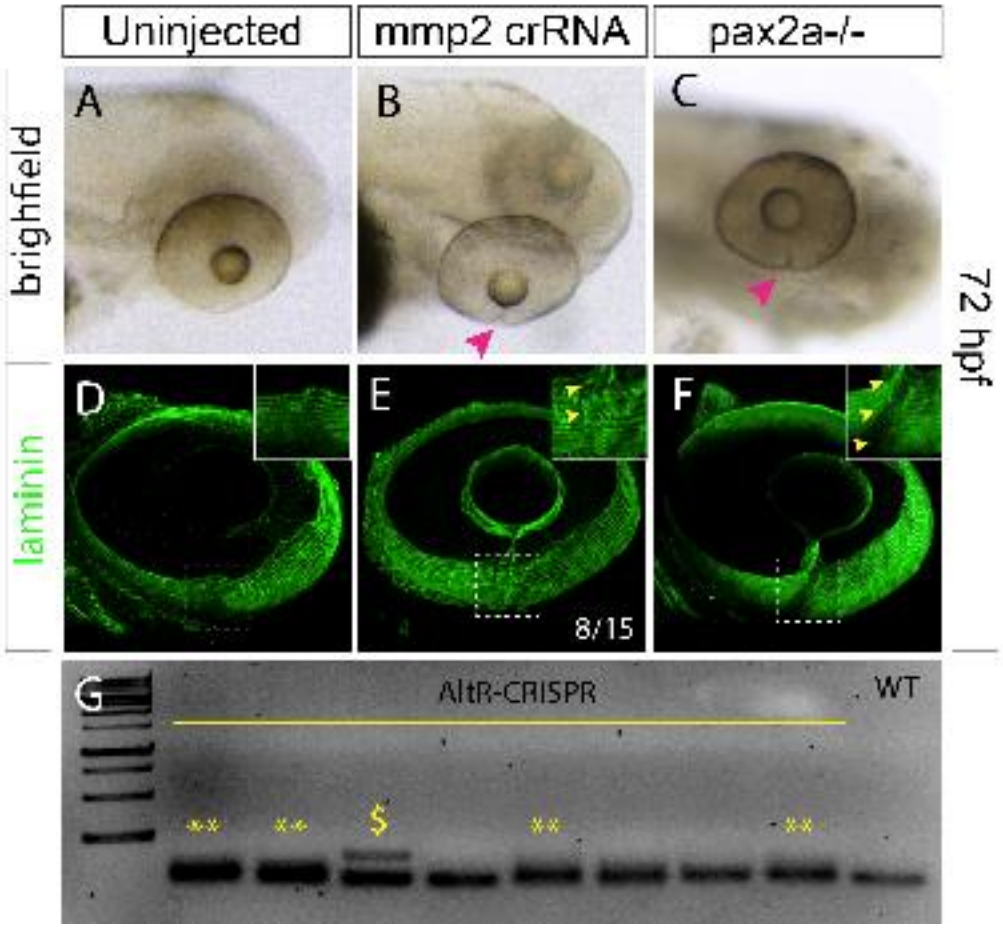

Appendix 2.7: mmp2 Alt-R crRNA injection results in OF fusion failure phenotypes. Brightfield images of **A)** uninjected, **B)** *mmp2* crRNA or **C)** pax2a$^{-/-}$ embryos at 72hpf. OF fusion failure is observed as a notch in the ventral retina in both *mmp2* crRNA injected embryos as well as in pax2$^{-/-}$. Confocal stacks of laminin stained embryos at 72hpf from **D)** uninjected, **E)** *mmp2* crRNA and **F)** pax2a$^{-/-}$ embryos. Pax2a$^{-/-}$ embryos display a clear fissure at 72hpf, while *mmp2* crRNA injected embryos achieve only partial fusion when compared to uninjected controls. **G)** *mmp2* crRNA efficacy was assayed using PCR flanking the region targeted. Lanes 1-8 represent gDNA assays from individual embryos assayed at 72hpf. Control is found in well 9. ** indicate changes in band size compared to control. $ corresponds to embryo imaged in B and E.

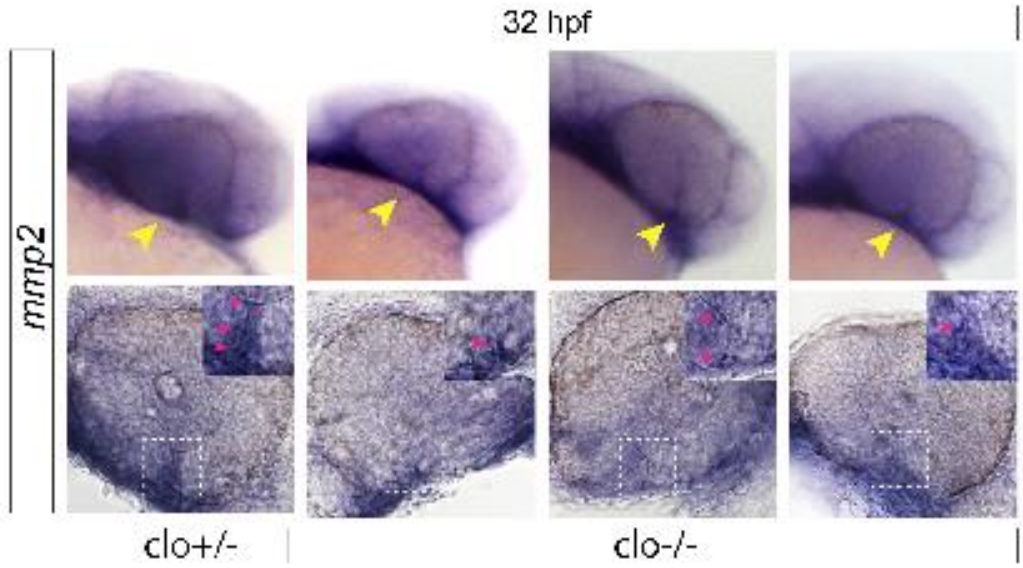

Appendix 2.8: mmp2 expression in *cloche* mutants
Whole mount in situ hybridization of *mmp2* expression at 32hpf in clo$^{+/+}$ and clo$^{m39/m39}$ embryos. Individual dissected eyes were imaged at 20X using DIC optics. Yellow arrowheads indicate OF expression in wholemount samples. Magenta arrowheads indicate expression within the OF as observed at higher magnification in dissected eyes.

APPENDIX 3: TEMPORAL CHARACTERIZATION OF OPTIC FISSURE BASEMENT MEMBRANE COMPOSITION SUGGESTS NIDOGEN MAY BE AN INITIAL TARGET OF REMODELING.

MW Contributions: Figure 5.

Developmental Biology 452 (2019) 43–54

Contents lists available at ScienceDirect

Developmental Biology

journal homepage: www.elsevier.com/locate/developmentalbiology

Temporal characterization of optic fissure basement membrane composition suggests nidogen may be an initial target of remodeling

Nicholas Carrara [1], Megan Weaver [1], Warlen Pereira Piedade [1], Oliver Vöcking, J.K. Famulski [*]

Department of Biology, University of Kentucky, USA

ARTICLE INFO

Keywords:
Basement membrane
Extracellular matrix
Nidogen
Coloboma
Retina
Optic fissure

ABSTRACT

Fusion of the optic fissure is necessary to complete retinal morphogenesis and ensure proper function of the optic stalk. Failure of this event leads to congenital coloboma, one of the leading causes of pediatric blindness. Mechanistically it is widely accepted that the basement membrane (BM) surrounding the maturing retina needs to be remodeled within the fissure in order to facilitate subsequent epithelial sheet fusion. However, the mechanism driving BM remodeling has yet to be elucidated. As a first step to understanding this critical molecular event we comprehensively characterized the core composition of optic fissure BMs in the zebrafish embryos. Zebrafish optic fissure BMs were found to express laminin a1, a4, b1a, c1 and c3, nidogen 1a, 1b and 2a, collagen IV a1 and a2 as well as perlecan. Furthermore, we observed that laminin, perlecan and collagen IV expression persists in the fissure during fusion, up to 56 hpf, while nidogen expression is downregulated upon initiation of fusion, at 36 hpf. Using immunohistochemistry we also show that nidogen is removed from the BM prior to that of laminin, indicating that remodeling of the BM is an ordered event. Lastly, we characterized retinal morphogenesis in the absence of nidogen function and documented retinal malformation similar to what is observed in laminin mutants. Taken together, we propose a model of BM remodeling where nidogen acts as a linchpin during initiation of optic fissure fusion.

1. Introduction

Development of vertebrates requires precise partitioning of developing tissues. This important function is bestowed on the outer covering of developing tissues, the basement membrane (BM). Located at the basal side of every epithelium, basement membranes play important roles in establishing and maintaining tissue borders, cell signaling, and providing biomechanical strength to physiologically active tissues. Comprised of various components specified to differing regions of the embryo, all BMs share a common core of 4 components including laminin, collagen IV, perlecan and nidogen (Yurchenco, 1990; Yurchenco and Schittny, 1990). Genomic comparisons conducted across numerous species have determined remarkable conservation of all four major basement membrane proteins even in distantly related phyla (Hutter et al., 2000; Hynes and Zhao, 2000). A critical aspect of BM biology during development involves their remodeling or dissociation, particularly during tissue fusion events. This is clearly apparent during the formation of the vertebrate retina, in particular fusion of the optic fissure. Upon the formation of a bi-layered optic cup, a fissure, the optic fissure, is formed in the ventral most region of the tissue. Serving as a conduit for endothelial cells to migrate and establish retinal vasculature, the fissure ultimately closes during an epithelial sheet fusion event to ensure a continuous and morphologically spherical structure of the retina (Barishak, 1992; Saint-Geniez and D'Amore, 2004). Failure of this fusion event leads to a congenital pediatric blinding disorder, coloboma, a leading cause of pediatric blindness (Chang et al., 2006; Stoll et al., 1997). Observed in several species, including zebrafish, chick and mouse, immunohistochemistry (IHC) of laminin clearly depicts a progressive removal of the BM during fissure fusion (Bernstein et al., 2018; Gestri et al., 2018; James et al., 2016). BM remodeling is therefore a critical component of the fusion process and it's failure is a likely culprit in the etiology of coloboma.

Coloboma has been the focus of scientific inquiry for well over a century, yet we still lack a general understanding of the molecular mechanism driving the fusion process. Major progress has been made in understanding the signaling and morphogenetic pathways that shape the fissure and subsequently signal for fusion. These pathways are known to involve Shh, BMP, TGFb and RA signaling in addition to several key

* Corresponding author.
E-mail address: jakub.famulski@uky.edu (J.K. Famulski).
[1] Indicates equal contribution.

https://doi.org/10.1016/j.ydbio.2019.04.012
Received 25 February 2019; Received in revised form 8 April 2019; Accepted 23 April 2019
Available online 26 April 2019

transcriptional regulators of fissure fusion such as vax1, vax2 and the best studied to date, pax2 (Hornby et al., 2003; Reis and Semina, 2015; Sanyanusin et al., 1995a; Sanyanusin et al., 1995b; Take-uchi et al., 2003; Gregory-Evans et al., 2004). However, we still lack a basic understanding of the molecular events that govern the physical fusion process. One such event undoubtedly involves the remodeling of the BM prior to fusion. Persistence of the BM presents as a physical barrier for fusion to occur and it is actually a hallmark of coloboma. Several coloboma models highlight the persistence of the BM as observed by laminin IHC (James et al., 2016; Liu et al., 2016; Tsuji et al., 2012). A key missing puzzle piece to our understanding of the molecular mechanisms driving fusion is therefore how and when does the BM undergo remodeling and subsequently removal from the fissure. To date only two ECM remodeling enzymes, MMP2 and ADAMTS16, have been associated with optic fissure fusion, however, their targets within the fissure have yet to be determined (Cao et al., 2018; Tsuji et al., 2018). Recent studies in several model organisms have elucidated the timing of fissure fusion by analyzing the removal of BMs as a readout for its initiation and its complete absence for its completion (Bernstein et al., 2018; James et al., 2016). Conclusions from these studies indicate an orderly progress of fusion originating at the most proximal region of the fissure, including the optic stalk and concluding at the distal most region of the optic cup. The molecular mechanisms involved in BM disassembly must therefore be regulated both temporally and regionally. Interestingly in all cases, laminin IHC was used to assess BM integrity. In fact, laminin is the only component of the BM that has been actively studied in regard to optic fissure fusion and/or BM remodeling (Lee and Gross, 2007; Parsons et al., 2002). While laminin is a critical component of the fissure it is only one of four core BM constituents. Furthermore, while laminin removal from the BM indicates that fusion is proceeding, it does not indicate how or when the remodeling started. It remains unknown whether BM core disassembly involves a step-wise process or occurs simultaneously. Examination of BM biology in other systems indicates that not all components are critical for assembly. Nidogen, for example, has been shown to be dispensable for BM assembly but is critical for its stability and rigidity (Aumailley et al., 1993). Collagen IV and laminin make up the bulk of the BM and are therefore also likely targets for remodeling. In addition, there are many matrix metalloprotease (MMP, ADAM, ADAMTS and cathepsin) enzymes known to be capable of targeting various components of the BM, but which have yet to be investigated during optic fissure fusion (Bonnans et al., 2014). Importantly, the exact composition of optic fissure BMs has yet to be defined. While collagen VI, laminin, nidogen and perlecan are expected to be represented in the optic fissure BM this has yet to be directly shown. Furthermore, each of the components, barring perlecan, is encoded by several orthologues and their expression has also not been examined in the context of fissure fusion. As such, we sought to fully characterize the molecular composition of the optic fissure BM during zebrafish retinal morphogenesis as the first logical step in deciphering the molecular mechanisms governing its remodeling.

Using whole mount *in situ* hybridization (WISH), we have confirmed the expression of perlecan and identified optic fissure expressed laminin, collagen IV and nidogen orthologues. In addition, we characterized their expression patterns throughout the process of fissure fusion. Interestingly, our findings indicate that the majority of BM components continue to be expressed well past the initiation of fissure fusion. Of note, we also observed that nidogen was the only component of the BM to be transcriptionally down regulated upon and during the initial stages of fissure fusion. Furthermore, when examining nidogen deposition in the fissure, we observed that nidogen was actively removed from the BM prior to that of laminin. Interestingly, this indicates that BM disassembly is an ordered event. Finally, we correlated nidogen loss of function with severe morphogenetic malformation of the optic cup and subsequent failure of optic fissure fusion.

2. Results

2.1. Optic fissure basement membrane comprises of laminin a1, a4, b1a, c1 and c3

Laminin is a heterotrimeric cross-shaped protein comprised of α, β, and γ chains (a, b and c hence forth) that plays roles in both BM structure and cell interaction via integrins (Aumailley, 2013). Genetic analyses have suggested that laminin provides the primary structural framework required for the recruitment and organization of other major BM components (Li et al., 2003). The terminal domain of laminin's long arm, the a chain, is responsible for both cell adhesion and self-assembly into polymers while the ends of laminin's short arms, b and c chains, are required for the formation of dimers and oligomers (reviewed in Aumailley (2013)). Previous examination of laminin gene family expression during zebrafish development indicated that majority of the alpha, beta and gamma subunits were expressed in the developing head and eye (Sztal et al., 2011). However, those studies did not focus on retinal anatomy or detailed pattern of expression. Analysis of laminin a1, b1 and laminin c1 expression and their corresponding mutant phenotypes, is to date the only direct examination of any BM gene expression in the optic fissure (James et al., 2016; Lee and Gross, 2007; Parsons et al., 2002). Laminin 111 is expected to be the predominant form of laminin heterodimers in the fissure, however this does not exclude the possibility of additional complexes. As such we sought to obtain a comprehensive outline of laminin gene expression during fissure fusion. To do so, we performed whole mount *in situ* hybridization (WISH) to track retinal expression of all 12 zebrafish laminin genes between 24 and 65hpf, spanning the course of fissure formation and fusion. Alpha chain laminin gene expression analysis included laminins a1, a2, a3, a4 and a5 (Fig. 1A). At 24hpf only laminin a1 and a4 display expression in the eye and in particular in the optic fissure (Fig. 1A, Fig. 1A). Similar expression patterns are observed at 48hpf. Laminin a2, a3 and a5 display varying expression throughout the cranial regions while laminin a5 is detected in the lens at 48hpf. Beta chain expression analysis included laminins b1, b1b, b2 and b4 (Fig. 1B). Only one beta chain laminin indicated expression in the optic fissure, laminin b1. Both 24 and 48hpf embryos clearly display laminin b1 signal in the fissure (Fig. 1B, Fig. S1A). Remaining laminin beta genes show weak expression in the cranial and periocular regions. Gamma chain laminins examined included laminin c1, c2 and c3 (Fig. 1C). Both laminin c1 and c3 display expression in the optic fissure at both 24 and 48hpf while laminin c2 expression appears to be epidermal at this stage of development (Fig. 1C, Fig. S1A).

Having established which laminin genes are expressed during optic fissure fusion, we next sought to determine whether their expression correlates to the initiation or completion of fissure fusion. Recent work has pinpointed the initiation of fissure fusion in zebrafish to commence at ~32-36hpf, actively fusing by 48hpf and mostly completed fusion by 72hpf (Bernstein et al., 2018; James et al., 2016). To precisely track timing of laminin expression during fissure fusion, we examined laminin expression at 24, 48, 56 and 65hpf (Fig. 1D). Isolated retinas imaged using DIC indicated that all 5 laminin genes were still expressed in the region of the fissure at 48hpf, while laminin c3 expression persisted until 56hpf. By 65hpf all of the laminin genes were no longer expressed in the fissure. Taken together, our results confirmed the expected expression of laminins a1, b1 and c1, in addition to uncovering laminin a4 and c3 as novel additions to the laminin repertoire included in optic fissure BMs. We also determined that laminin expression generally persists up to and including 48hpf, which is a time when fusion is actively occurring.

2.2. Perlecan expression in the optic fissure persists up to the conclusion fusion

Perlecan, the most prominent proteoglycan of the BM, consists of a 400–500 kDa (80 nm) core protein attached to three heparan sulfate and/or chondroitin sulfate chains (70 kDa-100kDa each) (Paulsson et al.,

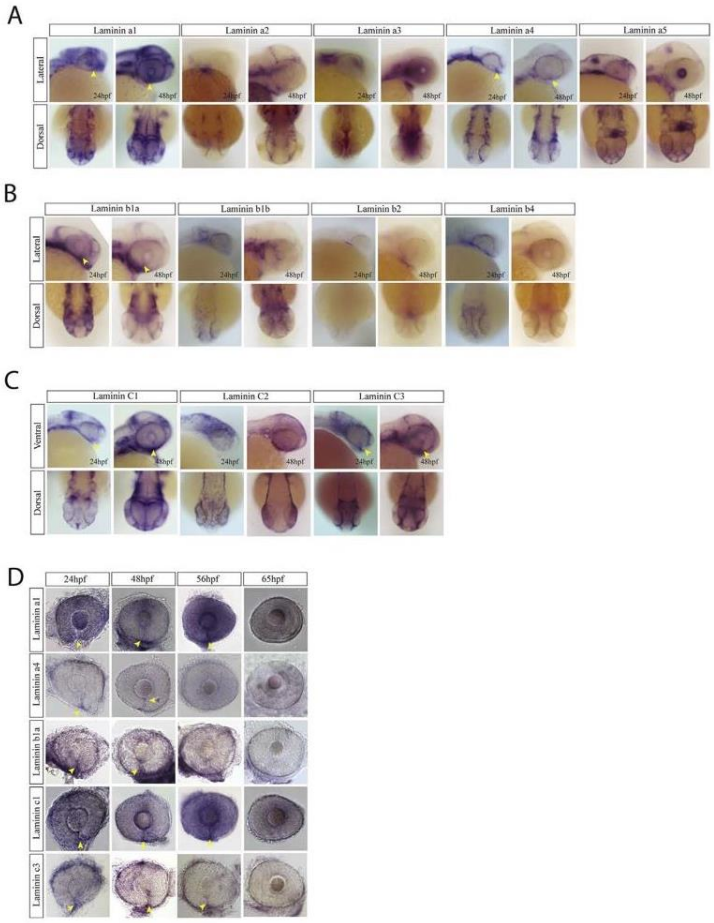

Fig. 1. Laminin expression during optic fissure formation and fusion. **A)** WISH for zebrafish laminin alpha chain genes a1, a2, a3, a4 and a5. Expression was analyzed at 24 and 48hpf and visualized in lateral and dorsal views. At 24 and 48hpf laminins a1, a4 and a5 were observed to express within the optic fissure (yellow arrow heads). Laminin a2 and a3 were largely absent from the retina while laminin a5 was expressed in the developing lens at 48hpf. **B)** WISH for laminin beta chain genes b1, b2 and b3 at 24 and 48hpf. Only laminin 1b was found to be expressed in the optic fissure (yellow arrow heads). Laminin b2 and b3 were largely absent from the retina. **C)** WISH for laminin genes c1, c2 and c3 at 24 and 48hpf. Laminin c1 and c3 were detected in the optic fissure (yellow arrow heads) while c2 appears to primarily be expressed in the ectoderm. **D)** WISH time course examination of laminin gene expression in the optic fissure. Laminin a4 and b1 are expressed in the fissure up to 48hpf, while a1, c1 and c3 retain expression up to 56hpf (yellow arrow heads).

1987; Timpl, 1993). It has been indicated as a key regulator of BM signaling (Smith et al., 2007). Zebrafish encode a single perlecan gene, hspg2, which was identified and characterized by Zoeller et al., in 2008 (Zoeller et al., 2008). Using WISH and IHC the authors showed that perlecan was expressed in the head, eye and somites. However, the authors did not focus their attention on retinal or optic fissure expression of perlecan. As such, we performed perlecan *in situ* hybridization at 24 hpf and observed a low level of expression in the optic fissure and periphery of the developing retina (Fig. 2A, Fig. S1B). By 48 hpf, perlecan is clearly expressed in the optic fissure and surrounding the forming lens (Fig. 2A, Fig. S1B). At 56hpf perlecan expression continues to outline the lobes of the fissure with a strong signal (Fig. 2B). Interestingly, at 65hpf, while perlecan expression is diminished it is still clearly observable as a single line of expression across where the fissure had fused. This suggests that on a transcriptional level, perlecan does not appear to be down regulated in anticipation of fissure fusion and or its mRNA persists in the fusing cells for an extended amount of time.

2.3. Collagen IV is represented in the optic fissure by col4a1 and col4a2

The second most abundant protein in the BM, collagen IV, encodes three functional domains a1, a2 and a globular domain NC1 at the carboxy-terminus (~550 kDa). Collagen IV's amino-terminus interacts with three other collagen IV proteins resulting in a characteristic chicken wire shaped quaternary assemblage (Brown et al., 2017). This uniquely shaped arrangement increases the elasticity of the matrix and ultimately its biomechanical strength. Col4a1 and 4a2 are predicted to be components of most BM, with other col4 genes exhibiting tissue and developmental variability in expression (Khoshnoodi et al., 2008). As we had previously done for laminin and perlecan, we sought to characterize the composition of the optic fissure BM by analyzing collagen IV expression. Zebrafish encode 6 collagen IV genes, col4a1-a6. Apart from col4a1 and col4a5 WISH images deposited to ZFIN, a search of the literature did not provide any significant results for analysis of collagen IV expression in early zebrafish. Therefore, we examined the expression of all 6 col4 genes using *in situ* hybridization at 24 and 48hpf with a focus on retinal and optic fissure expression (Fig. 3A). Upon analysis of our results we can conclude that all 6 genes had expression in the eye, with collagen 4a3-4a6 expression restricted to the periphery of the lens pit. On the other hand, col4a1 and col4a2 expression was absent from the lens region, but clearly present in the optic fissure (Fig. 3A, Fig. S1C). Col4a1 and col4a2 appear to also have overlapping expression throughout the

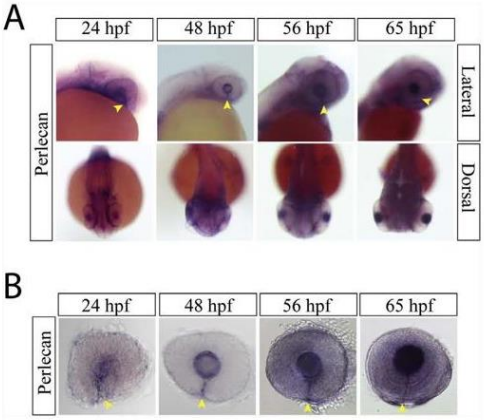

Fig. 2. Perlecan expression during optic fissure formation and fusion. **A)** WISH for zebrafish perlecan at 24, 48, 56 and 65hpf. Perlecan expression is observed in the lens and the optic fissure from 24 to 65 hpf (yellow arrow heads). **B)** Examining WISH in isolated zebrafish eyes at 24, 48, 56 and 65hpf indicates that perlecan expression persists in the optic fissure (yellow arrow heads) up to 65hpf.

head region (Fig. 3A). Having identified optic fissure associated collagen IV genes, we next tracked their expression patterns throughout optic fissure fusion. *In situ* analysis on isolated retinas indicates that both col4a1 and col4a2 expression persists until 56hpf and is largely absent from the region of the fissure by 65hpf (Fig. 3B). These findings run parallel with our analysis of laminin and perlecan gene expression, where although fusion is close to complete, these particular BM components continue to be expressed.

2.4. Nidogen 1a, 1b and 2a are expressed in the optic fissure

The final core component of the BM yet to be characterized for expression during optic fissure fusion is nidogen. Compared to the other BM core components, Nidogen is a relatively small BM protein (~150 Kd) comprised of three globular domains separated by two spacer regions. Nidogen's largest β-barrel shaped domain G2 has the ability to bind to both collagen IV and perlecan, while it's G3 domain binds to the γ chain of laminin (Aumailley et al., 1989, 1993; Chung and Durkin, 1990; Tsao et al., 1990). Similar to collagen IV and perlecan, little to no nidogen expression data from zebrafish embryos exists. Zebrafish encode 4 nidogen homologues, nid1a, 1b, nid2a and 2b and we therefore analyzed all 4 using WISH between 24 and 48hpf (Fig. 4A). To our knowledge, this is the first comprehensive examination of nidogen family expression in zebrafish embryos. Interestingly, all 4 nidogen orthologues display regions of unique expression patterns throughout the embryos, particularly in the tail and head regions. Nid1a is expressed throughout the somites while nid2a is expressed in the tail tip. Nid1a, 1b and 2a are all expressed in the head region and surrounding the eye between 24 and 48hpf. Furthermore, nid1a, 1b and 2a were all found to express in the optic fissure starting at 24hpf (Fig. 4A, Fig. S1D). Nid2b appears to be expressed at very low levels at 24hpf and further declines by 36 and 48hpf. We next correlated nidogen expression with timing of optic fissure fusion. Examining retina, and in particular optic fissure expression between 24 and 65hpf indicated that nid1a expression diminishes significantly by 36hpf while nid2a expression diminishes between 36 and 48hpf (Fig. 4B, Fig. S1D). By 48hpf, nid1a expression diminishes not only in the fissure, but also throughout the embryo while nid2a expression begins to corelate with the region of pharyngeal arches. In contrast, optic fissure and head expression of nid1b persists until 48hpf (Fig. 4B). By 56hpf all of the nidogen genes are no longer expressed in the optic fissure. These results indicate that optic fissure BMs contain nidogens 1a, 1b and 2a. Interestingly, our data also indicate that expression of nidogen orthologues may be temporally regulated in response to the initiation of optic fissure fusion.

2.5. Nidogen expression is uniquely regulated within the optic fissure basement membrane

When comparing and contrasting all of our optic fissure *in situ* hybridization data for laminin, collagen IV, perlecan and nidogen (Figs. 1–4) it becomes clear that during the course of optic fissure fusion only one core component of the basement membrane is transcriptionally responsive to the fusion process, that being nidogen (Figs. 4B and 5A). Nidogen expression is downregulated by 48hpf, with nid1a being downregulated as early as 36hpf, right at the predicted time of fusion initiation (Fig. 4 and A). All other BM components are still expressed in the fissure up to and/or later than 48hpf with perlecan expression persisting up to the conclusion of fissure fusion at 65hpf. These findings suggest that nidogen may be the first component of the BM to be remodeled or removed in order to enable wholesale disassembly of the BM thus facilitating epithelial fusion within the fissure. To test this hypothesis, we performed IHC to simultaneously detect laminin, a well-known marker for BM integrity, and nidogen. The nidogen antibody used was raised to mouse nidogen 1 and we therefore predict it detects nid1a and nid1b. We analyzed co-staining of laminin and nidogen from 22 to 48 hpf (Fig. 5B). At early time points, 22-36hpf, nidogen and laminin appear to co-localize in the BM and remain closely associated. However, by ~40-44hpf, a time when optic fissure fusion is predicted to be actively occurring and therefore BMs are being actively degraded or remodeled, within the central region of the fissure we begin to see regions of the BM having a reduction in nidogen signal prior to that of laminin (Fig. 5B). The absence of nidogen but persistence of laminin was not observed in every embryo examined ($n = 3/10$ embryos, at 42 and 44hpf), suggesting that BM remodeling is a highly dynamic event and soon after nidogen is removed so is laminin. However, we never observed the presence of nidogen in absence of laminin ($n = 67$ embryos between 32 and 56hpf). By the time fusion is complete, 48hpf or later, both signals are absent from the fusion sites. These results go hand in hand with our analysis of nidogen expression, where nidogen is the first BM component to be transcriptionally downregulated. This also suggests that nid1a and nid1b may in fact be the first components of the BM to be targeted in order to initiate disassembly, or remodeling, before the commencement of direct fusion of the optic fissure margins.

2.6. Nidogen is necessary for early retinal morphogenesis and optic fissure fusion

Previous studies of laminin subunits have pointed to a crucial function of the BM in shaping and maintaining the optic cup during early retinal morphogenesis (Bryan et al., 2016). To examine the functional role of nidogen during retinal morphogenesis and optic fissure fusion we performed morpholino injections for nid1a and/or nid1b in combination with Nid2a mutant analysis. Recent work from the Chen lab indicates that nid1a and 1b likely compensate each other upon loss of function (Zhu et al., 2017). As such, using morpholinos afforded us the opportunity to examine simultaneous loss of nid1a and 1b function (Fig. 6A). For nid2a we examined a mutant line sa15802 (ZIRC) which harbors a point mutation leading to a premature stop codon at amino acid 437 and subsequently exhibits nonsense mediated decay (Fig. 6B). Interestingly, examination of the nid2a mutant line did not reveal any observable phenotypes, even when generated as a maternal zygotic (Fig. 6B and data not shown). Nid2b was not functionally examined as it lacks optic fissure expression. Injection of nid1a or nid1b morpholinos into WT embryos resulted in a dose response of retinal and embryonic malformations (Fig. 6A). These included apparent developmental delays in the cranial

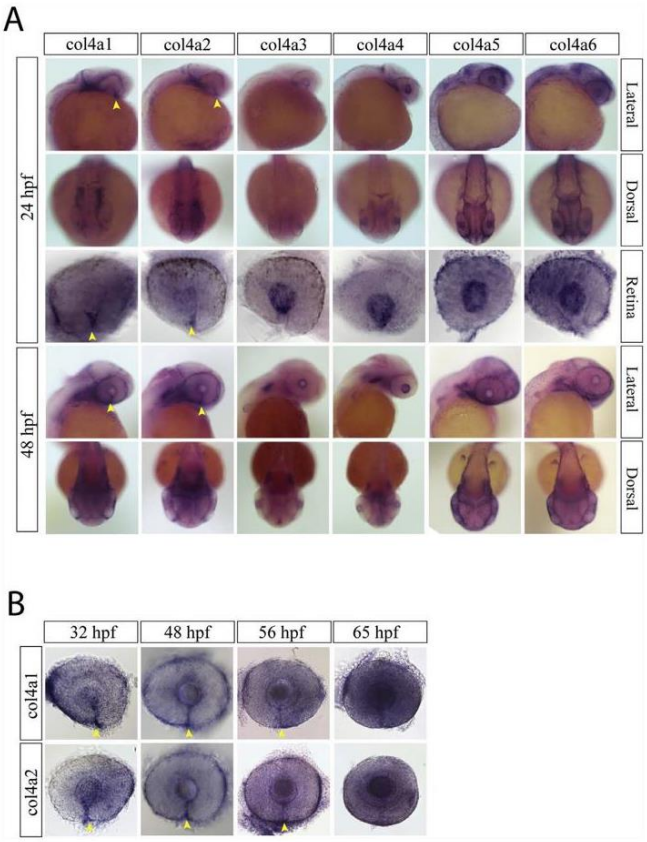

Fig. 3. Collagen IV expression during optic fissure formation and fusion. **A)** WISH for zebrafish collagen IV (col4) genes a1-a6 at 24hpf. At 24hpf, only collagen IV a1 and a2 had optic fissure expression (yellow arrow heads). Col4 a3-a6 were all detected in the retinal periphery and in the developing lens. **B)** WISH time course for col4 a1 and a2 expression from 24 to 65hpf. Both col4 a1 and a2 had detectable expression in the optic fissure up to 56hpf (yellow arrow heads).

regions (moderate) in combination with a decrease in overall embryo size (severe). Co-injection of both MOs had a synergistic effect leading to an increase in both moderate and severe phenotypes. Furthermore, injection of sub-effective doses of nid1a and nid1b MO into homozygous nid2a mutant embryos induced the highest proportion of severe phenotypes (Fig. 6C). This suggests that all three; nid1a, 1b and nid2a have potential compensatory function during early zebrafish development. Only moderately affected embryos were included in all subsequent functional studies. To visualize effects of nid1 loss of function on retinal morphogenesis we performed *in vivo* time lapse confocal microscopy using our retinal reporter line Tg[*rx3*:GFP] co-injected with nid1a/1b MOs. Nid2a−/− embryos injected with nid1a/1b MOs had too severe phenotypes to warrant detailed investigation of retinal morphogenesis. Starting at 20hpf we tracked retinal morphogenesis over 16 h (Fig. 6D, Movie 1 and 2). Already at 20hpf morphant embryos displayed a severely disorganized optic cup. As retinal development proceeded, morphant embryos did appear to complete optic cup formation but with several dire consequences. Throughout imaging we observed GFP + cells detaching from the retina, suggesting a lack of tissue integrity. In addition, even at 36 hpf, the retina has a very large gap between the two retinal lobes indicating a major extension of the N/T axis and unlikely ability to complete optic fissure fusion. Overall the morphant embryos displayed a very malformed and delayed retinal morphogenesis when compared to controls.

Supplementary video related to this article can be found at https://doi.org/10.1016/j.ydbio.2019.04.012.

Detailed analysis of nidogen loss of function during retinal morphogenesis was performed using IHC for laminin and in conjunction with the retinal reporter transgenic line Tg[*rx3*:GFP]. 24hpf embryos injected with nid1a, nid1b or both MOs were examined. Injection of both low and high dose of MO resulted in retinal malformation, in particular loss of symmetry in the retinal structure. This was evident with both laminin staining and the *rx3*:GFP signal (Fig. 7A). Higher doses (2 ng) of individual MOs or when co-injected resulted in a severely disorganized optic cup (Fig. 7B). We also observed regions of the retina where laminin deposition did not appear uniform or was absent. To quantify nidogen loss of function effects on retinal morphogenesis we measured both eye size (Fig. 7B) and eye symmetry (Fig. 7C) by calculating the nasal-temporal/dorsal ventral axis in morphant embryos with moderate phenotypes. Both nid1a and nid1b morphant embryos exhibited smaller eyes, ~16–20% reduction, with double morphants having significantly smaller eyes than either of the singles, up to a 24% reduction in size

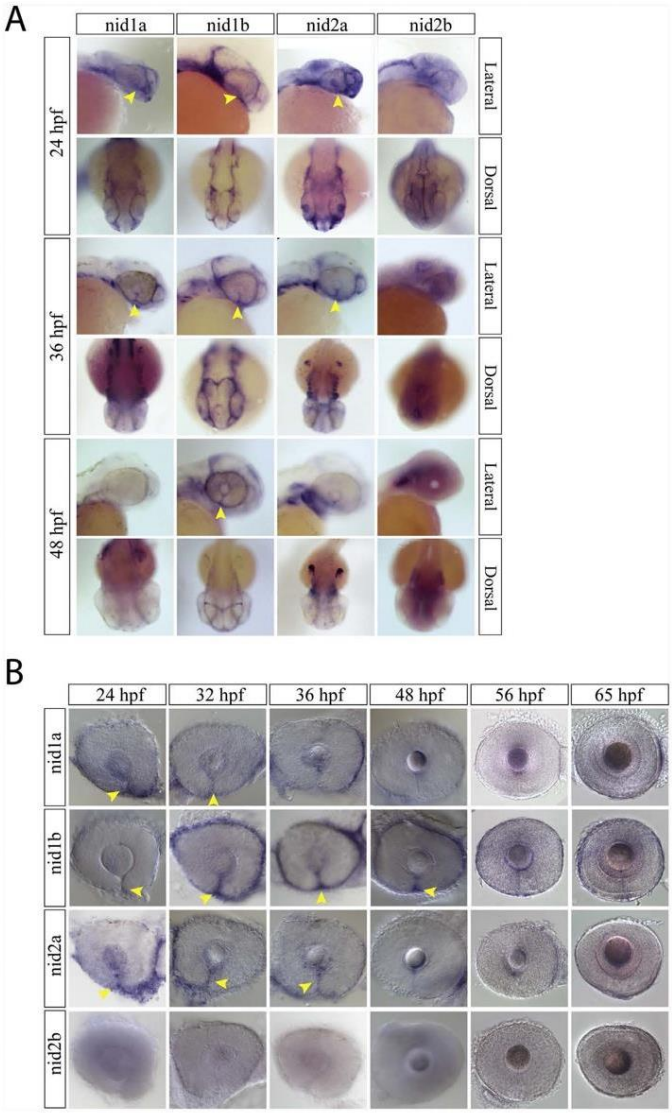

Fig. 4. Nidogen expression during optic fissure formation and fusion. **A)** WISH for zebrafish nidogen (nid) genes nid1a, nid1b, nid2a and nid2b at 24, 36 and 48hpf. At 24 and 36hpf nid1a, nid1b and nid2a were all expressed in the optic fissure (yellow arrow heads). Nid2b lack retinal expression between 24 and 48hpf. **B)** WISH time course for nid1a, 1b and 2a expression in the optic fissure (yellow arrow heads). Expression of nid1a and 2a is absent from the fissure by 48hpf, while nid1b persists past 48hpf but is absent by 56hpf.

(Fig. 7B). Decreased eye size was also associated with higher doses of the MOs. To determine a potential cause of smaller eyes we analyzed proliferation in nid1a/1b morphants by examining phospho-Histone H3 signal. At 24hpf we observed a significant reduction of retinal cells positive for PH3 when compared to controls (Fig. 7D). This reduction in proliferation could be a contributing factor to the decrease in eye size observed. As eye size decreased, we also observed an elongation of the NT axis in morphant embryos with the greatest effect also observed in double morphants and at higher MO concentrations (Fig. 7B) Elongation of the N/T axis ranged from 12 to 26% above that of controls. This was also evident in our *in vivo* time lapse imaging (Fig. 6C). To expand on these findings, we next examined N/T and D/V retinal patterning in morphant embryos. Whole mount *in situ* hybridization for FoxG1a (nasal), FoxD1 (temporal), Aldh1a2 (dorsal) and Vax2 (ventral) indicated that nidogen loss of function had specific effects on nasal-temporal retinal patterning. In particular, a shift of the dorsal domain, the aldh1a2 signal, in the nasal-ventral direction and a slight expansion of the dorsal domain, as observed with vax2 (Fig. 7E) Both the dorsal and ventral patterning abnormalities were observed at high penetrance (12/17 and 12/19 respectively). These findings indicate that morphogenesis of the retina, as well as D/V patterning, are significantly affected by the loss of nidogen (Fig. 7B–E).

As an alternative strategy for nidogen loss of function, we also generated a nidogen 1b dominant negative cDNA construct (nid1bDN) by removing the G3 domain. We predicted this construct would result in BM where nidogen would no longer be able to cross-link the other 3 core

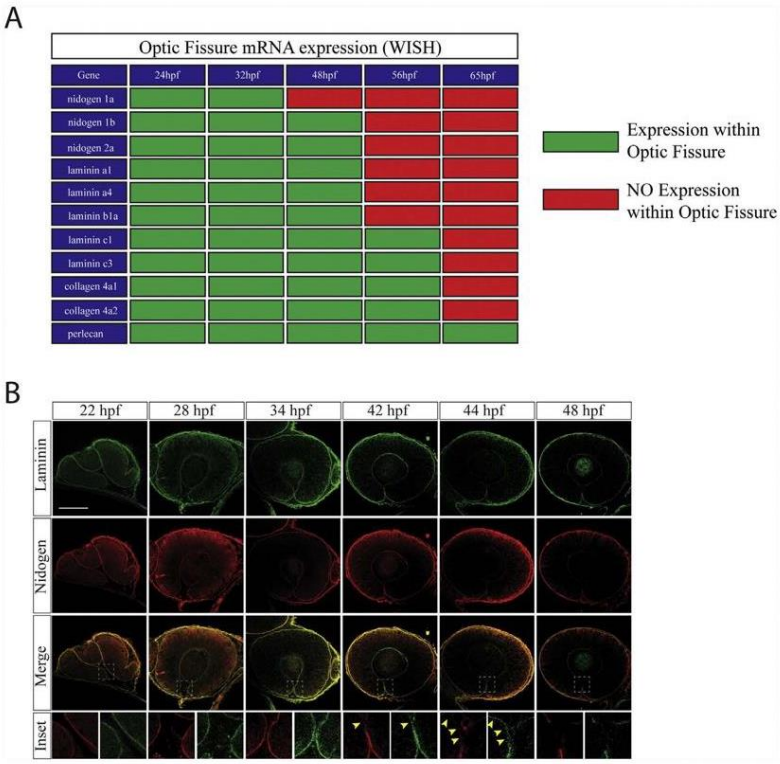

Fig. 5. Nidogen is down-regulated prior to laminin during optic fissure fusion. **A)** Summary of core basement membrane component expression within the optic fissure as observed by WISH (Figs. 1–4) between 24 and 65hpf. Green indicates expression (WISH signal), red indicates absence of expression (lack of WISH signal). **B)** Immunohistochemistry analysis for remodeling of laminin (green) and nidogen 1 (red) within the optic fissure during retinal morphogenesis (22-48hpf). At early time points, ~22-40hpf, laminin and nidogen signal is found to co-localize in the optic fissure BM. Starting at 42hpf nidogen signal in the optic fissure is reduced prior to that of laminin (yellow arrow heads). By 48hpf both laminin and nidogen are absent in the regions of the fissure where fusion has completed. Scale bar = 50 μm.

components and therefore weaken the structure. Injection of the nid1bDN mRNA resulted in malformation of the optic cup similar to what we observed in morphant embryos (Fig. S2). Taken together our data indicate that deposition of nidogen into the optic cup BM is essential for precise execution of retinal morphogenesis and maintenance of optic cup integrity. These findings are similar to what was observed in laminin mutant embryos.

Finally, we examined consequence of nidogen loss of function on optic fissure fusion. It was well documented that laminin mutant embryos experience a failure of fissure fusion and therefore a coloboma like phenotype (Lee and Gross, 2007). As such, we predicted that nidogen loss of function will results in similar outcomes. To examine fusion of the optic fissure we performed IHC for laminin at 72hpf in control and nid 1a/1b morphant embryos (Fig. 7F). When examining the central-distal region of the retina, control embryos exhibit little to no laminin or *rx3*:GFP signal in the region of the optic fissure as fusion has already completed. In contrast, more than 40% of nid1a/1b MO co-injected embryos retain laminin, and *rx3*:GFP signal in the region of the fissure outlining the two distinct lobes of the retina. This is an indication that BM remodeling has not completed, and that fissure fusion is either delayed or fails to initiate. As such, similar to laminin, nidogen is necessary during early development to ensure proper morphogenesis of the optic cup and subsequently the timely fusion of the optic fissure.

3. Discussion

The composition of the molecular machinery governing optic fissure fusion remains a black box. In our present study we begin to shed some light on this process by comprehensively analyzing the temporal expression of optic fissure basement membrane components. As such, our work is the first to define all of the core constituents of optic fissure basement membrane and observe an apparent order during to its remodeling. Based on our results we have concluded that optic fissure BMs are comprised of laminins a1, a4, b1, c1 and c3, perlecan, collagen 4a1 and 4a2 as well as nidogen 1a, 1b and 2a. Additionally, we have characterized the time course of their individual expression and determined that nidogen, in particular nidogen 1a and 2a is transcriptionally regulated in response to initiation of fissure fusion. While our study characterized the gross timing of core BM component expression, future studies will aim to decipher whether downregulation of nidogen expression has any distal-proximal temporal pattern and what is the corresponding transcriptional mechanism. Interestingly, we also observed that nidogen appears to be remodeled/removed in optic fissure BMs prior to that of laminin. Furthermore, nidogen loss of function appears to phenocopy laminin a1, b1 and c1 mutants, where retinal morphogenesis and subsequently optic fissure fusion are both impaired. Taken together we show that nidogen is a critical component of the retinal BM during optic fissure fusion and presents as a potential initial target of BM remodeling during fusion.

Limiting nidogen deposition in the zebrafish embryo via the use of morpholinos resulted in compromised BM structure and phenotypes similar to those observed in the murine model. Nidogen1 and 2 knockout mice have been shown to display BM defects in the heart, lung, and limbs resulting in perinatal lethality (Bader et al., 2005; Bose et al., 2006). These defects were observed to be a direct result of weakened BM integrity due to a decrease in the deposition of laminin, perlecan, and collagen IV. Additionally, knockout of nidogen 1 in mice has been reported to decrease the deposition of laminin γ1 resulting in a more

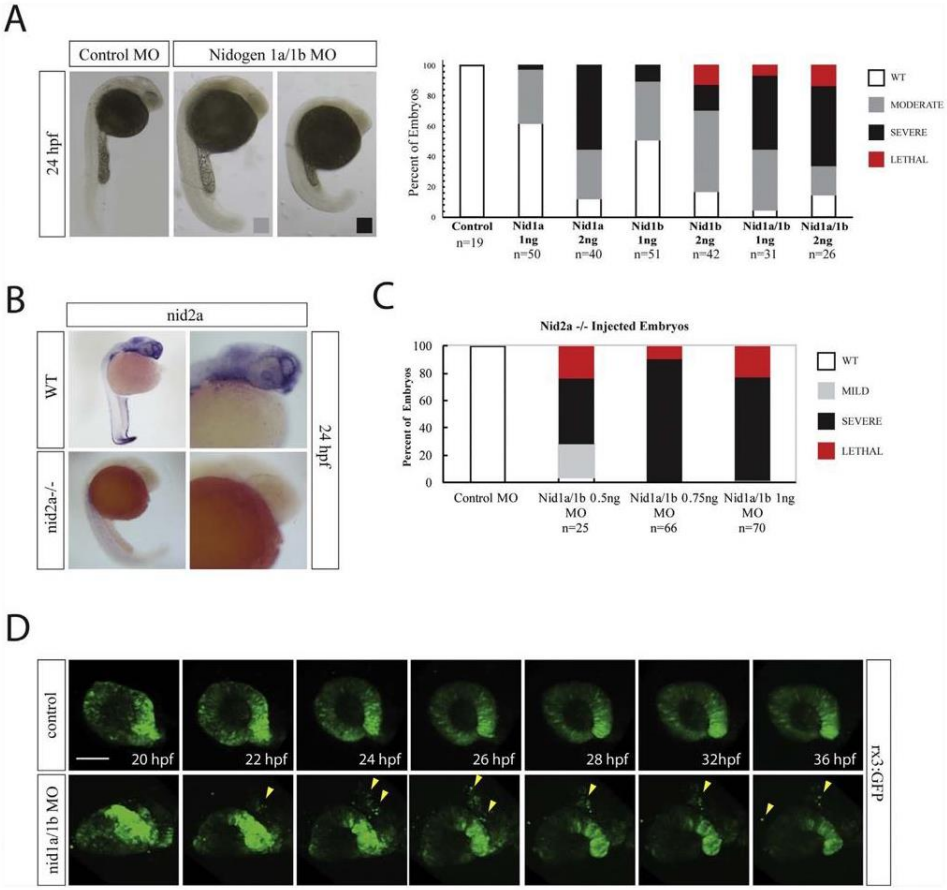

Fig. 6. Nidogen is required during retinal development. **A)** Nidogen 1a and 1b morpholino injection phenotypes at various concentrations and combinations. Moderate phenotypes (gray bar) included potential developmental delays but lacked overt morphological deficiencies. Severe phenotypes (black bar) included significant developmental delays and morphological deficiencies. Lethal phenotypes (red bar) included monster embryos and major developmental deficiencies. **B)** WISH for nid2a comparing expression in WT and nid2a^{sa15280} −/− embryos at 24hpf. Nid2a signal is completely absent in nid2a^{sa15280} −/− embryos. **C)** Nidogen 1a and 1b morpholino injections into nid2a^{sa15280} −/− embryos. Sub-effective doses of nid1a and nid1b MOs, 0.5 or 0.75 ng each, resulted in up to 80% of embryos exhibiting severe or lethal phenotypes. At 1 ng the injections resulted in exclusively severe or lethal phenotypes. **D)** *In vivo* real time imaging of *rx3*:GFP embryos co-injected with nid1a and nid1b morpholinos. 3D stacks were collected every 10min for 16 h. Compared to control, nid1 morphants display a disorganized optic cup, a significant delay in the formation of opposing retinal lobes, an elongation of the N/T axis and delamination of retinal progenitor cells (yellow arrowheads). Scale bar = 50 μm.

punctate and less uniform BM compared to controls (Baranowsky et al., 2010). Unfortunately, as far as we know coloboma or any ocular phenotypes were not examined in nid1, nid2 or double KO mice. Future analysis of ocular phenotypes of these animals would be very useful.

In addition to studies of nidogen mutants, there have been reports showing the ablation of other basement membrane components resulting in adverse effects on ocular development. For example, loss of laminin a1 has been observed to disrupt zebrafish vertebrate optic cup morphogenesis (Bryan et al., 2016). The authors documented multiple structural abnormalities in zebrafish embryos lacking laminin a1 including defects in focal adhesion, invagination, and optic stalk constriction. On a macroscopic level they observed morphogenic phenotypes similar to nidogen morphants including a misshapen lens, and smaller eyes. The authors also noted patches of dying cells they hypothesized could be a result of cells losing contact with the basement membrane and entering into apoptosis via anoikis. Similarly, in our live imaging study of nidogen morphants, we observed *rx3*:GFP + cells which appear to lose contact with the basement membrane and subsequently detach from the eye (Fig. 6D). In addition, we observed a decrease in retinal proliferation in nid1a/1b morphants (Fig. 7D). Previous studies examining laminin b1 and laminin c1 revealed basement membrane defects affecting both the developing eye and notochord of zebrafish (Lee and Gross, 2007; Parsons et al., 2002). Both mutants showed smaller eyes and lens abnormalities similar to those observed in our nidogen morphants. Furthermore, these embryos also displayed shortened body axis comparable to nidogen morphant embryos. Together, it is clear that BM integrity is essential for proper embryonic development and that loss of even one core component can robustly alter ocular morphogenesis.

Our study suggests that nidogen may act as the first target of BM remodeling during optic fissure fusion. We hypothesize that there are two

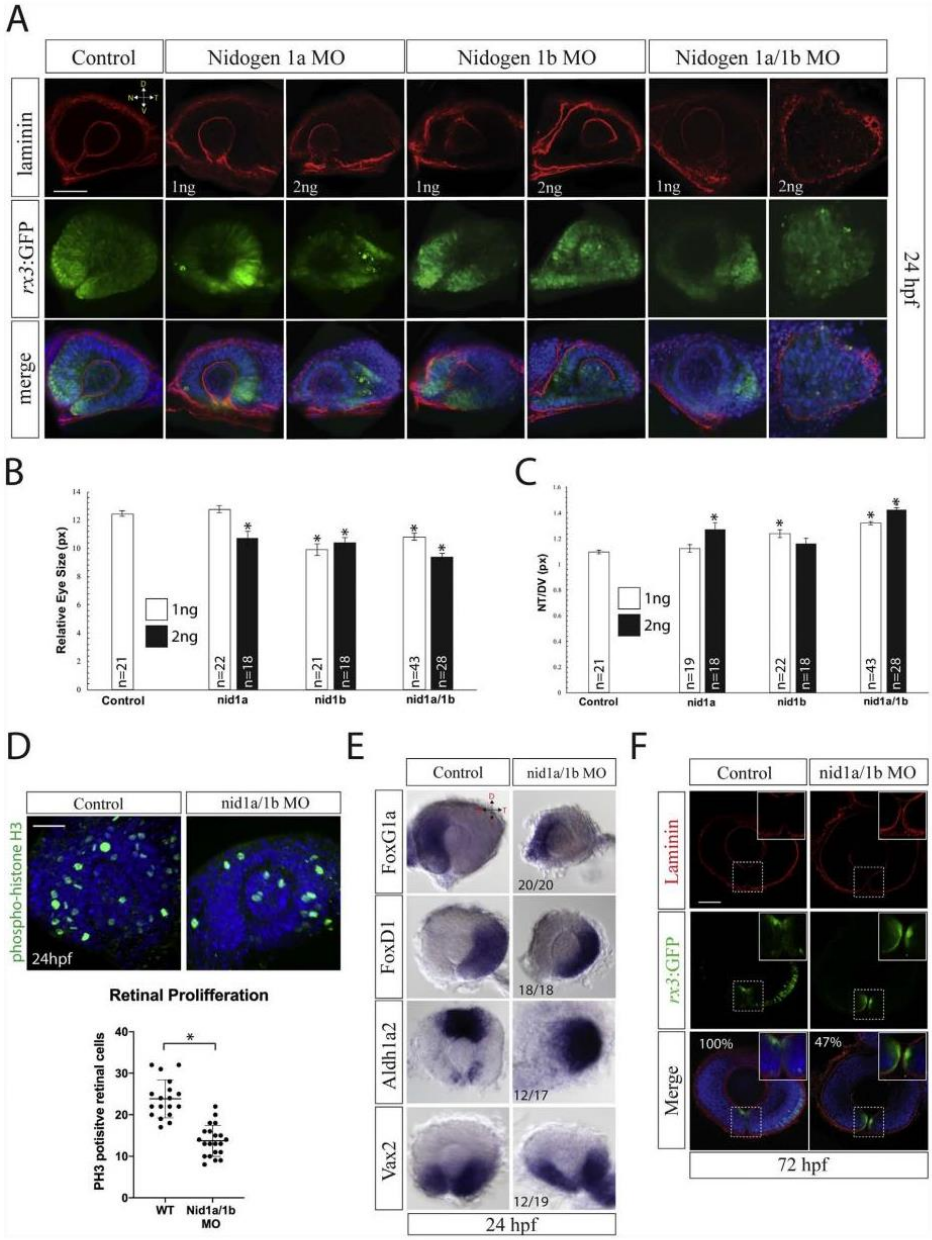

(caption on next page)

Fig. 7. Nidogen is essential for accurate retinal morphogenesis. **A)** Retinal phenotypes in 24hpf nid1 morphant *rx3*:GFP (green) expressing embryos were characterized using laminin IHC (red), and DAPI (blue). Representative single confocal sections are depicted. Retinal shape is moderately disrupted at low morpholino concentrations (1 ng) with most severe effects observed in double morphant embryos (2 ng). Laminin deposition appears to be mildly affected upon co-injection of nid1a and 1b MO at 2 ng 40–50 embryos were examined for each treatment. Scale bar 50 μm. **B)** Quantification of relative retinal size observed in 24hpf morphant embryos. Significantly smaller eyes were observed upon injection of either nid1a or nid1b morpholinos, with the smallest resulting from co-injection of nid1a and 1b morpholinos. Student T-tests were conducted between control and all treatment groups for each parameter measured. * $p < .005$. **C)** Quantification of retinal shape in 24hpf nidogen morphant embryos. Injection of nid1a or nid1b results in an extended NT axis, with co-injection having a synergistic effect. Student T-tests were conducted between control and all treatment groups for each parameter measured. * $p < .05$. **D)** Phospho-histoneH3 (PH3) staining (green) at 24hpf in control and nid1a/1b co-injected embryos. 3D reconstructions are displayed. PH3+ cell counts from individual embryos analyzed are graphed. DAPI is shown in blue. WT n 19, Nid1a/1b MO n 23. *p .0001, Student T-test. Scale bar 50 μm. **E)** WISH for temporal, foxG1a, nasal, foxD1, ventral, vax2 and dorsal, aldh1a2 in nid1a/nid1b morphant retinas at 24hpf. WT and morphant embryo eyes were dissected, mounted and imaged. Nid1a/1b morphant eyes show no significant effects on nasal/temporal patterning, while ventral domains appear shifted temporally and dorsal regions expanded. **F)** Examination of optic fissure fusion at 72hpf via laminin (red) IHC in *rx3*:GFP (green) expressing morphant embryos. Inset (dashed square) displays high magnification of the optic fissure. Single confocal planes of the central-distal region of the fissure are depicted. Results reveal the persistence of laminin signal in 47% (n 41 control, n 27 nid1a/1b MO, p .0001) of 72hpf morphant fissures, a time when control embryos have already completed fusion and removed laminin. Scale bar 50 μm.

potential modes in which the structural disassembly of the BM through the removal of nidogen facilitates optic fissure fusion. The first predicts that the removal of nidogen from the BM results in the exposure of proteolytic sites in the core BM components of laminin, collagen IV or perlecan. Specifically, removal of nidogen leads to a disrupted basement membrane architecture allowing for the subsequent liberation of newly exposed epitopes in other basement membrane components. In this model, matrix metalloproteases which recognize these newly exposed epitopes now have the ability to efficiently remodel the other core basement membrane components. A second, and alternative model predicts that in the absence of nidogen, BM integrity is compromised allowing for the extension of cellular protrusions involved in fusion, such as lamelopodia and filopodia. Ultimately, reducing the biomechanical strength of the BM allows for the necessary positioning of epithelial sheets and subsequent fusion. Interestingly, this possibility has recently been documented in the study of anchor cell invasion (Laura et al., 2019). Finally, it is not only possible, but likely, that these two proposed modes work in concert to enable fusion. Future studies using Atomic Force Microscopy to analyze the degree of optic fissure BM integrity in the absence of nidogen function would potentially answer these questions.

Regulation of nidogen function during fissure fusion appears to be regulated at both the transcriptional and posttranslational level. An examination of other BM remodeling events provides evidence that gene expression does have the ability to play consequential roles in altering BM structure. During heart failure for example, the myocardial BM is significantly remodeled which has been hypothesized to alter cellular shape and function ultimately resulting in decreased performance (Kim et al., 2016). A study examining the variance of gene expression of ischemic failing and non-failing hearts in human tissue suggests that the differential expression of BM components, including the down-regulation of nidogen and laminin, do indeed effect BM morphology (Kim et al., 2016). Transmission electron microscopy revealed, amorphous disrupted BMs in failing hearts known to have lower levels of nidogen and laminin gene expression. Our results suggest, that the integrity of the optic fissure BM may decrease via a similar developmental mechanism in which the expression of nidogen is purposely reduced.

Posttranslational targeting and removal of nidogen in the optic fissure via endogenous proteases provides a direct route for dismantling the BM. Interestingly, nidogen is the most proteolytically sensitive BM component, and is therefore uniquely capable of acting as an initiating factor during BM remodeling (Mayer et al., 1993, 1995; Sires et al., 1993). BM remodeling is predominantly predicted to involve the function of MMP, ADAM and ADAMTS proteases. However, to date only two such proteases, MMP2 and ADAMTS16, have been associated with function during optic fissure fusion (Cao et al., 2018; Tsuji et al., 2018). Unfortunately, direct targets within the optic fissure for ADAMTS16 or MMP2 have yet to be identified. Several proteases have shown to have affinity for nidogen cleavage *in vitro*, including MMP18 and 19 and as such will need to be a topic of future studies to determine whether they play functional roles in optic fissure BM remodeling (Alexander et al., 1996; Titz et al., 2004; Tonge et al., 2013). Lastly, recent work detailing the expression pattern of genes associated with the optic fissure indicates that expression of MMP24 and MMP23bb is upregulated during fissure fusion suggesting these proteases may also be playing a role in BM remodeling (Richardson et al., 2019).

In conclusion, our study has catalogued the core components of the BM expressed during optic fissure fusion and informed on their regulation. Armed with this information we can better prepare to investigate the molecular mechanisms governing optic fissure BM remodeling and subsequently fusion of the optic fissure.

4. Materials and methods

4.1. Zebrafish and embryo maintenance

Zebrafish were maintained using husbandry procedures approved by University of Kentucky IACUC committee. AB and TL strains were used as wild-type, *rx3*:GFP transgenic line (Holly et al., 2014; Rembold et al., 2006) was used to visualize retinal morphogenesis. Embryos were kept at 28.5 °C in E3 embryo media. Nid2a^{sa15280} embryos were purchased from ZIRC. RFLP analysis was conducted by amplifying the region of gDNA with the nidogen2a mutation using the forward primer: 5′-TGATCC-TATTACTCGAC AGATAATAAAG3-'and the reverse: 5′-CGTTTGGCAGGCAGTGGCGGC-3'. The resultant 460bp amplicon was digested with ApeKI (NEB) which would recognize and digest the mutated allele sequence but not the WT allele. Nid2a^{sa15280} homozygous fish were viable and maintained in a homozygous $^{sa15280/as15280}$ state.

4.2. Whole-mount in situ hybridization (WISH)

Whole-mount *in situ* hybridization was performed as previously described (Holly et al., 2014). WISH was performed on 50 + embryos in 2–3 distinct experiments for each time point and each probe. DIG labeled RNA probes were generated using PCR with T7 promoter sequence included in the reverse primer and subsequently transcribed using T7 polymerase (Roche). Primer sequences can be found in Supplementary Table 1. Images were captured using a Nikon Digital sight DS-Fi2 camera and Elements software. Dissected eyes from 24, to 65hpf embryos were mounted in 70% glycerol and imaged under DIC using a Nikon TiE compound microscope equipped with a 20X (0.95NA) objective and Elements software. Image adjustment was performed using Adobe Photoshop.

4.3. Immunofluorescence (IHC)

Dechorionated embryos were fixed with 4% PFA in PBS at room temperature for 3 h and washed with PBST 3 times for 10 min. Embryos were then permeabilized with Proteinase K, 30 μg/mL 15 min for 24 hpf, 50 μg/mL 30 min for 48 hpf and 75 μg/mL 30 min for 72 hpf, washed 3 times in PBST for 5 min and blocked overnight at 4 °C with 10% sheep

serum, 0.8% Triton X-100 and 1% BSA in PBS. Primary mouse anti-laminin antibody (3H11-c DSHB – 1:100) and rabbit anti-nidogen (Abcam 14511- 1:100) in blocking buffer (1% sheep serum, 1% BSA and 0.8% Triton X-100 in PBS) were incubated overnight at 4 °C and washed 5 times in PBST for 10 min. Secondary antibodies, donkey anti-rabbit Alexa Fluor® 555 (Molecular Probes – 1:1000) or mouse anti-GFP Daylight 488 (Rockland – 1:500) and DAPI 1:1000, were incubated for 1 h at room temperature in the dark. Primary rabbit anti-laminin antibody (ThermoFisher – 1:100) was used for IHC in morphant embryo analysis. The embryos were washed 5 times in PBST for 10 min and visualized using a Nikon C2+ confocal microscope equipped with a 40X (1.15NA) water immersion objective. Embryos were embedded in 1% low melting point agarose on glass bottom 35 mm dishes (Fluorodish, World Precision Instruments). Images were captured using Nikon Elements software and adjusted for brightness, contrast and positioning using Adobe Photoshop. All images were adjusted in similar fashion and according to standard image processing guidelines.

4.4. Phospho-histone H3 (PH3) proliferation assay

24hpf embryos were subjected to whole mount IHC as described above. Rabbit anti-PH3 antibody (Millipore 06–570, 1:100) was incubated O/N at 4 °C. Alexa Fluor® 488 anti rabbit secondary antibody (Molecular Probes, 1:1000 + DAPI) was incubated at RT for 2 h. Embryos were mounted in low gelling agarose in 35 mm Fluorodishes and imaged using a C2+ Nikon confocal microscope with a 20X, 0.95NA objective. ~90 μm stacks were collected using a 3 μm step size. 3D projections were generated and PH3 positive cells were counted from within the retina. Statistical analysis was conducted using Microsoft Excel Data Package. Student T-tests were conducted between all treatment groups for each parameter measured. The significance cutoff was $p < .005$.

4.5. Morpholino injections

Translation blocking Morpholinos were obtained from Gene Tools, LLC and used to knock down the expression of nidogen1a and nidogen1b. The following morpholinos were used in this study: Control MO: 5′-CCTCTTACCTCAGTTACAATTTATA-3′, nidogen1a: 5′-GTGCCGACCCA-TATCCAGTCCCAAA-3′, and nidogen1b: 5′-CGGCATCTTCCCCAGG-TAGTCAGAC-3'. Standard control morpholinos were used as controls at matching concentrations. Morpholino concentrations were determined by a dose response of concentration from 0.5 to 8 ng. Concentrations resulting in >90% survivability and absence of gross morphological phenotypes were selected. For analysis, injected morpholino concentrations were 1 ng and 2 ng of nid1a and 1b independently, and 1 ng and 2 ng of nid1a/1b. Morpholino concentrations injected into *nid2a−/−* embryos were nid1a/1b at 0.5 ng, 0.75 ng and 1 ng. Statistical analysis was conducted using Microsoft Excel Data Package. Student T-tests were conducted between all treatment groups for each parameter measured. The significance cutoff was $p < .005$.

4.6. Live imaging analysis

Live imaging of nidogen1a/1b morphant embryos was conducted using a Nikon C2+ confocal microscope equipped with at 20X (0.95NA) water immersion objective. 2 ng of nidogen1a and 1b or control morpholino were injected into 1 cell stage of *rx3*:GFP positive embryos. 20hpf Embryos were imbedded in 1% low gelling agarose in 1-inch glass bottomed Flourodish cell culture dishes (World Precision Instruments) and covered in embryo media, 3-amino benzoic acidethylester (tricaine) to anaesthetize the embryos and 1-phenyl 2-thiourea (PTU) to inhibit pigmentation. Z-stacks 75 μm thick with a step size of 2.5 μm were captured over the course of 16 h at 10 min intervals. ($n = 3$ control embryos and $n = 4$ nid1a/1b MO injected embryos) The ambient temperature was kept at 28 °C. The time lapse data was reconstructed in 4D using Elements software. Image adjustment for brightness, contrast and positioning was done using Adobe Photoshop. All images were adjusted in similar fashion and according to standard image processing guidelines.

4.7. Eye size measurements

Embryos injected with morpholino were fixed in 4% paraformaldehyde. Eye images were captured using a Nikon Digital sight DS-Fi2 camera equipped on a Nikon SMZ800 stereomicroscope. Following image capture, ImageJ software was used to quantify parameters of the morphant embryo eyes. To obtain a measurement of eye size, the area of the eye, measured in pixels (px) was divided by the length of the embryo (px) (from the distal tip of the head to the end of the tail) to normalize for variable embryo size. To obtain a measurement of eye shape, the embryos were positioned laterally, and the length of the nasal/temporal (NT) axis was measured (px) as well as the dorsal/ventral (DV) axis was measured (px) and the ratio of the two (NT/DV) was calculated. Statistical analysis was conducted using Microsoft Excel Data Package. Student T-tests were conducted between all treatment groups for each parameter measured. The significance cutoff was $p < .005$.

4.8. Dominant negative mRNA injection

Truncated nidogen 1b constructs were generated using PCR (primers found in Supplementary Table 1), cloned into pCS2+8 (Addgene) and confirmed via sequencing. mRNA was generated using the Sp6 mMessage mMachine kit (Ambion). Embryos were injected with 200 pg, 300 pg, and 350 pg of mRNA.

Funding

This work was supported by the Knights Templar Eye Foundation Career Starter Grant Awarded to JK. Famulski, 2016–2018.

Appendix A. Supplementary data

Supplementary data to this article can be found online at https://doi.org/10.1016/j.ydbio.2019.04.012.

References

Alexander, C.M., et al., 1996. Rescue of mammary epithelial cell apoptosis and entactin degradation by a tissue inhibitor of metalloproteinases-1 transgene. J. Cell Biol. 135 (6 Pt 1), 1669 1677.
Aumailley, M., 2013. The laminin family. Cell Adhes. Migrat. 7 (1), 48 55.
Aumailley, M., et al., 1989. Binding of nidogen and the laminin-nidogen complex to basement membrane collagen type IV. Eur. J. Biochem. 184 (1), 241 248.
Aumailley, M., et al., 1993. Nidogen mediates the formation of ternary complexes of basement membrane components. Kidney Int. 43 (1), 7 12.
Bader, B.L., et al., 2005. Compound genetic ablation of nidogen 1 and 2 causes basement membrane defects and perinatal lethality in mice. Mol. Cell Biol. 25 (15), 6846 6856.
Baranowsky, A., et al., 2010. Impaired wound healing in mice lacking the basement membrane protein nidogen 1. Matrix Biol. 29 (1), 15 21.
Barishak, Y.R., 1992. Embryology of the eye and its adnexae. Dev. Ophthalmol. 24, 1 142.
Bernstein, C.S., et al., 2018. The cellular bases of choroid fissure formation and closure. Dev. Biol. 440 (2), 137 151.
Bonnans, C., Chou, J., Werb, Z., 2014. Remodelling the extracellular matrix in development and disease. Nat. Rev. Mol. Cell Biol. 15 (12), 786 801.
Bose, K., et al., 2006. Loss of nidogen-1 and -2 results in syndactyly and changes in limb development. J. Biol. Chem. 281 (51), 39620 39629.
Brown, K.L., et al., 2017. Building collagen IV smart scaffolds on the outside of cells. Protein Sci. 26 (11), 2151 2161.
Bryan, C.D., Chien, C.B., Kwan, K.M., 2016. Loss of laminin alpha 1 results in multiple structural defects and divergent effects on adhesion during vertebrate optic cup morphogenesis. Dev. Biol. 416 (2), 324 337.
Cao, M., et al., 2018. Metalloproteinase Adamts16 is required for proper closure of the optic fissure. Invest. Ophthalmol. Vis. Sci. 59 (3), 1167 1177.
Chang, L., et al., 2006. Uveal coloboma: clinical and basic science update. Curr. Opin. Ophthalmol. 17 (5), 447 470.
Chung, A.E., Durkin, M.E., 1990. Entactin: structure and function. Am. J. Respir. Cell Mol. Biol. 3 (4), 275 282.
Gestri, G., et al., 2018. Cell behaviors during closure of the choroid fissure in the developing eye. Front. Cell. Neurosci. 12, 42.

Gregory-Evans, C.Y., et al., 2004. Ocular coloboma: a reassessment in the age of molecular neuroscience. J. Med. Genet. 41 (12), 881–891.
Holly, V.L., et al., 2014. Sfrp1a and Sfrp5 function as positive regulators of Wnt and BMP signaling during early retinal development. Dev. Biol. 388 (2), 192–204.
Hornby, S.J., Ward, S.J., Gilbert, C.E., 2003. Eye birth defects in humans may be caused by a recessively-inherited genetic predisposition to the effects of maternal vitamin A deficiency during pregnancy. Med. Sci. Monit. 9 (11), HY23–H26.
Hutter, H., et al., 2000. Conservation and novelty in the evolution of cell adhesion and extracellular matrix genes. Science 287 (5455), 989–994.
Hynes, R.O., Zhao, Q., 2000. The evolution of cell adhesion. J. Cell Biol. 150 (2), F89–F96.
James, A., et al., 2016. The hyaloid vasculature facilitates basement membrane breakdown during choroid fissure closure in the zebrafish eye. Dev. Biol. 419 (2), 262–272.
Khoshnoodi, J., Pedchenko, V., Hudson, B.G., 2008. Mammalian collagen IV. Microsc. Res. Tech. 71 (5), 357–370.
Kim, E.H., et al., 2016. Differential protein expression and basal lamina remodeling in human heart failure. Proteonomics Clin. Appl. 10 (5), 585–596.
Laura, C., Kelly, Q.C., Rodrigo Caceres, Eric Hastie, Schindler, Adam J., Jiang, Yue, Matus, David Q., Plastino, Julie, Sherwood, David R., 2019 Feb 11. Adaptive F-actin polymerization and localized ATP production drive basement membrane invastion in the absence of MMPs. Dev. Cell 48 (3), 313–328.
Lee, J., Gross, J.M., 2007. Laminin beta1 and gamma1 containing laminins are essential for basement membrane integrity in the zebrafish eye. Invest. Ophthalmol. Vis. Sci. 48 (6), 2483–2490.
Li, S., et al., 2003. The role of laminin in embryonic cell polarization and tissue organization. Dev. Cell 4 (5), 613–624.
Liu, C., et al., 2016. A secreted WNT-ligand-binding domain of FZD5 generated by a frameshift mutation causes autosomal dominant coloboma. Hum. Mol. Genet. 25 (7), 1382–1391.
Mayer, U., et al., 1993. Sites of nidogen cleavage by proteases involved in tissue homeostasis and remodelling. Eur. J. Biochem. 217 (3), 877–884.
Mayer, U., et al., 1995. Binding properties and protease stability of recombinant human nidogen. Eur. J. Biochem. 227 (3), 681–686.
Parsons, M.J., et al., 2002. Zebrafish mutants identify an essential role for laminins in notochord formation. Development 129 (13), 3137–3146.
Paulsson, M., et al., 1987. Structure of low density heparan sulfate proteoglycan isolated from a mouse tumor basement membrane. J. Mol. Biol. 197 (2), 297–313.
Reis, L.M., Semina, E.V., 2015. Conserved genetic pathways associated with microphthalmia, anophthalmia, and coloboma. Birth Defects Res. C Embryo Today 105 (2), 96–113.
Rembold, M., et al., 2006. Individual cell migration serves as the driving force for optic vesicle evagination. Science 313 (5790), 1130–1134.
Richardson, R., et al., 2019. Transcriptome profiling of zebrafish optic fissure fusion. Sci. Rep. 9 (1), 1541.
Saint-Geniez, M., D'Amore, P.A., 2004. Development and pathology of the hyaloid, choroidal and retinal vasculature. Int. J. Dev. Biol. 48 (8–9), 1045–1058.
Sanyanusin, P., et al., 1995. Mutation of PAX2 in two siblings with renal-coloboma syndrome. Hum. Mol. Genet. 4 (11), 2183–2184.
Sanyanusin, P., et al., 1995. Mutation of the PAX2 gene in a family with optic nerve colobomas, renal anomalies and vesicoureteral reflux. Nat. Genet. 9 (4), 358–364.
Sires, U.I., et al., 1993. Degradation of entactin by matrix metalloproteinases. Susceptibility to matrilysin and identification of cleavage sites. J. Biol. Chem. 268 (3), 2069–2074.
Smith, S.M., et al., 2007. Heparan and chondroitin sulfate on growth plate perlecan mediate binding and delivery of FGF-2 to FGF receptors. Matrix Biol. 26 (3), 175–184.
Stoll, C., et al., 1997. Congenital eye malformations in 212,479 consecutive births. Ann. Genet. 40 (2), 122–128.
Sztal, T., et al., 2011. Characterization of the laminin gene family and evolution in zebrafish. Dev. Dynam. 240 (2), 422–431.
Take-uchi, M., Clarke, J.D., Wilson, S.W., 2003. Hedgehog signalling maintains the optic stalk-retinal interface through the regulation of Vax gene activity. Development 130 (5), 955–968.
Timpl, R., 1993. Proteoglycans of basement membranes. Experientia 49 (5), 417–428.
Titz, B., et al., 2004. Activity of MMP-19 inhibits capillary-like formation due to processing of nidogen-1. Cell. Mol. Life Sci. 61 (14), 1826–1833.
Tonge, D., et al., 2013. Axonal growth towards Xenopus skin in vitro is mediated by matrix metalloproteinase activity. Eur. J. Neurosci. 37 (4), 519–531.
Tsao, T., et al., 1990. Characterization of the basement membrane glycoprotein entactin synthesized in a baculovirus expression system. J. Biol. Chem. 265 (9), 5188–5191.
Tsuji, N., et al., 2012. Organogenesis of mild ocular coloboma in FLS mice: failure of basement membrane disintegration at optic fissure margins. Exp. Eye Res. 94 (1), 174–178.
Tsuji, N., et al., 2018. Macrophage-associated gelatinase degrades basement membrane at the optic fissure margins during normal ocular development in mice. Invest. Ophthalmol. Vis. Sci. 59 (3), 1368–1373.
Yurchenco, P.D., 1990. Assembly of basement membranes. Ann. N. Y. Acad. Sci. 580, 195–213.
Yurchenco, P.D., Schittny, J.C., 1990. Molecular architecture of basement membranes. FASEB J. 4 (6), 1577–1590.
Zhu, P., et al., 2017. Short body length phenotype is compensated by the upregulation of nidogen family members in a deleterious nid1a mutation of zebrafish. J. Genet. Genom. 44 (11), 553–556.
Zoeller, J.J., et al., 2008. A central function for perlecan in skeletal muscle and cardiovascular development. J. Cell Biol. 181 (2), 381–394.

APPENDIX 4: SPATIOTEMPORAL CHARACTERIZATION OF ANTERIOR SEGMENT MESENCHYME HETEROGENEITY DURING ZEBRAFISH OCULAR ANTERIOR SEGMENT DEVELOPMENT

MW Contributions: Bioinformatic analyses for body of work.

frontiers in Cell and Developmental Biology

ORIGINAL RESEARCH
published: 27 May 2020
doi: 10.3389/fcell.2020.00379

Spatiotemporal Characterization of Anterior Segment Mesenchyme Heterogeneity During Zebrafish Ocular Anterior Segment Development

*Kristyn L. Van Der Meulen, Oliver Vöcking, Megan L. Weaver, Nishita N. Meshram and Jakub K. Famulski**

Department of Biology, University of Kentucky, Lexington, KY, United States

OPEN ACCESS

Edited by:
Claudia Tanja Mierke, Leipzig University, Germany

Reviewed by:
Min Zhang, Shanghai Children's Medical Center, China
Diego Franco, University of Jaén, Spain
Kristin Artinger, University of Colorado Denver, United States

****Correspondence:***
Jakub K. Famulski
jkfa226@uky.edu

Specialty section:
This article was submitted to Cell Adhesion and Migration, a section of the journal Frontiers in Cell and Developmental Biology

Received: *02 March 2020*
Accepted: *27 April 2020*
Published: *27 May 2020*

Citation:
Van Der Meulen KL, Vöcking O, Weaver ML, Meshram NN and Famulski JK (2020) Spatiotemporal Characterization of Anterior Segment Mesenchyme Heterogeneity During Zebrafish Ocular Anterior Segment Development. Front. Cell Dev. Biol. 8:379. doi: 10.3389/fcell.2020.00379

Assembly of the ocular anterior segment (AS) is a critical event during development of the vertebrate visual system. Failure in this process leads to anterior segment dysgenesis (ASD), which is characterized by congenital blindness and predisposition to glaucoma. The anterior segment is largely formed via a neural crest-derived population, the Periocular Mesenchyme (POM). In this study, we aimed to characterize POM behaviors and transcriptional identities during early establishment of the zebrafish AS. Two-color fluorescent *in situ* hybridization suggested that early AS associated POM comprise of a heterogenous population. *In vivo* and time-course imaging analysis of POM distribution and migratory dynamics analyzed using transgenic zebrafish embryos (Tg[*foxc1b:*GFP], Tg[*foxd3:*GFP], Tg[*pitx2:*GFP], Tg[*lmx1b.1:*GFP], and Tg[*sox10:*GFP]) revealed unique AS distribution and migratory behavior among the reporter lines. Based on fixed timepoint and real-time analysis of POM cell behavior a comprehensive model for colonization of the zebrafish AS was assembled. Furthermore, we generated single cell transcriptomic profiles (scRNA) from our POM reporter lines and characterized unique subpopulation expression patterns. Based on scRNA clustering analysis we observed cluster overlap between neural crest associated (*sox10*/*foxd3*), POM (*pitx2*) and finally AS specified cells (*lmx1b*, and *foxc1b*). scRNA clustering also revealed several novel markers potentially associated with AS development and/or function including *lum*, *fmoda*, *adcyap1b*, *tgfbi*, and *hmng2*. Taken together, our data indicates that AS-associated POM, or Anterior Segment Mesenchyme (ASM), is not homogeneous but rather comprised of several subpopulations with differing colonization patterns, migration behavior, and transcriptomic profiles.

Keywords: periocular mesenchyme, anterior segment, anterior segment dysgenesis, neural crest, *pitx2*, *foxc1*

INTRODUCTION

Vertebrate cranial development has benefitted significantly from the evolutionary addition of the multipotent neural crest cells (NCC). Originating in the dorsal neural ectoderm of the folding neural tube, neural crest cells (NCC) undergo an epithelial-to-mesenchymal transition, detaching themselves from the epithelial sheet and migrating in distinct streams to invade regions all over

the developing embryo. NCCs ultimately go on to form diverse mesodermal derivatives including cartilage, myofibroblasts, neurons, and glial cells (Trainor and Tam, 1995; Langenberg et al., 2008; Williams and Bohnsack, 2015). In the developing cranial region, migrating NCCs come together with lateral plate mesoderm to surround the developing optic cup and form the Periocular Mesenchyme (POM) (Trainor and Tam, 1995; Langenberg et al., 2008; Williams and Bohnsack, 2015). POM subsequently contribute to the development of the ocular anterior segment (AS) (**Supplementary Figure S1**) (Fuhrmann et al., 2000; Creuzet et al., 2005; Williams and Bohnsack, 2015; Akula et al., 2018). The AS, comprising of the cornea, lens, iris, ciliary body, and drainage structures of the iridocorneal angle, is essential for the function of the visual system. The AS focuses light onto the retina while maintaining intraocular homeostasis.

Anterior segment development begins after the establishment of the optic cup, when POM cells migrate into the periocular space between the retina and the newly established corneal epithelium (Creuzet et al., 2005; Cavodeassi, 2018). These mesenchymal cells will eventually differentiate into the corneal stroma and endothelium, iris and ciliary body stroma, and the iridocorneal angle, amongst others. Mis-regulation of POM migration or function has been associated with congenital blinding disorders under the term anterior segment dysgenesis (ASD). ASD includes, alone or in combination, corneal opacity, iris hypoplasia, polycoria, corectopia, posterior embryotoxon, juvenile glaucoma, and disorders including Peter's Anomaly and Axenfeld-Rieger Syndrome (Gould et al., 2004; Volkmann et al., 2011; Akula et al., 2018). These rare autosomal dominant disorders, in addition to ASD phenotypes, also often exhibit systemic issues including dental malformations and craniofacial defects (Volkmann et al., 2011; Bohnsack et al., 2012; Ji et al., 2016). In addition to congenital diagnoses, failure of proper AS formation may also result in a predisposition to ASD later in life. Despite its fundamental role in the establishment of the AS, little is understood about the mechanisms governing POM specification, migration or differentiation.

The most common mutations seen in ASD patients involve the transcription factor *pitx2* (Paired-like homeodomain) (Ji et al., 2016), as well as *foxc1* (Forkhead Box c1) (Berry et al., 2006; Bohnsack et al., 2012; Reis et al., 2012; Chen and Gage, 2016; Seo et al., 2017). Loss of function of either *pitx2* or *foxc1* has been shown to result in ASD phenotypes in mice and zebrafish (Berry et al., 2006; Liu and Semina, 2012; Reis et al., 2012; Chen and Gage, 2016; Ji et al., 2016; Seo et al., 2017; Hendee et al., 2018). *Pitx2* in particular has been associated with the survival and migration of NCCs, as well as the development of the optic stalk, establishment of angiogenic privilege within the cornea, and craniofacial development (Evans and Gage, 2005; Bohnsack et al., 2012; Liu and Semina, 2012; Gage et al., 2014; Chawla et al., 2016; Chen and Gage, 2016; Ji et al., 2016; Hendee et al., 2018). *Foxc1* and *pitx2* are also known to interact with one another, and their expression is regulated by retinoic acid signaling (Matt et al., 2005; Chawla et al., 2018). Not surprisingly, mutations in NCC regulatory genes have also been associated with ASD. *Foxd3* (Forkhead Box d3) has been implicated in ASD (Volkmann Kloss et al., 2012) and is known to regulate early NCC specification, migration and long-term cell survival (Lister et al., 2006; Stewart et al., 2006; Drerup et al., 2009; Wang et al., 2011). *Sox10* (SRY-Box 10), another key regulator of the NCC population (Dutton et al., 2001; Creuzet et al., 2005; Langenberg et al., 2008; Drerup et al., 2009; Williams and Bohnsack, 2015), is critical for NCC migration and viability during early development (Dutton et al., 2001). Finally, *lmx1b* (LIM homeobox Transcription Factor 1 beta) is associated with Nail-Patella syndrome and glaucoma predisposition (McMahon et al., 2009; Liu and Johnson, 2010). *Lmx1b* is expressed within the developing cornea, iris, ciliary bodies, and trabecular meshwork of the iridocorneal angle in mice (McMahon et al., 2009; Liu and Johnson, 2010) and is essential for POM migration in zebrafish (McMahon et al., 2009). While several genes have been linked to POM or ASD, few studies to date have shed light on how POM cells, migrate to and participate in AS formation.

One signaling molecule that is known to be involved in cranial neural crest cell migration and anterior segment specification is Retinoic Acid (RA). RA, a metabolite of vitamin A, is instrumental for the overall development of the eye. RALDHs (RA-synthesizing enzyme retinaldehyde dehydrogenases) are expressed in a gradient through the eye, specifically in the retina, cornea, RPE, and lens (Matt et al., 2005, 2008; Lupo et al., 2011). RA produced in these areas diffuses out toward the anterior space of the developing eye, which will be populated by the POM. RA signaling is activated through the heterodimer receptors RARα/RARβ and RARα/RARγ expressed within the POM (Matt et al., 2005, 2008; Lupo et al., 2011). This signal is a vital determinate in eye morphogenesis. Activation of these receptors helps to control *eya2* dependent apoptosis in the POM as well as control the expression levels of *foxc1* and *pitx2* and therefore anterior segment development (Matt et al., 2005, 2008). NCC-specific deactivation of RARα, RARβ, and RARγ results in a complete loss of *pitx2* in the POM and AS, while increased RA signaling leads to an increase in *pitx2*, *foxc1a*, and *lmx1b.1* (Matt et al., 2008; Lupo et al., 2011). Though not explicitly explored in this study, RA signaling is a crucial component of cell migration and overall eye morphogenesis.

Although information about the anatomy of the anterior segment in vertebrates and anatomical consequences of POM regulatory gene mutations has been well documented, few studies have investigated the mechanism of development for AS structures overall. Specifically, little is known about when or how POM cells acquire their AS targeting, behave during migration, interact with one another, and finally, specify into various AS structures. Within this study, we aimed to characterize the developmental underpinnings that drive the formation of the AS. Using zebrafish embryos, we characterized the precise migration patterns and transcriptional profiles of AS associated POM cells (ASM). We specifically examined ASM gene expression as well as cellular distribution by taking advantage of POM-associated transgenic lines; Tg[*foxc1b*:GFP], Tg[*foxd3*:GFP], Tg[*pitx2*:GFP], Tg[*lmx1b.1*:GFP], and Tg[*sox10*:GFP]. In doing so, we have cataloged distribution, migratory dynamics, and population size of ASM during early AS development. Furthermore, single cell transcriptomic comparison of isolated ASM cells revealed

four specific clusters, each associated with potentially novel AS regulatory genes. Our findings indicate that AS-associated POM is composed of several subpopulations, each identifiable by their own distributions, migratory patterns, and gene expression profile.

RESULTS

POM-Associated Genes Exhibit Unique Expression Patterns During Early Establishment of the Anterior Segment

With several genes being implicated in regulating POM migration and identity, we first chose to carefully characterize patterns of their expression during zebrafish ocular morphogenesis (12–72 hpf). Whole Mount *In Situ* Hybridization (WISH) using embryos aged 12, 18, 24, 32, 48, and 72 hpf revealed that POM-related genes *foxc1a*, *foxc1b*, *eya2*, *foxd3*, *pitx2*, *sox10*, *lmx1b.1* and *2*, display both overlapping and individualized expression patterns within their originating neural crest streams and surrounding the AS (**Figure 1**). Several POM-related genes showed expression at 12 hpf, the earliest time point we assayed, suggesting that POM acquire their identity early, perhaps immediately following their delamination from the neural tube. As the optic cup begins to take shape (18 hpf), *foxc1a*, *foxc1b*, and *sox10* expressing POM cells are already visible within the craniofacial space. At the same time, *pitx2* expression is absent from periocular regions and presents primarily in the lens. By 24 hpf we observed various degrees of periocular expression of all the aforementioned POM-associated genes. *Foxc1a* displays the prototypical POM expression pattern with signal extending from the forebrain and into the surrounding periphery, and on top of, the retina by 32 hpf (**Figure 1A** and **Supplementary Figure S1**). Similar, albeit much weaker expression of *foxc1b* and *eya2* can be observed at 24 and 32 hpf (**Figures 1B,H**). Both *foxd3* and *sox10* display partial periocular patterns of expression, predominantly in the temporal regions at 24 hpf and more homogenously by 32 hpf (**Figures 1C,G**). *Pitx2* also displays strong periocular expression staining at 32 hpf but is also uniquely expressed in the lens (**Figure 1D**). Periocular-like expression patterns become clearest by 48 hpf for *foxc1a*, *foxc1b*, *eya2*, *pitx2*, and *sox10*. *Foxd3* periocular expression is significantly diminished by 48 hpf. By 72 hpf only *foxc1a*, *pitx2*, *sox10*, and *eya2* still exhibit strong periocular expression. In spite of the implicated role of *lmx1b* genes in pathogenic features of the Nail-Patella Syndrome (McMahon et al., 2009; Liu and Johnson, 2010), both *lmx1b.1* and *lmx1b.2* genes did not display classical AS expression patterns in our WISH assay at early timepoints, 12–48 hpf, but are detected in the AS at later stages, 72 hpf+ (**Figures 1E,F**). Taken together, we observe that POM-associated genes are not uniformly co-expressed in POM cells during early AS formation. Early POM, 12–24 hpf, express high levels of *foxc1a*, and only at later stages of AS colonization, 24–32 hpf, do they initiate high levels of expression for *foxc1b*, *eya2,* and *pitx2*. POM cells which express *sox10*/*foxd3* display periocular patterns only after 24 hpf, suggesting they may arrive as a second wave. At late stages of AS colonization, 48–72 hpf, we observe the persistence of strong *foxc1a* expression and an upregulation of *foxc1b*, *pitx2*, and *eya2*. Between 48 and 72 hpf, *sox10* expression is detected throughout the AS but does not appear to increase significantly while *foxd3* expression is no longer detected in the AS after 48 hpf. Based on our WISH observations, we therefore hypothesized that AS colonizing POM populations are likely heterogenous.

Co-expression Analysis Confirms Anterior Segment Mesenchyme Heterogeneity

Based on our WISH study, we next sought to determine the extent of co-expression between the POM associated genes. To study these relationships, we performed two-color fluorescent whole mount *in situ* hybridization (FWISH) at 32 and 48 hpf. These timepoints represent early and intermediate steps of POM AS colonization. We focused our attention on the expression of *foxc1*, *foxd3*, *sox10*, and *pitx2* as they represent the best studied AS-associated POM marker genes. 3D confocal imaging qualitatively indicated that all these POM markers clearly exhibit both overlapping and individualized expression patterns at 32 hpf (**Figures 2A–F**). All of our described results are based on reproducible patterns observed in 12 hpf+ embryos from two independent experiments. At 32 hpf, *foxc1* expression appears restricted largely to the periphery of the AS while *sox10*, *foxd3*, and *pitx2* display varying degrees of expression throughout the dorsal, ventral, nasal, and temporal quadrants. *Pitx2* exhibited broad expression throughout the AS and a high degree of co-expression with *foxc1*, primarily in the dorsal quadrant, and *sox10*, throughout the entire AS, at 32 hpf (**Figures 2C,D**). *Foxc1* exhibited a high degree of co-expression with *pitx2* in the dorsal and ventro-temporal AS and partial co-expression with *foxd3* and *sox10* (**Figures 2A,B,D**). The expression of *sox10* was most pronounced in the dorsal AS and had the highest degree of co-expression with *foxd3* (**Figures 2B,C,F**). *Foxd3* expression was detected throughout the AS, albeit in fewer cells than the other markers, and exhibited a co-expression primarily with *sox10* and *pitx2* throughout the entire AS (**Figures 2A,E,F**). By 48 hpf, noticeably pronounced individualized expression patterns emerged (**Figures 2G–L**). *Pitx2* expression became restricted to the dorsal and ventral quadrants of the AS, while *foxc1* expression expanded into the entire AS (**Figures 2G–K**). Co-expression was still evident between *pitx2* and *foxc1*, but primarily in the dorsal and ventral quadrants. *Foxd3* and *sox10* maintained the same spatial pattern of expression as observed at 32 hpf and continued to have a high degree of co-expression, particularly surrounding the lens (**Figure 2L**). *Foxd3* and *sox10* continued to have only minor co-expression with *pitx2* or *foxc1* throughout the AS. We also analyzed expression of *eya2* and observed a high degree of co-expression with *pitx2* throughout the entire AS, and slight co-expression with all the other markers (**Supplementary Figure S2**). Taken together, we show that already at 32 hpf AS-associated POM do not exhibit a homogenous expression pattern of POM-associated regulatory genes. This suggest that the AS is colonized as an

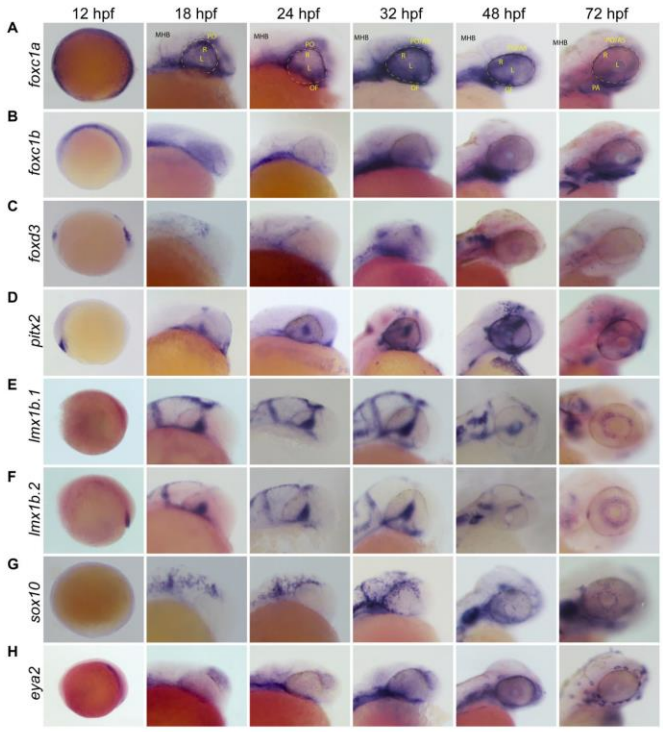

FIGURE 1 | Whole Mount *In Situ* Hybridization (WISH) of known POM and neural crest-related marker genes. Whole-mount *in situ* hybridization for POM marker gene mRNA expression patterns were observed during early to late stage eye development in the lateral view. POM genes examined were **(A)** *foxc1a*, **(B)** *foxc1b*, **(C)** *foxd3*, **(D)** *pitx2*, **(E)** *lmx1b.1*, **(F)** *lmx1b.2*, **(G)** *sox10*, and **(H)** *eya2*. *Foxc1a*, *foxc1b*, *pitx2*, *eya2*, and *sox10* in particular show strong expression surrounding the optic cup and on the surface of the anterior segment from 24 to 72 hpf. *Lmx1b.1* and *lmx1b.2* expression is detected within the anterior segment, surrounding the lens by 48–72 hpf. MHB, midbrain-hindbrain boundary; R, retina; L, lens; OV, optic vesicle; PO, periocular space (outlined with dashed line); OF, optic fissure; AS, anterior segment.

already heterogenous population rather than undergoing later diversification from a common progenitor.

POM Cells Display Distinct Targeting Patterns During Early AS Colonization

Based on our FWISH results we hypothesized that the heterogenous population of AS progenitors may display unique migration patterns and behavior. Furthermore, key to our understanding of AS formation will be the awareness of when and how the POM colonize. To begin characterizing this process, we first took advantage of available transgenic lines known to label POM: Tg[*foxc1b*:GFP], Tg[*pitx2*:GFP], Tg[*lmx1b.1*:GFP], or NCC: Tg[*foxd3*:GFP], Tg[*sox10*:GFP] (Matt et al., 2005, 2008; McMahon et al., 2009; Volkmann et al., 2011). These reporter lines enable single cell distribution analysis while also delineating lineage specification. Due to persistence of GFP protein, these lines do not necessarily represent active expression of their reporter driven promoter but do mark the lineage of POM/NCCs that have, at some point, expressed the respective POM-associated gene. To analyze AS colonization, transgenic embryos were fixed at key AS developmental stages (24, 26, 28, 30, 48, 56, and 72 hpf) and immunohistochemistry (IHC) was used to detect GFP. 3D confocal images of the AS were collected for each transgenic line at each timepoint and were employed to subsequently quantify distribution of the cells within the AS (**Figure 3A**). In particular, 3D rendered images of the AS were subdivided into four quadrants (**Figure 3A**, top left panel) and cells found in each were quantified at each timepoint.

Our assay revealed that initial colonization of the AS begins at approximately 22 hpf (data not shown) with GFP+ cells of the *pitx2*-derived population occupying the temporal AS regions

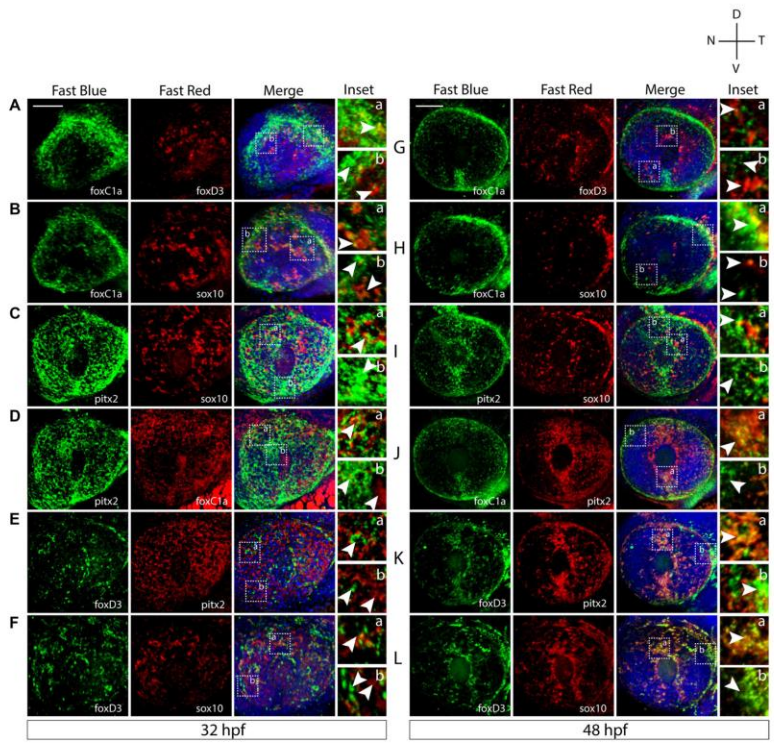

FIGURE 2 | Two-color fluorescent *in situ* hybridization supports ASM heterogeneity. Two-color fluorescent WISH (FWISH) performed for all possible combinations of *foxc1a*, *foxd3*, *pitx2*, and *sox10* at 32 **(A–F)** and 48 hpf **(G–L).** DAPI is in blue. Lateral images of 3D reconstructions are displayed. White arrows within inset panels (dashed squares) display instances of individual **(b)** and co-expression **(a)**. Scale bar = 50 μm.

(**Figure 3A**). At 24 hpf *foxc1b*, *foxd3*, and *lmx1b.1* derived GFP+ cells have begun to enter the AS across the dorsal most periocular regions, while *sox10*-derived cells begin to occupy all four regions. By 28 hpf all of the reporter lines, with the exception of *pitx2*, exhibit GFP+ cells primarily in the dorsal half of the AS. Tg[*foxc1b*:GFP] signal is also observed in the developing lens region up to 32 hpf, but was not considered for our analysis. Similarly, up to 32 hpf Tg[*lmx1b.1*:GFP] non-AS signal is observed in the dorsal-nasal region but is not considered in our analysis because it does not contribute to the AS. *Foxc1b*, *foxd3*, and *sox10* derived cells continue to spread to the ventral regions with roughly equal distribution throughout the AS by 48 hpf. Conversely, *pitx2*-derived cells remain exclusively associated with the temporal half of the AS while *lmx1b.1*-derived cells gradually re-distribute to occupy the nasal half of the AS. Starting at 54 hpf and continuing to 72 hpf, Tg[*pitx2*:GFP] expression turns off in POM cells and initiates in what is likely photoreceptor progenitor cells. Of note, our Tg[*pitx2*:GFP] transgenic line did not exhibit GFP signal in all regions of AS that were found to be positive for *pitx2* mRNA using FWISH (**Figures 2**, **3A**). We hypothesize this discrepancy arises from the fact that ASM progenitor cells induce *pitx2* expression upon arrival at the AS, while the GFP+ cells are a lineage mark of the early *pitx2*+ progenitors. The enhancer element driving the Tg[*pitx2*:GFP] line, C4, may be no longer responsive in ASM cells at the later time points and therefore explain the lack of GFP signal in all of the *pitx2* expressing cells.

All of our observations were subsequently validated by quantification of each GFP+ population (**Figure 3B**). At 24 hpf the majority of POM cells are located within the dorsal half of the AS, with the exception of *pitx2*-derived cells. By 30 hpf we note a significant reduction in the proportion of *foxc1b*, *foxd3*, and *lmx1b.1*-derived cells in the dorsal half combined with significant increase of these cells in the ventral half. At 48 hpf, we found equal distribution of *foxc1b*, *foxd3*, and *sox10* derived cells within all regions of the AS, while

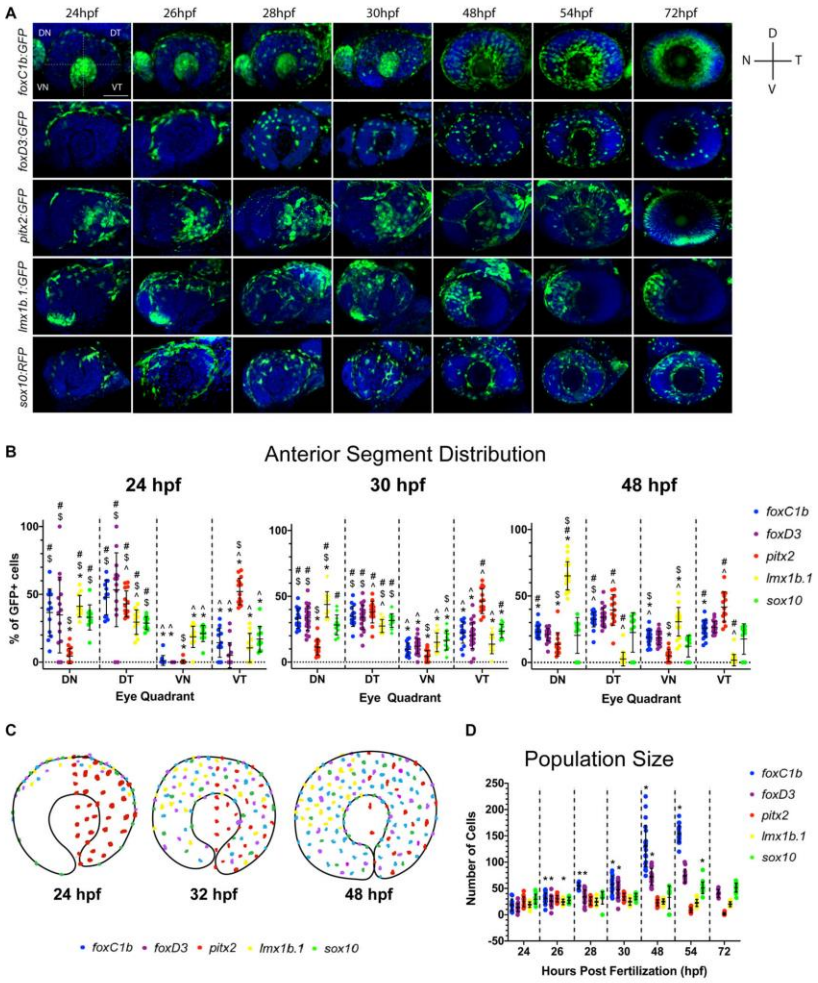

FIGURE 3 | Periocular mesenchyme subpopulation distribution analysis. **(A)** 3D rendering of confocal stacks encompassing the AS in POM transgenic lines between 24 and 72 hpf. GFP+ cells are green, DNA was stained with DAPI (blue). DN, dorsal-nasal; DT, dorsal-temporal; VN, ventral-nasal; VT, ventral-temporal. Scale bar = 50 μm. **(B)** Distribution of quantified GFP+ cells within each AS quadrant (DN, DT, VN, and VT) at 24, 30, and 48 hpf. Distribution is represented as an average percentage of the total number of GFP+ in each quadrant of the AS for each transgenic line. Statistically significant difference ($p < 0.05$): * vs. DT, # vs. VN, $ vs. VT and ^ vs. DN. **(C)** Model of POM colonization at 24, 30, and 48 hpf. **(D)** Average AS cell population size for each transgenic line at 24–72 hpf. * indicates statistically significant ($p < 0.05$) change from previous time point.

lmx1b.1-derived cells become predominantly associated with the nasal half of the AS.

Overall, we observe an ordered pattern of AS colonization, as summarized in **Figure 3C**. The majority of POM cells, *foxc1b*, *foxd3*, and *sox10*:GFP-derived cells, enter the AS along the dorsal retina and progress ventrally, while the *pitx2:*GFP sub-lineage enters the AS temporally and remains exclusively within the temporal AS. *lmx1b.1*:GFP cells enter the AS dorsally and initially migrate ventrally but by 48 hpf become restricted to the nasal regions of the AS.

Cell Proliferation Does Not Drive ASM Population Growth During AS Colonization

A distinct fluctuation in the total number of GFP+ cells within each transgenic line examined throughout the time course was also noted. While *lmx1b.1*, *pitx2*, and *sox10*-derived populations maintained a relatively consistent total number of cells, f*oxc1b* and *foxd3*-derived populations increased in size over time (**Figure 3D**). This is particularly evident in the *foxc1b*-population which increased size so significantly by 72 hpf that it was no longer quantifiable by our assay. Having documented the increase in population size of some ASM subpopulations, we next sought to understand the mechanisms responsible for this change. Specifically, we wanted to investigate whether the increase in population size of the *foxc1b:GFP* and *foxd3:GFP* subpopulations was the result of a continued influx of migratory cells into the AS or proliferation of cells already in the AS. Transgenic embryos were fixed at 32 and 48 hpf as this window in development sees the largest increase in population size. Proliferating cells were identified using pH3 antibody staining. 3D images of the AS were collected using a confocal microscope. Cells positive for both the GFP and the pH3 signal were quantified (**Supplementary Figure S3**). Little to no pH3 signal at either 32 or 48 hpf in *foxd3*:GFP or *foxc1b*:GFP embryos, or any of our transgenic lines, indicates that ASM cells are not actively dividing while migrating within the AS. Based on these data, we suggest that the increase in *foxc1b*:GFP and *foxd3*:GFP cell populations is the sole result of rapid and continuous migration of cells to the AS between 32 and 48 hpf.

ASM Subpopulations Exhibit Unique Migratory Behavior

In addition to cellular distribution over time, we also sought to catalog the migratory behavior of ASM cells. Specifically, we aimed to determine if they behaved in a similar fashion to cranial NCCs. Hence, we tracked their migration within the AS using *in vivo* 4D imaging. Using this approach we documented migration of *foxc1b*:GFP, *foxd3*:GFP, *pitx2*:GFP, *lmx1b.1*:GFP, and *sox10*:GFP-derived cells (**Figure 4A**). Qualitative examination of our data indicated that in all the transgenic lines, ASM cells migrated in a stochastic manner. This suggests that similar to cranial NCCs, ASM cells lack leader/follower cell identities or chain migration behavior (**Figure 4A** and **Supplementary Movies S1–S5**). The 4D data sets mirrored the cellular distribution trends we quantified in our previous time course assay (**Figure 3**). As expected based on our distribution studies, both *pitx2* and *lmx1b.1*:GFP cells displayed very specific distributions within the AS (**Figure 4B**), while *foxc1b*, *foxd3*, and *sox10*:GFP had more homogenous distribution patterns.

To analyze individual migratory behavior, we performed individual cell tracking. As expected, *foxc1b*:GFP, *foxd3*:GFP, *lmx1b.1*:GFP and *sox10*:GFP-derived cells migrated in a general dorsal to ventral pattern (**Figure 4B** and **Supplementary Movies S6–S10**). *Pitx2*:GFP cells migrated in a generally temporal to nasal direction (**Figure 4B**). Tracked cells were analyzed for their total distance traveled, directed migration, and velocity. *Foxc1b*-derived ASM had the highest velocities (0.115 ± 0.048 μm/min) while the cells of the *pitx2*-derived subpopulation were the slowest (0.049 ± 0.023 μm/min) (**Figure 4C**). *Foxd3*, *lmx1b.1*, and *sox10*-derived ASM cells had similar velocities (0.095 ± 0.042; 0.091 ± 0.050; and 0.079 ± 0.033 μm/min). When examining total distance traveled, *foxc1b*-derived cells displayed the farthest distances overall (44.667 ± 18.531 μm), while *pitx2*-derived cells exhibited the shortest (20.719 ± 9.936 μm) (**Figure 4D**). *Foxd3*, *lmx1b.1*, and *sox10*-derived ASM all exhibited similar overall distances traveled (37.339 ± 16.769; 33.267 ± 15.869; and 31.688 ± 13.289 μm). Differences in total migratory distance and velocity based on the AS quadrant of entry were also compared. Only *foxc1b*-dervied cells originating in the dorsal temporal quadrant showed differences in migration displaying shorter total distance traveled and slower velocity (data not shown). Based on analysis of migration velocity and distance traveled we conclude that ASM exhibit of a mixture of migration patterns and behaviors. This further supports our hypothesis that during colonization of the AS, the ASM are a heterogenous population.

Lastly, we measured the degree of directed migration by examining individual cell displacement within the AS (**Figure 4E**). Displacement was used as a measure of purposeful, or targeted, migration. We saw that cells within the *sox10* subpopulation showed the highest overall displacement (136.885 ± 63.327 pixels), followed by cells in the *foxd3* subpopulation (109.70 ± 75.434 pixels). Displacement of *foxc1b* and *lmx1b.1* was found to be 84.632 ± 49.223 and 95.559 ± 61.285 pixels, respectively. Similar to our previous observations for velocity and distance, the *pitx2* subpopulation exhibited the least amount of displacement (44.698 ± 33.008 pixels). Our data indicate that all ASM cells are highly migratory, but that as observed for POM marker gene expression, there is heterogeneity when comparing the various reporter lines.

ASM Subpopulations Cluster According to Developmental Transcriptomic Profiles

Having observed the AS-associated POM subdivide into several ASM subpopulations, based on distribution and migratory behavior, our final goal was to analyze single cell transcriptomic profiles of ASM cells during AS colonization. To do so, we dissected the eyes off of our transgenic embryos at 48 hpf, isolated GFP+ cells via FACS, and subsequently employed the Chromium 10X genomics platform to generate single cell transcriptomes (scRNA). Resulting transcriptomes were sequenced using Illumina technology and analyzed using Cell Ranger3.1 and Loupe software. In total we sequenced 2,460 individual cells with per cell reads of greater than 100,000 (**Supplementary Table S2**).

K-means clustering (t-SNE) of all five data sets resulted in four distinct clusters (**Figure 5A** and **Supplementary Figure S4**). We identified one predominantly NCC-like cluster

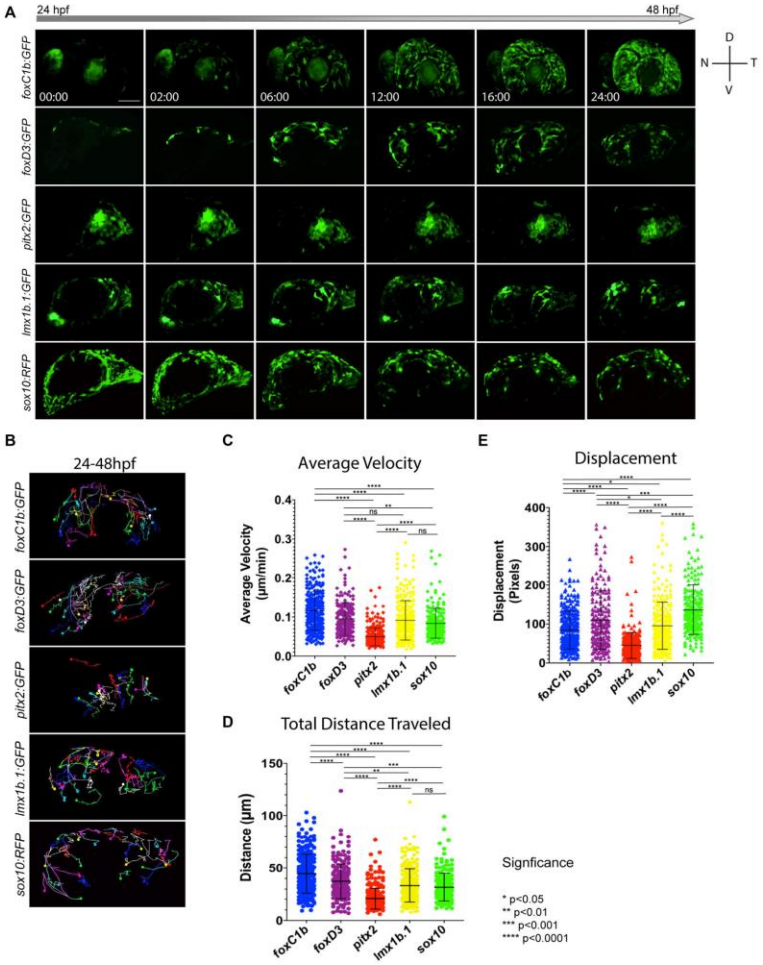

FIGURE 4 | *In vivo* 4D imaging of POM anterior segment colonization. **(A)** 4D *in vivo* imaging of the AS conducted between 24–48 hpf using POM transgenic lines. Time stamp hours:minutes. Scale bar = 50 µm. **(B)** Individual cell tracking for each POM transgenic line reveals migratory patterns during early AS colonization. Solid spheres indicate terminal end of track. **(C–E)** Cell tracking measurements of average migratory velocity (ANOVA $p < 0.0001$), total migration distance (ANOVA $p < 0.0001$), and migratory displacement within the AS (ANOVA $p < 0.0001$).

(Cluster 1) with cells largely originating from the *foxd3* and *sox10* transgenic lines (**Figure 5B**). 85.6% of *sox10*:GFP and 84.3% of *foxd3*:GFP cells were found in cluster 1. *Sox10*:GFP and *foxd3*:GFP cells were also found in cluster 3 with 11.5 and 15% of their total distribution, respectively. A majority of cells isolated from the *foxc1b*:GFP line were found in Cluster 2, 70.1%, with a small proportion also present in cluster 3, 10.2%, and cluster 4, 15.8% (**Figure 5B**). *Pitx2:GFP* isolated cells were predominantly found in cluster 3, 83.9%, and cluster 2, 7.1%, with a low proportion found in clusters 1 and 4, 5.3% and 3.6% distribution, respectively. *Lmx1b*:GFP derived cells have the unique classification of being almost equally represented throughout all 4 clusters, 24.3% in cluster 1, 15.7% in cluster 2, 29% in cluster 3

and 31% in cluster 4 (**Figure 5B**). When comparing spatially, UMAP-based plotting of the clusters indicated a continuous or connected expression profile suggestive of interaction or progression between the clusters (**Figure 5A** and **Supplementary Figure S4**). The placement of the clusters within the UMAP graph predicts interaction between *sox10/foxd3* with *pitx2*, *pitx2* and *lmx1b/foxc1b* and finally *lmx1b/foxc1b* with *foxc1b*-derived cells (**Figure 5C**). Interestingly, cluster 4 appears to represent a transition stage where multiple AS cell fates are possible. Taken together, we observed that none of the clusters are made up solely of cells originating from one individual transgenic line. This observation is supported by our two-color fluorescent *in situ* expression analysis (**Figure 2**) and is particularly relevant in terms of the relationships amongst POM associated genes, particularly *pitx2* and *foxc1* whose products are actually known to physically interact (Matt et al., 2005; Chawla et al., 2018). Finding four distinct subpopulations of ASM cells further supports our previous findings that suggest ASM are a developmentally heterogenous population during colonization of the AS.

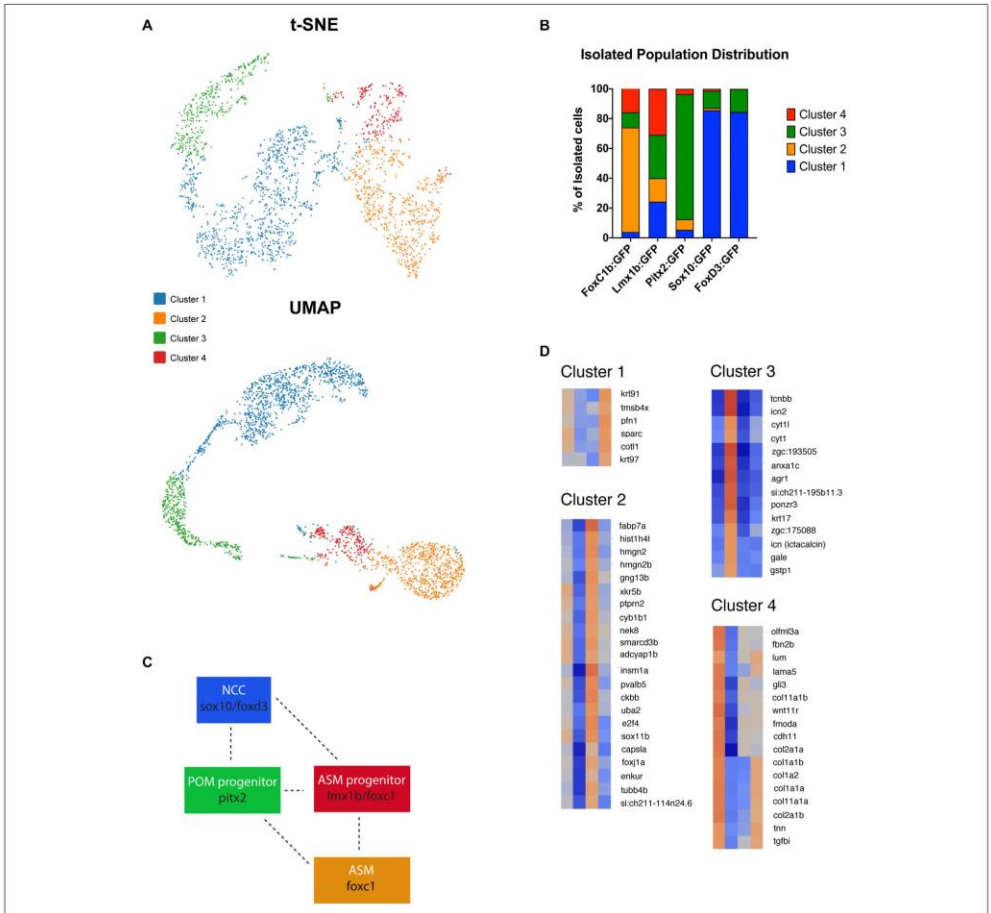

FIGURE 5 | Anterior segment mesenchyme single cell clustering analysis at 48 hpf. **(A)** *K*-means clustering of scRNA sequencing of isolated 48 hpf *foxc1b*:GFP, *lmx1b*:GFP, *sox10*:GFP, *foxd3*:GFP, and *pitx2*:GFP ASM cells in both tSNE and UMAP readouts. Both plots identified four general clusters. **(B)** Distribution of isolated ASM cells within each of the clusters generated by the Cell Ranger3.1 software. **(C)** Model of identified cluster interactions. Interaction and overlap is indicated by dashed lines. **(D)** Heat maps of cluster specific gene expression patterns.

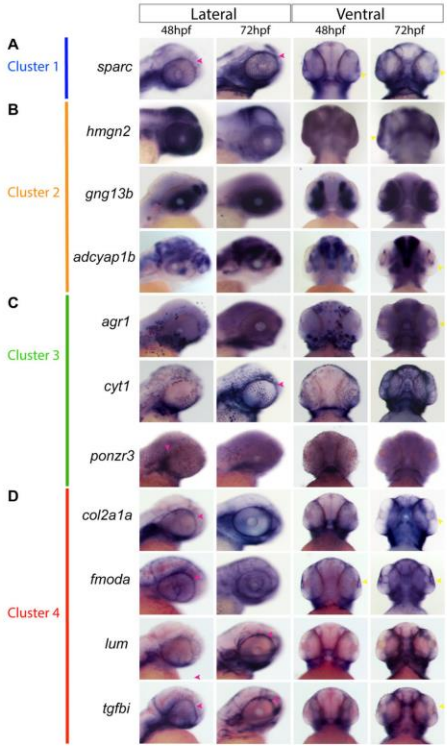

FIGURE 6 | Gene expression of sequencing-derived genes. Whole-mount *in situ* hybridization for novel ASM marker gene mRNA expression patterns was performed during early (48 hpf) and intermediate stages (72 hpf) of AS development and observed in lateral and ventral views. **(A)**, *Sparc* expression representing cluster 1. **(B)** *gng13b*, *hmgn2*, and *adcyap1b* expression representing cluster 2. **(C)** *cyt1*, *agr1*, and *ponzr3* expression representing cluster 3. **(D)** *lum*, *fmoda*, *col2a1a*, and *tgfbi* expression representing cluster 4. Yellow arrowheads indicate AS expression, magenta arrowheads indicate periocular expression.

scRNA Analysis of ASM Uncovers Novel AS Markers

Based on the clustering analysis we generated heatmaps and gene ontology analysis of the most representative expression patterns for each cluster (**Figure 5D** and **Supplementary Figure S5**). Within some of the clusters, genes with possible links to one or more AS structures were identified based on association with ASD-related disorders or potential similarities to POM/NCC-like expression patterns. For example, *cyp1b1*, known to be associated with glaucoma predisposition (Zhao et al., 2015), was identified in cluster 2, while *tgfbi*, isolated in cluster 4, is associated with corneal dystrophy (Poulaki and Colby, 2008). We also noted expression of several collagen (*col2a1a*, *1a1b*, *1a2*, *1a1a*, *2a1b*, *11a1a*, and *11a1b*) and laminin (*lama5*) genes, known to be associated with extracellular matrix properties of AS trabecular meshwork cells (Abu-Hassan et al., 2014), in cluster 4 (**Figure 5D**). Importantly, our analysis also identified novel candidate genes potentially associated with AS specification and development. We therefore analyzed expression of several potential novel target genes to assess their contribution to AS development at 48 and 72 hpf. Our expression analysis included *sparc* (cluster 1); *gng13b*, *hmgn2* and *adcyap1b* (cluster 2); *cyt1*, *arg1*, *ponzr3*, and *si:ch211-195b11.3* (cluster 3); and *lum*, *fmoda*, *tgfbi*, and *col2a1a* (cluster 4) (**Figure 6**). Examining expression of cluster 1 associated gene *sparc* revealed that at 48 and 72 hpf *sparc* mRNA was associated with the developing AS, in particular the periphery of the lens and iris regions (**Figure 6A**). From cluster 2, we examined expression of *hmgn2*, *gng13b*, and *adcyap1b*. We observed strong expression of *hmgn2* throughout the AS by 72 hpf, and strong expression of *adcyap1b* in the lens periphery and future iris region (**Figure 6B**). Cluster 3 targets included *agr1*, *cyt1*, *ponzr3*, and the currently uncharacterized *si:ch211-195b11.3*. Both *cyt1* and *agr1* appear to label dermal cells in the periocular and AS regions (**Figure 6C**). *Ponzr3* did not display AS associated expression patterns (**Figure 6C**), while *si:ch211-195b11.3* does not appear to be related to the AS development (data not shown). Lastly, from cluster 4 we examined *col2a1a*, *fmoda*, *lum,* and *tgfbi* expression. By 72 hpf, we observed strong expression of *fmoda* in the AS as well as some overlapping expression of *tgfbi* and *col2a1a* (**Figure 6D**). Several genes in our list including *sparc*, *col2a1a*, *lum*, and *tgfbi* also demonstrated periocular expression patterns similar to other known ASM genes at 48 hpf. In particular, *sparc* expression was reminiscent of *sox10*, *lum* expression was reminiscent of *foxc1a* while *tgfbi*, *col2a1a,* and *fmoda* expression were reminiscent of *foxc1b* and *eya2* (**Figures 1**, **6**). In summary, our single cell transcriptomic analysis of ASM cells identified several novel markers associated with early AS formation which may represent uncharacterized regulators of AS development and/or function.

CONCLUSION

In the literature, POM has become an umbrella term associated with a host of developmental events including cranial-facial, vascular, retinal as well as anterior segment development. In order to provide some much-needed clarity, our study aimed to characterize specifically the AS associated subset of POM cells, which we term the ASM. As such, our focus was strictly on POM cells that have entered the AS and ultimately contributed to its formation. We used a combination of *in situ* hybridization, real-time imaging of transgenic reporter lines and single cell transcriptomic analysis. Based on our results of ASM distribution, migration dynamics and lastly single cell transcriptional profiles, we conclude that AS colonization employs several distinct, yet developmentally connected, subpopulations of ASM. Overall, our work is the first comprehensive examination of ASM during AS development in

zebrafish which we believe will serve as a starting point for future studies of novel regulators of this critical developmental event.

Observing a lack of total co-expression for POM marker genes in ASM cells suggested to us a lack of uniformity within the population. Furthermore, when co-expression of POM markers occurred, the degree and localization within the AS varied between genes examined (**Figures 1**, **2**). *Sox10* and *foxd3*, both NCC markers, appear to be co-expressed in ASM cells distributed over the entire AS at 32 hpf (**Figures 2A–C,E,F**). Co-expression of *pitx2* and *foxc1* was limited to the periphery of the AS while co-expression of *pitx2* and *eya2* was detected throughout the AS (**Figure 2D** and **Supplementary Figure S2**). *Pitx2* displayed a high degree of co-expression with all other POM and NCC markers which likely coincides with its predicted wide-reaching role during AS development. Although we do see some degree of co-localization amongst all POM marker genes, the distinction between each gene's expression pattern remains evident. Individual ASM cells therefore exhibit a range of POM marker expression patterns which supports our hypothesis that the ASM is heterogenous during AS development. Our findings also speak for the fact that when deciding on a marker for analysis of ASM, not all of the classical POM marker genes may be representative of the entire population and this should be taken into consideration during experimental design.

Utilizing transgenic lines: *foxc1b*:GFP, *foxd3*:GFP, *pitx2*:GFP, *lmx1b.1*:GFP, and *sox10*:GFP we examined the dispersal and distribution of ASM cells during the critical window of POM AS colonization (24–72 hpf). Our detailed imaging studies indicated that the first POM cells arrive on the AS between 22–24 hpf (**Figure 3A**). GFP+ cells of the *pitx2* subpopulation appear to arrive the earliest of all observed ASM populations, entering the AS as early as 22 hpf, and specifically from the temporal quadrant. When examined as a whole, ASM colonization is, however, primarily dorsal in origin and ASM cells proceed to spread throughout the AS as development proceeds. This pattern was observed for *foxc1b*:GFP, *foxd3*:GFP, *sox10*:GFP, and *lmx1b*:GFP ASM cells. In addition to several differing entry points, we also observed varying targeting behavior of ASM cells. By 48 hpf homogenous AS distribution was observed for *foxc1b*:GFP, *foxd3*:GFP, and *sox10*:GFP cells. Conversely, *lmx1b.1*:GFP and *pitx2*:GFP cells remained strictly restricted to the nasal and temporal quadrants of the AS, respectively. This is a clear indication that heterogeneity during AS colonization is also a potential mechanism for specific targeting within the AS. Lastly, we observed that migratory ASM are not actively undergoing cellular division. The rapid increase in ASM cell number between 24–48 hpf within some subpopulations, in particular *foxc1b*:GFP and *foxd3*:GFP, may therefore be primarily attributed to the continual arrival of migratory cells to the AS. This notion is supported by the fact that cranial NCCs, the main source of POM/ASM, originate dorsal to the AS and that we observe *foxd3*:GFP and *foxc1b*:GFP cells entering the AS predominantly within the dorsal quadrant. Alternatively, it remains possible that GFP+ cells represent a non-proliferative pool of ASM. Analyzing co-expression of ASM markers and cell cycle transcripts will be necessary to test this alternative. When combining all of our ASM distribution data, we propose a progressive colonization model outlined in **Figure 3C**.

The ability to migrate long distances and respond to specific cues is a crucial and well documented behavior of NCCs. Cranial NCCs migrate without designated leader or follower identities, instead maintaining a large homogenous population wherein each member exhibits the same migratory capabilities as its neighbors (Clay and Halloran, 2010; Kulesa et al., 2010; Richardson et al., 2016). 4D live imaging of *foxc1b*:GFP, *foxd3*:GFP, *sox10*:GFP, *pitx2*:GFP, and *lmx1b.1*:GFP transgenic embryos aged 24–48 hpf showed a uniform migration behavior pattern in ASM subpopulations indicative of cranial neural crest-like migration (**Supplementary Movies S1–S5**). Tracking analyses indicated cells had stochastic and independent migratory capabilities, frequently pausing during migration, altering directionality, and extending filipodia to communicate with one another (**Supplementary Movies S6–S10**). Quantification of total distance and average velocity indicated that *foxc1b*:GFP ASM cells traveled the farthest distance and with the highest velocity (**Figures 4C,D**). Conversely, *pitx2*:GFP ASM cells traveled the shortest distances and with the slowest velocities, but also with the least amount of stochastic movement (**Figures 4B–D**). Interestingly, since *pitx2*:GFP+ cells are the first POM cells to colonize the AS, we hypothesize that they may serve as sentinels to mark the AS for later arriving POM. Their need for timely arrival at the AS may explain their unique, highly targeted, migratory behavior. Displacement, also referred to as directed migration, was measured as a way to characterize the purposeful migration of ASM cells. We wanted to quantify whether certain ASM cells migrated with more directionality than their counterparts. Interestingly, our data indicates that cells in the *sox10*:GFP and *foxd3*:GFP subpopulation, associated with NCC identity (Stewart et al., 2006; Drerup et al., 2009; Wang et al., 2011), engage the most in directed migration (**Figure 4E**). These likely pluripotent, NCC-like cells may be directly targeting to specific regions of the AS in order to ensure equal distribution. Cells likely associated with a more traditional POM identity, *foxc1b*:GFP and *pitx2*:GFP (Liu and Semina, 2012; Reis et al., 2012), appear to have more stochastic migration paths (**Figure 4E**). A more stochastic migration pattern may be indicative of ASM cells further along the differentiation spectrum and no longer needing to target to specific AS regions. Similar to our observations of ASM expression patterns and distribution (**Figures 1–3**), migratory behavior is also clearly variable amongst ASM cells which further supports the notion of a heterogenous population.

Lastly, we investigated the transcriptomic differences amongst the ASM. Utilizing the 10× Genomics process of scRNA sequencing, we isolated 48 hpf eyes from transgenic embryos (*foxc1b*:GFP, *foxd3*:GFP, *lmx1b*:GFP, *sox10*:GFP, and *pitx2*:GFP) and used FACS to isolate our GFP+ ASM cells. This approach aimed to ensure only AS associated cells were included in our analysis. ASM specific single cell cDNA libraries were generated, sequenced, and based on transcriptomic profiles, grouped into four distinct clusters (**Figures 5A,B**). We classified these clusters into a NCC-like cluster (*sox10/foxd3*), POM progenitor cluster

(*pitx2*), a ASM progenitor cluster (*lmx1b/foxc1b*) and finally a specified ASM cluster (*foxc1b*) (**Figures 5B,C**). UMAP analysis of the data indicates a connection between clusters suggesting that ASM cells may be found along a heterogenous, but connected, spectrum during AS colonization. This connection is also apparent when examining the cluster associated percentage distribution of our isolated cells. The four clusters all appear to be connected along a plausible trajectory of AS development starting with the NCC-like cluster (cluster 1), then the POM progenitor cluster (cluster 3) followed by the ASM progenitor cluster (cluster 4) and finally an ASM-like cluster (cluster 2). We predict that early AS is therefore likely colonized by a heterogenous population of ASM that may represent different stages of differentiation along the path to an AS cell fate. This combination could ensure that while some ASM enter already poised to begin differentiation and assembly of functional AS structures, such as the *pitx2*, *foxc1b*, or *lmx1b* driven subpopulations, others that are likely more pluripotent, *foxd3/sox10* driven, serve to ensure that proper numbers of ASM arrive at all points along the AS and then further differentiate in response to local signaling cues. It is therefore not surprising that distributions, migratory patterns and transcriptomic profiles of *sox10*:GFP and *foxd3*:GFP cells are highly similar when compared to *foxc1b*:GFP, *lmx1b.1*:GFP, or *pitx2*:GFP. Finally, while transcriptomic differences observed in our data support the notion of a heterogenous ASM population, they do not infer lineage marking. Future fate mapping experiments will need to be performed to determine whether specific transcriptomic differences directly determine cell fate or simply represent transitional states along the ASM differentiation pathway.

Expression analysis of cluster specific targets identified by our scRNA assay revealed a number of genes of particular interest including *sparc*, *hmgn2*, *adcyap1b*, *agr1*, *col2a1a tgfbi*, and *fmoda* (**Figure 6**). Several of these genes are associated with regulation and function of the extracellular matrix including *sparc*, *col2a1a*, and *fmoda*, indicating a possible relationship with the drainage systems of the iridocorneal angle (Abu-Hassan et al., 2014). While the drainage networks are the last to fully differentiate in the AS, their importance to the function of the eye cannot be understated. *Tgfbi* is associated with head mesenchyme and neural crest and is also predicted to be localized to the extracellular matrix (Chakravarthi et al., 2005; Kannabiran and Klintworth, 2006). Interestingly, the t*gfbi* gene is associated with a subset of familial corneal dystrophies (Nielsen et al., 2020). *Hmgn2* is a non-histone component of nucleosomal DNA and is associated with transcriptionally active chromatin, especially in cells that remain undifferentiated, and is involved in DNA replication, transcription, and repair (Lucey et al., 2008; Furusawa and Cherukuri, 2010). Although not yet associated with AS development or ASD pathology, *hmgn2* is abundantly expressed throughout the ocular structures of the AS and retina in mice, especially in the lens fibers and epithelium layer of the cornea (Lucey et al., 2008). *Adcyap1b* is a neuropeptide also known as PACAP associated with brain and camera-type eye development, meaning that it plays a role in the development of the lens and retina of the eye (Wu et al., 2006; Denes et al., 2019). PACAP also appears to have retinoprotective attributes (Shioda et al., 2016). The mechanisms of *adcyap1b* function during AS development is unclear at this time. Finally, *agr1* is associated with the negative regulation of cell death, regenerative abilities of fish and frogs and is strongly associated with liver function (Ivanova et al., 2015, 2018). While it's function within the eye remains unclear at this time, *agr1* does show expression in the corneal region (**Figure 6**) (Ivanova et al., 2015). Future studies will focus on examining the functional roles of the aforementioned AS associated target genes as well as others from our transcriptomic screen (**Figure 5D**). We will also seek to determine whether the identified clusters also represent lineages of specific AS structures, such as the cornea, iridocorneal angle (annular element in zebrafish) or iris.

Heterogeneity within the early colonizing POM and subsequent ASM poses an important question: what is the functional interplay between such subpopulations? Previous studies of AS development in several models suggest that there are in fact "master regulators" of this process, in particular *foxc1* and *pitx2*. Loss of function of either has significant consequences on AS formation and function. However, the status of other POM/ASM markers, or subpopulations, in these circumstances has not been thoroughly examined. It therefore remains unknown whether all ASM subpopulations are affected and to what degree. We know even less about the consequences of other POM/ASM regulators, such as *eya2*, *foxd3*, or *lmx1b*, in this context. Future work will need to concentrate on carefully teasing out how individual regulators of POM influence the entire process of AS colonization, rather than simply observing for physiological consequences in juvenile or adult AS tissues.

In conclusion, our findings, based on distribution, migration and transcriptomic profiles, indicate that POM cells targeted to the anterior segment, which we have termed the Anterior Segment Mesenchyme (ASM), are not homogenous. Rather, the ASM simultaneously comprises of several subpopulations likely divided along the ASM differentiation pathway. Our findings open a wide range of possible new investigative paths in the area of AS development and ASD disorders. Future examination of the interplay between these subpopulations will be prudent to further our understanding of eye development and ultimately predisposition to ASD associated blinding disorders.

MATERIALS AND METHODS

Zebrafish Maintenance

Zebrafish lines were bred and maintained in accordance with IACUC regulations (IACUC protocol 2015-1380) at the University of Kentucky. AB strain was used as wildtype. Transgenic lines used were: Tg[*foxc1b:GFP]* (Dr. Bryan Link), Tg[*foxd3:GFP]* (Dr. Lister), Tg[*pitx2C4:GFP]* (Dr. Elena Semina), and Tg[*lmx1b.1:GFP]* (Dr. Brian Link), Tg[*sox10:RFP]* (Dr. Lister). All embryos were raised for the first 24 h post fertilization in embryo media (E3) at 28°C. After 24 h, E3 media was replaced with embryo media containing 1-phenyl 2-thiourea (PTU) every 24 h to maintain embryo transparency.

Whole-Mount *in situ* Hybridization (WISH)

Whole-mount *in situ* hybridizations were performed using a minimum of 20–25 embryos for each time point (12, 18, 24, 32, 48, and 72). DIG and FITC labeled RNA probes were created using PCR incorporating T7 promoters in the primers and transcribed with T7 polymerase (Roche). Forward and Reverse primer sequences are listed in **Supplementary Table S1**. WISH protocol was performed as previously described (Holly et al., 2014). Dorsal, lateral, and ventral images of embryos were captured using a Nikon Digital Sight DS-U3 camera and Elements software. Images were adjusted for brightness using Adobe Photoshop and assembled into figures using Adobe Illustrator.

Immunohistochemistry (IHC) for Distribution and Proliferation Analysis

Approximately 30 embryos were imaged for each transgenic line at each of the given time points (24, 26, 28, 30, 48, 54, and 72 hpf). Embryos were fixed overnight at 4°C using 4% PFA. PFA was washed out with PBST 4 times for 5 min each. Embryos were permeabilized with Proteinase K (10 μg/ml) at the following times (24 hpf = 5 min; 26 hpf = 6 min; 28 hpf = 7 min; 30 hpf = 9 min; 48 hpf = 20 min; 54 hpf = 25 min; 72 hpf = 40 min), washed with PBST and then blocked with 5% goat serum (1 g/100 ml), 1% BSA in a solution of 1x PBST for at least 2 h at room temperature. Primary antibody (Rockland rabbit anti-GFP) was diluted at 1/200 in blocking buffer and incubated overnight at 4°C on rotation. The following day, the primary antibody solution was washed out with PBST 5 times for 15 min each. Secondary antibody (Alexa Fluor 488 anti rabbit, 1/1000) and DAPI (1/2500) were diluted in blocking buffer and incubated for 1 h on rotation in the dark at room temperature. Embryos were washed 2× for 15 min with PBST in the dark.

After staining, embryos were embedded in a 1.2% Low-gelling agarose in a 1-inch glass bottom cell culture dish (Fluorodish, World Precision Instruments) and visualized using a Nikon C2+ confocal microscope with a 20× (0.95 NA) oil immersion objective. The anterior segment of the eye was imaged in 3D in the lateral position as a 100 μm z-stack using 3.50 μm steps. All images were captured using Nikon Elements software, adjusted for contrast and brightness using Adobe Photoshop and assembled into figures using Adobe Illustrator. Images generated from IHC analysis were rendered in 3D using Nikon Elements Viewer software. Eyes were divided into 4 quadrants: dorsal nasal, dorsal temporal, ventral nasal, and ventral temporal. Nasal and temporal regions were divided by a vertical straight line through the center of the lens, while dorsal and ventral were divided by a horizontal straight line through the center of the lens. For distribution analysis, GFP+ cells were manually counted based on their position within one of the four quadrants of a 3D constructed anterior segment. For each timepoint 25+ embryos from three independent trials were imaged for quantification.

Two-Color Fluorescent WISH

RNA probes were generated using the MEGAscript T7 transcription Kit (Ambion) in combination with RNA labeling mixes for both DIG and FITC (Roche). Double *in situ* hybridization was performed according to the protocol by Lauter et al. (2011). This included exposing embryos to acidified methanol and adding Dextran Sulfate into the hybridization reaction. Staining was done by combining Fast Blue and Fast Red dyes (Sigma) (50 μg/ml). After successful *in situ* double staining, embryos were additionally stained using DAPI and imaged using a NIKON C2+ confocal microscope. Images were adjusted for brightness and contrast using Adobe Photoshop and assembled into figures using Adobe Illustrator. 15–20 embryos were analyzed for each probe combination.

Time-Lapse Confocal *in vivo* Imaging

Embryos from each of the previously mentioned transgenic lines were collected and raised in E3 media at 28°C. Fluorescent embryos were placed in E3 PTU media including 3-amino benzoic acid ethyl ester (Tricaine) to prevent pigmentation and to anesthetize them, respectively. They were then dechorionated and embedded laterally in 1% low-gelling agarose in a 35 mm glass bottom cell culture dish (Fluordish, World Precision instruments). Real-time imaging was conducted at 28°C using a Nikon C2+ confocal microscope and a 20× (0.95 NA) oil immersion objective. 3D *z*-stacks over a 75 μm thickness with a slice size of 3.5 μm were collected to encompass the entire developing anterior segment. *Z*-stack images were taken at 10 min intervals over a 24 h period (embryos imaged: n = 12 *foxc1b:GFP*, n = 9 *foxd3:GFP*, n = 13 *pitx2:GFP*, n = 10 *lmx1b.1:GFP*, n = 7 *sox10:RFP*). Data were collected and rendered using Nikon Elements software. Images were adjusted for brightness using Adobe Photoshop and assembled into figures using Adobe Illustrator.

Cell Migration Tracking and Displacement Analysis

Completed 4D live imaging files were uploaded into FIJI software for analysis. Approximately 25 cells were manually tracked per video file using manual tracking tools. Tracked cells were measured for total distance traveled (μm), average velocity (μm/min), and total displacement (pixels). Tracked cells were randomly selected from all four eye quadrants to ensure all eye regions were represented, as well as all time frames. After tracking, data were exported to Microsoft Excel for statistical analysis. Displacement was measured using the line measurement tool in FIJI software. Previously tracked lines were identified as "completed" tracks in one of two ways: (1) at the end of the migration video or (2) the track was seen in the last frames of video before the specific track disappeared. Once the completed track was identified, the line measurement tool was used to measure the straight-line distance (in pixels) from the first point of the track to the last point of the track. Stats were analyzed in Microsoft Excel and Graphpad Prism8.

Single Cell Transcriptomic Analysis

Embryos from each of the POM subpopulation transgenic lines were dechorionated and incubated in E3 media at 28°C until 48 hpf. At this time, embryos were anesthetized using 3-amino benzoic acid ethyl ester (Tricaine) and their eyes dissected and collected on ice. Eyes were incubated for 2 min in 0.25% Trypsin + EDTA at 37°C. After incubation, a 20G needle and syringe were used to dissociate the tissue before the tube was placed back at 37°C for 2 min. This process was repeated four times. After incubation, the dissociated cells were strained using a 40 μm filter (VWR) and spun down for 10 min at 3,500 rpm at 4°C. The supernatant was removed and the pellet resuspended in 1x PBS + 2 mM EDTA and goat serum. Cells were sorted for GFP+ identity at the University of Kentucky Flow Cytometry and Immune Monitoring Core at the Markey Cancer Center. After sorting, cells were spun down and resuspended using PBS and goat serum. Approximately 1,000 cells from each transgenic line were then loaded onto the Chromium 10× V3 chip (10× genomics) and processed in the University of Kentucky Department of Biology Imaging Core to generate single cell barcoded cDNA. Sequencing was performed using NovaSeq SP, 2 × 150 bp paired ends to achieve 100,000 reads per cell at University of Illinois at Urbana-Champaign Roy J. Carver Biotechnology Center. Sequencing results were processed and subsequently aggregated (incorporating mapped normalization), using the Cell Ranger3.1 pipeline and results analyzed using Loupe Cell Browser 3.1.1 software (10× genomics).

Statistics

One-way ANOVA analysis (multiple point analysis) and unpaired *t*-tests (individual comparison analysis) were performed using Microsoft Excel and GraphPad Prism8 software. All graphs are shown with their respective means and standard deviations. Values were considered significant by the conventional standard: *P*-value of 0.05 or less.

DATA AVAILABILITY STATEMENT

The raw data supporting the conclusions of this article will be made available by the authors, without undue reservation, to any qualified researcher.

ETHICS STATEMENT

The use of zebrafish in this study was approved by the University of Kentucky IACUC committee, Institutional PHS Assurance #D16-00217 (A3336-01) with a protocol number: 2015-1370. All experimental protocols were approved by the University of Kentucky Institutional Biosafety Committee, registration number B18-3186-M.

AUTHOR CONTRIBUTIONS

JF and KV wrote the manuscript. KV, OV, MW, and NM performed the experiments and analysis. JF oversaw the project secured funding. JF and KV contributed to conception and design of the study. All authors contributed to manuscript revision, read and approved the submitted version.

FUNDING

This work was supported by the NIH-NEI grant EY027805-01. MW was supported by the Lyman T. Johnson Scholarship from the University of Kentucky. OV was supported by the Knights Templar Eye Foundation Career Starter Grant.

ACKNOWLEDGMENTS

We thank Dr. Link, Dr. Semina, and Dr. Lister for providing transgenic zebrafish lines. We thank members of the Famulski lab for helpful discussions. We also thank Dr. Jeramiah Smith for assistance with single cell sequencing analysis. This manuscript has been released as a pre-print at Biorxiv (Van Der Meulen et al., 2019).

SUPPLEMENTARY MATERIAL

The Supplementary Material for this article can be found online at: https://www.frontiersin.org/articles/10.3389/fcell.2020.00379/full#supplementary-material

FIGURE S1 | Schematic representation of AS colonization in a zebrafish embryo. Upon closure of the neural tube (NT) neural crest cells (NCC) delaminate and begin to migrate throughout the embryo (12–18 hpf), including the cranial NCC within the developing head (pictured as black outline; OV, optic vesicle). Upon retinal morphogenesis and lens (L) induction (18–28 hpf), NCC begin to surround the retina (R) in anticipation of AS colonization and become periocular mesenchyme (POM). POM targeted to the AS subsequently migrate onto the surface of the retina and occupy the future AS (28–48 hpf).

FIGURE S2 | Anterior segment ASM heterogeneity for *eya2* expression. **(A–D)** Two-color fluorescent WISH (FWISH) performed for all possible combinations of *eya2* vs. *foxc1a*, *foxd3*, *pitx2*, and *sox10* at 32 and 48 hpf. DAPI is in blue. White arrows within inset panels (dashed squares) display instances of individual **(b)** and co-expression **(a)**. Scale bar = 50 μm.

FIGURE S3 | PH3 proliferation staining assay. 3D rendering of confocal stacks of the AS at 32 and 48 hpf. GFP+ cells (green) are the result of transgenic lines, pH3+ cells (red) indicate active cell division, and DAPI (blue) stains the nucleus. **(A)** Few pH3+ cells can be seen on the surface of the AS at 32 hpf, indicating little to no cell division is taking place. No co-expression was seen between the GFP+ cells and pH3+ cells in any of the POM subpopulations. **(B)** Similarly, the AS at 48 hpf also lacked pH3+ cells and had little to no co-expression with the various POM subpopulations.

FIGURE S4 | cDNA library-based t-SNE and UMAP clusters. *K*-means clustering of scRNA sequencing of isolated 48 hpf *foxc1b*:GFP (pink), *lmx1b.1*:GFP (green), *sox10*:GFP (blue), *foxd3*:GFP (mustard) and *pitx2*:GFP (teal) ASM cells in both tSNE and UMAP readouts.

FIGURE S5 | PANTHER Gene Ontology for 48 hpf ASM clusters. Protein function Gene Ontology was applied to gene lists from clusters 1–4. Pie graphs display the distribution of each GO term applied.

TABLE S1 | *WISH* Primer Sequences. mRNA forward and reverse primer sequences for all POM and NCC-related genes.

TABLE S2 | scRNA sequencing aggregation gene list. Distribution of all gene expression analyzed during aggregation analysis.

MOVIE S1 | *Foxc1b:GFP* 4D imaging (24–28 hpf).

MOVIE S2 | *Foxd3:GFP* 4D imaging (24–48 hpf).

MOVIE S3 | *Pitx2:GFP* 4D imaging (22–46 hpf).

MOVIE S4 | *Lmx1b.1:GFP* 4D imaging (24–48 hpf).

MOVIE S5 | *Sox10:RFP* 4D imaging (23–47 hpf).

MOVIE S6 | *Foxc1b:GFP* Tracking analysis.

MOVIE S7 | *Foxd3:GFP* Tracking analysis.

MOVIE S8 | *Pitx2:GFP* Tracking analysis.

MOVIE S9 | *Lmx1b.1* Tracking analysis.

MOVIE S10 | *Sox10:RFP* Tracking analysis.

REFERENCES

Abu-Hassan, D. W., Acott, T. S., and Kelley, M. J. (2014). The trabecular meshwork: a basic review of form and function. *J. Ocul. Biol.* 2, 1–9.

Akula, M., Park, J. W., and West-Mays, J. (2018). Relationship between neural crest cell specification and rare ocular diseases. *J. Neurosci. Res.* 97, 7–15. doi: 10.1002/jnr.24245

Berry, F., Lines, M., Oas, J., Footz, T., Underhill, D., Gage, P., et al. (2006). Functional interactions between foxc1 and pitx2 underlie the sensitivity to foxc1 gene dose in axenfeld-rieger syndrome and anterior segment dysgenesis. *Hum. Mol. Genet.* 15, 905–919. doi: 10.1093/hmg/ddl008

Bohnsack, B., Kasprick, D., Kish, P., Goldman, D., and Kahana, A. (2012). A zebrafish model of axenfeld-rieger syndrome reveals that pitx2 reglation by retinoic acid is essential for cular and craniofacial development. *Invest. Ophthalmol. Vis. Sci.* 53, 7–22. doi: 10.1167/iovs.11-8494

Cavodeassi, F. (2018). Dynamic tissue rearrangments during vertebrate eye morphogenesis: insights from fish models. *J. Dev. Biol.* 6:4. doi: 10.3390/jdb6010004

Chakravarthi, S. V., Kannabiran, C., Sridhar, M. S., and Vemuganti, G. K. (2005). TGFBI gene mutations causing lattice and granular corneal dystrophies in Indian patients. *Invest, Ophthalmol. Vis. Sci.* 46, 121–125. doi: 10.1167/iovs.04-0440

Chawla, B., Schley, E., Williams, A., and Bohnsack, B. (2016). Retinoic acid and pitx2 regulate early neural crest survival and migration in craniofacial and ocular development. *Birth Defect Res. Part B* 107, 126–135. doi: 10.1002/bdrb.21177

Chawla, B., Swain, W., Williams, A., and Bohnsack, B. (2018). Retinoic acid maintains function of neural crest-derived ocular and craniofacial structures in adult zebrafish. *Invest. Ophthalmol. Vis. Sci.* 59, 1924–1935. doi: 10.1167/iovs.17-22845

Chen, L., and Gage, P. (2016). Heterozygous Pitx2 null mice accurately recapitulate the ocular features of axenfeld-rieger syndrome and congenital glaucoma. *Investig. Ophthalmol. Vis. Sci.* 57, 5023–5030. doi: 10.1167/iovs.16-19700

Clay, M., and Halloran, M. (2010). Control of neural crest cell behavior and migration. *Cell Adh. Mig.* 4, 586–594. doi: 10.4161/cam.4.4.12902

Creuzet, S., Vincent, C., and Couly, G. (2005). Neural crest derivatives in ocular and periocular structures. *Int. J. Dev. Biol.* 49, 161–171. doi: 10.1387/ijdb.041937sc

Denes, V., Hideg, O., Nyisztor, Z., Lakk, M., Godri, Z., Berta, G., et al. (2019). The neuroprotective peptide PACAP1-38 Contributes to horizontal cell development in postnatal rat retina. *Invest. Ophthalmol. Vis. Sci.* 60, 770–778. doi: 10.1167/iovs.18-25719

Drerup, C., Wiora, H., Topczewski, J., and Morris, J. (2009). Disc1 regulates foxd3 and sox10 expression, affecting neural crest migration and differentiation. *Development* 136, 2623–2632. doi: 10.1242/dev.030577

Dutton, K., Pauliny, A., Lopes, S., Elworthy, S., Carney, T., Rauch, J., et al. (2001). Zebrafish colourless encodes sox10 and specifies non-ectomesenchymal neural crest fates. *Development* 128, 4113–4125.

Evans, A., and Gage, P. (2005). Expression of the homeobox gene Pitx2 in neural crest is required for optic stalk and ocular anterior segment development. *Hum. Mol. Genet.* 14, 3347–3359. doi: 10.1093/hmg/ddi365

Fuhrmann, S., Levine, E., and Reh, T. (2000). Extraocular mesenchyme patterns the optic vesicle during early eye development in the embryonic chick. *Development* 127, 4599–4609.

Furusawa, T., and Cherukuri, S. (2010). Developmental function of HMGN proteins. *Biochim. Biophys. Acta* 1799, 69–73. doi: 10.1016/j.bbagrm.2009.11.011

Gage, P., Kaung, C., and Zacharias, A. (2014). The homeodomain transcription factor pitx2 is required for specifying correct cell fates and establishing angiogenic privilege in the developing cornea. *Dev. Dyn.* 243, 1391–1400. doi: 10.1002/dvdy.24165

Gould, D., Smith, R., and John, S. (2004). Anterior segment development relevent to glaucoma. *Int. J. Dev. Biol.* 48, 1015–1029.

Hendee, K., Sorokina, E., Muheisen, S., Reis, L., Tyler, R., Markovic, V., et al. (2018). ., Pitx2 deficiency and associated human disease: insights from the zebrafish model. *Hum. Mol. Genet.* 27, 1675–1695. doi: 10.1093/hmg/ddy074

Holly, V. L., WIden, S. A., Famulski, J. K., and Waskiewicz, A. J. (2014). Sfrp1a and Sfrp5 function as positive regulators of Wnt and BMP signaling during early retinal development. *Dev. Biol.* 388, 192–204. doi: 10.1016/j.ydbio.2014.01.012

Ivanova, A. S., Korotkova, D. D., Ermakova, G. V., Martynova, N. Y., Zaraisky, A. G., and Tereshina, M. B. (2018). Ras-dva small GTPases lost during evolution of amniotes regulate regeneration in anamniotes. *Sci. Rep.* 8:13035. doi: 10.1038/s41598-018-30811-0

Ivanova, A. S., Shandarin, I. N., Ermakova, G. V., Minin, A. A., Tereshina, M. B., and Zaraisky, A. G. (2015). , The secreted factor Ag1 missing in higher vertebrates regulates fins regeneration in Danio rerio. *Sci. Rep.* 5,:8123. doi: 10.1038/srep08123

Ji, Y., Buel, S., and Amack, J. (2016). Mutations in zebrafish pitx2 model congenital malformations in axenfeld-rieger syndrome but do not disrupt left-right placement of visceral organs. *Dev. Biol.* 416, 69–81. doi: 10.1016/j.ydbio.2016.06.010

Kannabiran, C., and Klintworth, G. K. (2006). TGFBI gene mutations in corneal dystrophies. *Hum. Mutat.* 27, 615–625.

Kulesa, P., Bailey, C., Kasemeier-Kulesa, J., and McLennan, R. (2010). Cranial neural crest migration: new rules for an old road. *Dev. Biol.* 344, 543–554. doi: 10.1016/j.ydbio.2010.04.010

Langenberg, T., Kahana, A., Wszalek, J., and Halloran, M. (2008). ., The eye organizes neural crest cell migration. *Dev. Dyn.* 237, 1645–1652. doi: 10.1002/dvdy.21577

Lauter, G., Söll, I., and Hauptmann, G. (2011). Two-color fluorescent *in situ* hybridization in the embryonic zebrafish brain using differential detection systems. *BMC Dev. Biol.* 11:43. doi: 10.1186/1471-213X-11-43

Lister, J., Cooper, C., Ngyen, K., Modrell, M., Grant, K., and Raible, D. (2006). Zebrafish foxd3 is required for development of a subset of neural crest derivatives. *Dev. Biol.* 290, 92–104. doi: 10.1016/j.ydbio.2005.11.014

Liu, P., and Johnson, R. (2010). Lmx1b is required for murine trabecular meshwork formation and for the maintenance of corneal transparency. *Dev. Dyn.* 239, 2161–2171. doi: 10.1002/dvdy.22347

Liu, Y., and Semina, E. (2012). Pitx2 deficiency results in abnormal ocular and craniofacial development in zebrafish. *PLoS One* 7:e30896. doi: 10.1371/journal.pone.0030896

Lucey, M. M., Wang, Y., Bustin, M., and Duncan, M. K. (2008). Differential expression of the HMGN family of chromatin proteins during ocular development. *Gene Expr. Patterns* 8, 433–437. doi: 10.1016/j.gep.2008.04.002

Lupo, G., Gestri, G., O'Brien, M., Denton, R. M., Chandraratna, R. A., Ley, S. V., et al. (2011). Retinoic acid receptor signaling regulates choroid fissure closure through independent mechanisms in the ventral optic cup and periocular mesenchyme. *Proc. Natl. Acad. Sci. U.S.A.* 108, 8698–8703. doi: 10.1073/pnas.1103802108

Matt, N., Dupe, V., Garnier, J., Dennefeld, C., Chambon, P., Mark, M., et al. (2005). Retinoic acid-dependent eye morphogenesis is orchestrated by neural crest cells. *Development* 132, 4789–4800. doi: 10.1242/dev.02031

Matt, N., Ghyselinck, N. B., Pellerin, I., and Dupe, V. (2008). Impairing retinoic acid signalling in the neural crest cells is sufficient to alter entire eye morphogenesis. *Dev. Biol.* 320, 140–148. doi: 10.1016/j.ydbio.2008.04.039

McMahon, C., Gestri, G., Wilson, S., and Link, B. (2009). Lmx1b is essential for survival of periocular mesenchymal cells and influences fgf-mediated retinal pattering in zebrafish. *Dev. Biol.* 332, 287–298. doi: 10.1016/j.ydbio.2009.05.577

Nielsen, N. S., Poulsen, E. T., Lukassen, M. V., Chao Shern, C., Mogensen, E. H., Weberskov, C. E., et al. (2020). Biochemical mechanisms of aggregation in TGFBI-linked corneal dystrophies. *Prog. Retin. Eye Res.* 100843. (in press). doi: 10.1016/j.preteyeres.2020.100843

Poulaki, V., and Colby, K. (2008). Genetics of anterior and stromal corneal dystrophies. *Semin. Ophthalmol.* 23, 9–17. doi: 10.1080/08820530701745173

Reis, L., Tyler, R., Kloss, V. B., Schilter, K., Levin, A., Lowry, R. B., et al. (2012). Pitx2 and Foxc1 spectrum of mutations in ocular syndromes. *Eur. J. Hum. Genet.* 20, 1224–1233. doi: 10.1038/ejhg.2012.80

Richardson, J., Gauert, A., Montecinos, L., Fanlo, L., Alhashem, Z., Assar, R., et al. (2016). Leader cells define directionality of trunk, but not cranial, neural crest cell migration. *Cell Rep.* 15, 2076–2088. doi: 10.1016/j.celrep.2016.04.067

Seo, S., Chen, L., Liu, W., Zhao, D., Schultz, K., Sasman, A., et al. (2017). ., FoxC1 and FoxC2 in the neural crest are required for the ocular anterior segment development. *Invest. Ophthalmol. Vis. Sci.* 58, 1368–1377. doi: 10.1167/iovs.16-21217

Shioda, S., Takenoya, F., Wada, N., Hirabayashi, T., Seki, T., and Nakamachi, T. (2016). Pleiotropic and retinoprotective functions of PACAP. *Anat. Sci. Int.* 91, 313–324. doi: 10.1007/s12565-016-0351-0

Stewart, R., Arduini, B., Berghmans, S., George, R., Kanki, J., Henion, P., et al. (2006). Zebrafish foxd3 is selectively required for neural crest specification, migration, and survival. *Dev. Biol.* 292, 174–188. doi: 10.1016/j.ydbio.2005.12.035

Trainor, P., and Tam, P. (1995). Cranial paraxial mesoderm and the neural crest cells of the mouse embryo: co-distribution in the craniofacial mesenchyme but distinct segregation in the branchial arches. *Development* 121, 2569–2582.

Van Der Meulen, K. L., Vocking, O., Meshram, N. N., and Famulski, J. K. (2019). Spatiotemporal characterization of anterior segment mesenchyme heterogeneity during anterior segment development. *BioRxiv* [preprint]. doi: 10.1101/726257,

Volkmann, B. A., Zinkevich, N. S., Mustonen, A., Schilter, K. F., Bosenko, D. V., Reis, L. M., et al. (2011). Potential novel mechanism for Axenfeld-Rieger syndrome: deletion of a distant region containing regulatory elements of PITX2. *Invest. Ophthalmol. Vis. Sci.* 52, 1450–1459. doi: 10.1167/iovs.10-6060

Volkmann Kloss, B., Reis, L., Bremond-Gignac, D., Glaser, T., and Semina, E. (2012). Analysis of FoxD3 sequence variation in human ocular disease. *Mol. Vis.* 18, 1740–1749.

Wang, W., Melville, D., Montero-Balaguer, M., Hatzopoulos, A., and Knapik, E. (2011). Tfap2a and Foxd3 regulate early steps in the development of the neural crest progenitor population. *Dev. Biol.* 360, 173–185. doi: 10.1016/j.ydbio.2011.09.019

Williams, A., and Bohnsack, B. (2015). Neural crest derivatives in oular development: discerning the eye of the storm. *Birth Defects Res. Part C* 105, 87–95. doi: 10.1002/bdrc.21095

Wu, S., Adams, B. A., Fradinger, E. A., and Sherwood, N. M. (2006). Role of two genes encoding PACAP in early brain development in zebrafish. *Ann. N. Y. Acad .Sci.* 1070, 602–621. doi: 10.1196/annals.1317.091

Zhao, Y., Sorenson, C. M., and Sheibani, N. (2015). Cytochrome P450 1B1 and primary congenital glaucoma. *J. Ophthalmic. Vis. Res.* 10, 60–67. doi: 10.4103/2008-322X.156116

Conflict of Interest: The authors declare that the research was conducted in the absence of any commercial or financial relationships that could be construed as a potential conflict of interest.

REFERENCES

1. Shindo, A., *Models of convergent extension during morphogenesis.* Wiley Interdiscip Rev Dev Biol, 2018. **7**(1).
2. Tada, M. and C.P. Heisenberg, *Convergent extension: using collective cell migration and cell intercalation to shape embryos.* Development, 2012. **139**(21): p. 3897-904.
3. Skoglund, P., et al., *Convergence and extension at gastrulation require a myosin IIB-dependent cortical actin network.* Development, 2008. **135**(14): p. 2435-44.
4. Lapébie, P., C. Borchiellini, and E. Houliston, *Dissecting the PCP pathway: one or more pathways?: Does a separate Wnt-Fz-Rho pathway drive morphogenesis?* Bioessays, 2011. **33**(10): p. 759-68.
5. Winter, C.G., et al., *Drosophila Rho-associated kinase (Drok) links Frizzled-mediated planar cell polarity signaling to the actin cytoskeleton.* Cell, 2001. **105**(1): p. 81-91.
6. Fanto, M., et al., *Nuclear signaling by Rac and Rho GTPases is required in the establishment of epithelial planar polarity in the Drosophila eye.* Curr Biol, 2000. **10**(16): p. 979-88.
7. Solnica-Krezel, L., *Conserved patterns of cell movements during vertebrate gastrulation.* Curr Biol, 2005. **15**(6): p. R213-28.
8. Bruce, A.E., *Zebrafish epiboly: Spreading thin over the yolk.* Dev Dyn, 2016. **245**(3): p. 244-58.
9. Kane, D.A., K.N. McFarland, and R.M. Warga, *Mutations in half baked/E-cadherin block cell behaviors that are necessary for teleost epiboly.* Development, 2005. **132**(5): p. 1105-16.
10. Köppen, M., et al., *Coordinated cell-shape changes control epithelial movement in zebrafish and Drosophila.* Development, 2006. **133**(14): p. 2671-81.
11. Behrndt, M., et al., *Forces driving epithelial spreading in zebrafish gastrulation.* Science, 2012. **338**(6104): p. 257-60.
12. Magie, C.R., et al., *Mutations in the Rho1 small GTPase disrupt morphogenesis and segmentation during early Drosophila development.* Development, 1999. **126**(23): p. 5353-64.
13. VanHook, A. and A. Letsou, *Head involution in Drosophila: genetic and morphogenetic connections to dorsal closure.* Dev Dyn, 2008. **237**(1): p. 28-38.
14. Olsen, C.L. and W.R. Jeffery, *A forkhead gene related to HNF-3beta is required for gastrulation and axis formation in the ascidian embryo.* Development, 1997. **124**(18): p. 3609-19.
15. Skromne, I. and C.D. Stern, *Interactions between Wnt and Vg1 signalling pathways initiate primitive streak formation in the chick embryo.* Development, 2001. **128**(15): p. 2915-27.
16. Ridley, A.J., *Life at the leading edge.* Cell, 2011. **145**(7): p. 1012-22.
17. Nakaya, Y., et al., *RhoA and microtubule dynamics control cell-basement membrane interaction in EMT during gastrulation.* Nat Cell Biol, 2008. **10**(7): p. 765-75.

18. Shoval, I., A. Ludwig, and C. Kalcheim, *Antagonistic roles of full-length N-cadherin and its soluble BMP cleavage product in neural crest delamination.* Development, 2007. **134**(3): p. 491-501.
19. Lamouille, S., J. Xu, and R. Derynck, *Molecular mechanisms of epithelial-mesenchymal transition.* Nat Rev Mol Cell Biol, 2014. **15**(3): p. 178-96.
20. Davies, J.A., *Mechanisms of Morphogenesis*. Second ed. Invagination and Evagination: The Making and Shaping of Folds and Tubes. 2013: Elsevier Ltd. 414.
21. Sawyer, J.M., et al., *Apical constriction: a cell shape change that can drive morphogenesis.* Dev Biol, 2010. **341**(1): p. 5-19.
22. Davidson, L.A., et al., *Measurements of mechanical properties of the blastula wall reveal which hypothesized mechanisms of primary invagination are physically plausible in the sea urchin Strongylocentrotus purpuratus.* Dev Biol, 1999. **209**(2): p. 221-38.
23. Beane, W.S., J.M. Gross, and D.R. McClay, *RhoA regulates initiation of invagination, but not convergent extension, during sea urchin gastrulation.* Dev Biol, 2006. **292**(1): p. 213-25.
24. Lane, M.C., et al., *A role for regulated secretion of apical extracellular matrix during epithelial invagination in the sea urchin.* Development, 1993. **117**(3): p. 1049-60.
25. Schoenwolf, G.C., D. Folsom, and A. Moe, *A reexamination of the role of microfilaments in neurulation in the chick embryo.* Anat Rec, 1988. **220**(1): p. 87-102.
26. Ybot-Gonzalez, P. and A.J. Copp, *Bending of the neural plate during mouse spinal neurulation is independent of actin microfilaments.* Dev Dyn, 1999. **215**(3): p. 273-83.
27. Pai, Y.J., et al., *Epithelial fusion during neural tube morphogenesis.* Birth Defects Res A Clin Mol Teratol, 2012. **94**(10): p. 817-23.
28. Cortes, C., et al., *Epithelial Properties of the Second Heart Field.* Circ Res, 2018. **122**(1): p. 142-154.
29. Sakuma, C., et al., *Cleft palate formation after palatal fusion occurs due to the rupture of epithelial basement membranes.* J Craniomaxillofac Surg, 2018. **46**(12): p. 2027-2031.
30. Orellana, J. and A.H. Friedman, *Ocular Coloboma*, in *Clinico-Pathological Atlas of Congenital Fundus Disorders*. 1993, Springer New York: New York, NY. p. 123-126.
31. Bosman, E.A., et al., *Multiple mutations in mouse Chd7 provide models for CHARGE syndrome.* Hum Mol Genet, 2005. **14**(22): p. 3463-76.
32. Lachke, S.A. and R.L. Maas, *Building the developmental oculome: systems biology in vertebrate eye development and disease.* Wiley Interdiscip Rev Syst Biol Med, 2010. **2**(3): p. 305-323.
33. Zuber, M.E., et al., *Specification of the vertebrate eye by a network of eye field transcription factors.* Development, 2003. **130**(21): p. 5155-67.
34. Lagutin, O.V., et al., *Six3 repression of Wnt signaling in the anterior neuroectoderm is essential for vertebrate forebrain development.* Genes Dev, 2003. **17**(3): p. 368-79.

35. Loosli, F., S. Winkler, and J. Wittbrodt, *Six3 overexpression initiates the formation of ectopic retina.* Genes Dev, 1999. **13**(6): p. 649-54.
36. Carl, M., F. Loosli, and J. Wittbrodt, *Six3 inactivation reveals its essential role for the formation and patterning of the vertebrate eye.* Development, 2002. **129**(17): p. 4057-63.
37. Braun, M.M., et al., *Wnt signaling is required at distinct stages of development for the induction of the posterior forebrain.* Development, 2003. **130**(23): p. 5579-87.
38. Sinigaglia, C., et al., *The bilaterian head patterning gene six3/6 controls aboral domain development in a cnidarian.* PLoS Biol, 2013. **11**(2): p. e1001488.
39. Hill, R.E., et al., *Mouse small eye results from mutations in a paired-like homeobox-containing gene.* Nature, 1991. **354**(6354): p. 522-5.
40. Wawersik, S., P. Purcell, and R.L. Maas, *Pax6 and the genetic control of early eye development.* Results Probl Cell Differ, 2000. **31**: p. 15-36.
41. Mathers, P.H., et al., *The Rx homeobox gene is essential for vertebrate eye development.* Nature, 1997. **387**(6633): p. 603-7.
42. Chow, R.L. and R.A. Lang, *Early eye development in vertebrates.* Annu Rev Cell Dev Biol, 2001. **17**: p. 255-96.
43. Andreazzoli, M., et al., *Role of Xrx1 in Xenopus eye and anterior brain development.* Development, 1999. **126**(11): p. 2451-60.
44. Feldman, B., et al., *Zebrafish organizer development and germ-layer formation require nodal-related signals.* Nature, 1998. **395**(6698): p. 181-5.
45. England, S.J., et al., *A dynamic fate map of the forebrain shows how vertebrate eyes form and explains two causes of cyclopia.* Development, 2006. **133**(23): p. 4613-7.
46. Carl, M. and J. Wittbrodt, *Graded interference with FGF signalling reveals its dorsoventral asymmetry at the mid-hindbrain boundary.* Development, 1999. **126**(24): p. 5659-67.
47. Barbieri, A.M., et al., *A homeobox gene, vax2, controls the patterning of the eye dorsoventral axis.* Proc Natl Acad Sci U S A, 1999. **96**(19): p. 10729-34.
48. Svoboda, K.K. and K.S. O'Shea, *An analysis of cell shape and the neuroepithelial basal lamina during optic vesicle formation in the mouse embryo.* Development, 1987. **100**(2): p. 185-200.
49. Brown, K.E., et al., *Nlcam modulates midline convergence during anterior neural plate morphogenesis.* Dev Biol, 2010. **339**(1): p. 14-25.
50. Keller, P.J., et al., *Reconstruction of zebrafish early embryonic development by scanned light sheet microscopy.* Science, 2008. **322**(5904): p. 1065-9.
51. Rembold, M., et al., *Individual cell migration serves as the driving force for optic vesicle evagination.* Science, 2006. **313**(5790): p. 1130-4.
52. Eiraku, M., et al., *Self-organizing optic-cup morphogenesis in three-dimensional culture.* Nature, 2011. **472**(7341): p. 51-6.
53. Hyer, J., et al., *Optic cup morphogenesis requires pre-lens ectoderm but not lens differentiation.* Dev Biol, 2003. **259**(2): p. 351-63.
54. Martinez-Morales, J.R., et al., *ojoplano-mediated basal constriction is essential for optic cup morphogenesis.* Development, 2009. **136**(13): p. 2165-75.

55. Sidhaye, J. and C. Norden, *Concerted action of neuroepithelial basal shrinkage and active epithelial migration ensures efficient optic cup morphogenesis.* Elife, 2017. **6**.
56. Wang, Z., et al., *Assessment and Characterization of Hyaloid Vessels in Mice.* J Vis Exp, 2019(147).
57. Brooks, B.P. and E.I. Traboulsi, *Genetic Diseases of the Eye*, in *Anophthalmia, Colobomatous, Microphthalmia, and Optic Fissure Closure Defects*. 2012, Oxford University Press.
58. AS, A.L., C.Y. Gregory-Evans, and K. Gregory-Evans, *An update on the genetics of ocular coloboma.* Hum Genet, 2019. **138**(8-9): p. 865-880.
59. Onwochei, B.C., et al., *Ocular colobomata.* Surv Ophthalmol, 2000. **45**(3): p. 175-94.
60. Schimmenti, L.A., *Renal coloboma syndrome.* Eur J Hum Genet, 2011. **19**(12): p. 1207-12.
61. Bower, M., et al., *Update of PAX2 mutations in renal coloboma syndrome and establishment of a locus-specific database.* Hum Mutat, 2012. **33**(3): p. 457-66.
62. Wen, W., et al., *Sox4 regulates choroid fissure closure by limiting Hedgehog signaling during ocular morphogenesis.* Dev Biol, 2015. **399**(1): p. 139-153.
63. Gage, P.J., H. Suh, and S.A. Camper, *Dosage requirement of Pitx2 for development of multiple organs.* Development, 1999. **126**(20): p. 4643-51.
64. Skarie, J.M. and B.A. Link, *FoxC1 is essential for vascular basement membrane integrity and hyaloid vessel morphogenesis.* Invest Ophthalmol Vis Sci, 2009. **50**(11): p. 5026-34.
65. Zhao, L., et al., *Sonic hedgehog is involved in formation of the ventral optic cup by limiting Bmp4 expression to the dorsal domain.* Mech Dev, 2010. **127**(1-2): p. 62-72.
66. Behesti, H., J.K. Holt, and J.C. Sowden, *The level of BMP4 signaling is critical for the regulation of distinct T-box gene expression domains and growth along the dorso-ventral axis of the optic cup.* BMC Dev Biol, 2006. **6**: p. 62.
67. Knickmeyer, M.D., et al., *TGFβ-facilitated optic fissure fusion and the role of bone morphogenetic protein antagonism.* Open Biol, 2018. **8**(3).
68. Eckert, P., et al., *Morphogenesis and axis specification occur in parallel during optic cup and optic fissure formation, differentially modulated by BMP and Wnt.* Open Biol, 2019. **9**(2): p. 180179.
69. Morcillo, J., et al., *Proper patterning of the optic fissure requires the sequential activity of BMP7 and SHH.* Development, 2006. **133**(16): p. 3179-90.
70. Moore, K.B., et al., *Morphogenetic movements underlying eye field formation require interactions between the FGF and ephrinB1 signaling pathways.* Dev Cell, 2004. **6**(1): p. 55-67.
71. Chen, S., et al., *Defective FGF signaling causes coloboma formation and disrupts retinal neurogenesis.* Cell Res, 2013. **23**(2): p. 254-73.
72. Cai, Z., et al., *Deficient FGF signaling causes optic nerve dysgenesis and ocular coloboma.* Development, 2013. **140**(13): p. 2711-23.
73. Rudolph, G., et al., *[LEOPARD syndrome with iris-retina-choroid coloboma. Discordant findings in monozygotic twins (MIM # 151 100)].* Ophthalmologe, 2001. **98**(11): p. 1101-3.

74. George, A., et al., *Biallelic Mutations in MITF Cause Coloboma, Osteopetrosis, Microphthalmia, Macrocephaly, Albinism, and Deafness.* Am J Hum Genet, 2016. **99**(6): p. 1388-1394.
75. Helms, J.A., et al., *Sonic hedgehog participates in craniofacial morphogenesis and is down-regulated by teratogenic doses of retinoic acid.* Dev Biol, 1997. **187**(1): p. 25-35.
76. Lupo, G., et al., *Retinoic acid receptor signaling regulates choroid fissure closure through independent mechanisms in the ventral optic cup and periocular mesenchyme.* Proc Natl Acad Sci U S A, 2011. **108**(21): p. 8698-703.
77. Miesfeld, J.B., et al., *Yap and Taz regulate retinal pigment epithelial cell fate.* Development, 2015. **142**(17): p. 3021-32.
78. Khan, K.N., et al., *Vitamin A deficiency due to bi-allelic mutation of RBP4: There's more to it than meets the eye.* Ophthalmic Genet, 2017. **38**(5): p. 465-466.
79. Casey, J., et al., *First implication of STRA6 mutations in isolated anophthalmia, microphthalmia, and coloboma: a new dimension to the STRA6 phenotype.* Hum Mutat, 2011. **32**(12): p. 1417-26.
80. Yahyavi, M., et al., *ALDH1A3 loss of function causes bilateral anophthalmia/microphthalmia and hypoplasia of the optic nerve and optic chiasm.* Hum Mol Genet, 2013. **22**(16): p. 3250-8.
81. Oatts, J.T., et al., *Novel heterozygous mutation in YAP1 in a family with isolated ocular colobomas.* Ophthalmic Genet, 2017. **38**(3): p. 281-283.
82. Mic, F.A., et al., *Raldh2 expression in optic vesicle generates a retinoic acid signal needed for invagination of retina during optic cup formation.* Dev Dyn, 2004. **231**(2): p. 270-7.
83. See, A.W. and M. Clagett-Dame, *The temporal requirement for vitamin A in the developing eye: mechanism of action in optic fissure closure and new roles for the vitamin in regulating cell proliferation and adhesion in the embryonic retina.* Dev Biol, 2009. **325**(1): p. 94-105.
84. Smith, R., et al., *The Transcription Factor Foxg1 Promotes Optic Fissure Closure in the Mouse by Suppressing Wnt8b in the Nasal Optic Stalk.* J Neurosci, 2017. **37**(33): p. 7975-7993.
85. Liu, C. and J. Nathans, *An essential role for frizzled 5 in mammalian ocular development.* Development, 2008. **135**(21): p. 3567-76.
86. Zhou, C.J., et al., *Ocular coloboma and dorsoventral neuroretinal patterning defects in Lrp6 mutant eyes.* Dev Dyn, 2008. **237**(12): p. 3681-9.
87. Liu, C., et al., *A secreted WNT-ligand-binding domain of FZD5 generated by a frameshift mutation causes autosomal dominant coloboma.* Hum Mol Genet, 2016. **25**(7): p. 1382-91.
88. Bernstein, C.S., et al., *The cellular bases of choroid fissure formation and closure.* Dev Biol, 2018. **440**(2): p. 137-151.
89. Halfter, W., et al., *New concepts in basement membrane biology.* Febs j, 2015. **282**(23): p. 4466-79.
90. Sekiguchi, R. and K.M. Yamada, *Basement Membranes in Development and Disease.* Curr Top Dev Biol, 2018. **130**: p. 143-191.
91. Hohenester, E. and P.D. Yurchenco, *Laminins in basement membrane assembly.* Cell Adh Migr, 2013. **7**(1): p. 56-63.

92. Miner, J.H., et al., *Compositional and structural requirements for laminin and basement membranes during mouse embryo implantation and gastrulation.* Development, 2004. **131**(10): p. 2247-56.
93. Pöschl, E., et al., *Collagen IV is essential for basement membrane stability but dispensable for initiation of its assembly during early development.* Development, 2004. **131**(7): p. 1619-28.
94. Pozzi, A., P.D. Yurchenco, and R.V. Iozzo, *The nature and biology of basement membranes.* Matrix Biol, 2017. **57-58**: p. 1-11.
95. Bader, B.L., et al., *Compound genetic ablation of nidogen 1 and 2 causes basement membrane defects and perinatal lethality in mice.* Mol Cell Biol, 2005. **25**(15): p. 6846-56.
96. Costell, M., et al., *Perlecan maintains the integrity of cartilage and some basement membranes.* J Cell Biol, 1999. **147**(5): p. 1109-22.
97. Herzog, C., et al., *Dystroglycan in skin and cutaneous cells: beta-subunit is shed from the cell surface.* J Invest Dermatol, 2004. **122**(6): p. 1372-80.
98. Inomata, T., et al., *Perlecan-deficient mutation impairs corneal epithelial structure.* Invest Ophthalmol Vis Sci, 2012. **53**(3): p. 1277-84.
99. Lee, J. and J.M. Gross, *Laminin beta1 and gamma1 containing laminins are essential for basement membrane integrity in the zebrafish eye.* Invest Ophthalmol Vis Sci, 2007. **48**(6): p. 2483-90.
100. Barbieri, A.M., et al., *Vax2 inactivation in mouse determines alteration of the eye dorsal-ventral axis, misrouting of the optic fibres and eye coloboma.* Development, 2002. **129**(3): p. 805-13.
101. Carrara, N., et al., *Temporal characterization of optic fissure basement membrane composition suggests nidogen may be an initial target of remodeling.* Dev Biol, 2019. **452**(1): p. 43-54.
102. Xue, M. and C.J. Jackson, *Extracellular Matrix Reorganization During Wound Healing and Its Impact on Abnormal Scarring.* Adv Wound Care (New Rochelle), 2015. **4**(3): p. 119-136.
103. Delaissé, J.M., et al., *Matrix metalloproteinases (MMP) and cathepsin K contribute differently to osteoclastic activities.* Microsc Res Tech, 2003. **61**(6): p. 504-13.
104. Rempe, R.G., A.M.S. Hartz, and B. Bauer, *Matrix metalloproteinases in the brain and blood-brain barrier: Versatile breakers and makers.* J Cereb Blood Flow Metab, 2016. **36**(9): p. 1481-507.
105. Liu, Y., et al., *MT2-MMP induces proteolysis and leads to EMT in carcinomas.* Oncotarget, 2016. **7**(30): p. 48193-48205.
106. Martins, D., et al., *MMP-14 overexpression correlates with the neurodegenerative process in familial amyloidotic polyneuropathy.* Dis Model Mech, 2017. **10**(10): p. 1253-1260.
107. Holmbeck, K., et al., *MT1-MMP-deficient mice develop dwarfism, osteopenia, arthritis, and connective tissue disease due to inadequate collagen turnover.* Cell, 1999. **99**(1): p. 81-92.
108. Pollard, T.D. and J.A. Cooper, *Actin, a central player in cell shape and movement.* Science, 2009. **326**(5957): p. 1208-12.

109. Small, J.V., et al., *The lamellipodium: where motility begins.* Trends Cell Biol, 2002. **12**(3): p. 112-20.
110. Shakir, M.A., et al., *The Arp2/3 activators WAVE and WASP have distinct genetic interactions with Rac GTPases in Caenorhabditis elegans axon guidance.* Genetics, 2008. **179**(4): p. 1957-71.
111. Steffen, A., et al., *Sra-1 and Nap1 link Rac to actin assembly driving lamellipodia formation.* Embo j, 2004. **23**(4): p. 749-59.
112. Nakagawa, H., et al., *N-WASP, WAVE and Mena play different roles in the organization of actin cytoskeleton in lamellipodia.* J Cell Sci, 2001. **114**(Pt 8): p. 1555-65.
113. Millard, T.H. and P. Martin, *Dynamic analysis of filopodial interactions during the zippering phase of Drosophila dorsal closure.* Development, 2008. **135**(4): p. 621-6.
114. Jacinto, A., et al., *Dynamic actin-based epithelial adhesion and cell matching during Drosophila dorsal closure.* Curr Biol, 2000. **10**(22): p. 1420-6.
115. Sumida, G.M. and S. Yamada, *Rho GTPases and the downstream effectors actin-related protein 2/3 (Arp2/3) complex and myosin II induce membrane fusion at self-contacts.* J Biol Chem, 2015. **290**(6): p. 3238-47.
116. Shimizu, Y., et al., *ROCK-I regulates closure of the eyelids and ventral body wall by inducing assembly of actomyosin bundles.* J Cell Biol, 2005. **168**(6): p. 941-53.
117. Takada, Y., X. Ye, and S. Simon, *The integrins.* Genome Biol, 2007. **8**(5): p. 215.
118. Molè, M.A., et al., *Integrin-Mediated Focal Anchorage Drives Epithelial Zippering during Mouse Neural Tube Closure.* Dev Cell, 2020. **52**(3): p. 321-334.e6.
119. James, A., et al., *The hyaloid vasculature facilitates basement membrane breakdown during choroid fissure closure in the zebrafish eye.* Dev Biol, 2016. **419**(2): p. 262-272.
120. Chinthalapudi, K., E.S. Rangarajan, and T. Izard, *The interaction of talin with the cell membrane is essential for integrin activation and focal adhesion formation.* Proc Natl Acad Sci U S A, 2018. **115**(41): p. 10339-10344.
121. Brown, N.H., et al., *Talin is essential for integrin function in Drosophila.* Dev Cell, 2002. **3**(4): p. 569-79.
122. Lutty, G.A. and D.S. McLeod, *Development of the hyaloid, choroidal and retinal vasculatures in the fetal human eye.* Prog Retin Eye Res, 2018. **62**: p. 58-76.
123. Trost, A., et al., *Neural crest origin of retinal and choroidal pericytes.* Invest Ophthalmol Vis Sci, 2013. **54**(13): p. 7910-21.
124. Liu, Y. and E.V. Semina, *pitx2 Deficiency results in abnormal ocular and craniofacial development in zebrafish.* PLoS One, 2012. **7**(1): p. e30896.
125. Kaufman, R., et al., *Development and origins of zebrafish ocular vasculature.* BMC Dev Biol, 2015. **15**: p. 18.
126. Chen, Y., et al., *Cited2 is required for the proper formation of the hyaloid vasculature and for lens morphogenesis.* Development, 2008. **135**(17): p. 2939-48.
127. Garcia, C.M., et al., *The function of VEGF-A in lens development: formation of the hyaloid capillary network and protection against transient nuclear cataracts.* Exp Eye Res, 2009. **88**(2): p. 270-6.

128. Rattner, A., J. Williams, and J. Nathans, *Roles of HIFs and VEGF in angiogenesis in the retina and brain.* J Clin Invest, 2019. **129**(9): p. 3807-3820.
129. Feeney, S.A., et al., *Role of vascular endothelial growth factor and placental growth factors during retinal vascular development and hyaloid regression.* Invest Ophthalmol Vis Sci, 2003. **44**(2): p. 839-47.
130. Saint-Geniez, M. and P.A. D'Amore, *Development and pathology of the hyaloid, choroidal and retinal vasculature.* Int J Dev Biol, 2004. **48**(8-9): p. 1045-58.
131. Lee, S., et al., *Processing of VEGF-A by matrix metalloproteinases regulates bioavailability and vascular patterning in tumors.* J Cell Biol, 2005. **169**(4): p. 681-91.
132. Jászai, J. and M.H.H. Schmidt, *Trends and Challenges in Tumor Anti-Angiogenic Therapies.* Cells, 2019. **8**(9).
133. Bhisitkul, R.B., *Vascular endothelial growth factor biology: clinical implications for ocular treatments.* Br J Ophthalmol, 2006. **90**(12): p. 1542-7.
134. Alvarez, Y., et al., *Genetic determinants of hyaloid and retinal vasculature in zebrafish.* BMC Dev Biol, 2007. **7**: p. 114.
135. Lorenz, L., et al., *Mechanosensing by β1 integrin induces angiocrine signals for liver growth and survival.* Nature, 2018. **562**(7725): p. 128-132.
136. Rafii, S., J.M. Butler, and B.S. Ding, *Angiocrine functions of organ-specific endothelial cells.* Nature, 2016. **529**(7586): p. 316-25.
137. Honnegowda, T.M., et al., *Role of angiogenesis and angiogenic factors in acute and chronic wound healing.* Plastic and Aesthetic Research, 2015. **2**: p. 243-249.
138. Benedicto, I., et al., *Concerted regulation of retinal pigment epithelium basement membrane and barrier function by angiocrine factors.* Nat Commun, 2017. **8**: p. 15374.
139. Gestri, G., et al., *Cell Behaviors during Closure of the Choroid Fissure in the Developing Eye.* Front Cell Neurosci, 2018. **12**: p. 42.
140. Patel, A. and J.C. Sowden, *Genes and pathways in optic fissure closure.* Semin Cell Dev Biol, 2019. **91**: p. 55-65.
141. Wang, Y., et al., *Moesin1 and Ve-cadherin are required in endothelial cells during in vivo tubulogenesis.* Development, 2010. **137**(18): p. 3119-28.
142. Hocking, J.C., et al., *Morphogenetic defects underlie Superior Coloboma, a newly identified closure disorder of the dorsal eye.* PLoS Genet, 2018. **14**(3): p. e1007246.
143. Reischauer, S., et al., *Cloche is a bHLH-PAS transcription factor that drives haemato-vascular specification.* Nature, 2016. **535**(7611): p. 294-8.
144. Holly, V.L., et al., *Sfrp1a and Sfrp5 function as positive regulators of Wnt and BMP signaling during early retinal development.* Dev Biol, 2014. **388**(2): p. 192-204.
145. Pereira Piedade, W., S. Veith, and J.K. Famulski, *Ubiquitin-mediated proteasome degradation regulates optic fissure fusion.* Biol Open, 2019. **8**(6).
146. Lauter, G., I. Söll, and G. Hauptmann, *Two-color fluorescent in situ hybridization in the embryonic zebrafish brain using differential detection systems.* BMC Dev Biol, 2011. **11**: p. 43.

147. Hoshijima, K., et al., *Highly Efficient CRISPR-Cas9-Based Methods for Generating Deletion Mutations and F0 Embryos that Lack Gene Function in Zebrafish.* Dev Cell, 2019. **51**(5): p. 645-657.e4.
148. Hartsock, A., et al., *In vivo analysis of hyaloid vasculature morphogenesis in zebrafish: A role for the lens in maturation and maintenance of the hyaloid.* Dev Biol, 2014. **394**(2): p. 327-39.
149. Hashiura, T., et al., *Live imaging of primary ocular vasculature formation in zebrafish.* PLoS One, 2017. **12**(4): p. e0176456.
150. Yoshikawa, Y., et al., *Developmental regression of hyaloid vasculature is triggered by neurons.* J Exp Med, 2016. **213**(7): p. 1175-83.
151. AS, A.L., C.Y. Gregory-Evans, and K. Gregory-Evans, *An update on the genetics of ocular coloboma.* Hum Genet, 2019.
152. Chang, L., et al., *Uveal coloboma: clinical and basic science update.* Curr Opin Ophthalmol, 2006. **17**(5): p. 447-70.
153. Gregory-Evans, C.Y., et al., *Ocular coloboma: a reassessment in the age of molecular neuroscience.* J Med Genet, 2004. **41**(12): p. 881-91.
154. Stoll, C., et al., *Congenital eye malformations in 212,479 consecutive births.* Ann Genet, 1997. **40**(2): p. 122-8.
155. Huynh, N. and B.P. Brooks, *Uveal coloboma.* JAMA Ophthalmol, 2013. **131**(10): p. 1274.
156. Patel, A. and J.C. Sowden, *Genes and pathways in optic fissure closure.* Semin Cell Dev Biol, 2017.
157. Take-uchi, M., J.D. Clarke, and S.W. Wilson, *Hedgehog signalling maintains the optic stalk-retinal interface through the regulation of Vax gene activity.* Development, 2003. **130**(5): p. 955-68.
158. Macdonald, R. and S.W. Wilson, *Pax proteins and eye development.* Curr Opin Neurobiol, 1996. **6**(1): p. 49-56.
159. Ray, H.J. and L. Niswander, *Mechanisms of tissue fusion during development.* Development, 2012. **139**(10): p. 1701-11.
160. Hayes, P. and J. Solon, *Drosophila dorsal closure: An orchestra of forces to zip shut the embryo.* Mech Dev, 2017. **144**(Pt A): p. 2-10.
161. Jacinto, A., A. Martinez-Arias, and P. Martin, *Mechanisms of epithelial fusion and repair.* Nat Cell Biol, 2001. **3**(5): p. E117-23.
162. Vasioukhin, V., et al., *Directed actin polymerization is the driving force for epithelial cell-cell adhesion.* Cell, 2000. **100**(2): p. 209-19.
163. Gumbiner, B.M., *Cell adhesion: the molecular basis of tissue architecture and morphogenesis.* Cell, 1996. **84**(3): p. 345-57.
164. Hero, I., *The optic fissure in the normal and microphthalmic mouse.* Exp Eye Res, 1989. **49**(2): p. 229-39.
165. Hero, I., *Optic fissure closure in the normal cinnamon mouse. An ultrastructural study.* Invest Ophthalmol Vis Sci, 1990. **31**(1): p. 197-216.
166. Geeraets, R., *An electron microscopic study of the closure of the optic fissure in the golden hamster.* Am J Anat, 1976. **145**(4): p. 411-31.
167. Carrara, N., et al., *Temporal characterization of optic fissure basement membrane composition suggests nidogen may be an initial target of remodeling.* Dev Biol, 2019.

168. Hardy, H., et al., *Detailed analysis of chick optic fissure closure reveals Netrin-1 as an essential mediator of epithelial fusion.* Elife, 2019. **8**.
169. Monkley, S.J., et al., *Endothelial cell talin1 is essential for embryonic angiogenesis.* Dev Biol, 2011. **349**(2): p. 494-502.
170. Dhakal, S., et al., *Abnormal retinal development in Cloche mutant zebrafish.* Dev Dyn, 2015. **244**(11): p. 1439-1455.
171. Heissig, B., et al., *Angiogenesis: vascular remodeling of the extracellular matrix involves metalloproteinases.* Curr Opin Hematol, 2003. **10**(2): p. 136-41.
172. Macdonald, R., et al., *The Pax protein Noi is required for commissural axon pathway formation in the rostral forebrain.* Development, 1997. **124**(12): p. 2397-408.
173. Sanyanusin, P., et al., *Mutation of PAX2 in two siblings with renal-coloboma syndrome.* Hum Mol Genet, 1995. **4**(11): p. 2183-4.
174. Sanyanusin, P., et al., *Mutation of the PAX2 gene in a family with optic nerve colobomas, renal anomalies and vesicoureteral reflux.* Nat Genet, 1995. **9**(4): p. 358-64.
175. Torres, M., E. Gómez-Pardo, and P. Gruss, *Pax2 contributes to inner ear patterning and optic nerve trajectory.* Development, 1996. **122**(11): p. 3381-91.
176. Brand, M., et al., *Mutations in zebrafish genes affecting the formation of the boundary between midbrain and hindbrain.* Development, 1996. **123**: p. 179-90.
177. Moosajee, M., et al., *Translational bypass of nonsense mutations in zebrafish rep1, pax2.1 and lamb1 highlights a viable therapeutic option for untreatable genetic eye disease.* Hum Mol Genet, 2008. **17**(24): p. 3987-4000.
178. Viringipurampeer, I.A., et al., *Pax2 regulates a fadd-dependent molecular switch that drives tissue fusion during eye development.* Hum Mol Genet, 2012. **21**(10): p. 2357-69.
179. Xie, J., et al., *A novel transgenic zebrafish model for blood-brain and blood-retinal barrier development.* BMC Dev Biol, 2010. **10**: p. 76.
180. Hao, J., et al., *In vivo structure-activity relationship study of dorsomorphin analogues identifies selective VEGF and BMP inhibitors.* ACS Chem Biol, 2010. **5**(2): p. 245-53.
181. Jeffrey, E.J. and B.D. Crawford, *The epitope-mediated MMP activation assay: detection and quantification of the activation of Mmp2 in vivo in the zebrafish embryo.* Histochem Cell Biol, 2018. **149**(3): p. 277-286.
182. Tsuji, N., et al., *Macrophage-Associated Gelatinase Degrades Basement Membrane at the Optic Fissure Margins During Normal Ocular Development in Mice.* Invest Ophthalmol Vis Sci, 2018. **59**(3): p. 1368-1373.
183. Nishida, Y., et al., *Activation of matrix metalloproteinase-2 (MMP-2) by membrane type 1 matrix metalloproteinase through an artificial receptor for proMMP-2 generates active MMP-2.* Cancer Res, 2008. **68**(21): p. 9096-104.
184. Strongin, A.Y., et al., *Mechanism of cell surface activation of 72-kDa type IV collagenase. Isolation of the activated form of the membrane metalloprotease.* J Biol Chem, 1995. **270**(10): p. 5331-8.
185. Theodore, L.N., et al., *Distinct Roles for Matrix Metalloproteinases 2 and 9 in Embryonic Hematopoietic Stem Cell Emergence, Migration, and Niche Colonization.* Stem Cell Reports, 2017. **8**(5): p. 1226-1241.

186. Hoshijima, K., et al., *Highly Efficient CRISPR-Cas9-Based Methods for Generating Deletion Mutations and F0 Embryos that Lack Gene Function in Zebrafish.* Dev Cell, 2019. **51**(5): p. 645-657 e4.
187. Heermann, S., et al., *Eye morphogenesis driven by epithelial flow into the optic cup facilitated by modulation of bone morphogenetic protein.* Elife, 2015. **4**.
188. Knickmeyer, M.D., et al., *TGFbeta-facilitated optic fissure fusion and the role of bone morphogenetic protein antagonism.* Open Biol, 2018. **8**(3).
189. Chen, S., et al., *Cadherin-mediated cell adhesion is critical for the closing of the mouse optic fissure.* PLoS One, 2012. **7**(12): p. e51705.
190. Lahrouchi, N., et al., *Homozygous frameshift mutations in FAT1 cause a syndrome characterized by colobomatous-microphthalmia, ptosis, nephropathy and syndactyly.* Nat Commun, 2019. **10**(1): p. 1180.
191. Richardson, R., et al., *Transcriptome profiling of zebrafish optic fissure fusion.* Sci Rep, 2019. **9**(1): p. 1541.
192. Cao, M., et al., *Metalloproteinase Adamts16 Is Required for Proper Closure of the Optic Fissure.* Invest Ophthalmol Vis Sci, 2018. **59**(3): p. 1167-1177.
193. Anthis, N.J., et al., *The structure of an integrin/talin complex reveals the basis of inside-out signal transduction.* Embo j, 2009. **28**(22): p. 3623-32.
194. Wegener, K.L., et al., *Structural basis of integrin activation by talin.* Cell, 2007. **128**(1): p. 171-82.
195. Calderwood, D.A., I.D. Campbell, and D.R. Critchley, *Talins and kindlins: partners in integrin-mediated adhesion.* Nat Rev Mol Cell Biol, 2013. **14**(8): p. 503-17.
196. Prout, M., et al., *Autosomal mutations affecting adhesion between wing surfaces in Drosophila melanogaster.* Genetics, 1997. **146**(1): p. 275-85.
197. Brown, J.D., et al., *Expression profiling during ocular development identifies 2 Nlz genes with a critical role in optic fissure closure.* Proc Natl Acad Sci U S A, 2009. **106**(5): p. 1462-7.
198. Cao, M., et al., *Regional Gene Expression Profile Comparison Reveals the Unique Transcriptome of the Optic Fissure.* Invest Ophthalmol Vis Sci, 2018. **59**(15): p. 5773-5784.
199. Thompson, M.A., et al., *The cloche and spadetail genes differentially affect hematopoiesis and vasculogenesis.* Dev Biol, 1998. **197**(2): p. 248-69.
200. Martínez-Alvarez, C., et al., *Medial edge epithelial cell fate during palatal fusion.* Dev Biol, 2000. **220**(2): p. 343-57.
201. Shen, J., et al., *Complex epithelial remodeling underlie the fusion event in early fetal development of the human penile urethra.* Differentiation, 2016. **92**(4): p. 169-182.
202. Zhang, H., et al., *Eyelid fusion and epithelial differentiation at the ocular surface during mouse embryonic development.* Jpn J Ophthalmol, 2005. **49**(3): p. 195-204.
203. Weaver, M.L., et al., *Hyaloid vasculature and mmp2 activity play a role during optic fissure fusion in zebrafish.* Sci Rep, 2020. **10**(1): p. 10136.
204. Lee, N.V., et al., *ADAMTS1 mediates the release of antiangiogenic polypeptides from TSP1 and 2.* Embo j, 2006. **25**(22): p. 5270-83.

205. Luque, A., D.R. Carpizo, and M.L. Iruela-Arispe, *ADAMTS1/METH1 inhibits endothelial cell proliferation by direct binding and sequestration of VEGF165.* J Biol Chem, 2003. **278**(26): p. 23656-65.
206. Amin, E., et al., *Rho-kinase: regulation, (dys)function, and inhibition.* Biol Chem, 2013. **394**(11): p. 1399-410.
207. Tan Ide, A., C. Ricciardelli, and D.L. Russell, *The metalloproteinase ADAMTS1: a comprehensive review of its role in tumorigenic and metastatic pathways.* Int J Cancer, 2013. **133**(10): p. 2263-76.
208. Lai, S.L., et al., *Rho mediates cytokinesis and epiboly via ROCK in zebrafish.* Mol Reprod Dev, 2005. **71**(2): p. 186-96.
209. Wang, G., et al., *The Rho kinase Rock2b establishes anteroposterior asymmetry of the ciliated Kupffer's vesicle in zebrafish.* Development, 2011. **138**(1): p. 45-54.
210. Weiss, O., et al., *Abnormal vasculature interferes with optic fissure closure in lmo2 mutant zebrafish embryos.* Dev Biol, 2012. **369**(2): p. 191-8.
211. Boerboom, D., et al., *Partially redundant functions of Adamts1 and Adamts4 in the perinatal development of the renal medulla.* Dev Dyn, 2011. **240**(7): p. 1806-14.
212. Bryan, B.A., et al., *RhoA/ROCK signaling is essential for multiple aspects of VEGF-mediated angiogenesis.* Faseb j, 2010. **24**(9): p. 3186-95.
213. Kim, S., et al., *Convergence and extrusion are required for normal fusion of the mammalian secondary palate.* PLoS Biol, 2015. **13**(4): p. e1002122.
214. Noh, H., et al., *Proper closure of the optic fissure requires ephrin A5-EphB2-JNK signaling.* Development, 2016. **143**(3): p. 461-72.
215. Patel, A., et al., *A molecular and cellular analysis of human embryonic optic fissure closure related to the eye malformation coloboma.* Development, 2020.
216. Sehgal, R., et al., *Ectopic Pax2 expression in chick ventral optic cup phenocopies loss of Pax2 expression.* Dev Biol, 2008. **319**(1): p. 23-33.
217. Zwerts, F., et al., *Lack of endothelial cell survivin causes embryonic defects in angiogenesis, cardiogenesis, and neural tube closure.* Blood, 2007. **109**(11): p. 4742-52.

VITA

Education

University of Kentucky (Lexington, KY)

August 2015 – January 15th, 2021

Biology Department Graduate Student, PhD Program

University of Kentucky (Lexington, KY)

August 2012 – May 2014

Bachelor of Science in Biology – Departmental Honors

Bluegrass Community and Technical College (Lexington, KY)

January 2010 – May 2012

Associate of Science – High Distinction

Published Manuscripts

Hyaloid vasculature and mmp2 activity play a role in optic fissure fusion in zebrafish. M.L. Weaver, W. Pereira Piedade, J. Smith, and J.K. Famulski. Scientific Reports, vol. 10, issue 1, June 2020

Spatiotemporal characterization of periocular mesenchyme heterogeneity during anterior segment development. Kristyn L. Van Der Meulen, Oliver Vöcking, Megan L. Weaver and Jakub K. Famulski. BioRxiv, August 2019.

Spatiotemporal characterization of optic fissure basement membrane suggests nidogen as a potential initiating factor during fissure fusion. Carrara Nicholas*, Megan Weaver*, Warlen Pereira Piedade*, Oliver Vöcking, and J.K Famulski. Developmental Biology, vol. 452, no. 1, 2019, pp. 43–54. (* denotes co-first authors)

Published Abstracts

Weaver, M, and J.K. Famulski. *Pax2a Regulates Endothelial Cell Invasion into the Optic Fissure Resulting in Degradation of the Basement Membrane by mmp2.* **Experimental Biology 2020**, San Diego, CA, April 2020.

Weaver, M, and J.K. Famulski. *Pax2 positively regulates angiogenesis in order to initiate optic fissure fusion.* **2019 Midwest Zebrafish Conference**, Lexington, KY, June 2019.

Weaver, M, and J.K. Famulski. *Pax2 positively regulates angiogenesis in order to initiate optic fissure fusion.* **The Association for Research in Vision and Ophthalmology**, Vancouver, BC, April 2019. Abstract has been chosen for a talk.

Megan Weaver, Jakub Famulski. *Pax2 Negatively Regulates Anti-Angiogenic Factors During Choroid Fissure Fusion.* **International Zebrafish Conference**, Madison, WI, June 2018.

Megan Weaver, Jakub Famulski. *Examining the Interplay Between the Extracellular Matrix and the Actin Cytoskeleton During Epithelial Fusion in the Choroid Fissure.* **2017 Midwest Zebrafish Meeting**, Cincinnati, OH, June 2017.

Megan Weaver, Michelle Geidt, and Douglas Harrison. *Unpaired3 is required for reliable formation of the Drosophila micropyle*. **National Conference on Undergraduate Research (NCUR)**, Lexington, KY April 2014

Chelsea C. Weaver, Connor Appelman, Andrea Gonzalez, Megan Weaver, Michelle Giedt, and Douglas Harrison. *Morphological Characterization of Male Reproductive Aging in Drosophila melanogaster*. **Kentucky Academy of Science (KAS) Annual Meeting**, Morehead, KY November 2013.

Rebecca Petersen, Shannon Brady, Casey Clark, Sandra Onekhena, Victoria Thompson, Connor Appelman, Andrea Gonzalez, Megan Weaver, Chelsea C. Weaver, Michelle Giedt, and Douglas Harrison. *A Genome-Wide Association Study to Identify Factors Regulating Reproductive Aging in Male Drosophila melanogaster*. **Kentucky Academy of Science (KAS) Annual Meeting**, Morehead, KY November 2013.

Honors and Awards

Graduate Research Fellowship Program (GRFP) Honorable Mention: Spring 2017

Lyman T. Johnson Fellowship: Fall 2015, $7,500 a year for up to 3 years

Transfer Scholarship: Fall 2012, $1,000 per semester for 2 years

Dr. Deborah L. Floyd Leadership Scholarship: Fall 2012, $500 a semester for a year

Megan Weaver